

OPTICAL STUDIES OF VLA FIRST SURVEY RADIO SOURCES

A thesis submitted to the
UNIVERSITY OF PUNE
for the degree of
DOCTOR OF PHILOSOPHY
in Physics

by

YOGESH G. WADADEKAR

Inter-University Centre for
Astronomy and Astrophysics
Post Bag 4, Ganeshkhind
Pune 411 007, INDIA

August 2000

To Aai, Baba and Aji
for making me the person I am

Contents

Acknowledgements	vii
Declaration	viii
Abstract	1
1 Large Area Radio Surveys	3
1.1 Advantages of radio surveys	3
1.2 A brief history of radio surveys	4
1.3 WENSS	4
1.4 NVSS	5
1.5 Sydney University Molonglo Sky Survey (SUMSS)	5
1.6 Faint Images of the Radio Sky at Twenty-cm (FIRST)	5
1.6.1 The FIRST source catalog	7
2 Large Area Optical Surveys	10
2.1 Palomar Observatory Sky Survey and the ESO-SERC Survey	10
2.2 Digitized Palomar Observatory Sky Survey (DPOSS)	10
2.3 Sloan Digital Sky Survey (SDSS)	11
3 Optical counterparts of radio sources	12
3.1 What kind of objects are they?	12
3.2 Unification models for extragalactic radio sources	13
3.3 How many sources can FIRST expect to see?	14
3.3.1 How many radio sources are there?	14
3.3.2 How far can FIRST see?	15
3.3.3 Limitations on morphological classification	15
3.3.4 Differential source counts: the mysterious blue galaxy population	15
3.3.5 Which of these sources can (should) we study using FIRST?	16
3.4 Techniques for obtaining optical identifications	16
4 Radio Emission from Quasars	18
4.1 Introduction	18
4.2 Radio/optical comparisons	19
4.2.1 1343+266: not a gravitationally lensed quasar?	23
4.3 Radio and optical properties	23
4.3.1 Bivariate luminosity functions	23
4.3.2 Distribution of radio luminosity	25
4.3.3 Distribution of radio-to-optical luminosity ratio R	27
4.4 Radio-loud Fraction	29
4.5 Summary	30
5 Radio emission from AGN	32
5.1 Introduction	32
5.2 Radio/optical comparisons	33
5.3 Distribution of radio luminosity	36

5.4	Radio luminosities of Seyfert galaxies	38
5.4.1	Normalized radio luminosities	39
5.5	Summary	40
6	Optical Identification of FIRST sources with DPOSS	41
6.1	Introduction	41
6.2	CCD calibration of DPOSS sources	42
6.3	DPOSS-FIRST cross correlation	42
6.3.1	The DPOSS source catalog	43
6.3.2	Matching the catalogs	43
6.3.3	Morphology of the identifications	44
6.4	Finding new quasars	44
6.4.1	FIRST Bright Quasar Survey (FBQS)	45
6.4.2	Low redshift quasar candidates	45
6.4.3	High redshift quasar candidates	49
6.5	Future work - a proposed FIRST faint quasar survey	50
7	On the detectability of AGN at high redshifts	53
7.1	Introduction	53
7.2	Surface Brightness	54
7.2.1	The Host Galaxy	54
7.2.2	The Active Galactic Nucleus	55
7.2.3	The k-Correction	55
7.2.4	The Point Spread Function	57
7.3	Limiting Redshift for Detection of Host Galaxy	58
7.3.1	Galaxy Without an AGN	58
7.3.2	Galaxy With AGN	60
7.4	Dependence of Limiting Redshift on Galaxy and Quasar Properties	62
7.4.1	Parameter Ranges and Correlations	62
7.4.2	Results	63
7.4.3	Comparison With Observations	70
7.5	Discussion	73
8	Optical morphology of low flux radio sources: astrometry and photometry	75
8.1	Introduction	75
8.2	Observations and reductions	76
8.2.1	Sample definition	76
8.2.2	CCD Imaging Observations	76
8.2.3	Basic reductions of the CCD images	77
8.2.4	Astrometry	77
8.2.5	Source identification and photometry	78
8.2.6	Photometric calibration with standard stars	79
8.3	Finding charts for our optical identifications	80
9	Optical imaging of low flux radio sources: morphology and decomposition	88
9.1	Morphology of the identifications	88
9.2	Some statistical correlations	90
9.2.1	Identification rate as a function of radio flux	90
9.2.2	Identification rate as a function of optical flux	90
9.2.3	Radio and optical flux distributions	90
9.3	Bulge disk decomposition of bright identifications	93
9.3.1	Modeling galaxy light distributions	93
9.3.2	Bulge disk decomposition for our identifications	93

10 Summary and future prospects	96
10.1 Summary	96
10.2 Where to go from here?	97
10.3 Surveys: the future of astronomy	97
A Two Dimensional Galaxy Image Decomposition Technique	99
A.1 Introduction	99
A.2 Simulation of Galaxy Images	99
A.3 2-D Decomposition Technique	100
A.3.1 Building The Model	100
A.3.2 The Decomposition Procedure	100
A.4 Reliability of Galaxy Image Decomposition	101
A.4.1 Large-Scale Testing under Idealized Conditions	101
A.4.2 Tests of stability	106
A.4.3 Effect of changing S/N ratio	106
A.4.4 Detecting a point source	109
A.5 Fitting real galaxy images	110
A.5.1 Possible pitfalls	110
A.5.2 Comparison of extracted parameters	110
A.6 Error estimation	111
A.7 Conclusions	111
B Angular cross-correlation Code	113
B.1 Description	113
B.2 The code	113
Bibliography	115

List of Figures

1.1	FIRST survey northern sky coverage as of July 2000	6
1.2	FIRST survey southern sky coverage as of July 2000	6
3.1	Schematic representation of the unified model for AGN	14
3.2	Radio flux as a function of redshift, for different classes of sources	15
3.3	Angular size as a function of redshift for different classes of radio sources	16
3.4	Differential source count at 1.4 GHz	17
4.1	The approximate boundaries of the FIRST survey	20
4.2	A histogram of the angular separation	21
4.3	Absolute magnitude of quasars in our sample as a function of redshift	24
4.4	Radio luminosity as a function of redshift	25
4.5	Radio luminosity as a function of absolute magnitude	26
4.6	Distribution of radio luminosity for the three kinds of quasars	27
4.7	R as a function of redshift	28
4.8	Distribution of R for quasars with radio detections and for upper limits	28
4.9	Radio loud fraction as a function of absolute magnitude	30
4.10	Radio loud fraction of quasars as a function of redshift	31
5.1	Histogram of angular separation between the AGN and FIRST source	34
5.2	Radio luminosity as a function of redshift	36
5.3	Absolute magnitude of the AGN as a function of redshift	37
5.4	Radio luminosity as a function of absolute magnitude	37
5.5	Integrated radio flux as a function of apparent magnitude	38
5.6	Redshift distribution of the detections for the Seyfert 1 (top panel) and the Seyfert 2 (bottom panel) galaxies.	39
6.1	Optical counterparts of some FIRST sources from DPOSS	44
6.2	Spectrum of the quasar 3C 273	46
6.3	Color-color plot for the quasar candidates	51
6.4	Integrated radio flux versus apparent magnitude	51
6.5	Histogram of the radio to optical flux ratio R^*	52
7.1	k-corrections obtained by Rocca-Volmerange & Guiderdoni	56
7.2	k-corrections obtained by Poggianti	57
7.3	Surface brightness of a Sc and an elliptical galaxy	59
7.4	The total surface brightness profiles of a Sc galaxy	61
7.5	Limiting redshifts for an Sa galaxy	64
7.6	Limiting redshifts for Sa galaxies	65
7.7	Limiting redshift for detection as an extended source	66
7.8	Limiting redshift for detection against total absolute magnitude	68
7.9	Limiting redshift for detection for different galaxy+AGN combinations	69
7.10	Limiting redshifts against total absolute magnitude for galaxies of different types	70
7.11	Limiting redshift for detection as an extended source as a function of host galaxy absolute magnitude	71
7.12	Limiting redshift for detection for different AGN luminosities	72

8.1	Finding charts for FIRST survey sources	81
8.1	(continued)	82
8.1	(continued)	83
8.1	(continued)	84
8.1	(continued)	85
8.1	(continued)	86
8.1	(continued)	87
9.1	Detection fraction as a function of integrated and peak radio flux densities	91
9.2	Detection fraction as a function of total V band magnitude	92
9.3	Integrated radio flux of the identifications as a function of V band total magnitude. The Y-axis has been plotted on a logarithmic scale. See the text for an explanation of the various symbols used.	92
9.4	Results of a bulge disk decomposition of J010252.33-005359.0	94
A.1	Sample output from the graphical routines in fitgal	102
A.2	Scatter plots of extracted versus input parameters with $n = 4$	104
A.3	Scatter plots of extracted versus input parameters with n free	105
A.4	Effects of incorrect estimation of PSF on extracted parameters	108
A.5	Results of point source extraction in 25 runs	109

List of Tables

1.1	Summary of recent large area radio surveys.	5
1.2	The FIRST source catalog	9
3.1	Local space densities and typical radio luminosities of some extragalactic radio sources	14
4.1	Summary of quasar radio detections	22
4.2	FIRST detections of quasars	23
5.1	Summary of radio detections	34
5.2	Number of radio detections of various classes of AGN	35
5.3	FIRST detections of AGN	35
5.4	Mean radio source size and mean radio luminosity for Seyfert 1 and Seyfert 2 galaxies.	38
6.1	Coordinates of the high galactic latitude DPOSS fields chosen for cross correlation with FIRST.	42
6.2	DPOSS-FIRST matches	43
6.3	Low redshift quasar candidates	46
6.4	High redshift quasar candidates	50
8.1	Weather conditions	76
8.2	Observed fields	77
8.3	Optical counterparts of FIRST survey sources	79
9.1	Results of bulge-disk decomposition	95
A.1	Effect of changing exposure time.	106
A.2	Comparison of extracted parameters.	111

Acknowledgements

My guide, Ajit Kembhavi has been a constant source of ideas and encouragement for me all through the thesis. He took charge when my own enthusiasm was flagging and made sure that I did not spend too much time stuck in the rut. Most importantly, he gave me the independence to develop my ideas and techniques.

The project that formed the seed of this thesis was initiated at the suggestion of Patrick McCarthy. Although the final product is far different from what he had envisaged, Pat has had an important role to play in this work. I thank him for his guidance and help.

My collaborators made work varied and interesting and taught me many new things. In chronological order they are Braxton Robbason, Patrick McCarthy, Ranjeev Misra, Habib Khoshroshahi, Bahram Mobasher and Ashish Mahabal. I am grateful to them.

The work contained in this thesis was made possible by computer software, all of it freely available and available for free. I would like to thank the creators of gcc, IRAF, KDE, L^AT_EX, Linux, Lyx, Perl, Pgperl, PGPLOT, SAOtnng, SExtractor, tcsh, vim and XEmacs for creating wonderful tools without which most of the work reported in this thesis would have been difficult if not impossible.

Last, but not the least, I wish to express my gratitude towards the students and postdocs of IUCAA for the wonderful time I had in their company. The treks, the movies, the snakes, the dinners and the mealtime gossip remain cherished memories. A special thank you to Srianand for being ever ready to discuss science with me, day or night and to Nirranjan Sambhus for a careful reading of an early draft of this thesis.

Declaration

CERTIFIED that the work incorporated in the thesis

Optical studies of VLA FIRST Survey radio sources

submitted by **Yogesh G. Wadadekar** was carried out by the candidate under my supervision. Such material as has been obtained from other sources has been duly acknowledged in the thesis.

Place: IUCAA, Pune
Date: 25 August 2000

Ajit K. Kembhavi
(Research Guide)

Abstract

This thesis is about the properties of the optical counterparts of the sources detected by the VLA FIRST (Faint Images of the Radio Sky at Twenty centimeters) radio survey.

The National Radio Astronomy Observatory (NRAO), USA, is undertaking a dedicated effort to produce a deep high-resolution survey of 25% of the celestial sphere at 1400 MHz. The Faint Images of the Radio Sky at Twenty centimeters (FIRST) survey currently being carried out by the Very Large Array (VLA) telescope is providing astronomers with high quality data with high sensitivity (1 mJy), good resolution (1 arc second) and large sky coverage (over 6000 square degrees already, eventually 10000 square degrees). The FIRST survey represents a 50-fold improvement in sensitivity, resolution and positional accuracy over previous large area radio surveys. The first half of the survey has been completed and the data have been publicly released. The FIRST catalog already lists over 560,000 radio sources with flux densities greater than 1 mJy at 20 cm. The surface density of radio sources is roughly 90 per square degree.

In this thesis we have adopted three distinct strategies for obtaining the optical counterparts of FIRST sources: (1) by cross correlation of the FIRST source catalog with catalogs of active galaxies and quasars, (2) by cross correlation of the FIRST catalog with an optical catalog from a complete photographic survey (DPOSS) and (3) by obtaining deep CCD images of a small portion of the FIRST survey area.

We begin the thesis by presenting an overview of major radio and optical surveys, focusing on the new surveys that are currently underway. We also list the various classes of objects that form the optical counterparts of extragalactic radio sources and summarize the unified orientation based scheme for understanding their phenomenology.

We then present an extensive analysis of radio emission from distant quasars and relatively nearby active galaxies, where the radio information was obtained from the FIRST survey. We report on *new* radio detections of 69 quasars and 206 active galaxies. We present several statistical correlations between the radio and optical properties of these objects and examine the implications of these to quasar evolution. In particular, we examine the bimodal distribution of radio luminosity in quasars. Our work with the FIRST survey allows us to measure the distribution of radio to optical flux ratios over a wide range from a single large but inhomogeneous sample.

Our second approach involves matching FIRST source positions with an unbiased, complete optical source catalog constructed from 3 plates from the DPOSS survey. We have obtained optical counterparts for over 2100 radio sources. As before, we examine the correlations between optical and radio properties. We construct a candidate list of over 250 quasars using selection criteria based on radio flux and optical colors.

The third approach is to obtain deep CCD images of a small area of the sky to allow optical identification, photometry and morphological classification of optical counterparts of a statistically significant number of FIRST sources. We have obtained data on 9 deep fields using a wide field CCD imager on the 2.5 m Dupont telescope at the Las Campanas Observatory in Chile. We have obtained photometric and morphological information on about 40 faint identifications, some of which are as faint as $m_v = 24$.

We have also developed a sophisticated two dimensional bulge disk decomposition software. This software called *fitgal* and our cross identification code have been described in the Appendix.

We end the thesis with a summary of the new results reported, and discuss the new lines of investigation that have been suggested by the present work.

This thesis is largely based on work reported in the following publications.

- **Y. Wadadekar**, B. Robbason & A. Kembhavi, *Two-dimensional Galaxy Image Decomposi-*

tion, AJ, 117, 1219 (1999)

- **Y. Wadadekar** & A. Kembhavi, *A Study of Quasar Radio Emission from the VLA FIRST Survey*, AJ, 118, 1435 (1999)
- A. Kembhavi, & **Y. Wadadekar** & R. Misra, *The appearance of AGN host galaxies at moderate redshifts*, Proceedings X Rencontres de Blois "The Birth of Galaxies", eds. B. Guiderdoni et al., Editions Frontiere (in press)
- A. Kembhavi, R. Misra & **Y. Wadadekar**, *The appearance of AGN host galaxies at moderate redshifts*, ApJ, (submitted)
- **Y. Wadadekar** & A. Kembhavi, *A Study of Radio Emission from AGN using the VLA FIRST Survey*, AJ, (to be submitted)
- **Y. Wadadekar**, A. Kembhavi & P. McCarthy, *Faint radio sources from the VLA FIRST survey I. Optical identifications*, AJ, (to be submitted)

My other publications are:

- H. Khosroshahi, **Y. Wadadekar** & A. Kembhavi, *Correlations among global photometric properties of disk galaxies*, ApJ, 533, 162 (2000)
- H. Khosroshahi, **Y. Wadadekar**, A. Kembhavi & B. Mobasher, *An infrared photometric plane for ellipticals and early type disk galaxies*, ApJ, 531, L103 (2000)

Chapter 1

Large Area Radio Surveys

Most studies of astronomical objects have their origins in surveys of one sort or another. Our understanding of radio galaxies and radio quasars in particular is deeply rooted in well-defined samples drawn from large radio surveys. Radio surveys are also strongly motivated by their utility in identifying classes of objects at other wavelengths, which can be used for studies going beyond radio source physics *per se*. In these multi-wavelength studies, optical identification of radio sources is particularly important since it is still true for the most part that an object is not *understood* until it has been identified and studied in the optical region. Atomic spectroscopy at optical and other nearby wavelengths provides a tremendous boost in diagnosing the physical conditions in these distant objects. Consequently, since the early days of radio astronomy, perspicuous astronomers have launched optical observation programs to find what optical sources might be identified with radio sources and to study their properties.

1.1 Advantages of radio surveys

Radio surveys can be used to generate large samples for followup observations in optical and other wavelength bands. Such radio selected samples of (extragalactic) sources have several advantages.

1. At moderate to high galactic latitudes, confusion by galactic stars and absorption by galactic dust are both negligible.
2. Neutral gas and dust surrounding the radio source itself cannot obscure it, and ionized gas (which is frequently found in starbursts) is transparent at radio frequencies $\nu > 3$ GHz. In fact, the most compact nuclear starbursts are transparent only at radio and far infrared (FIR) wavelengths (Condon Anderson & Helou 1991), and thus it is only at these wavelengths that a reliable measurement of their luminosity can be made.
3. Radio sources have smooth, nearly power-law spectra without any sharp redshift cutoffs. This is quite unlike the strong Lyman limit at 912 \AA which results in a redshift cutoff for detection of high redshift objects in the visible regions of the spectrum. The most luminous radio sources could easily be detected in sensitive radio surveys (such as FIRST) even if they were moved to redshifts $z > 10$.

Unfortunately, cosmological effects are not just a perturbation on the distance distribution of radio sources, they are the dominating factor. The median redshift of radio source samples is $z \sim 0.8$, with little dependence on limiting flux density (Condon 1989). Because of the rather high median redshift, only a few radio sources are close enough to be bright optically, making optical identifications, for redshift and other measurements, extremely difficult. The situation can be remedied only by carrying out deep radio surveys that will increase the absolute number of radio sources available for study, to be followed by deep optical surveys that will increase the fraction of radio sources with detectable optical counterparts. Fortunately, both types of surveys are now becoming available - the NVSS and FIRST surveys in the radio and the Sloan Digital Sky Survey (SDSS) in the optical.

We will begin this thesis with a summary of deep, large area, sky surveys in the radio and optical bands.

1.2 A brief history of radio surveys

The 3C survey of the 1960's was the first high quality survey for radio sources. This survey discovered nearly 500 sources to a flux level of 9 Jy at a frequency of 178 MHz. A later revision with more accurately calibrated fluxes called the 3CR catalogue includes all 328 sources brighter than 9 Jy and situated north of declination -05° . An extensive effort to identify the optical counterparts of 3CR sources was carried out over a period of three decades; as a result virtually all sources in the survey have been optically identified (Djorgovski et al. 1988 and references therein).

Several deeper surveys followed the 3CR. The 4C survey covered nearly all the northern sky to a flux limit of 2 Jy at 178 MHz. A comparable survey covering the southern sky was performed at the Parkes radio telescope in Australia. Other surveys completed in the early 1970's include those at the Molonglo (Australia) and Bologna (Italy) radio observatories.

As high frequency receiver technology continued to improve, higher frequencies could be explored with excellent angular resolution made possible by radio interferometry. The overall improvement in sensitivity resulted in a great increase in the number of sources per unit solid angle of sky, making deep surveys over the *whole sky* cumbersome. Consequently the next generation of surveys tended to divide themselves into relatively shallow *all sky* surveys and deep *pencil-beam* surveys that covered only a small field of view.

Complete high frequency sky coverage has been provided by a pair of surveys, one in the north and one in the south. The entire northern sky was surveyed at 1.4 and 5 GHz by the NRAO at Green Bank down to a limiting flux of 0.8 Jy at 5 GHz while the Parkes Radio telescope cataloged southern sky sources to 0.7 Jy at 2.7 GHz. The brightest sources from these surveys are listed in the 2 Jansky catalog by Wall & Peacock (1985) which contains all sources brighter than 2 Jy at 2.7 GHz over 9.8 steradian (78%) of the sky. Virtually all of these sources now have optical identifications.

There have been many pencil beam surveys as well. Typically, as their sensitivity grows, their sky coverage shrinks. For example, the 5C survey is a series of observations with pencil beams, each ~ 10 square degrees in size, within which sources are found at 408 MHz down to 10 mJy and at 1.4 GHz down to 2 mJy. In another such survey, Windhorst et al. (1985), also working at 1.4 GHz, covered only 3 square degrees but identified sources as faint as 0.3 mJy. The Phoenix Deep Survey (Hopkins et al. 1998) reached a 5σ sensitivity of 0.3 mJy but covered a larger area - a circular region about 2 degrees in diameter. At higher frequencies, surveys have gone deeper still over even smaller areas: as faint as 15 μ Jy at both 5 GHz (Fomalont et al. 1991) and 8.4 GHz (Windhorst et al. 1993). The former survey covered a region 16 arcmin in diameter, the latter two fields each 7 arcmin on a side.

With further improvements in radio telescope technology, contemporary surveys can do better - they can combine high sensitivity with large sky coverage. We now summarize four of the most important large area, deep radio surveys of our time - WENSS, NVSS, SUMSS and **FIRST**.

1.3 WENSS

The Westerbork Northern Sky Survey (WENSS) is a low-frequency radio survey, designed to cover the whole sky north of 30° declination at a wavelength of 92 cm (325 MHz) to a 5σ limiting flux density of approximately 18 mJy. Additionally, about a quarter of this region, concentrated at high galactic latitudes, has been covered at a wavelength of 49 cm (609 MHz), to a 5σ limiting flux density of approximately 15 mJy. The survey was carried out with the Westerbork Synthesis Radio Telescope (WSRT) in the Netherlands. The data products from WENSS are flux density maps and source lists for all four Stokes parameters (I, Q, U, V). Maps have been produced at a resolution (FWHM of the restoring beam) of 54×54 arcsec at 92 cm and 28×28 arcsec at 49 cm. The astrometric accuracy for strong sources is 1.5 arcsec at both 92 cm and 49 cm.

WENSS is particularly useful since radio spectral information on an unprecedented number of sources over a substantial fraction of the sky has become available. WENSS will provide spectral information, both internally (from fluxes at 325 and 609 MHz), and by comparison with radio surveys at other frequencies such as NVSS and FIRST (1400 MHz). Thus WENSS will permit the study of very large numbers of sources with extreme radio spectra. These include ultra steep spectrum (USS) sources (e.g. high-redshift radio galaxies and cluster halos), and flat spectrum

Parameter	FIRST	NVSS	SUMSS	WENSS
Frequency (MHz)	1400	1400	843	325
Sky coverage (deg ²)	10000	33700	8000	10100
Resolution (arcsec)	5	45	43	54
Detection limit (mJy)	1	2.5	5	18
Source density (deg ⁻²)	90	60	37	21

Table 1.1: Summary of recent large area radio surveys.

sources (e.g. high-redshift quasars). For more details of this survey see Rengelink et al. (1997) or the WENSS website at <http://www.strw.leidenuniv.nl/wenss/>

1.4 NVSS

The NRAO VLA Sky Survey (NVSS) covered 82% of the sky north of -40° at 1.4 GHz (33700 square degrees), using the VLA in its D configuration. NVSS is based on 217,446 *snapshot* observations of partially overlapping primary-beam areas, each of which was imaged separately. The small snapshot images were weighted, corrected, and combined to yield a set of 2326 large ($4^\circ \times 4^\circ$) image *cubes* whose three axes span the Stokes polarization parameters I, Q, and U. The NVSS, which was completed in 1999, was used to generate a catalog of almost 2 million discrete sources stronger than 2.5 mJy. The images all have 45 arcsec FWHM resolution and nearly uniform sensitivity. The angular resolution used is much larger than the median size of faint extragalactic sources in order to achieve the high surface-brightness sensitivity needed for flux-limited completeness and good photometric accuracy. The large images have rms brightness fluctuations of 0.45 mJy in total intensity. The rms uncertainties in right ascension and declination vary from 1 arcsec for the 4×10^5 sources stronger than 15 mJy to 7 arcsec at the survey limit of 2.5 mJy.

For more details of this survey see Condon et al. (1998) and the NVSS website at <http://www.cv.nrao.edu/~jcondon/nvss.html>

1.5 Sydney University Molonglo Sky Survey (SUMSS)

The Molonglo Observatory Synthesis Telescope (MOST), operating at 843 MHz with a $5^\circ \times 5^\circ$ field of view is being used for a radio imaging survey of the sky south of declination -30° . This survey (the Sydney University Molonglo Sky Survey, or SUMSS) produces images with a resolution of 43×43 arcsec and an rms noise level of 1 mJy per beam (Bock, Large & Sadler 1999). The SUMSS is therefore similar in sensitivity and resolution to the NVSS described above. The survey is progressing at a rate of about 1000 square degrees per year, yielding individual and statistical data for thousands of weak radio sources.

SUMSS covers some areas of the southern sky not covered by the NVSS, at a comparable resolution and sensitivity. It will provide valuable radio spectral index information in the regions of overlap, since the frequency at which the survey is being carried out is different from the NVSS frequency.

1.6 Faint Images of the Radio Sky at Twenty-cm (FIRST)

FIRST - Faint Images of the Radio Sky at Twenty-cm - is an ongoing project designed to produce the radio equivalent of the Palomar Observatory Sky Survey over 10,000 square degrees (π steradian) around the North Galactic Cap. Using the NRAO Very Large Array (VLA) in its B-configuration, 3-minute snapshots covering a hexagonal grid using 2×7 3-MHz frequency channels centered at 1365 and 1435 MHz are obtained. The data are edited, self-calibrated, mapped, and CLEANed using an automated pipeline based largely on routines in the Astronomical Image Processing System (AIPS) software. Maps of the individual pointings (the grid images) are weighted and summed to yield a

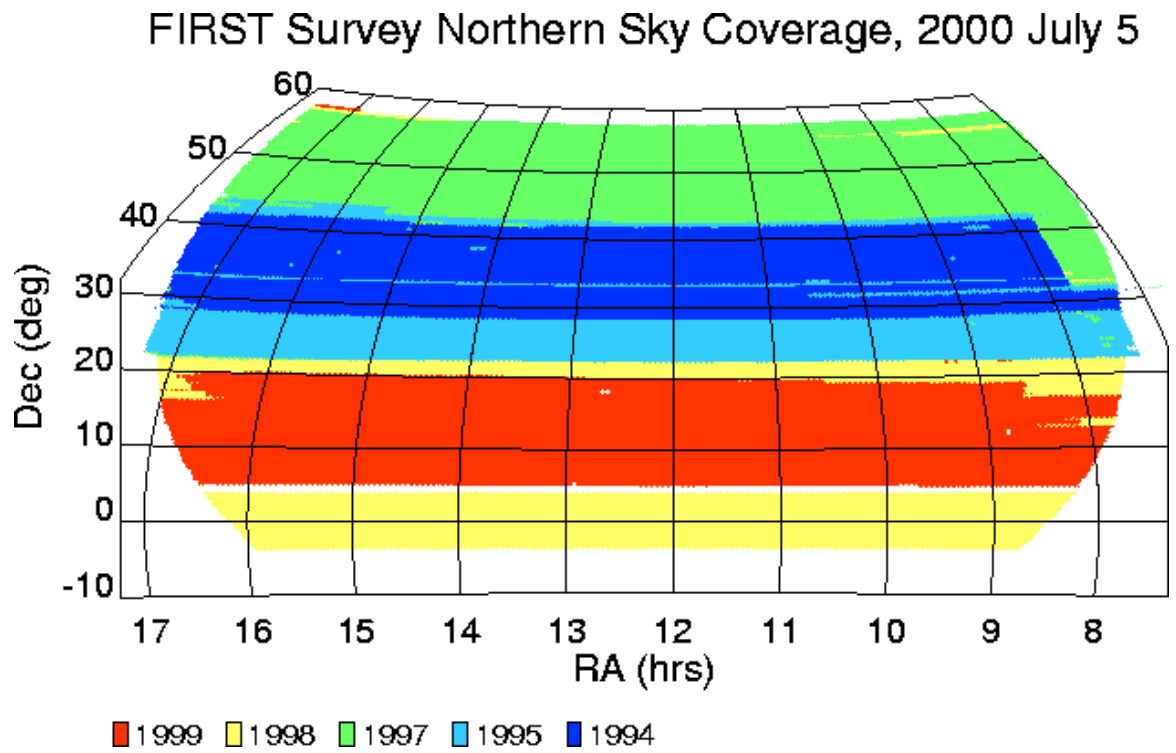


Figure 1.1: FIRST survey northern sky coverage as of July 2000

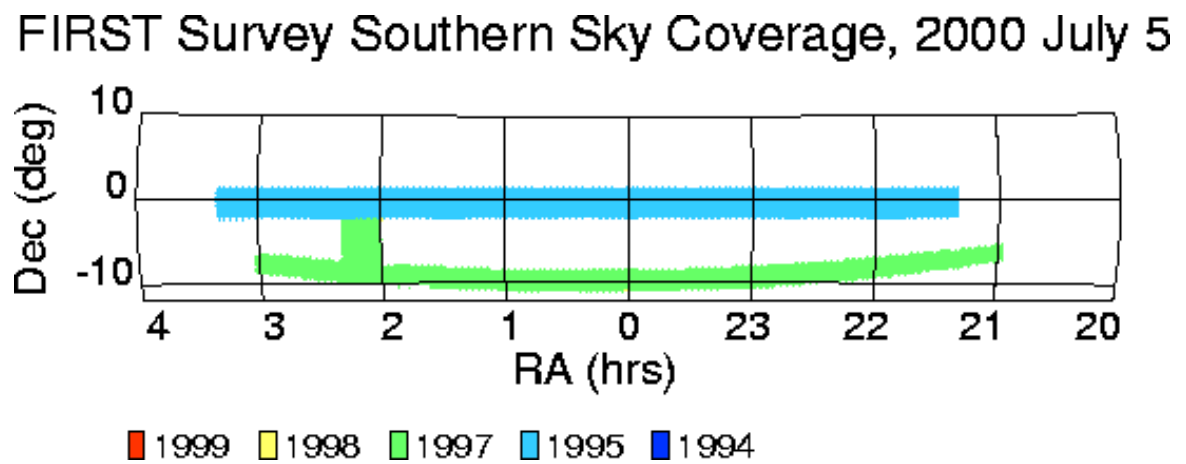


Figure 1.2: FIRST survey southern sky coverage as of July 2000

set of final co-added images with 1550×1150 pixels each. The CLEAN beam size is 5.4 arcsec FWHM, and the peak-to-peak sensitivity variations over each image are $\sim 8\%$. The median rms for the coadded images is $140 \mu\text{Jy}$. The final intensity maps have 1.8 arcsec pixels, a typical rms of 0.15 mJy, and a resolution of 5 arcsec. At the 1 mJy source detection threshold, there are ~ 90 sources per square degree, $\sim 35\%$ of which have resolved structure on scales from 2-30 arcsec (Cress et al. 1996). The astrometric reference frame of the maps is accurate to 0.05 arcsec, and individual sources have 90% confidence error circles of radius < 0.5 arcsec at the 3 mJy level and 1 arcsec at the survey threshold of 1 mJy.

As of July 2000, images and catalog data for about 8000 square degrees of sky have been made public by the FIRST team. In Figure 1.1 and Figure 1.2 we show the portions of the sky (in equatorial coordinates) that have been covered by these data.

1.6.1 The FIRST source catalog

Deriving a catalog of discrete sources from astronomical images is not a new problem, and a number of well-documented computer programs already exist for this purpose (e.g. DAOPHOT, SExtractor). However, most of these programs were developed specifically for extracting point sources from *optical* images and are generally not well suited for use with high-resolution radio images, in which a significant fraction of the sources are clearly extended. To overcome this limitation the FIRST team developed an AIPS-based routine for source extraction which is called HAPPY.

HAPPY starts by searching an image for pixels with flux that exceeds a user-provided threshold. It then defines the minimum-size rectangle around each contiguous set of threshold-exceeding pixels. The resulting rectangles, or islands, are padded with a border 3 pixels wide. If this border touches another island, any border-strip pixels exceeding the threshold are ignored in the subsequent fit. The pixels in each island are searched for local maxima, which are used as initial estimates for a two-dimensional Gaussian fitting algorithm. The individual islands are analyzed in order of decreasing brightness. As the components in each island are fitted, the results of the fitting algorithm must pass several acceptance criteria. If any of these criteria are not met, the island is re-fitted with one fewer component. Islands are also rejected if they intersect the edge of the image; such areas of sky are always covered more completely in the adjacent image. The results of a successful fit are subtracted from the original image before the next island is fitted.

The end product of HAPPY is a list of elliptical Gaussian components. For each component, HAPPY provides a right ascension and declination, peak and integrated flux densities, major and minor axes, and the position angle of the major axis measured east from north. In addition, an error estimate is calculated for each parameter.

Duplicate entries in the catalog are deleted using certain criteria to identify them. However the catalog still contains a small number of spurious sources that are sidelobes of imperfectly CLEANed, nearby, bright sources. A machine-learning method was adopted to identify and flag as many of the spurious sources as possible. Several hundred fields containing bright sources were examined by eye and catalog sources that appeared to be sidelobes were marked. The complete list of sources in these fields, marked and unmarked were used as a training set for an oblique decision-tree program. The decision-tree program then attempted to identify a series of tests based on linear combinations of the parameters that would partition the training set objects into sidelobes and non-sidelobes. After a reliable, reasonably simple decision tree had been developed, it was applied to all the sources in the catalog in order to determine which objects might be sidelobes. For sources identified as possible sidelobes a sidelobe warning flag is included in the catalog. Although this automated classification of sidelobes is fairly robust, examination of the images by eye is necessary to unambiguously determine whether any particular flagged source is a sidelobe or not.

The methodology for generating the radio source catalog summarized above and the reliability and accuracy of the extracted catalog parameters are discussed in detail by White et al. (1997).

The FIRST source catalog is sorted by right ascension; a few sample lines are shown in Table 1.2 for illustration regarding its form and content. We provide below brief explanatory notes about each column of the catalog. For more details, refer to the catalog documentation at the FIRST Homepage from where this information has been taken:

- RA, Dec are the position (J2000) of the source. The accuracy of the position depends on the

brightness and size of the source and the noise in the map. Point sources at the detection limit of the catalog have positions accurate to better than 1 arcsec at 90% confidence; 2 mJy point sources in typically noisy regions have positions good to 0.5 arcsec. An empirical expression for the positional accuracy is

$$\text{unc}(90\% \text{ confidence}) = \text{Size} (1/\text{SNR} + 1/20) \text{ arcsec}$$

where **Size** is either the major or minor axis fitted FWHM (**fMaj** or **fMin**) as given in the catalog and **SNR** is the peak flux density signal-to-noise ratio:

$$\text{SNR} = (\text{Fpeak} - 0.25) / \text{Rms}$$

The best possible positional uncertainty is limited to about 0.1 arcsec by the requirement to fit source positions in maps with 1.8 arcsec pixels and by various random calibration uncertainties. Systematic errors in the positions are smaller than 0.05 arcsec.

- **W** is a warning flag indicating that the source may be a sidelobe of a nearby bright source. In the July 1999 version of the catalog, 19,696 sources (3.6%) are flagged as possible sidelobes. A visual analysis of the northern catalog indicates that <10% of the objects flagged as sidelobes are real sources and that <1% of the unflagged sources in the catalog are sidelobes.
- **Fpeak** and **Fint** are the peak and integrated flux densities measured in mJy. They are derived by fitting an elliptical Gaussian model to the source using HAPPY. To correct for the CLEAN bias effect, 0.25 mJy has been added to the peak flux density and the integrated flux density has been multiplied by $(1 + 0.25/\text{Fpeak})$. The uncertainty in **Fpeak** is given by the rms noise at the source position, while the uncertainty in **Fint** can be considerably greater depending on the source size and morphology. For bright sources the accuracies of **Fpeak** and **Fint** are limited to about 5% due to systematic effects. Note that for sources that are not well-described by an elliptical Gaussian model, **Fint** is not an accurate measure of the integrated flux density.
- **Rms** is a local noise estimate at the source position measured in mJy. **Rms** is computed by combining the measured noise from all grid pointing images contributing to this coadded map position. Note that the significance of detection for a source is $(\text{Fpeak} - 0.25)/\text{Rms}$, not Fpeak/Rms , because of the CLEAN bias correction to the peak flux density. The catalog includes only sources brighter than 5 **Rms**.
- **Maj**, **Min**, and **PA** give the major and minor axes (FWHM in arcsec) and position angle (degrees east of north) derived from the elliptical Gaussian model for the source. **Maj** and **Min** have been deconvolved to remove blurring by the elliptical Gaussian point-spread function. (The fitted parameters before deconvolution are given in the **fMaj**, **fMin**, and **fPA** columns.) In the north the beam is circular with 5.4 arcsec FWHM; in the south it is elliptical, 6.4×5.4 arcsec FWHM, with the major axis running north-south. Noise can cause the fitted values of the major and minor axes (before deconvolution) to be smaller than the beam. The corresponding deconvolved size is given as zero in those cases. The uncertainties in the deconvolved sizes depend on both the brightness and the sizes. Objects at the catalog flux density limit have uncertainties of about 2 arcsec in their sizes (so faint objects with $\text{Maj} < 2$ arcsec are consistent with point sources). A simple empirical estimate of the uncertainty is

$$\text{Sigma}(\text{Size}) = 10 \text{ arcsec} (1/\text{SNR} + 1/75)$$

where **SNR** is the signal-to-noise ratio defined above.

- **fMaj**, **fMin**, and **fPA** give the major and minor axes (FWHM in arcsec) and position angle (degrees east of north) derived from the elliptical Gaussian model for the source. These are the fitted sizes measured directly from the image; the elliptical point-spread function has not been deconvolved.

The work reported in this thesis focuses on statistical properties of large numbers of radio sources, without regard to the details of their radio morphology. For such work, it is convenient to use a catalog rather than the original imaging data. The FIRST catalog has been used as the source of radio data throughout this thesis.

Table 1.2: The FIRST source catalog. This catalog is available in its entirety in the electronic form from the FIRST Homepage (<http://sundog.stsci.edu/>). A portion is shown here to illustrate its form and content.

RA	Dec (2000)	W	Fpeak	Fint	Rms	Maj	Min	PA	fMaj	fMin	fPA
06 50 44.043	+31 10 00.09		1.16	0.64	0.147	0.00	0.00	42.0	4.50	3.59	42.0
06 51 02.181	+31 11 13.33		1.58	2.66	0.139	4.99	3.94	91.6	7.35	6.69	91.6
06 51 03.826	+31 13 03.32	W	1.02	1.42	0.137	7.63	0.00	2.4	9.35	4.34	2.4
06 51 06.134	+31 19 02.00		7.29	9.64	0.145	4.09	1.82	131.3	6.77	5.70	31.3
06 51 10.784	+31 11 28.80		72.36	100.79	0.141	4.18	2.49	9.8	6.83	5.95	9.8

Chapter 2

Large Area Optical Surveys

2.1 Palomar Observatory Sky Survey and the ESO-SERC Survey

Large telescopes make large surveys necessary to identify objects for them to study. The pioneering all sky photographic survey was the Palomar Observatory Sky Survey. This survey, partially funded by the National Geographic Society, was carried out at Mt. Palomar using a dedicated 48-inch Schmidt telescope between 1950 and 1958. A mosaic of almost 1000 fields covered the entire northern sky down to -33° declination in two filters. Although the survey was originally conceived simply as a tool for finding interesting stars, nebulae and galaxies for further study with large optical telescopes, it has turned out to be of immense value in the identification of objects found at other wavelengths, first radio sources and more recently X-ray, ultraviolet and infrared sources. The data have also been invaluable in their own right, for example in studies of the large scale structure of the Universe. The success of this northern survey led the builders of the large southern telescopes in the 1970's to erect companion Schmidt telescopes, the UK 1.2 m Schmidt telescope alongside the 3.9 m Anglo Australian telescope in Australia and the ESO 1.0 m Schmidt beside the 3.6 m telescope in Chile. These two southern Schmidts extended the survey work to the southern sky - the ESO-SERC survey was carried out between 1974 and 1990. Given the advances in photographic emulsions and telescope technologies over the intervening twenty years, the ESO-SERC survey reached about 1.5 magnitudes fainter than its northern counterpart, without any increase in telescope time requirements.

The $6.5^\circ \times 6.5^\circ$ photographic plates from both the northern and southern surveys were subsequently digitized using a modified PDS micro-densitometer to a scale of about 1.7 arcsecond per pixel. The entire survey is available as a set of 102 CDROMs.

There were two serious limitations to these early surveys: (1) the coarse 1.7 arcsecond pixel size of the digitized scans led to some loss of information and more seriously (2) accurate photometric calibration was lacking. These issues were addressed by the next generation of digitized photographic surveys, the most important of which is the Digitized Palomar Observatory Sky Survey, the DPOSS.

2.2 Digitized Palomar Observatory Sky Survey (DPOSS)

DPOSS is an ongoing, next generation digitized survey of the northern sky, based on the POSS-II photographic sky atlas. POSS-II covers the entire sky north of declination $\delta = -3^\circ$ in the 3 photographic *JFN* bands, which have been calibrated using CCD data to Gunn *gri*. It reaches an equivalent limiting magnitude of $B_{lim} \sim 22$ using 894 overlapping fields (6.5° square each with 5° spacings). A modified PDS scanner is currently being used to digitize the photographic plates and a very extensive CCD calibration program ensures photometric uniformity of $\sim 5 - 10\%$ in magnitude zero-points. The digitized images are processed using a specially developed software called SKICAT (Weir et al. 1995), which incorporates some standard astronomical image processing packages, a commercial Sybase database management system, as well as a number of artificial intelligence and machine learning modules to measure over 60 parameters per object on each plate, a subset of which is used for object classifications.

The end product of the survey will be the Palomar-Norris Sky Catalog, anticipated to contain 50 million galaxies and 2 billion stars. For further details of this survey see Djorgovski et al. (1997) and the DPOSS website at http://astro.caltech.edu/~rrg/science/dposs_public.html.

Even a sophisticated photographic survey such as DPOSS has limitations, most of them caused by the deficiencies of photographic plates. In the last decade, a solid state electronic detector called the Charge Couple Device (CCD) has become universally available. Fully digital cameras based on CCD detectors can overcome many of the deficiencies of photographic plates, and so recent surveys use them extensively. By far the largest of these third millennium CCD surveys is the Sloan Digital Sky Survey (SDSS).

2.3 Sloan Digital Sky Survey (SDSS)

SDSS is an ongoing, digital, photometric and spectroscopic survey of the northern sky using a dedicated 2.5 m telescope at Apache Point, New Mexico, USA. It will cover a large fraction of the sky - 10,000 deg² around the north Galactic cap and will be complete within precisely defined selection criteria. The survey also includes much deeper imaging of an area covering 225 deg² in the southern Galactic hemisphere.

The photometric map of the sky constructed from the SDSS will measure accurate flux densities of objects almost simultaneously in five bands (u' , g' , r' , i' , and z') with effective wavelengths of 3540 Å, 4760 Å, 6280 Å, 7690 Å, and 9250 Å respectively. It will complete to limiting (5:1 signal-to-noise) point source magnitudes of 22.3, 23.3, 23.1, 22.3, and 20.8 respectively in these bands around the North Galactic cap. The large sky coverage of about π steradian will result in photometric measurements to the above detection limits for about 5×10^7 galaxies and a somewhat larger number of stars. The morphological and color information from the images will allow robust star-galaxy-quasar separation yielding a photometric sample of about 10^6 quasar candidates. Astrometric positions will be produced which will be accurate to ~ 50 milliarcseconds for sources brighter than ~ 20.5 magnitude, aiding unambiguous cross identification with sources from surveys at other wavelengths (such as the FIRST survey). Medium resolution spectra will be obtained for the 10^6 galaxies brighter than about $r' \sim 18.1$, approximately 10^5 quasars brighter than $g' \sim 19.7$, and carefully selected samples of stars. The deeper southern survey will go about 2.0 magnitudes fainter in all bands, and, in addition to being a bridge between the main northern survey and much deeper pencil-beam surveys possible with very large telescopes, will contain much information about faint variable sources, supernovae, and proper motions.

The SDSS is also expected to make a substantial contribution to all deep surveys by characterizing the nearby Universe in a detailed and quantitative manner. Without this information, which does not exist in any satisfactorily accurate and complete form at present, one cannot statistically compare the Universe observed at high redshifts and early epochs by the deep surveys, to the Universe today.

The primary photometric data products will be merged 5-band catalogs of image parameters (position, flux, size, profile); *atlas images* (cut-out pixel maps around each detected object) and a link to its spectrum, if available. The primary spectroscopic data products will include a one-dimensional flux-calibrated spectrum, a derived redshift (separately for emission lines and absorption lines), a emission and absorption line list, a link to photometric and astrometric data and information detailing why the object was selected as a spectroscopic target.

The data will be made available to the astronomical community as soon as processing and calibration is complete. The data will be distributed on various data storage formats, and will also be accessible on the Internet. More details about this survey, including recent science results from the commissioning data are available at the SDSS website at <http://www.sdss.org/>.

Chapter 3

Optical counterparts of radio sources

3.1 What kind of objects are they?

The optical counterparts of faint radio sources make up a veritable zoo of astronomical objects. In this chapter we will list the possible astronomical sources that may host a radio source, and briefly describe the unification scheme for these sources. We will also look at the local number densities and typical luminosities of each class of radio source.

The following classes of astronomical objects have been identified as the optical counterparts of radio sources in the literature. Although they are arranged roughly in increasing order of mean radio luminosity, there is often considerable overlap in the range of radio luminosities spanned by adjacent classes. A more detailed discussion of most of these classes can be found in Kembhavi & Narlikar (1999).

1. **Radio stars:** These have a typical radio luminosity of 10^{16} erg sec⁻¹ Hz⁻¹. They include Algol-type systems, RS CVn binaries, massive O-star binaries, and even some of the X-ray binary systems. Stellar radio emission is known to be variable in nature. At the 1 mJy flux limit these objects can be (and have been) detected only out to a few hundred parsecs. Less than 0.1% of FIRST sources are expected to be radio stars (Helfand et al. 1999).
2. **Low ionization nuclear emission line regions (LINERS):** are located in the nuclear region of galaxies. They are characterized by relatively strong lines of low ionization species (O-I, S-II etc.).
3. **Nuclear HII regions:** Many galactic nuclei show narrow lines (Balmer, [OIII]), characteristic of H-II regions ionized by hot stars. This phenomenon is the low intensity version of starbursts; the radio emission is consequently weak and can only be detected at very low redshifts with a survey such as FIRST.
4. **Starburst galaxies:** These are galaxies in which star formation takes place at a rate far higher than the average during a galactic lifetime. The phenomenon may be identified through optical colors and spectra (young stars) and through a large IR output. Star formation activity is known to be triggered by mergers of galaxies. Their radio emission originates in H-II regions surrounding massive short lived stars in the starburst, and in cosmic rays accelerated in the supernova remnants of these stars. This population of radio sources powered by stars is known to obey a remarkably tight correlation between radio and far infrared flux (Condon, Anderson & Helou 1991 and references therein).
5. **Seyfert 1 galaxies:** The nuclei of these galaxies have very wide hydrogen lines with broad wings. Seyfert nuclei are typically found in early type spiral galaxies. The difference between Seyferts and quasars mentioned in the literature often reflect more the method of discovery than a well defined classification. At low redshifts, where the host galaxy is usually visible, the object is classified as a Seyfert; at higher redshifts the same object may be classified as a quasar (e.g. Kembhavi, Misra & Wadadekar 2000).
6. **Seyfert 2 galaxies:** Whereas the Sy 1 nuclei have broad wings in the permitted emission lines in their spectra and narrow forbidden lines, the Sy 2 nuclei tend to have equally narrow

permitted and forbidden lines. The precise classification of Sy 1, Sy 2 and several intermediate classes is discussed by Osterbrock (1981). Seyfert 2 nuclei are also hosted predominantly by early type disk galaxies. Radio emission from Seyfert nuclei is discussed in Chapter 5.

7. **Radio quiet quasars:** These objects optically resemble the radio loud quasars, but their radio luminosity is much lower. A few objects in the class do not have any detectable radio emission even at the $1 \mu\text{Jy}$ level.
8. **Radio galaxies:** These tend to be associated with luminous elliptical galaxies. They show strong cosmological evolution, their number per unit of comoving volume being much larger at $z = 2$ than locally at $z = 0$. Frequently, elaborate structures like cores, jets, hotspots and radio lobes are seen. For a detailed discussion of the radio properties of these objects see Kembhavi & Narlikar (1999).
9. **Radio loud quasars:** The radio characteristics of these objects are similar to those of the radio galaxies, but the optical image is dominated by a bluish, unresolved, luminous nucleus with strong broad emission lines in its optical spectrum. Radio emission from quasars detected by the FIRST survey is discussed in Chapter 4.
10. **BL Lac objects:** These resemble the flat spectrum radio loud quasars, except that the optical emission lines are absent or are very weak. They tend to be highly variable at radio, optical and X-ray wavelengths with strong and variable optical polarization. The variability timescale at optical and X-ray wavelengths can be less than a day. All known BL Lacs are strong radio sources. The radio variability timescale is considerably longer than a day.
11. **Optically violent variables (OVV):** are a subclass of (mainly) radio loud quasars with optical characteristics similar to the BL Lacs, except that broad emission lines are present though they are weaker than those found in quasars. BL Lac and OVV type radio sources are very similar except with regard to the strength of their emission lines. They are often grouped together into a single class called *blazars*.

3.2 Unification models for extragalactic radio sources

All the extragalactic sources of radio emission listed in the previous section (except starbursts) can be understood in the context of an orientation based unified scheme illustrated schematically in Figure 3.1. An absorbing torus (shaded circles) with a radius of a few parsec surrounds the radiating nucleus. Within the torus are fast moving clouds of the Broad Line Region and outside it are the slower clouds of the Narrow Line Region. In the upper half of the figure we represent situations where relativistic jets are generated in the nucleus; the lower half represents active galactic nuclei where such jets are absent. Looking nearly into the jet the rapid variability of OVV's and BL Lacs would be seen due to relativistic Doppler boosting; when the broad line clouds would be absent or the boosting very strong, no broad emission lines would be visible. At a larger angle from the jet a radio quasar would result. When the central source is obscured, but some of the broad line clouds are still in view, the appearance is that of a radio galaxy with broad lines and at still larger angles a radio galaxy with only narrow lines would remain.

When, as in the lower half of the figure, no jet (or only a very weak one) is present radio quiet quasars and Sy 1 would result if the nucleus is in view and Seyfert 2 if the nucleus is not. Even though a collimated jet is missing, a fast jet from the nucleus could be expected. It is possible that such a wind ablates the torus or a broad line cloud and the Broad Absorption Line (BAL) quasars result.

This figure shows how much of the complex phenomenology of AGN may be produced in a simple model. Although the model does explain most of the current data, there are counter examples to almost everything. This is because the real situation is likely to be more complex with variability of the nucleus and intrinsic differences in the distribution of the gas clouds also playing a role.

For a more extensive discussion of the unification scheme outlined above see the review articles by Antonucci (1993) and Urry & Padovani (1995).

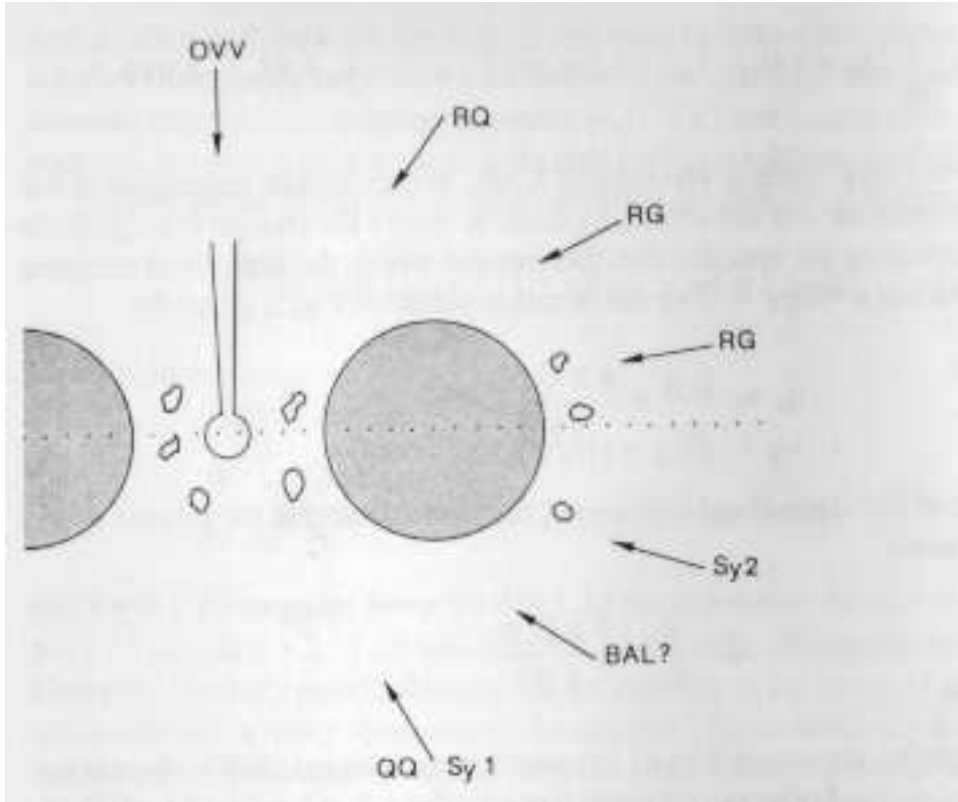


Figure 3.1: Schematic representation of the unified model for AGN. OVV: optically violent variables, RQ: radio quasars, RG: radio galaxies, Sy1,Sy2: Seyfert 1,2, BAL: Broad Absorption Line quasars, QQ: radio quiet quasars. Figure reproduced from Blandford, Netzer & Woltjer (1990).

3.3 How many sources can FIRST expect to see?

The fraction of sources in each of the above classes that can be detected in the radio is a function of many properties of the sources like their local radio luminosity function and its evolution and the source radio spectral index. The detected fraction also depends upon the frequency, beam size and flux limit of the survey.

3.3.1 How many radio sources are there?

Table 3.1 lists the local number densities of different classes of objects in the local universe along with their radio luminosities. It can be seen from the table that the most luminous radio sources are extremely rare.

Object	Number Gpc^{-3}	Typical radio luminosity $\text{erg sec}^{-1} \text{Hz}^{-1}$
Field galaxies	10^6	10^{27}
Radio galaxies	3×10^3	10^{30}
Seyfert 1	4×10^4	10^{30}
Seyfert 2	1×10^5	10^{30}
Radio quiet quasars	100	10^{32}
Radio loud quasars	3	10^{34}

Table 3.1: Local space densities and typical radio luminosities of some extragalactic radio sources. The densities below 100 Gpc^{-3} are particularly uncertain because of incompleteness and cosmological evolution.

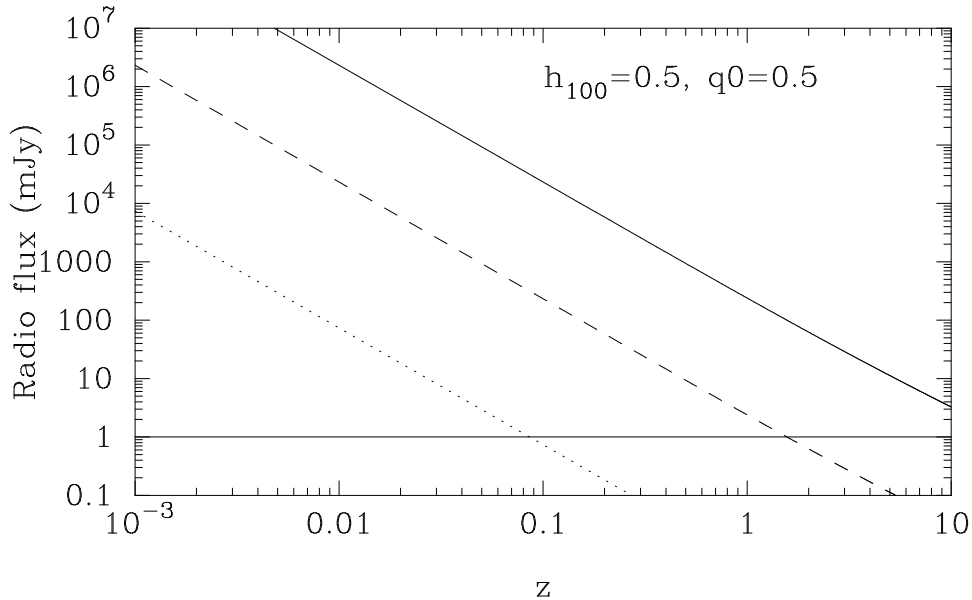


Figure 3.2: Radio flux as a function of redshift, for different classes of sources. The solid line represents radio loud quasars, the dashed line the radio quiet quasars and the dotted line the Seyfert galaxies. Typical radio luminosities for these objects are used, as listed in Table 3.1. Note that both axes have been plotted on a logarithmic scale.

3.3.2 How far can FIRST see?

A flux limited radio survey such as FIRST, can detect different classes of objects out to a redshift that is a function of their radio spectral index, their radio luminosity and the values chosen for the cosmological parameters. In Figure 3.2 we show such a plot of the variation of radio flux with redshift, for a given radio luminosity. The values of the cosmological parameters used here are Hubble's constant $H_0 = 50 \text{ km sec}^{-1} \text{ Mpc}^{-1}$ and deceleration parameter $q_0 = 0.5$; h_{100} denotes the value of Hubble's constant expressed in units of $100 \text{ km sec}^{-1} \text{ Mpc}^{-1}$. The horizontal line is placed at 1 mJy and represents the FIRST survey limit. From the figure it is apparent that Seyfert galaxies can be detected out to a redshift of ~ 0.1 , radio quiet quasars can be spotted to a redshift of ~ 1 , while radio loud quasars can be seen to redshifts way beyond those currently observed.

3.3.3 Limitations on morphological classification

The classification of the galaxies hosting the radio sources may also change as a function of the redshift. There are two reasons why this may happen. Firstly, the angular size of the galaxy may become so small so as to make it indistinguishable from the point spread function (PSF). Secondly, the light from a bright active nucleus may swamp out the rest of the galaxy. Such active galaxies may then get classified as quasars. A detailed discussion of the implications of these possibilities is provided in Chapter 7.

In Figure 3.3 we show the variation of angular size with redshift for different classes of radio sources. We choose a typical physical extent for the radio emission, 100 kpc for radio galaxies, 15 kpc for starbursts and 3 kpc for nuclear emission from active galaxies. From the figure it is apparent that with a ~ 1 arcsec resolution such as FIRST, both radio galaxies and starbursts will be recorded as either extended or resolved radio sources over the redshift range of interest.

3.3.4 Differential source counts: the mysterious blue galaxy population

In Figure 3.4 we present the $\log N$ - $\log S$ curve for radio sources observed at 20 cm Condon (1984). This curve represents the number of sources within a flux range. At flux densities ≥ 3 mJy the radio population is dominated by active galactic nuclei including radio galaxies, BL Lac objects and radio loud quasars. Below 3 mJy however, the $\log N$ - $\log S$ curve flattens considerably, indicating the presence of a new population. Several authors (e.g. Windhorst et al. 1985) have identified this new component with moderate redshift star forming galaxies.

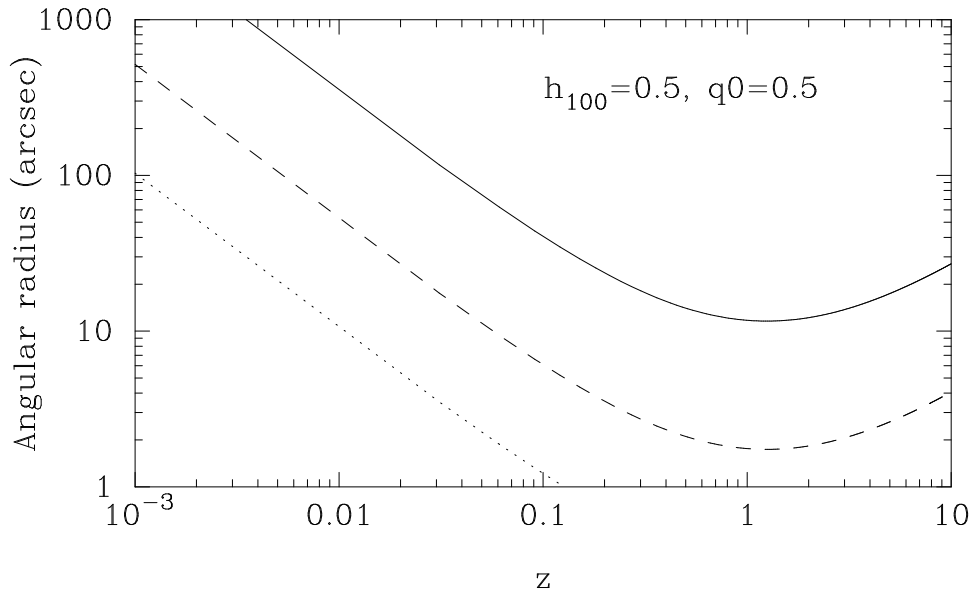


Figure 3.3: Angular size as a function of redshift for different classes of sources. The solid line represents the size of radio emission from a radio galaxy, the dashed line emission from a starburst galaxy and the dotted line size represents size of nuclear emission from an AGN. Note that both axes have been plotted on a logarithmic scale.

The model curves at low flux levels have been constructed from small data samples and could be subject to revision as more identifications of low flux radio sources become available. In Chapter 8 of this thesis, I present new photometric and morphological information on faint FIRST sources.

3.3.5 Which of these sources can (should) we study using FIRST?

FIRST is a uniform high sensitivity, large area, high resolution survey with accurate astrometric positions. As compared to the NVSS survey, FIRST has better sensitivity, resolution and astrometric accuracy. The high resolution makes it ideally suited for studying radio emission from compact radio sources, such as radio stars, quasars, active galactic nuclei (AGN) and distant galaxies. For the same reason, it is not well suited for studies of sources with extended radio structure such as radio galaxies, protogalaxies, non-nuclear emission from quasars and so on. The u, v -plane coverage of the survey is also not very good. It is therefore not appropriate to use it for detailed studies of radio morphology.

The particular strength of the survey is its *uniform sensitivity*, over a large area of the sky. It can therefore be used to construct and study *complete* radio flux limited samples. Such complete samples can be used for robust statistical studies of correlations between properties of sources in the radio and at other wavelengths. All through this thesis, I have carefully chosen projects that exploit the strengths of the FIRST survey, without being unduly restricted by its deficiencies.

3.4 Techniques for obtaining optical identifications

Given a very large and complex radio survey such as FIRST, four separate, complementary strategies can be employed to obtain the maximum number of optical identifications possible.

1. The simplest approach involves comparing positions of sources from the FIRST catalog with source positions from catalogs of other objects such as quasars and AGN (Wadadekar & Kembhavi 1999).
2. A more involved approach is to use optical catalogs constructed from digitized, large area photographic surveys such as the Palomar Observatory Sky Survey (POSS I) (Helfand et al. 1998a) and DPOSS (Chapter 6). Approximately 20 percent of FIRST sources have optical counterparts at the limiting magnitude of the red Palomar POSS I plates ($E = 20.0$). A

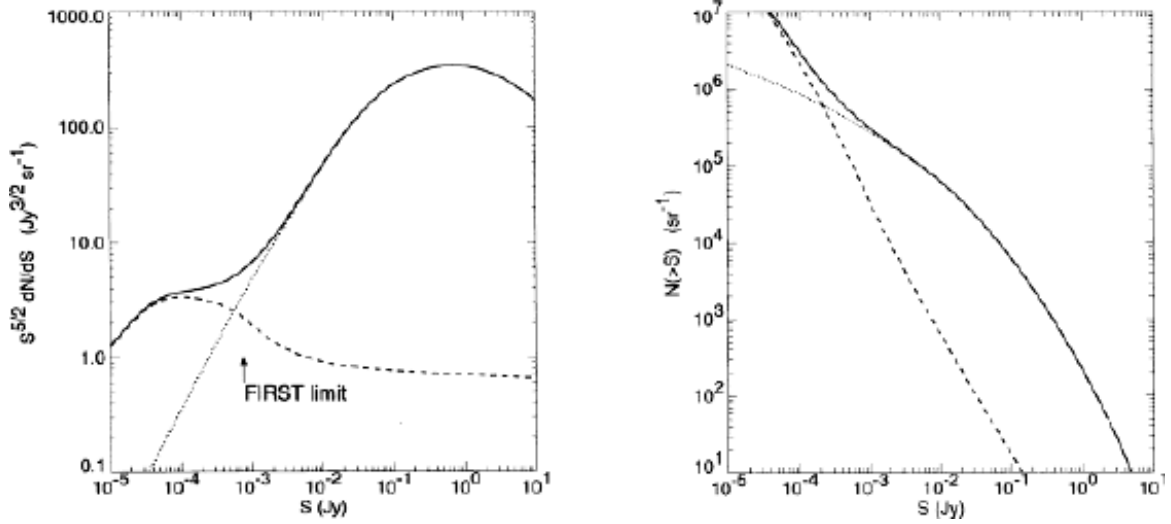


Figure 3.4: Left panel: The differential source count $S^{5/2}n(S)$ would be constant in a static Euclidean universe. These observed source counts at $\nu = 1.4$ GHz can be modeled as the sum of contributions by evolving true AGN (dotted curve) and star forming galaxies dashed curve). Figure reproduced from Becker, White & Helfand (1995). Right Panel: Number counts of the AGN and star forming galaxy population as a function of radio flux.

preliminary identification of FIRST survey radio sources on the second Palomar Observatory Sky Survey (POSS-II) resulted in optical detection of ~ 21 percent of the sources (Djorgovski et al. 1998a).

3. A third approach is to use data from deep surveys (typically to $m_v \sim 24$) covering a much smaller area, typically a few square degrees (Helfand et al. 1998b, Yedigargolu et al. 1998).
4. A fourth approach is to use deep data from a new survey such as the SDSS. At the $m(v) \sim 24$ limit of SDSS, ~ 50 percent of the optical counterparts to FIRST sources should be detected.

In this thesis, I report on projects that employ the first three strategies of obtaining optical identifications. The fourth approach will only be feasible after the SDSS survey data are released in 2005. In the next two chapters we present studies of quasars and AGN using the first technique described above.

Chapter 4

Radio Emission from Quasars

This chapter is mainly based on Wadadekar & Kembhavi (1999). Using a recent (1998) version of the VLA FIRST survey radio catalog, we have searched for radio emission from 1704 quasars taken from the most recent (1993) version of the Hewitt and Burbidge quasar catalog. These quasars lie in the ~ 5000 square degrees of sky already covered by the VLA FIRST survey. Our work has resulted in positive detection of radio emission from 389 quasars of which 69 quasars have been detected for the first time at radio wavelengths. We find no evidence of correlation between optical and radio luminosities for optically selected quasars. We find indications of a bimodal distribution of radio luminosity, even at a low flux limit of 1 mJy. We show that radio luminosity is a good discriminant between radio loud and radio quiet quasar populations, and that it may be inappropriate to make such a division on the basis of the radio to optical luminosity ratio. We discuss the dependence of the radio loud fraction on optical luminosity and redshift.

4.1 Introduction

It has been well known for some time that only about 10% of quasars are radio loud, with radio luminosity comparable to optical luminosity. This is surprising, because over a very wide wavelength range from $\sim 100 \mu\text{m}$ through X-ray wavelengths, the properties of radio loud and radio quiet quasars are very similar. The presence or absence of a radio component may be a pointer to different physical processes occurring in the two types of quasar, but it is not yet clear as to what these processes are.

The relationship between quasar radio and optical emission was initially studied using radio selected objects, which generally had high radio luminosities because the early radio surveys had relatively high limiting radio fluxes. Sandage (1965) showed that not all quasars are powerful radio emitters, and that a substantial population of *radio quiet* quasars exists, undetectable at high radio flux levels. Since then, in addition to radio surveys, radio follow up observations of large surveys conducted in the optical have been used to study the radio properties of quasars (eg. Sramek & Weedman 1980; Condon et al. 1981; Marshall 1987; Kellerman et al. 1989; Miller, Peacock & Mead 1990). Such targeted radio observations, of quasars selected by other means, typically go deeper than the large radio surveys, as a result of which the median radio luminosity of these samples is lower. Taken together, these two survey methods have detected quasars with a range of more than 6 orders of magnitude in radio luminosity, but the populations detected by the two methods come from different regions of the overall radio luminosity distribution.

The radio emission from quasars can be used to divide them into two classes: a radio loud population where the ratio R of radio to optical emission is greater than some limiting value R_{lim} , and a radio quiet population with $R < R_{\text{lim}}$. Such a separation is commonly employed in the literature dealing with the radio properties of quasars, with $R_{\text{lim}} = 1$ or $R_{\text{lim}} = 10$ (eg. Kellerman et al. 1989; Visnovsky et al. 1992; Stocke et al. 1992; Kellerman et al. 1994). Alternately, the separation between radio loud and radio quiet quasars, may be defined by their radio luminosity. Such a criterion has been advocated by Miller, Peacock & Mead (1990), who noticed that for a sample of optically selected quasars, which spanned a wide range of optical luminosity but a narrow range of redshift, there was no correlation between their optical and radio luminosity. This implied that the distribution of R was optical luminosity dependent, thus making it unsuitable as the discriminant between radio loud and radio quiet populations. Miller et al. found that the distribution of radio luminosity was highly bimodal, and from an examination of the luminosities of radio detections and upper limits accepted a 5 GHz limiting radio luminosity of $10^{25} \text{ W Hz}^{-1} \text{ str}^{-1}$ (following them we use $H_0 = 50 \text{ km sec}^{-1} \text{ Mpc}^{-1}$, $q_0 = 0.5$, quasar radio spectral index $\alpha_r = 0.5$ and optical spectral index

$\alpha_{\text{op}} = 0.5$ throughout this chapter) as the dividing line between radio loud and radio quiet quasars. The gap in the radio luminosity function of the two populations is pronounced, with very few objects occupying the region between quasars that are radio loud and those that are radio quiet. A fact to be noted here is that the detection technique used to find quasars from these two populations is different. An overwhelming majority of radio loud quasars have been first detected in the radio and then confirmed using optical spectroscopy, while radio quiet quasars have been detected using optical, X-ray or other techniques. An important question in such a situation is: are radio quiet and radio loud quasars indeed two physically different populations, or is the distinction merely an artifact caused by selection biases in the detection techniques? Previous efforts at answering this question have been plagued by the small size of the datasets and their incompleteness. Most radio observations of optically selected quasars have lacked the sensitivity to detect their radio emission. There have been a few high sensitivity radio surveys (eg. Hooper et al. 1996, Kukula et al. 1998) but the size of their samples is quite small. The FIRST survey allows us to address this question meaningfully, by combining a large sky coverage with a low flux limit.

FIRST allows us to address the issue of quasar bimodal radio luminosity distribution in two different but complementary ways. Firstly, optical identifications of FIRST sources using large optical surveys such as the Palomar Observatory Sky Survey (POSS) provide a large database of quasar candidates, whose true nature can then be verified spectroscopically. Such efforts (eg. Gregg et al. 1996; Becker et al. 1997; White et al. 2000) are currently underway. Secondly, the large area covered by the FIRST survey allows us to look for radio emission from a significant fraction of already known quasars and correlate their radio properties with other observables. In the present work, we have used this approach to determine the radio properties of quasars from the catalog of Hewitt & Burbidge (1993, hereafter HB93).

Such an approach has also been taken, though with a different radio survey and quasar catalog, by Bischof & Becker (1997, hereafter BB97) who compared positions of radio sources from the NVSS radio survey, with the positions of 4079 quasars from the Veron catalog (Veron-Cetty & Veron 1991). They detected radio emission from 799 quasars, of which 168 were new radio detections. The FIRST survey has better sensitivity and resolution than the NVSS, but covers a smaller area. There is a small area of overlap between NVSS and FIRST. FIRST has a smaller beam size than NVSS, and so it is expected to have better sensitivity to point sources.

We use radio data from the FIRST survey to look for radio emission from the 1704 quasars from HB93 ($\sim 23\%$ of the quasars listed therein) which lie in the area covered by the survey. This set of quasars is not statistically complete in any sense. Wherever appropriate, we distinguish between radio selected quasars and those selected by other means.

4.2 Radio/optical comparisons

We compare the positions of quasars in HB93 to the positions of radio sources in the FIRST radio source catalog (February 4, 1998 version available at <http://sundog.stsci.edu/>), and calculate the angular separation between each quasar and each FIRST source. About 4% of sources in the FIRST catalog have been tagged as possible sidelobes of bright sources. Of these, $<10\%$ are real sources and considerably less than 1% of the unflagged sources in the catalog are sidelobes (White et al. 1997). We have excluded these flagged sidelobe sources from our cross correlation. We are then left with a total of 421,447 unflagged sources in the northern and southern strips, covering a total area of about 4760 square degrees. Of these, 368,853 sources lie in the northern strip while 52,594 sources are in the southern strip. On an average, there are 88.54 FIRST sources per square degree of sky.

Our quasar sample consists of 1704 quasars from HB93 that lie in the area covered by FIRST. We have excluded the BL Lacs listed in the catalog from the present work. In HB93, the authors use a simple selection criterion for quasars. Any object that is starlike (with or without fuzz) and has redshift $z \geq 0.1$ is called a quasar and is included in the catalog. The positions listed in the catalog are for the optical object, most of which are taken from the identification paper or from the paper containing the redshift measurement. If a quasar is very close to a bright galaxy, and the quasar coordinates are not available in the literature, the galaxy coordinates have been listed by HB93 for the quasar position.

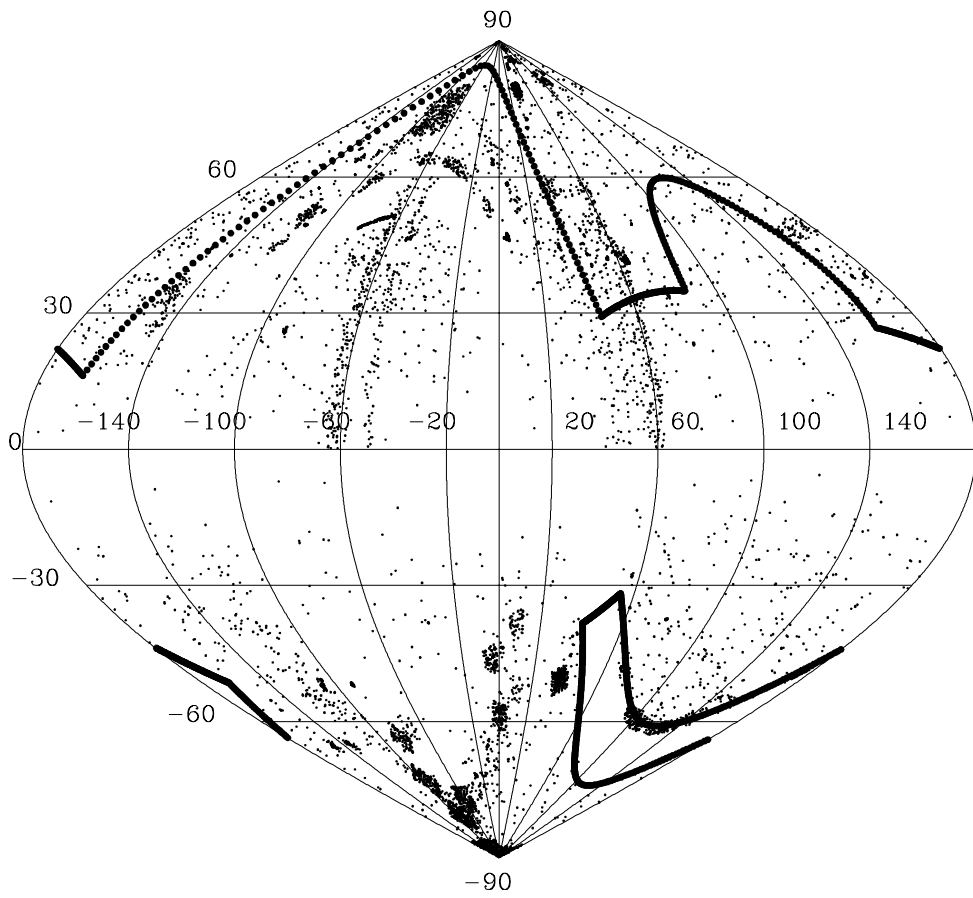


Figure 4.1: The approximate boundaries in galactic coordinates of the areas covered by the FIRST survey are indicated by bold points. The northern and southern strips are separately shown. The dots indicate quasars from the Hewitt and Burbidge (1993) catalog.

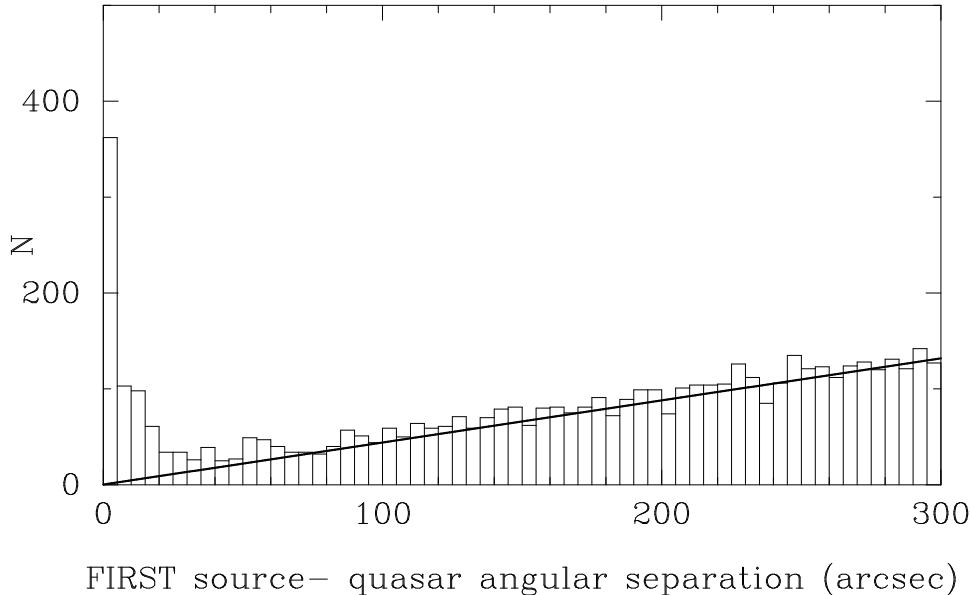


Figure 4.2: A histogram of the angular separation between the Hewitt and Burbidge (1993) quasars and the corresponding FIRST source. The straight line is the number of chance matches expected, in annuli of radius shown on the X-axis having a width of 5 arcsec, if the FIRST sources were randomly distributed in the sky.

In Figure 4.1 we show the distribution of the HB93 quasars on the sky in galactic coordinates. The apparent clustering of known quasars is due to the limited solid angle covered by deep quasar surveys (most of them optical) that have uncovered the largest number of quasars. The approximate area for which FIRST survey data has been released is also marked in the figure. FIRST has currently covered an area of 4150 square degrees around the North Galactic Cap in addition to two narrow strips totaling about 610 square degrees near the South Galactic Cap. The southern strip has a peculiar shape and the box shown here is a very approximate representation. Detailed sky coverage maps are available at the FIRST homepage.

In order to find coincidences between HB93 and FIRST sources, we begin with a search circle of radius 300 arcsec centered on each HB93 quasar, and look for FIRST radio sources within this circle. When there is more than one FIRST source in the search circle, we tentatively accept all such sources as matches. In Figure 4.2 we show a histogram of the angular separation between the HB93 quasars and the FIRST sources found in the search circles.

The angular auto correlation function for FIRST has shown that 35% of sources have resolved structure on scales from 2-30 arcsec (Cress et al. 1996). Since our aim in this work is to only look for radio emission from the compact (flat spectrum) component of quasars, we have considered only quasars which contain at least one FIRST source within 10 arcsec of them. This would make us miss out on some quasars which may have elaborate extended radio structure, but a core emission lower than the FIRST flux limit. To see which of the radio sources found can be accepted as true identifications, we estimate the quasar-FIRST source chance coincidence rate for a random distribution of FIRST survey sources. For a random distribution, the chance coincidence rate is directly proportional to the area of sky covered by the search circle around each quasar, i.e. the the square of the search radius. The straight line in Figure 4.2 is the expected number of chance coincidences between quasars and FIRST sources, in annuli of radius shown on the abscissa and width 5 arcsec around the quasars. It is seen from the figure that the expected number of chance coincidences closely matches the number of actual coincidences beyond about 40 arcsec, indicating that most FIRST sources found more than 40 arcsec away from a quasar are chance coincidences. On the other hand, matches within 10 arcsec are mostly real (less than 1% chance identification probability).

We therefore choose a search circle of radius 10 arcsec and count all matches found within this radius as true matches. All subsequent discussion about the radio properties of quasars in this

Number of HB93 quasars in FIRST area:	1704
Number of quasars with radio detections:	389
Number of radio selected quasars:	263
Number of non-radio selected quasars:	126
Number of non-detections:	1315
Percentage of quasars with detected radio emission:	$\sim 22\%$
Percentage of non-radio selected quasars with detected radio emission:	$\sim 7\%$

Table 4.1: Summary of quasar radio detections

chapter only uses matches obtained with this search radius.

The positions of quasars listed in HB93 have astrometric errors of a few arcseconds or more in some cases. In such cases, there will be missed matches when the positional error places a HB93 quasar outside the 10 arcsec search radius around the FIRST radio source with which it is actually associated. Some of these missed quasars can be recovered by using the accurate positions of star like objects from the USNO-A2.0 catalog (available at <http://www.nofs.navy.mil/projects/pmm/a2.html>), which is an all sky astrometric and photometric catalog of over 500 million starlike objects. For this purpose we considered FIRST radio sources which had a HB93 quasar in an annulus of inner radius 10 arcsec and outer radius 20 arcsec around it. We cross correlated the positions of such radio sources with starlike sources from the USNO-A2.0 catalog. The search radius used for this purpose was of 3 arcsec, which is three times the RMS uncertainty in the first survey positions (the positions in USNO-A2.0 are known to better than this accuracy). When an USNO-A2.0 object is found in this circle we compare its blue magnitude with the blue magnitude of the corresponding HB93 quasar. When the difference δm was less than one magnitude, we considered the USNO-A2.0 object and the HB93 quasar to be the same object. We have a total of 158 FIRST sources with a HB93 quasar within the 10-20 arcsec annulus around it. Out of these 158 sources, 16 had a USNO-A2.0 source within a 3 arcsec circle around it, and of these 8 had blue magnitudes which passed our criterion. We accepted the corresponding 8 HB93 quasars as valid matches with FIRST survey sources, and added these to our list of 381 radio detections mentioned above.

We find that positions of radio selected quasars match the FIRST source positions better than the non-radio selected quasars. This is because the radio positions have been more accurately determined than optical positions. Accurate astrometry on optically selected quasars is often not available and quasar positions are computed approximately using finding charts. The mean astrometric error, in non-radio selected quasar surveys, is typically a few arcseconds. In high resolution radio selected surveys, the astrometric error is often less than an arcsecond. About 12% of quasars detected have more than one (usually two) FIRST sources within the search circle of 10 arcsec radius. In such cases, we have used *all* the FIRST sources associated with the quasar in our analysis. This is because generally the combined error in quasar and FIRST source positions is too large to allow us to reliably determine which of the two radio sources actually corresponds to the quasar core. There are ~ 1320 non detections, amongst the HB93 quasars covered by FIRST, and we assign an upper limit of 1 mJy to their radio flux at 1.4 GHz. Table 4.1 provides a summary of our radio detections and non-detections. The radio and optical properties of the quasars with FIRST detections (which includes all the new detections in the radio) are summarized in Table 4.2. Detections in the radio reported after the quasar catalog was published (mostly in BB97) are mentioned in the last column. Those quasars which do not have the letter R in the selection technique code and do not have a recent radio detection mentioned in the last column may be considered to be the new detections. There are 69 such quasars in Table 4.2. The last eight entries are the additional list of matches obtained using a correlation with the USNO-A2.0 catalog. These 8 matches were obtained using an indirect comparison technique, and have *not* been used in the statistical correlations reported in subsequent sections.

IAU Designation	Selection Technique	m_{pg}	F_{peak} (mJy)	z	Separation (arcsec)	Alternative designation	Recent radio detection
0002-018	O	18.70	62.26	1.71	1.2		
0003-003	R	19.35	3111.27	1.03	0.6	3CR 2	
0004+006	O	17.80	1.55	0.32	1.3		
0009-018	O	18.4	1.61	1.07	2.2	UM 212	
0012-002	O	17	1.45	1.55	5.0	UM 221	
0012-004	O	18.6	12.67	1.70	0.7		
0013-005	R	20.8	1050.26	1.57	1.6	PKS	
0013-005	O	18.6	1.72	0.31	0.5	A	
0019+003	O	18.4	8.31	0.69	0.4		
0020-020	O	18.2	1.17	0.76	0.7		

Table 4.2: FIRST detections of quasars. This table is presented in its entirety in the electronic edition of the *Astronomical Journal*. A portion is shown here to illustrate its form and content. Selection Technique O: Objective Prism, R: Radio, C: UV-Excess, X: X-Ray, U: Selection technique not mentioned.

4.2.1 1343+266: not a gravitationally lensed quasar?

This is a close pair of quasars with identical redshift, similar spectra and separated by only ~ 10 arcsec. Detailed spectroscopic observations have shown qualitative (eg. presence of certain lines) as well as quantitative (eg. ratio of line strengths) *differences* between the two quasars, strengthening the claim that this is *not* a gravitationally lensed pair, but a physically associated pair of quasars, possibly residing in a cluster of galaxies at $z = 2.03$ (Crampton et al. 1988; Crofts et al. 1994). The optical luminosities are comparable, with 1343+266B having a luminosity higher by about 5% than 1343+266A. We find radio emission from only one of the quasars: 1343+266B has a flux of 8.9 mJy. The separation between the gravitationally lensed quasar and the FIRST source is 2.18 arcsecond, which is consistent with an error of ~ 1 arcsec each in the quasar optical position and the FIRST radio position. There is no radio emission associated with 1343+266A at the FIRST flux limit of 1 mJy, because the FIRST source associated with 1343+266B is 7.4 arcsec away, too far to be associated with 1343+266A, considering the highly accurate astrometry done for this well studied pair of quasars. There is no other FIRST source associated with 1343+266A. This implies that the radio luminosity of 1343+266B is at least 8.9 times higher than that of 1343+266A, in sharp contrast to only 5% difference in their optical luminosity. Such radio asymmetry is strong evidence that the pair is *not* gravitationally lensed.

4.3 Radio and optical properties

4.3.1 Bivariate luminosity functions

The number of quasars with optical luminosity in the range $(L_{op}, L_{op} + dL_{op})$, radio luminosity in the range $(L_r, L_r + dL_r)$ and redshift in the range $(z, z + dz)$ is in general given by $\Phi(L_{op}, L_r, z) dL_{op} dL_r dv(z)$, where the *luminosity function* $\Phi(L_{op}, L_r, z)$ is the comoving number density of quasars for unit ranges of the respective luminosities, and $dv(z)$ is a comoving volume element at z . If the radio and optical luminosities are independently distributed, it is possible to separate the luminosity function as

$$\Phi(L_{op}, L_r, z) dL_{op} dL_r dv(z) = \Phi_{op}(L_{op}, z) dL_{op} dv(z) \Phi_r(L_r) dL_r. \quad (4.3.1)$$

There will be no correlation between the optical and radio luminosities of the quasars described by Equation 4.3.1.

Another form of the bivariate luminosity function extensively considered in the literature has been

$$\Phi(L_{op}, L_r, z) dL_{op} dL_r dv(z) = \Phi_{op}(L_{op}, z) dL_{op} dv(z) \Phi_R(R) dR, \quad (4.3.2)$$

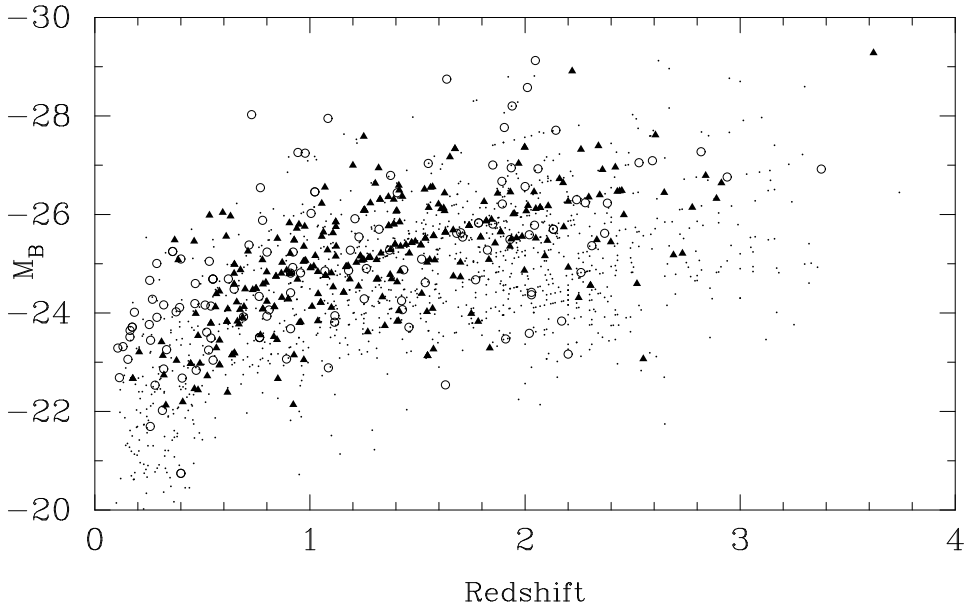


Figure 4.3: Absolute magnitude M_B of quasars in our sample as a function of redshift. Non-radio selected (mostly optical) quasars with FIRST detection are indicated by open circles, solid triangles indicate radio selected quasars. The upper limits are represented by dots.

where

$$R = \frac{L_r}{L_{op}} = \frac{F_r}{F_{op}}(1+z)^{\alpha_r - \alpha_{op}} \quad (4.3.3)$$

and F_{op} and F_r are the optical and radio flux densities at some fiducial points in the spectrum, which we will take to be at 2500 Å and 5 GHz respectively. Since we take $\alpha_{op} = \alpha_r = 0.5$, the ratio of the luminosities is simply equal to the ratio of the fluxes. It is assumed here that the distribution of R is independent of the other variables. This form of the luminosity function was first introduced by Schmidt (1970) to describe the bivariate luminosity distribution of 3CR radio quasars. For a given optical luminosity L_{op} , it follows from Equation 4.3.3 that the radio luminosity ranges from $R_{min}L_{op}$ to $R_{max}L_{op}$ for R in the range $R_{min} < R < R_{max}$, and the mean radio luminosity is given by

$$\langle L_r \rangle = \langle R \rangle L_{op}, \quad \langle R \rangle = \int_{R_{min}}^{R_{max}} R \Phi_R(R) dR, \quad (4.3.4)$$

with the function $\Phi_R(R)$ being normalized to unity. The luminosity function in Equation 4.3.2 therefore implies that the mean radio luminosity increases with the optical luminosity.

In the following sections we will see whether the data from the FIRST survey is consistent with either of the two forms of luminosity function. In our discussion, we will use the following nomenclature to refer to different classes of quasars:

- RSQ: Radio selected quasars,
- OSQD: non-radio (mostly optical) selected quasars detected by FIRST,
- OSQU: non-radio selected quasars with radio upper limits.

The OSQD and OSQU include a few X-ray selected quasars, but their numbers are too small to warrant separate treatment. All radio selected quasars lying in the area covered by FIRST have radio emission higher than the FIRST limit of 1 mJy.

We have shown in Figure 4.3 the variation of absolute magnitude with redshift for all the quasars in our sample. In this figure, triangles represent RSQ while the OSQD are represented by open circles and the OSQU by dots. The optical luminosity of the sample ranges over ~ 4 orders of magnitude, and the redshift goes upto ~ 3.6 . All three kinds of quasar are distributed over much of these wide ranges.

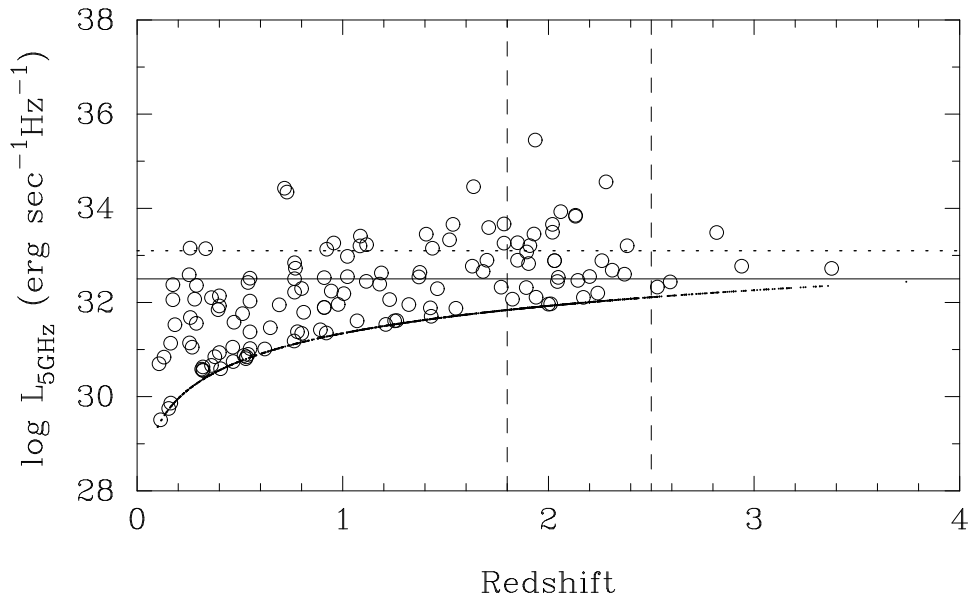


Figure 4.4: Radio luminosity as a function of redshift. The locus of dots indicates the 1 mJy upper limits. The horizontal dotted line is the dividing radio luminosity between radio loud and radio quiet objects used by MPM90. The solid horizontal line is the dividing luminosity that we have chosen. The region of redshift space explored by MPM90 is between the two vertical dashed lines.

4.3.2 Distribution of radio luminosity

The radio-selected quasars (RSQ) in our sample have all been discovered in radio surveys with flux limits much higher than the 1 mJy limit of the FIRST survey. For a given redshift, these quasars will have much higher radio luminosity than most of the non-radio selected component of our population. The radio luminosity distribution of the RSQ is consequently not representative of the distribution for the overall quasar population. We shall therefore omit the RSQ from the following considerations, except where they are needed in some specific context.

We have shown in Figure 4.4 a plot of the 5 GHz radio luminosity against redshift for non-radio selected quasars. The OSQD are shown as unfilled circles, while the OSQU are shown as dots, and form the almost continuous lower envelope which indicates the radio luminosity corresponding to a radio flux of 1 mJy over the redshift range. In Figure 4.5 is shown a plot of the 5 GHz radio luminosity against the absolute blue magnitude for the non-radio selected quasars. In this figure too, radio detections are shown as open circles, and the radio upper limits as dots. There appears to be a correlation between the logarithm of the radio luminosity and absolute magnitude, in spite of the large scatter in radio luminosity for a given absolute magnitude. The linear correlation coefficient for the 135 radio detections alone is 0.22, which is significant at the > 99.9 percent confidence level. However, it is seen from Figure 4.3 and Figure 4.4 that mean radio as well as optical luminosity increase with redshift, which is due to the existence of a limiting radio flux and apparent magnitude in the surveys in which quasars are discovered. A situation can arise in which an observed correlation between radio luminosity and absolute magnitude is mainly due to the dependence of each luminosity on the redshift z . It is important to see if the correlation remains significant when such an effect of the redshift on the observed correlation is taken into account. This can be done by evaluating a *partial linear correlation coefficient* as follows (Havilcek & Crain 1988; Kembhavi & Narlikar 1999).

Let $r_{L_r, M}$, $r_{L_r, z}$ and $r_{M, z}$ be the correlation coefficients between the pairs $\log L_r$ and M , $\log L_r$ and z , and M and z respectively. The partial linear correlation coefficient is then defined by

$$r_{L_r, M; z} = \frac{r_{L_r, M}^2 - r_{L_r, z} r_{M, z}}{\sqrt{1 - r_{L_r, z}^2} \sqrt{1 - r_{M, z}^2}} \quad (4.3.5)$$

The partial correlation coefficient has the same statistical distribution as the

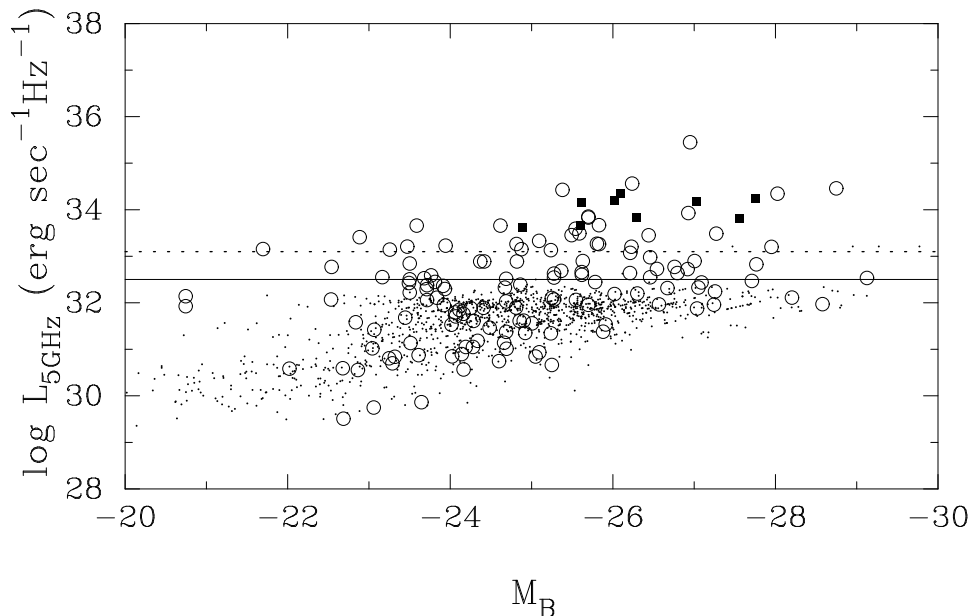


Figure 4.5: Radio luminosity as a function of absolute magnitude. The filled squares are radio detections of quasars studied in MPM90. The other symbols are as in Figure 4.4. The dotted horizontal line is the MPM90 dividing luminosity between radio loud and radio quiet quasars, in our units. The solid horizontal line is the dividing luminosity that we have chosen.

ordinary correlation coefficient and therefore the same tests of significance can be applied to it. A statistically significant value for it means that the luminosities are correlated at that level of significance even after accounting for their individual dependence on the redshift.

For our sample of 135 radio detections, the partial linear correlation coefficient is 0.09, which is significant only at the 72 percent confidence level. The observed correlation between the radio luminosity and absolute magnitude thus appears to be largely induced by the effect of the large range in redshift over which the sample is observed. The lack of correlation found here is consistent with the results of Miller, Peacock and Mead (1990, hereafter MPM90) and Hooper et al. (1995).

MPM90 have observed a sample of optically selected quasars, with redshift in the range $1.8 < z < 2.5$, with the VLA to a limiting sensitivity of ~ 1 mJy at 5 GHz. They detected nine quasars out of a sample of 44; these objects are shown in Figure 4.5 as filled squares. The radio upper limits of MPM90 occupy the same range as our upper limits shown in the figure, and are not separately indicated. MPM90 have commented at length on the luminosity gap found between their radio detections and upper limits. They concluded that the gap was indicative of a bimodality in the distribution of radio luminosity, which divides quasars into a radio loud population, with radio luminosity $> 10^{25} \text{ W Hz}^{-1} \text{ str}^{-1}$, and a radio quiet population with luminosity $< 10^{24} \text{ W Hz}^{-1} \text{ str}^{-1}$. The radio loud quasars were taken to be highly luminous representatives of the population of radio galaxies, and the radio quiet population was taken to be like Seyfert galaxies. The conspicuous gap between radio detections and upper limits is absent in our data. It is seen in Figure 4.5 that the region $\sim 10^{32} \lesssim L_r(5 \text{ GHz}) \lesssim 10^{33} \text{ erg sec}^{-1} \text{ Hz}^{-1}$ (which corresponds to the gap found by MPM90 for our units and constants) is occupied by many quasars. Only seven of these are in the redshift range of the MPM90 sample, which probably explains why they did not find any quasars in the gap: our sample is about 30 times larger, and even then we find only a small number in the range. This does not however imply that there are no quasars with radio luminosity in the intermediate range. It is plausible that there are subtle selection biases that prevent us from detecting such objects in optical quasar surveys. Preliminary results from the FIRST Bright Quasar Survey (Becker et al. 2000) seem to indicate that a bimodal distribution does *not* exist.

In Figure 4.6 we show the distribution of the log of radio luminosity for the RSQ, the OSQD and the OSQU. The mean value for each distribution is indicated by an arrow. The radio luminosity of the OSQD has a mean value of $10^{32.24} \text{ erg sec}^{-1} \text{ Hz}^{-1}$, which is approximately 1.5 orders of magnitude fainter than the mean luminosity of the RSQ, because the latter were selected in high

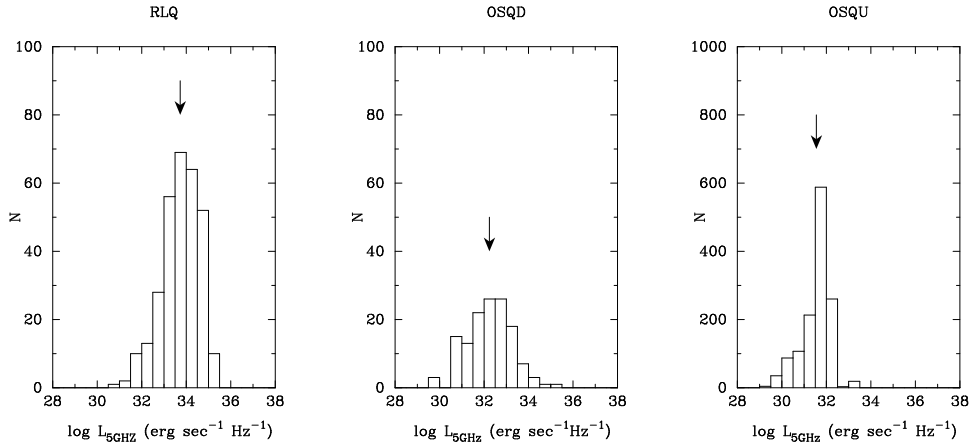


Figure 4.6: Distribution of radio luminosity for the three kinds of quasars. The arrow indicates the mean value.

flux limit surveys. The RSQ have a median radio flux of ~ 400 mJy, while there are only three OSQD with radio flux ≥ 100 mJy. The radio luminosity upper limits of the OSQU are well mixed with the fainter half of the luminosity distribution of the OSQD. The rather sharp cutoff in the luminosity upper limit distribution of the OSQU is due to the flattening in the 1 mJy luminosity envelope in Figure 4.4 at high redshifts. The upper limits peak at a luminosity which is approximately half a decade lower than the peak in the luminosity distribution of the OSQD. The mean value for the OSQU is $10^{31.55}$ erg sec⁻¹ Hz⁻¹. A Kolmogorov-Smirnov test on the distribution of radio luminosity of the OSQD and OSQU shows that these are drawn from different distributions with a significance of 99.9 percent. This is consistent with a bimodal distribution amongst the radio detections and upper limits. If the radio luminosity distribution is indeed bimodal, the present radio upper limits, when observed to a limiting flux significantly less than 1 mJy, would be found to have radio luminosities considerably lesser than the present set of detections.

4.3.3 Distribution of radio-to-optical luminosity ratio R

The ratio R is defined using rest frame monochromatic radio and optical luminosities at some fiducial rest frame wavelengths. In the following we will choose these to be at 5 GHz and 2500 Å in the radio and optical case respectively. With our choice of spectral indices $\alpha_r = \alpha_{op} = 0.5$, $\log R$ is given in terms of observed flux densities at observed wavelengths at 5 GHz and 2500 Å by

$$\log R = \log F_r(5 \text{ GHz}) - \log F_{op}(2500). \quad (4.3.6)$$

Figure 4.7 shows the variation of R with redshift. There is considerable overlap for $R \lesssim 3$ between the radio detections and upper limits, but there are only detections at the highest values of R . There is only one upper limit with $R > 3$. At each redshift, there is a maximum to the R upper limits, and this increases slowly with redshift, so that an envelope is seen. For an upper limit to be found above the envelope, it would be necessary to have quasars at fainter optical magnitudes than are presently to be found in the HB catalogue. In the case of the detections, the maximum value $R_{\text{max}}(z) = L_{r,\text{max}}(z)/L_{op,\text{min}}(z)$ decreases with redshift. This occurs because the increase in $L_{r,\text{max}}(z)$ with redshift is slower than the increase in $L_{op,\text{min}}(z)$ with redshift, as can be seen from Figure 4.3 and Figure 4.4. Similarly, the minimum value of R for the detections, $R^{\text{min}}(z) = L_{r,\text{min}}(z)/L_{op,\text{max}}(z)$, increases with redshift, because $L_{op,\text{max}}(z)$ increases slower than $L_{r,\text{min}}(z)$.

Figure 4.8 shows a histogram of $\log R$ for radio detections (solid line) and radio upper limits (dashed line). For comparison, the distribution of R for the radio selected quasars is shown as a dotted line. An important question here is whether the distribution of R is bimodal. The number of radio detections is not large enough to provide information about the distribution of R over its wide range. However, as mentioned above, there is considerable overlap in the distributions of

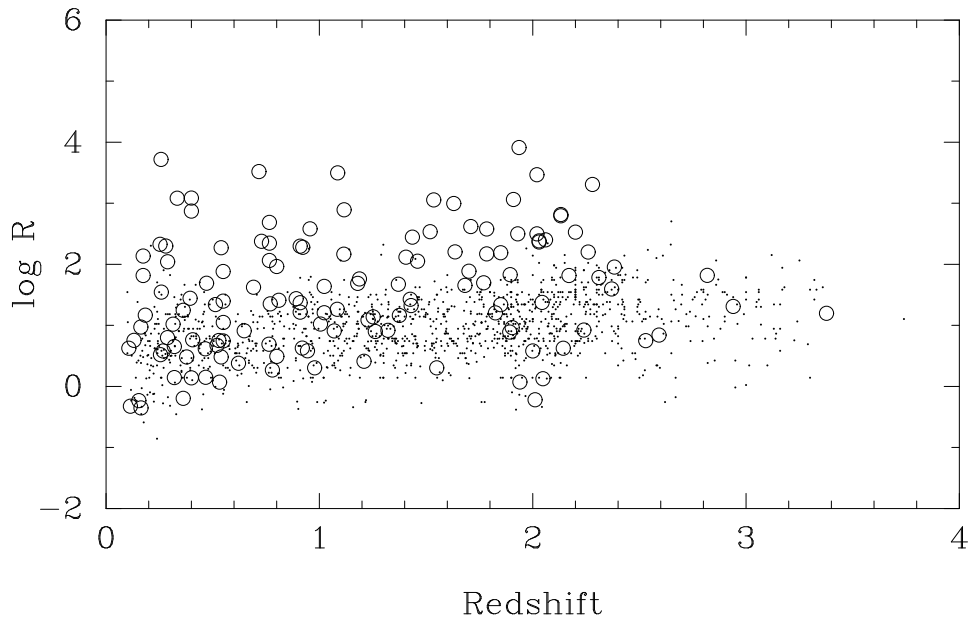


Figure 4.7: R as a function of redshift. Symbols are as in Figure 4.3.

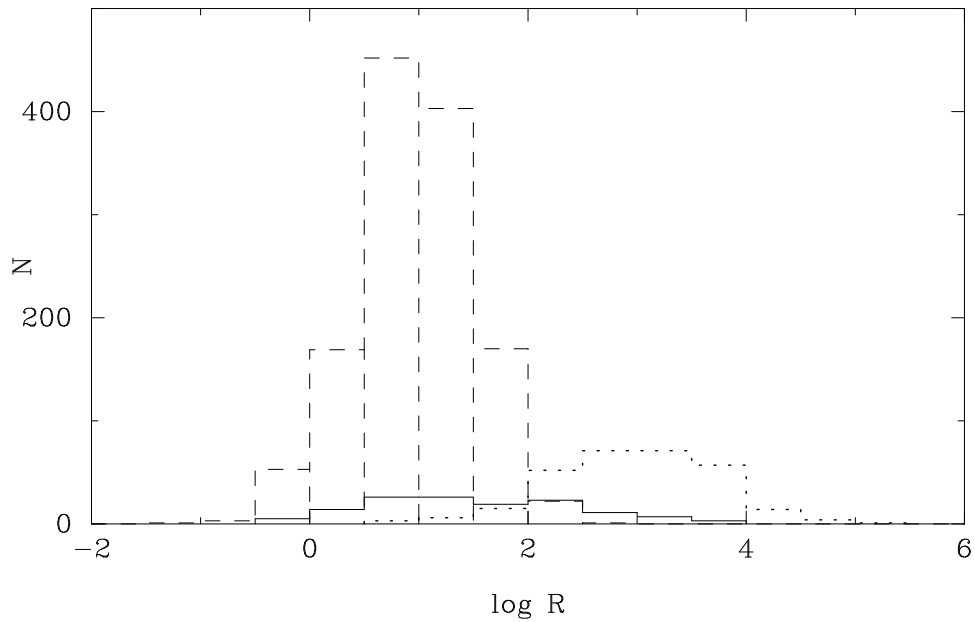


Figure 4.8: Distribution of R for quasars with radio detections (solid line), compared to that for upper limits (dashed line). Radio selected quasars are shown with a dotted line, for comparison.

the detections and upper limits in the region $0 \leq R \leq 3$. The question then is: can statistical techniques from the field of survival analysis (see e.g. Feigelson and Nelson 1985) be used to determine the underlying distribution for a mixed sample of detections and upper limits? If this joint distribution, and the overall distribution of detections have distinct maxima, then one could say that the distribution of R amongst all quasars is bimodal. The appropriate technique to derive the joint distribution would be the Kaplan-Meier estimator included as part of the ASURV package (LaValley, Isobe & Feigelson, 1992). One of the requirements of this estimator is that the probability that an object is censored (i.e. it has an upper limit), is independent of the value of the censored variable. If such *random censoring* applies to our sample, then the shape of the observed distribution of R for the detections and upper limits should be the same, in the region of overlap $0 \leq R \leq 3$. A Kolmogorov-Smirnov test shows that the two distributions may be considered to be drawn from the same population at only ~ 20 percent level of significance. Due to the low level of significance it is not possible to use the Kaplan-Meier estimator, or another similar to it, to obtain a joint distribution. A radio survey with a lower limiting flux than FIRST would be needed to convert the upper limits to detections and to constrain the distribution of R at its lower end. Additional quasars with higher R values can be found by increasing the area covered by the FIRST survey.

We have mentioned in subsection 4.3.1 that the separation of the bivariate luminosity function as in Equation 4.3.2 is most useful if R is independent of the optical luminosity. Moreover, such a separation implies that the mean radio luminosity must increase with the optical luminosity. Such a correlation between the luminosities is not seen in Figure 4.5, and as discussed in subsection 4.3.2, L_r appears to be distributed independently of L_{op} (i.e. absolute magnitude). This requires that the distribution of R depends on L_{op} and separation as in Equation 4.3.2 is not possible. Separation of the bivariate function as in Equation 4.3.1 therefore appears to be the preferred alternative.

4.4 Radio-loud Fraction

As mentioned in the introduction, the boundary between radio loud and radio quiet quasars can be defined either (1) in terms of a characteristic value of the radio to optical luminosity ratio R , say $R = 1$, or (2) in terms of a characteristic radio luminosity. These two criteria are related to the two ways in which the bivariate luminosity function can be split up between the optical and radio parts as discussed in subsection 4.3.1. We have found no correlation between the radio and optical luminosities, which implies that a separation involving R , as in Equation 4.3.2 is not consistent with the data. The distribution of R therefore must be luminosity dependent, and using a single value of R for separation between radio loud and quiet populations is not appropriate. In this situation, we prefer to adopt the criterion for radio loudness which uses radio luminosity as the discriminant as in MPM90.

The dividing radio luminosity chosen by MPM90, in our units, is $10^{33.1} \text{ erg sec}^{-1} \text{ Hz}^{-1}$. This choice was made on the basis of a clear separation between radio detections and upper limits observed by them, which we do not find, as explained in subsection 4.3.2. We have shown the MPM90 division with a dashed line in Figure 4.5. It is seen that there is a region below this line with a number of FIRST survey radio detections, but no upper limits. It is therefore possible for us to reduce the dividing luminosity to a level of $10^{32.5} \text{ erg sec}^{-1} \text{ Hz}^{-1}$, which is indicated by a solid line in the figure. We define as radio loud all quasars with $L_r(5 \text{ GHz}) > 10^{32.5} \text{ erg sec}^{-1} \text{ Hz}^{-1}$, and as radio quiet all quasars below this limit, even though they may have detectable radio emission. The radio loud objects tend to have bright absolute magnitudes, while a dominating fraction of the radio quiet detections have $M_B > -25$. The faintest of the latter objects could perhaps be active galaxies like Seyferts, which in the local neighborhood are known to have lower radio luminosities than radio galaxies. The radio loud quasars can be considered to be luminous counterparts of the radio galaxies, as in the unification model (Barthel 1989). If the radio loud and quiet classes indeed represent such a physical division, then the host galaxies of the former would perhaps be elliptical, as is the case with radio galaxies, while the hosts of the quiet objects would be disk galaxies like the Seyferts. Deep optical and near-IR imaging of different types of quasars would help in settling this issue.

We have plotted in Figure 4.9 the variation of radio loud fraction of all quasars as a function

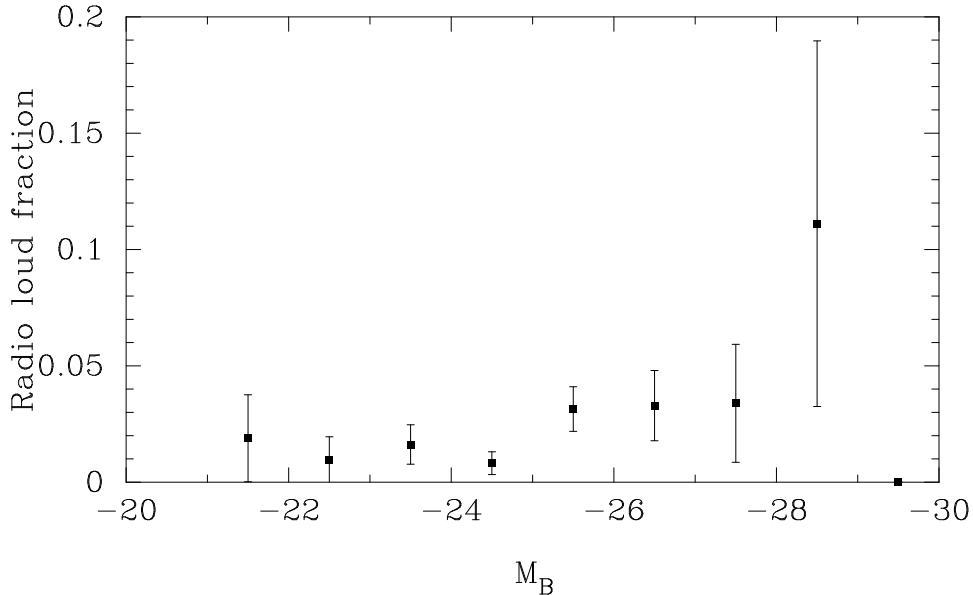


Figure 4.9: Radio loud fraction as a function of absolute magnitude. The error bar shown is the standard deviation for a random binomial distribution in the radio detection fraction.

of absolute magnitude. The fraction here is taken to be the ratio of the number of radio loud quasars to the number of all non-radio selected quasars in one absolute magnitude wide bin. Each point in Figure 4.9 is plotted at the centre of the absolute magnitude bin that it represents. The error bar shown is the $\pm 1\sigma$ deviation about the detected fraction for a random binomial distribution in the radio loud fraction. We find that the radio loud fraction is independent of the absolute magnitude for $M_B \gtrsim -25$, while it increases at brighter absolute magnitudes. The reason for this is the increase in radio luminosity towards brighter absolute magnitudes seen in Figure 4.5, which arises due to the existence of optical and radio flux limits and the consequent redshift dependence of the observed luminosities. An explicit dependence of the radio loud fraction on absolute magnitude would imply a real correlation between the radio and optical luminosities, which is not consistent with the data as we argued in subsection 4.3.2.

In Figure 4.10 we have shown the radio loud fraction as a function of redshift. Each point in the figure represents quasars in a bin of width 0.1 in redshift. The error bars are computed as in Figure 4.9. In contrast with Hooper et al. (1996), we do not find a clear peak in the radio loud fraction between a redshift of 0.5 and 1. We find that the radio loud fraction remains nearly constant upto a redshift of $z \simeq 2.2$. There is an indication of increase in the radio loud fraction at higher redshift, but the number of objects here is rather small, as is apparent from the size of the error bars. A very sharp reduction in the radio loud fraction for $z < 0.5$ was found by BB97. Such a reduction is seen only when radio selected and non-radio selected quasars are considered together, and is also apparent in our data if the two kinds of objects are mixed. We have chosen not to do that, to keep our results free from biases introduced by the radio selected objects, as explained in subsection 4.3.2.

The large 1σ error bars, on the plots presented in this section, are caused by the relatively few non-radio selected quasar detections. Due to these error bars it is not possible to distinguish unambiguously between alternatives regarding the dependence of radio loud fraction on other observable properties. More data would be required to confirm or refute our preliminary conclusions regarding the evolution of radio loud fraction with absolute magnitude and redshift.

4.5 Summary

The main results of the work described in this chapter are:

- We have reported radio detections of 69 previously undetected quasars.

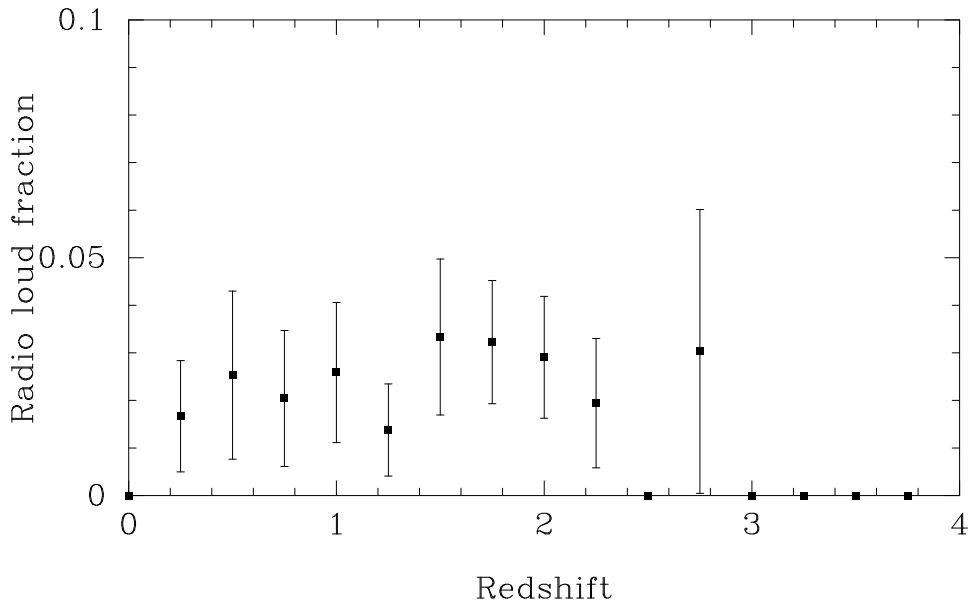


Figure 4.10: Radio loud fraction of quasars as a function of redshift. The error bars are obtained as in Figure 4.9.

- We have found additional evidence that the close pair of quasars 1343+266A and 1343+266B are *not* gravitationally lensed.
- We have found no correlation between radio luminosity and optical luminosity for the non-radio selected quasars. Our data is consistent with a bimodal distribution in radio luminosity. The distribution of the ratio of radio to optical luminosity is also bimodal, but this may have little relevance because of the lack of a clear correlation between radio and optical luminosities.
- The data indicate that radio loud fraction is not strongly dependent on absolute magnitude, which is consistent with the lack of correlation between radio and optical luminosities.
- The data indicate that radio loud fraction does vary significantly with redshift.

The highly heterogeneous nature of the sample used here makes it inappropriate for studies in parameter ranges where it is seriously incomplete e.g. at high redshift and high radio luminosities. Large surveys like the Digitized Palomar Observatory Sky Survey (DPOSS) and the Sloan Digital Sky Survey (SDSS) will remedy this situation, by providing a large number of quasar candidates for spectroscopic follow up.

It is possible that the radio emission from radio loud and radio quiet quasars may be powered by entirely different physical mechanisms. In recent years, there have been suggestions that radio emission in radio quiet quasars originates in a nuclear starburst rather than accretion onto a central engine (Terlevich et al. 1992). A logical step in testing this idea is to look for differences in the radio and optical morphology of the quasar environment for the two quasar populations (eg. Kellerman 1994). This will require a systematic study of radio morphology of quasar environments obtained from a deep, high resolution survey with good coverage of the u,v -plane.

It is also of great interest to see how the results reported in this chapter apply to the low redshift, low luminosity counterparts of quasars - the active galactic nuclei. We proceed to do that in the next chapter.

Chapter 5

Radio emission from AGN

This chapter is largely based on Wadadekar & Kembhavi (2000). Using the most recent (July 1999) version of the VLA FIRST survey radio catalog, we have searched for radio emission from 1219 AGN taken from the most recent (2000) version of the Veron-Cetty and Veron AGN catalog. These AGN lie in the ~ 6000 square degrees of sky already covered by the VLA FIRST survey. Our work has resulted in positive detection of nuclear radio emission from 521 AGN of which 206 AGN have been detected for the first time at radio wavelengths.

5.1 Introduction

In the simplified hypothesis for unification of AGN, there are basically just two types of AGN - the radio quiet and the radio loud. For each type there is a range of intrinsic radio luminosity. However, at a given intrinsic luminosity, *all* other properties of AGN from spectroscopic classification to VLBI component speeds can be ascribed to orientation effects. Such a strong hypothesis is ruled out by many observations. The true situation may be somewhere in between this and the opposite possibility that orientation does not affect classification at all.

A straightforward test of the unification hypothesis is to see if a property that is *not* orientation dependent has similar values for different classes of AGN. Assuming that the standard unification scheme for AGN is valid (See Section 3.2), radio and FIR luminosities of AGN are expected to be orientation independent, except over a small angle where Doppler boosting of radio jets occurs. This is because neutral gas and dust surrounding the radio source itself cannot obscure it, and even ionized gas (found in nuclear starbursts) is transparent at radio frequencies $\nu > 3$ GHz. In fact, the most compact nuclear starbursts are transparent only at radio and far infrared (FIR) wavelengths. At other wavelengths, absorption of the radiation by the intervening matter surrounding the nucleus is significant and it is very difficult to measure the intrinsic luminosity. The unification scheme can thus be effectively tested by radio observations of different kinds of AGN.

Radio observations of several samples of AGN (specifically Seyfert galaxies) have been made in recent years. The aim of these studies was to use statistical properties of radio sources in these galaxies to draw conclusions about their physical character, and to test the unification scheme. De Bruyn & Wilson (1976,1978) surveyed a sample of 43 Markarian Seyferts and found that Seyfert 2 galaxies have a higher radio luminosity than Seyfert 1 galaxies. Ulvestad & Wilson (1984) used high resolution data from the VLA on a radio flux limited sample of 79 Markarian Seyferts and a distance limited sample of 25 Seyfert galaxies. They found that Seyfert 2 galaxies are systematically more luminous than Seyfert 1 galaxies and that a weak correlation exists between sizes and powers of nuclear radio sources in Seyferts. On average, Seyfert 2 radio sources are larger than those of type 1 Seyferts. However, in a subsequent study, Ulvestad & Wilson (1989) found that their sample of Seyfert 2's could have been a biased one. Their analysis of a distance limited sample of 27 Seyfert galaxies that was free of these biases showed that the earlier conclusions was not statistically significant. This new result supported the finding of Edelson (1987) that there was no significant difference between the radio luminosities of the Seyfert 2 and Seyfert 1 galaxies in his magnitude limited sample of 42 Seyferts.

All the above studies of radio emission in AGN have been plagued by small sample sizes, and some of them also by selection biases that were only discovered many years later. In this work we use FIRST survey data to look for radio emission from over 1600 AGN, lying in the current FIRST

survey area. Our sample is over an order of magnitude larger than samples in previous studies. However, it is a motley collection of active galaxies rather than a well defined, complete sample. The large sample size, however, makes it possible for us to recognize useful statistical trends in the data.

Radio emission in the low luminosity AGN such as Seyfert galaxies can be caused by two distinct physical mechanisms: (i) Non-thermal synchrotron emission from the disk is powered by thermal processes in H-II regions surrounding massive short lived stars and by cosmic rays accelerated in the supernova remnants of these stars. Such radio emission shows a tight correlation with the far infrared (FIR) emission (Condon, Anderson, & Helou 1991). These star forming regions may be distributed anywhere within the disk including the nuclear region. The FIR emission is thought to be mostly thermal emission from nuclear dust that is heated by the optical-ultraviolet continuum source, rather than non-thermal synchrotron emission (Roy et al. 1998). (ii) Nuclear radio emission in Seyfert galaxies can also be powered by a central engine, as in the case of radio galaxies and of quasars. This non-thermal nuclear emission originates from a compact, high brightness temperature core, and from the surrounding ~ 100 parsec scale structures that are low power analogues of the jets in powerful radio galaxies. The nuclear jets are intimately associated with narrow-line region clouds (Evans et al. 1991). The clouds are excited by non-thermal accretion related processes and the radio knots are not expected to display the radio-FIR correlation.

The existence of two mechanisms for the radio emission gives rise to two possibilities: (i) Seyfert galaxies that lack a compact radio core should display a good radio-FIR correlation while (ii) Seyferts with strong radio cores should have an excess of radio emission and should not follow the radio-FIR correlation. In the extreme case for AGN with strong core radio emission such as in radio loud quasars, no radio-FIR correlation should be seen. This is indeed the case (Sopp & Alexander 1991).

Our AGN sample is drawn from the most recent (9th) edition of the Veron-Cetty and Veron (2000) catalog (hereafter VV00), which is a complete survey of the literature and lists all quasars and active nuclei known to the authors of the catalog prior to March 1, 2000. They define a quasar as a starlike object, or object with a starlike nucleus, brighter than absolute magnitude $M_B = -23$ (using $H_0 = 50 \text{ km sec}^{-1} \text{ Mpc}^{-1}$, $q_0 = 0$, and optical spectral index $\alpha_{op} = 0.3$). Objects fainter than this limit appear in Table 3 of the catalog, which we have used in our work. Some of the objects listed in this table would move to Table 1 (which lists quasars) and vice versa for a different choice of cosmological parameters. Variability and the size of the diaphragm used for the apparent magnitude measurement may have a similar effect, as the contribution of the underlying host galaxy may be significant for the faint quasars. Such a criterion has the additional shortcoming that at higher redshifts the AGN luminosity function is artificially truncated. However, these caveats in sample identification are offset by the large size of the sample - 4428 active galaxies are listed in Table 3 of the catalog, of which 1614 lie in the area currently covered by the FIRST survey.

5.2 Radio/optical comparisons

We compare the positions of AGN listed in VV00 to the positions of radio sources in the FIRST radio source catalog (July 21, 1999 version publicly available at <http://sundog.stsci.edu/>), and calculate the angular separation between each AGN and each FIRST source. Note that we use here a version of the catalog that is more recent and contains about 20% more sources than the version used in the work reported in the Chapter 4. As mentioned in Section 4.2, 4% of sources in the FIRST catalog have been tagged as possible sidelobes of bright sources. Of these, <10% are real sources and considerably less than 1% of the unflagged sources in the catalog are sidelobes. We have excluded such flagged sidelobe sources from our cross correlation. We are then left with a total of 530,011 unflagged sources in the northern and southern strips, covering a total area of about 6060 square degrees. On an average, there are 87.46 unflagged FIRST sources per square degree of sky.

In order to find coincidences between VV00 and FIRST sources, we adopt the same technique as used in the previous chapter. We begin with a search circle of radius of 300 arcsec centered on each VV00 AGN, and look for FIRST radio sources within this circle. When there is more than one FIRST source in the search circle, we tentatively accept all such sources as matches. In Figure 4.2 we show a histogram of the angular separation between the VV00 quasars and the FIRST sources

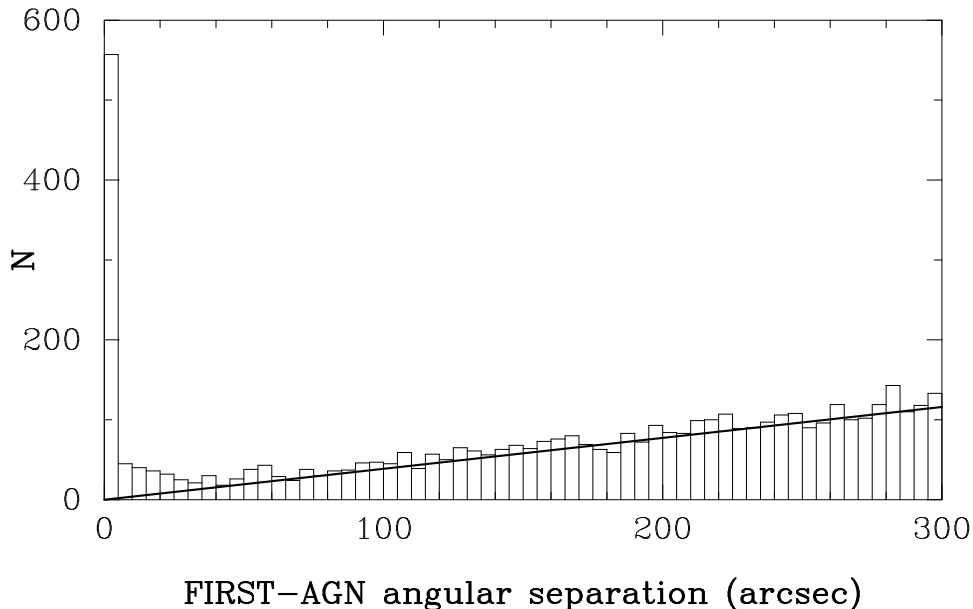


Figure 5.1: A histogram of the angular separation between the AGN and the corresponding FIRST source. The straight line is the number of chance matches expected, in annuli of radius shown on the X-axis having a width of 5 arcsec, if the FIRST sources were randomly distributed in the sky.

Number of VV00 AGN in FIRST area:	1614
Number of AGN with radio detections:	521
Number of non-detections:	1093
Percentage of AGN with radio emission detected by FIRST:	32%

Table 5.1: Summary of radio detections

found in the search circles.

To see which of the radio sources found can be accepted as true identifications, we estimate the AGN-FIRST source chance coincidence rate for a random distribution of FIRST survey sources using a technique identical to the one discussed in Section 4.2. The straight line in Figure 5.1 is the expected number of chance coincidences between quasars and FIRST sources, in annuli of radius shown on the abscissa and width 5 arcsec around the quasars. It is seen from the figure that the expected number of chance coincidences closely matches the number of actual coincidences for radius ≥ 40 arcsec, indicating that most FIRST sources found more than 40 arcsec away from the AGN are chance coincidences. On the other hand, matches within 3 arcsec are almost all real (less than 0.05% chance identification probability).

The high resolution and excellent astrometric accuracy of the FIRST survey makes it well suited for studies of compact radio sources. Nuclear regions of AGN are known to have compact radio sources, and these are the focus of the present study. For our choice of cosmological parameters ($H_0 = 50 \text{ km sec}^{-1} \text{ Mpc}^{-1}$ and $q_0 = 0.5$), for an overwhelming majority of AGN in our sample, an angular size of 3 arcsec corresponds to a spatial scale of < 3 kpc, and we are essentially studying radio emission from a region less than 3 kpc away from the center of the galaxy. We, therefore, miss out those AGN which may have significant radio emission coming from the extended radio lobes, but no active nuclear emission. Although such a scenario is quite likely in a sample of radio galaxies, it is not very likely to occur for the Seyfert galaxies in our sample which are known to possess relatively strong radio cores with most of the radio emission coming from the nuclear region (e.g. Ulvestad & Wilson 1989). We would however miss the radio sources located in starforming regions more than 3 arcsec from the center of the galaxy.

We use a search circle of radius 3 arcsec and count all matches found within this radius as *true* matches. All subsequent discussion about the radio properties of the AGN only uses matches obtained with this search radius.

Class	Number in area covered by FIRST	Number detected by FIRST
Seyfert 1	264	89
Intermediate type Seyferts	212	117
Seyfert 2	170	96
Seyfert 3 (LINERS)	39	29
Unconfirmed Seyferts ^a	111	97
H-II regions	54	26
Unlisted ^b	764	67

Table 5.2: Number of radio detections of various classes of AGN at the 1 mJy flux limit of the FIRST survey. ^aMost of these identifications are from White et al. (2000) and will require further spectroscopic observations to confirm their status. ^bThese sources do not have a class listed in the VV00 catalog.

We have 521 AGN with a FIRST source located less than 3 arcsec away from the centre of the AGN. Only 1 AGN (NGC 1068) has two FIRST sources within three arcsec of its nucleus. There are 1093 non detections, amongst the VV00 AGN covered by FIRST, and we assign an upper limit of 1 mJy to their radio flux at 1.4 GHz. Table 5.1 provides a summary of our radio detections. Table 5.2 lists the number of detections for the various types of AGN listed in VV00.

The radio and optical properties of the AGN with detections are summarized in Table 5.3. The columns are follows:

Column 1: The most common name for the object as listed in VV00. The 206 radio detections with a * preceding their designation have not been previously detected as a radio source and this work presents the first radio detection of the objects. The lack of previous radio detection is either because the object had not been observed or because its flux was lower than the sensitivity limit reached by previous radio observations of that object. There was therefore no uniform upper limit to the flux density of these previously undetected objects.

Column 2: Object class as listed in VV00

Column 3: The redshift as published in the literature. A * in front of the redshift means that it has been estimated from a low dispersion slitless spectrum and is of lesser accuracy.

Column 4: The photoelectric or photographic V magnitude. We have converted the various magnitudes listed in VV00 to V magnitudes using $B - V = 0.4$, $V - R = 0.17$ and $V - I = 0.7$

Columns 5,6: Coordinates for the radio source from the FIRST source catalog.

Columns 7,8: Peak and integrated radio flux densities for the radio source.

Column 9: Angular separation between AGN and FIRST source.

Table 5.3: FIRST detections of AGN. The complete table is available in electronic form with us. A portion is shown here for guidance regarding its form and content. The various columns listed are described in the text.

Designation	Category	z	V	R.A. (J2000)	Dec. (J2000)	F_{peak} (mJy)	F_{int} (mJy)	Sep. (arcsec)
MS 00071-0231	S1	0.087	16.33	00:09:39.59	-02:14:36.5	1.82	1.87	1.49
*UM 213	H2	0.041	16.	00:12:17.81	-00:06:09.4	1.15	1.43	1.50
Q 0019+0022A		0.314	18.6	00:21:41.04	+00:38:41.3	1.72	1.38	0.60
*MARK 549	S1	0.039	15.55	00:21:53.80	-01:36:36.6	2.84	3.03	0.61
*UM 246	S2	0.060	16.0	00:29:44.89	+00:10:11.1	3.75	4.26	0.24
*UM 254	H2	0.044	17.	00:31:34.34	-02:09:18.5	2.32	3.35	0.76
IRAS 00321-0018	S2	0.043	14.4	00:34:43.50	-00:02:26.9	55.18	56.68	1.11
*MARK 955	S2	0.035	14.09	00:37:35.83	+00:16:50.6	5.95	7.06	0.60
*MS 00390-0145	S1	0.110	17.86	00:41:36.79	-01:29:12.6	1.27	0.80	0.40
MS 00533-1035		0.308	19.4	00:55:50.70	-10:19:06.2	2.07	3.03	1.85

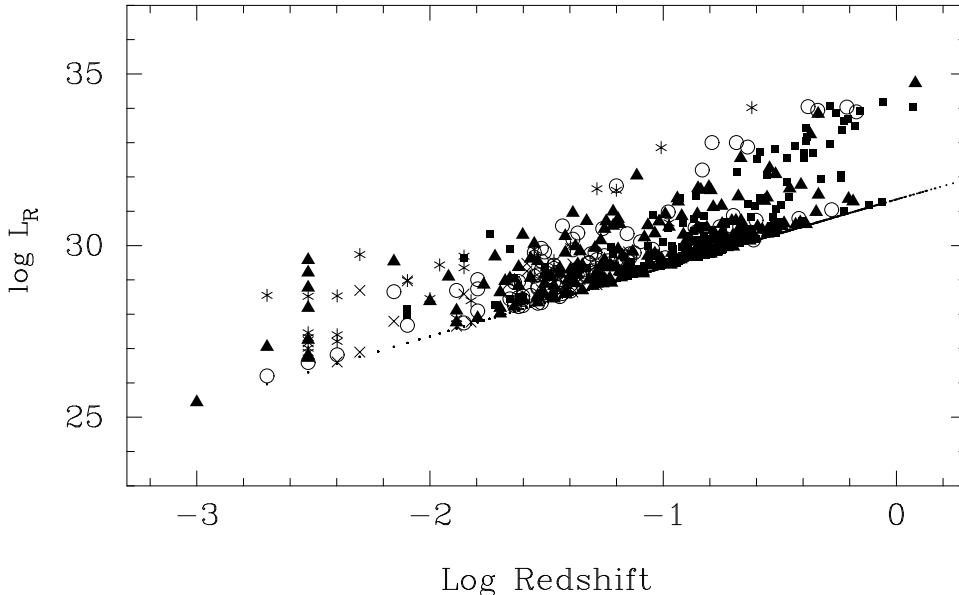


Figure 5.2: Radio luminosity as a function of redshift. The various symbols used correspond to the various kinds of AGN, as explained in the text. The lower locus of dots indicates the 1 mJy upper limits.

5.3 Distribution of radio luminosity

We have shown in Figure 5.2 a plot of the 5 GHz radio luminosity against redshift for the AGN. The non-detections are shown as dots, and form the almost continuous lower envelope which indicates the radio luminosity corresponding to a radio flux of 1 mJy over the redshift range shown. The triangles indicate Seyfert 1 galaxies, the open circles indicate Seyfert 2 galaxies, the asterisks indicate Seyfert 3 (LINER) galaxies, crosses indicate H-II regions, while the filled squares indicate those sources for which a category is not listed in the VV00 catalog. The same symbols are used in subsequent figures.

Seyfert 1 and Seyfert 2 galaxies span the entire redshift range shown in the figure. However, H-II regions and LINERS are predominantly seen at low redshifts. This is because the low average radio luminosity of these objects makes them detectable above the FIRST flux limit only at low redshifts. Another trend seen is that many of the highest redshift AGN do not have a classification in VV00 (these are indicated by filled squares). Many of these objects are in reality moderate redshift quasars, which have been included in Table 3 of VV00, only because they have absolute magnitude $M_B > -23$.

In Figure 5.4 is shown a plot of the 5 GHz radio luminosity against the absolute magnitude for the radio detections. In this figure, there is a clear correlation between the logarithm of the radio luminosity and absolute magnitude. The linear correlation coefficient for the radio detections is -0.54 , which is significant at the $> 99.9\%$ confidence level.

However, it is seen from Figure 5.3 and Figure 5.2 that mean radio and optical luminosity both increase with redshift, which is due to the existence of a limiting radio flux and apparent magnitude in the surveys in which quasars are discovered. It is possible that the observed correlation between radio and optical luminosities is mainly due to the separate dependence of each luminosity on the redshift z . It is important to see if the correlation remains significant when such an effect of the redshift on the observed correlation is taken into account. This is done by evaluating a *partial linear correlation coefficient* as described in subsection 4.3.2.

For our sample of 521 radio detections, the partial linear correlation coefficient is just 0.003, which is significant only at the 66% confidence level. The observed correlation between the radio luminosity and absolute magnitude is thus entirely induced by the effect of the range in redshift over which the sample is observed. Within the redshift range which we have explored, radio and optical luminosities of AGN are *not* correlated with each other. This lack of correlation between radio and optical luminosities is also reflected in the large scatter and lack of correlation in a plot of radio versus optical flux (Figure 5.5). Edelson (1987) has reported a highly significant correlation

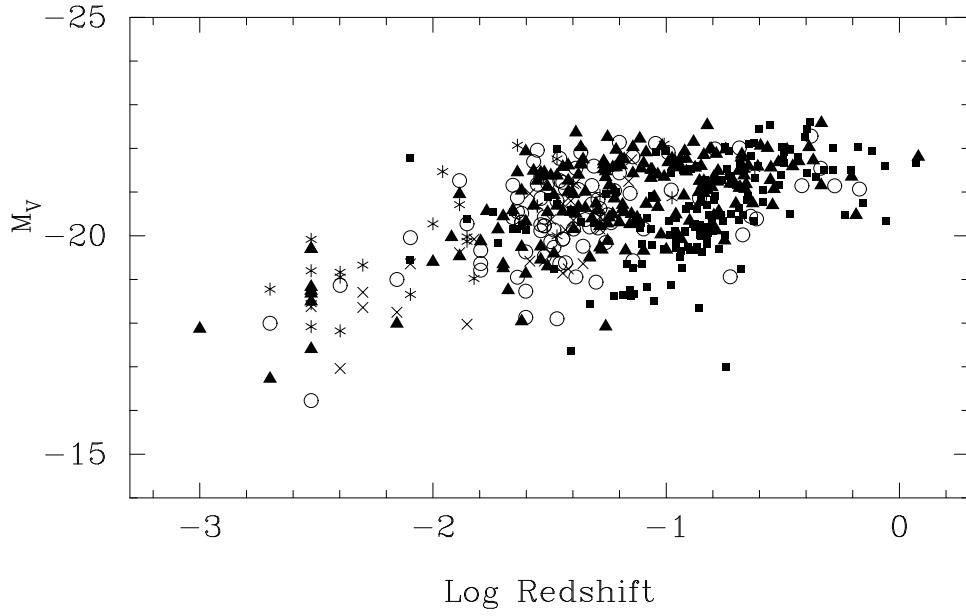


Figure 5.3: Absolute magnitude of the AGN in our sample as a function of redshift. The symbols are as in Figure 5.2.

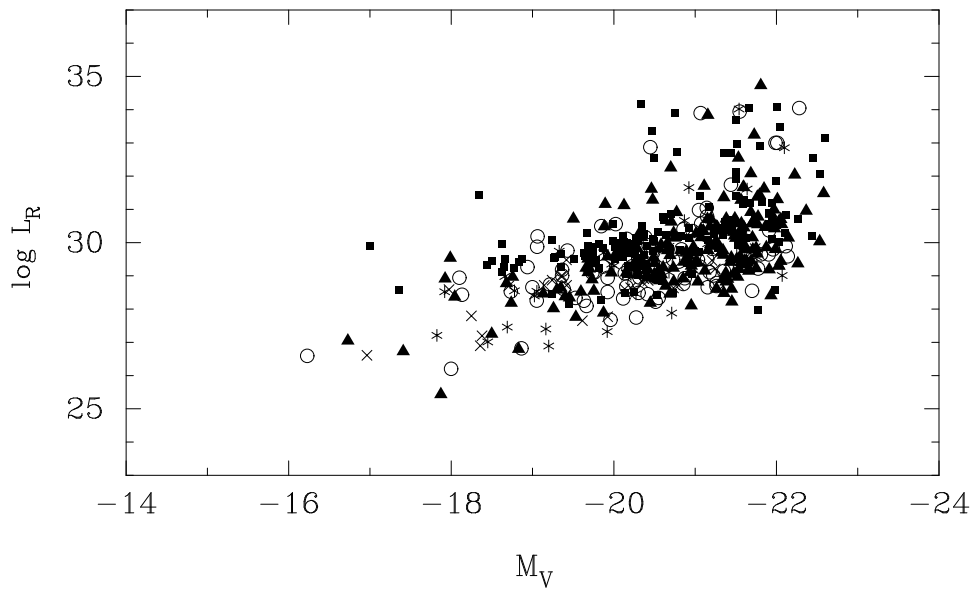


Figure 5.4: Radio luminosity as a function of absolute magnitude. The symbols are as in Figure 5.2.

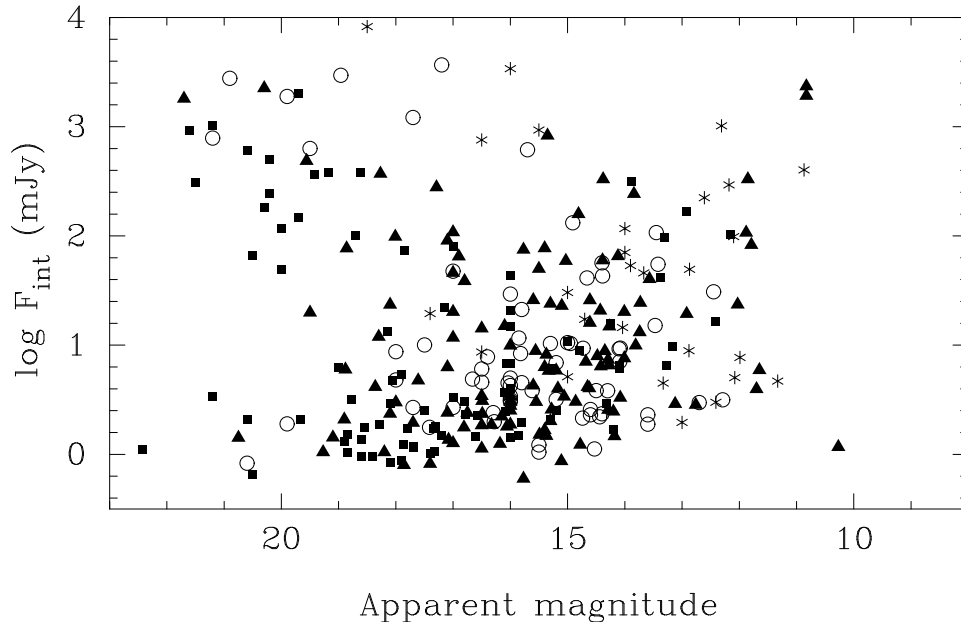


Figure 5.5: Radio flux as a function of apparent magnitude. The symbols are as in Figure 5.2.

	Seyfert 1	Seyfert 2
Mean radio source size (kpc)	2.07 ± 1.97	2.67 ± 2.24
Mean log radio luminosity ($\text{erg sec}^{-1} \text{Hz}^{-1}$)	30.27 ± 0.96	29.64 ± 1.46

Table 5.4: Mean radio source size and mean radio luminosity for Seyfert 1 and Seyfert 2 galaxies.

between the radio and optical luminosities of Seyfert galaxies. However, the conclusions in that paper are erroneous because the author failed to take into account the effect of the redshift, as we have done here. Our conclusions are not affected when we consider the radio-optical correlation separately for Seyfert 1 and Seyfert 2 galaxies. The lack of correlation is not altogether unexpected, because the radio emission very likely originates entirely in a non-thermal nuclear source while the optical emission has significant contribution from stars in the disk of the underlying galaxy.

5.4 Radio luminosities of Seyfert galaxies

We looked for differences in radio source luminosity and size for the Seyfert 1 and Seyfert 2 galaxies. We have used the Seyfert classifications listed in the VV00 catalog, without attempting to verify them independently. To avoid confusion from borderline classifications, we used only those galaxies with a reliable classification of Seyfert 1 or Seyfert 2, rejecting the intermediate types (Seyfert 1.2, 1.5, 1.8 etc.). We have FIRST detections for 89 out of the 264 Seyfert 1 and 96 out of the 170 Seyfert 2 galaxies in our sample. The detection rate is thus about 34% for the Seyfert 1 and 56% for the Seyfert 2 at the 1 mJy level. This is broadly consistent with the findings of other researchers such as Roy et al. (1994) who also find that the Seyfert 2 have a higher radio detection rate (46%) than the Seyfert 1 (26%).

We list in Table 5.4 the mean radio source size and mean radio luminosity (with their respective standard deviations) for the two types of galaxies in our sample. The mean radio luminosity of both types of Seyferts is two orders of magnitude lower than even the optically selected quasars (see Figure 4.6), most of which fall in the category of radio quiet quasars. Though the radio emission from Seyferts is weak, it is still two orders of magnitude higher than the typical emission from normal galaxies (Wunderlich, Klein & Wielebinski 1987). A Kolmogorov-Smirnov test shows that the null hypothesis that the radio luminosity distributions of Seyfert 1 and Seyfert 2 are drawn from the same populations is disproved only at the 97% significance level.

The table indicates that the mean radio luminosity of the Seyfert 1 is greater than that of

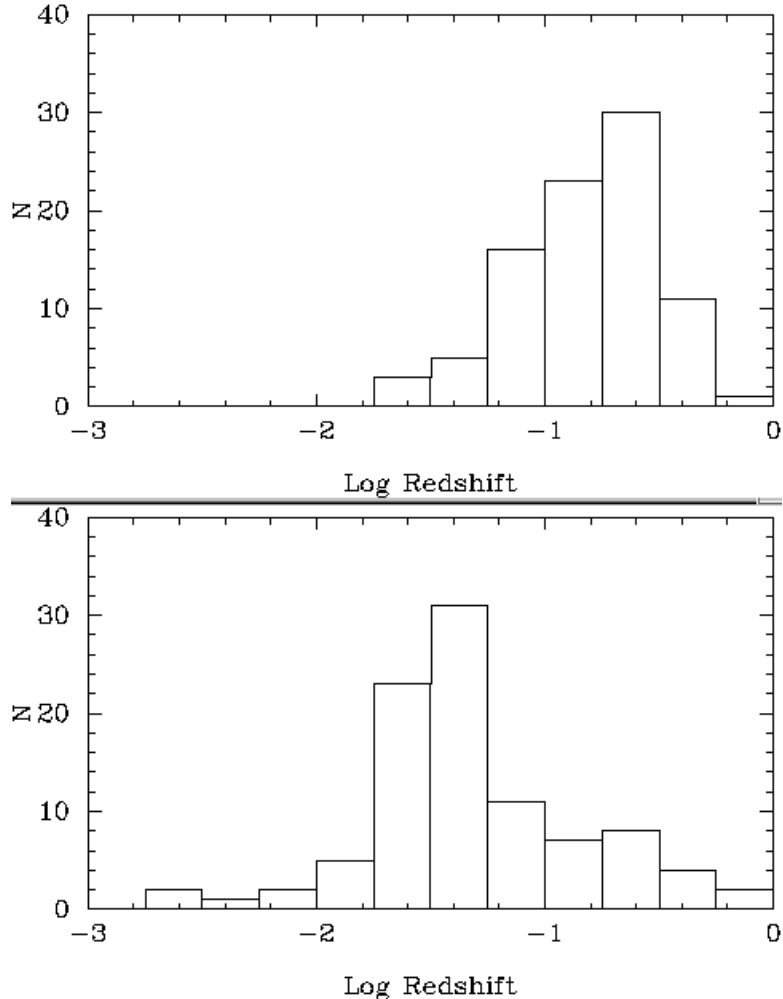


Figure 5.6: Redshift distribution of the detections for the Seyfert 1 (top panel) and the Seyfert 2 (bottom panel) galaxies.

the Seyfert 2. This rather surprising result which is contrary to the findings of previous work, may be understood by examining the redshift distribution of our Seyfert detections shown in Figure 5.6. The figure shows that our sample is slightly biased in redshift - the Seyfert 2 have a slightly lower mean redshift compared to the Seyfert 1 galaxies. Their flux distribution on the other hand, is almost identical. This implies that the mean luminosity of the Seyfert 1 in our sample would be higher, which indeed it is. However the standard deviation of the radio luminosity is higher than the difference in mean luminosities and therefore a strong statistical conclusion cannot be drawn from our data.

The standard deviations for the radio source size are rather large because several sources are unresolved in the FIRST survey and are listed with a deconvolved source size of 0.00 arcsec in the FIRST catalog. The table shows that the difference in radio source size between the two Seyfert types is *not* significant.

The similarity between radio luminosity and radio source sizes for the two classes of Seyferts is consistent with the expectation from the orientation based unification scheme.

5.4.1 Normalized radio luminosities

Edelson (1987) found no significant difference between the radio luminosities of Seyfert 1 and Seyfert 2 galaxies in his sample. Nevertheless, when Edelson normalized his radio luminosities to the total optical luminosity, he did find that Seyfert 2 galaxies are on the average twice as luminous as Seyfert 1 galaxies, at the 99% confidence level. We used the radio to optical luminosity ratio R as defined in subsection 4.3.3 as a measure of normalized radio luminosities for the the two types of Seyferts. For Seyfert 1 galaxies the mean value of $\log R$ is -0.02 ± 2.69 , while for Seyfert 2 galaxies, the mean value of $\log R$ is 0.00 ± 2.13 . In fact, we find that the mean normalized radio luminosity of the

Seyfert 1 is nearly identical to that of the Seyfert 2. A Kolmogorov-Smirnov test disproves the null hypothesis that the distributions of R are the same only at the 97% significance level.

5.5 Summary

The results of the work reported in this chapter are:

- We have detected nuclear radio emissions from 521 AGN of which 206 were previously undetected in the radio. We have detected nuclear emission from $\sim 32\%$ of the known AGN at a flux limit of 1 mJy.
- We do not find a statistically significant correlation between radio luminosity of the AGN and the optical luminosity of the underlying host galaxy. The apparent correlation seen is caused entirely by the effects of redshift.
- We find no significant statistical difference in the distribution of radio luminosity, the radio source size and the radio to optical luminosity ratio of Seyfert 1 and Seyfert 2 galaxies, contrary to some previous studies. Our findings are consistent with the expectation from standard Seyfert unification models.

An important shortcoming of the optical source samples used in the previous two chapters is that they are not *complete* samples in any sense, but are merely compilations of different samples, each with its own known and unknown biases. Practically, this implies that a luminosity function for these sources cannot be constructed from the present data. In order to make that possible, data from a complete sample of optical sources must be combined with the complete sample of radio sources from FIRST. The DPOSS survey provides such an optical survey. Preliminary results of our work to correlate FIRST with DPOSS form the subject of the next chapter.

Chapter 6

Optical Identification of FIRST sources with DPOSS

The second strategy for obtaining the optical identifications of FIRST sources is to use an unbiased optical survey for obtaining optical counterparts. In this chapter, we provide some results from a correlation of FIRST sources with an optical catalog constructed from the DPOSS survey. We have identified over 200 *faint* quasar candidates for spectroscopic followup. A candidate list for high z quasars has also been constructed.

6.1 Introduction

The Palomar Digitized Sky Survey (DPOSS), which we briefly described in Section 2.2 is a digitized version of the POSS-II photographic sky atlas. It is based on the scans of the original plates, done at the Space Telescope Science Institute, USA.

The goal of this survey is to provide a modern, uniform digitized data set covering the entire northern sky in 3 survey bands (photographic *JFN*, calibrated using CCD observations to Gunn *gri*), with a high photometric and object-classification accuracy to enable a wide range of scientific follow-up studies.

While any digitized survey such as DPOSS, that uses scanned photographic plates, is inferior in quality to the fully digital sky surveys such as the SDSS, the SDSS data will not be generally available over the entire northern sky until 2005. In the meantime, DPOSS can provide to the astronomical community data of adequate quality for many scientific studies envisioned for the SDSS. DPOSS has the additional advantage that it will also cover the lower Galactic latitudes, where SDSS data will not exist. DPOSS can therefore be used to study those galactic sources as well which predominate at lower galactic latitudes.

The POSS-II covers the entire northern sky ($\delta > -3^\circ$) with 894 overlapping fields (6.5° square each with 5° spacings), and, unlike the older POSS-I, it has no gaps in coverage. Approximately half of the survey area has been covered at least twice in each band, due to plate overlaps. Plates are taken in three bands: blue-green, IIIa-J + GG395, $\lambda_{eff} \sim 480$ nm; red, IIIa-F + RG610, $\lambda_{eff} \sim 650$ nm; and very near-IR, IV-N + RG9, $\lambda_{eff} \sim 850$ nm. Typical limiting magnitudes reached are $B_J \sim 22.5$, $R_F \sim 20.8$, and $I_N \sim 19.5$, i.e., $\sim 1 - 1.5$ magnitudes deeper than the POSS-I. The image quality is improved relative to the POSS-I, and is comparable to the southern photographic sky surveys. Preliminary astrometric solutions are good to a r.m.s. of ~ 0.5 arcsec, and more detailed solutions are expected to reach a r.m.s. of ~ 0.3 arcsec. An artificial neural network based star/galaxy classification is accurate to 90% or better down to ~ 1 magnitude brighter than the detection limit.

DPOSS data are superior to the widely available DSS scans made from POSS-I for the following reasons:

1. the original plates, rather than second copies, are scanned.
2. the plates have a finer grain, better image quality, and reach ~ 1 magnitude deeper than POSS-I.
3. the scans have an improved dynamical range and finer pixels, viz., 1.0 arcsec instead of 1.73 arcsec used in the DSS scans.

Field name	R.A. range	Dec. range
f441	12:04:21.26 - 12:32:31.19	+26:45:04.9 - 32:46:49.3
f443	12:50:25.59 - 13:18:14.18	+26:47:15.2 - 32:45:24.2
f445	13:35:14.88 - 14:05:14.88	+26:36:03.4 - 32:57:28.5

Table 6.1: Coordinates of the high galactic latitude DPOSS fields chosen for cross correlation with FIRST.

- extensive CCD calibration data on the DPOSS is being obtained using the Palomar 60-inch telescope with some additional data on the equatorial fields being obtained at CTIO and ESO. The data are calibrated to the Gunn *gri* system to make comparisons with the SDSS easier.

The digitized plates constitute about 4 terabytes of data. To make this vast data set usable by the astronomical community, the final data product of the survey will be released as the Palomar-Norris Sky Catalog (PNSC), which will contain cataloged data on all objects down to the survey limit (equivalent to $B_{lim} \sim 22$), with classifications and their statistically estimated accuracy available down to ~ 1 magnitude above the detection threshold. The catalog will be confusion limited at low Galactic latitudes, where the surface density of sources exceeds ~ 20 million per plate; most of these objects are galactic stars. The catalog is estimated to contain > 50 million galaxies, and > 2 billion stars, including $\sim 10^5$ quasars. The expected median redshift for the galaxies is $z \sim 0.2$.

There are several motivations for obtaining optical identifications of sources detected in the FIRST survey using a large area sky survey such as DPOSS. The identifications will include many kinds of astrophysically interesting objects - ultraluminous IR galaxies, distant and/or peculiar quasars and many kinds of active galaxies. It is also possible that the identifications will contain rare, or even previously unknown types of objects, as defined by clustering in the parameter space, e.g., objects with unusual colors and/or morphological structure. Statistical studies of even rare objects will become possible, because the correlation of the entire FIRST survey with DPOSS will provide a matched dataset of over 10^5 sources.

6.2 CCD calibration of DPOSS sources

An average of two CCD fields per plate are being obtained by the DPOSS team for calibration purposes, in the three Gunn *gri* bands. A photometric transformation equation is derived for each plate, that allows the conversion of photographic *JFN* magnitudes to the standard Gunn *gri* magnitudes. The Gunn photometric system was chosen as the standard to facilitate comparison of DPOSS photometry with that from the SDSS which also uses this system.

Each DPOSS source is marked on a plot of photographic magnitude versus the corresponding calibrated magnitude in the Gunn system. A best-fit curve is obtained for these data points. It has been found that for stars, a spline fit gives accurate transformations, while for extended sources, even a linear transformation is sufficiently accurate. In this work, we have used the appropriate photometric transformations for our DPOSS plates (A. Mahabal, private communication) to convert the photographic magnitudes to the Gunn system.

6.3 DPOSS-FIRST cross correlation

In the present work, carried out in collaboration with A. Mahabal, we have used the DPOSS source catalog to identify over two thousand optical counterparts of FIRST radio sources. We chose three adjacent but non overlapping fields at the North Galactic Pole for the cross-correlation. Choosing fields at high galactic latitude minimizes contamination by galactic stars. The coordinates of the fields we used are listed in Table 6.1.

6.3.1 The DPOSS source catalog

Catalogs of DPOSS sources constructed from F band data were used for the correlation, since this filter gives the highest S/N ratio for most objects (A. Mahabal, private communication). Some of the objects detected in the F band are not detected in the J and/or N bands. The catalogs we used were constructed from the scanned plates using the SKICAT software (Weir et al. 1995). The DPOSS source catalog for each plate (which covers approximately 40 square degrees) typically contains 150,000 sources brighter than a magnitude limit of 21. This corresponds to nearly 4,000 sources per square degree. In the area of sky occupied by each plate, there are ~ 3300 FIRST sources.

6.3.2 Matching the catalogs

We used the July 1999 version of the FIRST catalog as in Chapter 5. We matched the positions between sources in DPOSS and FIRST using the technique described in Chapter 4. We adopted a search radius of 3 arcsec. A small value of the search radius was motivated by two factors.

1. The excellent astrometric accuracy of DPOSS (the 90% error circle is about 0.5 arcsec in radius) combined with the good accuracy of the FIRST survey, made reliable matches possible even with such a small search radius.
2. Since the source density of DPOSS is as high as 4000 per square degree, even a small search radius like 3 arcsec gives us a chance coincidence rate of 1%. With a larger search radius the error rate would be unacceptably high.

With this search radius we found an average of ~ 700 matches per plate. The three plates together gave us a matched list of 2132 sources. In Table 6.3.2 we provide a sample partial page of the optical and radio data for the matches. The full table (with additional columns) is available in electronic form with us.

Table 6.2: DPOSS FIRST matches, sample partial page. The positions of the DPOSS and the corresponding FIRST sources is given. Optical colors (where available) and radio fluxes are also listed.

R.A. (DPOSS)	Dec. (DPOSS)	R.A. (FIRST)	Dec. (FIRST)	r	$g-r$	$r-i$	F_{peak} (mJy)	F_{int} (mJy)
12:04:52.78	+31:38:07.8	12:04:52.72	+31:38:08.0	21.774	0.995	...	1.40	1.72
12:04:52.88	+29:30:03.3	12:04:52.76	+29:30:04.2	19.079	1.009	-1.251	62.83	69.75
12:04:55.96	+30:09:49.4	12:04:55.92	+30:09:49.4	22.306	2.093	0.232	1.11	1.29
12:04:56.83	+31:28:59.5	12:04:56.76	+31:28:59.6	17.262	0.947	-1.222	1.41	1.64
12:04:59.44	+31:47:55.8	12:04:59.35	+31:47:56.4	20.543	1.749	-0.985	1.96	2.29
12:05:04.90	+30:41:04.7	12:05:04.81	+30:41:05.5	19.471	0.554	...	195.85	201.38
12:05:05.96	+32:12:57.4	12:05:05.73	+32:12:58.0	20.648	-0.161	...	2.71	3.16
12:05:10.83	+31:13:41.8	12:05:10.78	+31:13:43.4	20.578	2.232	-2.246	1.08	0.79
12:05:12.19	+28:48:13.2	12:05:12.13	+28:48:14.8	19.859	1.759	-1.576	2.43	1.82
12:05:18.72	+30:03:00.0	12:05:18.62	+30:03:01.3	19.036	1.548	-1.573	1.40	1.22
12:05:22.86	+30:21:08.0	12:05:22.77	+30:21:08.2	18.744	1.472	-1.665	2.89	4.72
12:05:24.26	+29:08:22.2	12:05:24.27	+29:08:22.9	20.212	-0.547	...	1.48	1.03
12:05:24.47	+29:22:21.3	12:05:24.27	+29:22:21.1	20.444	1.012	-0.662	2.44	2.35
12:05:26.22	+32:13:13.6	12:05:26.09	+32:13:14.3	20.282	0.944	-0.526	1.50	1.55
12:05:31.84	+29:01:48.0	12:05:31.79	+29:01:49.5	21.021	1.049	...	1.51	1.46

About 21% of the 10050 radio sources lying in the area covered by us thus have optical identifications. But taking the other view, only 2132 (0.65%) out of the 326546 DPOSS sources lying in the region of sky we covered have radio counterparts brighter than 1 mJy. This great discrepancy can be understood by examining the median redshift of the radio and optical sources. As mentioned above, the DPOSS sources have a median redshift of $z \sim 0.2$ while the FIRST sources have a median redshift of $z \sim 0.8$. Our matches are dominated by two kinds of sources: (i) Nearby galaxies (and a few stars) which are so close that even their weak radio emission is detectable at the FIRST flux limit and (ii) distant galaxies and quasars which have a radio luminosity that is high enough for them to be detectable at moderate to high redshifts. Most optical sources in the DPOSS catalog do not fall into either of the two categories above. Thus only a very small fraction of optically detected objects in the sky have radio counterparts brighter than 1 mJy.

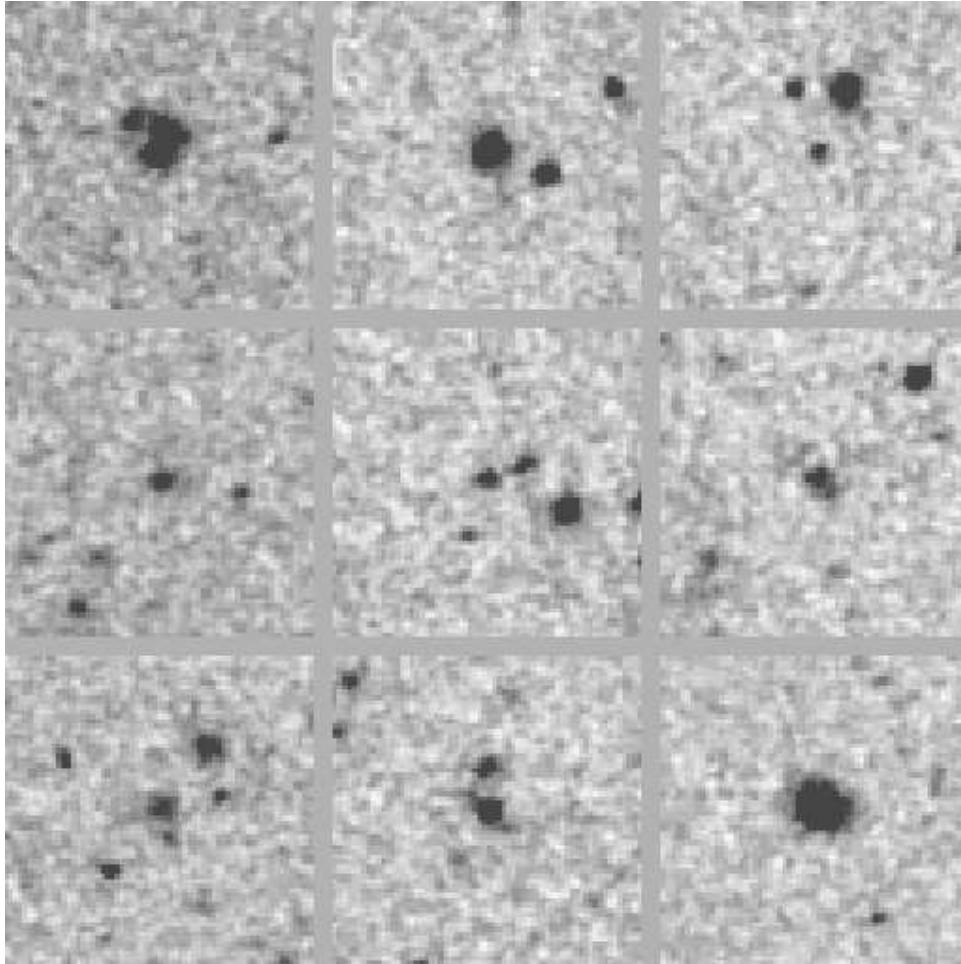


Figure 6.1: Optical counterparts of some FIRST sources from DPOSS. Each cutout is 64×64 arcsec, constructed from the F band data that gives the highest S/N for most objects. The optical counterpart is at the center of each panel. The center of the radio source is located less than 3 arcsec away from the optical source.

6.3.3 Morphology of the identifications

In Figure 6.1 we show a few typical cutouts of the identifications in the F band. For most of the identifications the S/N ratio is too poor for a reliable estimation of optical morphology of the source to be made as in Chapter 8. In a few cases, where the optical counterparts are very bright, images are photographically saturated. Because of these limitations, a systematic study of optical morphology with DPOSS is not very useful, especially considering the wide availability of deep CCD imaging data, such as the ESO Imaging Survey (Nonino et al. 1999).

6.4 Finding new quasars

One of the most important and yet straightforward applications of a high resolution radio survey is to use the accurate radio source positions to identify quasar candidates, whose nature can be confirmed with spectroscopy. The earliest quasars were identified in this way. But later, techniques were developed that allowed the identification of quasar candidates using optical observations alone, without recourse to radio data. Quasars were found to have spectral characteristics so different from most stars and galaxies that broad band optical surveys using only three effective wavelengths could differentiate most quasars from other objects with reasonable reliability. Despite the existence of many other techniques for identifying quasars, the great majority of quasars known today has been identified from optically selected candidates, and it is probable that this will remain true over the near future. Nevertheless, the older radio selection technique has some advantages over optical techniques:

1. The selection efficiency is very high, mainly because detectable radio emission from stars is rare. Only about one in 10^4 of 12th magnitude stars has radio emission detectable by the FIRST survey. This small fraction becomes even smaller at fainter apparent magnitudes (Helfand et al. 1999).
2. The radio selection technique can discover classes of quasars that are rare or unknown in other surveys because of biases against them e.g. (i) The radio loud BAL quasars, the first example of which was discovered using the FIRST survey (Becker et al. 1997). The spectra of these objects are remarkable; the emission lines are almost completely masked by absorption, and the colors of these objects are quite *red*. Such objects would be very unlikely to be recognized in any optically selected survey which focuses on *blue* stellar objects. (ii) A population of radio-quiet Type 2 quasars have been identified using radio selected candidates (Djorgovski et al. 2000). Type 2 quasars have accretion disks aligned edge on to the line of sight. In these objects, the central black hole and accretion disk are obscured by hot gas and dust, making them nearly invisible at optical wavelengths. However, radio emission from the quasar can penetrate the obscuring dust. Their discovery lends crucial support to AGN unification schemes and these sources may also prove to be the source of the diffuse X-ray background.

This makes a radio selected survey using FIRST a very attractive proposition. The FIRST Bright Quasar Survey (FBQS) is an ongoing effort in this direction.

6.4.1 FIRST Bright Quasar Survey (FBQS)

The FBQS is currently the largest radio selected quasar survey that aims to define a complete sample of quasars. The candidates are selected from positional coincidences of FIRST sources with stellar objects on the POSS-I plates. The survey is expected to pick up all quasars that are brighter than $E = 17.8$. It aims to define a sample of quasars that bridges the gap between traditional radio loud and radio quiet objects (Gregg et al. 1996; White et al. 2000). It has already identified 467 new quasars in addition to the 169 quasars already known over 2682 square degrees of the sky.

The FBQS is limited to observing relatively bright quasar candidates because it uses the digitized POSS-I plates to identify quasar candidates. In order to detect quasars at fainter apparent magnitudes, a deeper optical survey such as DPOSS needs to be used in candidate selection. In our work we identify such *faint* quasar candidates.

6.4.2 Low redshift quasar candidates

For the last three decades, the optical hunt for low and moderate redshift quasars ($z < 2.1$) has proceeded by examining photographs/CCD images in search of *blue stellar objects* or *ultraviolet excess objects* as quasar candidates for spectroscopic followup. The main contamination in such surveys is from hot white dwarfs which have colors that are similar to quasars. A number of these show up in surveys based only upon quasar colors, but the percentage of contaminating white dwarfs drops rapidly with magnitude, exceeding 95% at 16 magnitude (Schmidt & Green 1983) but being under 5% at 22 magnitude (Koo & Szalay 1984). The detection statistics improve significantly when a redder color is also incorporated, because the quasar continuum spectrum continues into the red whereas hot star spectra drop rapidly at higher wavelengths.

The quasar detection statistics can be further improved by the use of an additional criterion (such as a detection in a radio survey) for candidate selection, as radio emission from white dwarfs at the flux levels of the FIRST survey is not at all likely. The detection rate is even higher if the candidates are also located at high galactic latitude where the number density of stars falls off dramatically. In our work, we have deliberately chosen three fields located very close to the North Galactic Pole, to minimize the contamination of our identifications by galactic stars.

Surveys based only on color have a serious bias as a function of redshift. This bias arises because of strong emission lines affecting colors and distorting them from what they would be from the continuum alone. The most serious effects come from the Ly α line which comes into the optical bands at $z \sim 2$ (see Figure 6.2). At these redshifts, Ly α typically has an equivalent width of several hundred angstroms, comparable to that of the filter bandpass, so the flux from it can actually exceed that from the continuum within a particular filter. At $z \sim 2.1$ the Ly α emission line creeps into

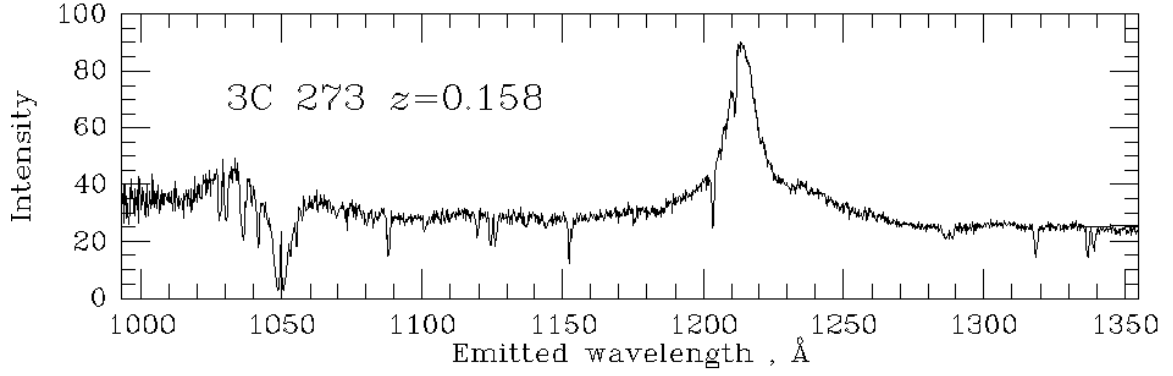


Figure 6.2: Spectrum of the quasar 3C 273 obtained using the Faint Object Camera (FOC) of the Hubble Space Telescope. The Ly- α emission line at 1216 Å in the rest frame of the quasar is clearly seen.

the B band, enhancing the B band flux and reddening the $U - B$ color. Color surveys that use a negative value of $U - B$ color as the primary selection criterion become progressively more inefficient at searching for quasars with $z \geq 2.1$ (Weedman 1980).

In this work we designate as the low z quasar candidates, all sources with a stellar identification, a FIRST detection and color criteria *not* satisfying those for the high z candidates. Optical positions, colors and integrated radio flux for the 214 low z quasar candidates that we have identified is provided in Table 6.3.

For very high redshifts ($z > 4$) a drastically different technique for quasar candidate selection is required.

Table 6.3: Low redshift quasar candidates. The identification criteria used are discussed in the text. The DPOSS position, Gunn r magnitude, colors (where available) and the integrated radio flux of the corresponding FIRST source are listed here.

R.A. (J2000)	Dec. (J2000)	r	$g - r$	$r - i$	Int. Radio flux (mJy)
12:05:24.47	+29:22:21.3	20.184	0.660	0.851	2.35
12:05:31.84	+29:01:48.0	20.759	0.776	...	1.46
12:05:40.50	+30:21:53.8	20.620	1.74
12:05:51.10	+30:22:39.8	20.678	...	1.239	2.59
12:06:19.75	+28:22:54.1	16.705	-0.053	-0.213	35.16
12:06:48.54	+31:36:58.4	20.047	0.964	0.954	7.98
12:07:28.05	+27:54:58.5	19.035	-0.893	0.266	611.24
12:07:42.24	+28:29:44.8	21.066	-0.700	...	1.39
12:07:47.92	+29:58:10.1	19.897	-0.762	0.539	11.53
12:07:54.78	+28:02:59.4	21.815	1.53
12:08:04.36	+30:15:49.4	19.667	-0.050	-0.560	31.58
12:08:10.33	+30:00:11.6	20.766	3.36
12:08:41.28	+29:14:11.6	19.303	0.701	-0.811	2.97
12:08:49.01	+28:04:52.5	19.358	0.913	-0.114	1.73
12:08:52.84	+32:24:19.2	17.330	0.792	0.897	1.20
12:08:54.59	+29:33:32.2	20.779	-0.118	1.208	3.08
12:09:14.13	+30:06:04.7	21.417	2.17
12:09:22.97	+31:47:24.0	20.390	-0.800	0.632	1.91
12:09:44.96	+32:27:22.6	19.466	-0.547	-0.764	70.03
12:09:45.28	+32:16:59.8	17.267	-0.632	0.290	1.95
12:09:47.73	+29:11:09.6	19.506	1.450	0.556	7.98
12:10:15.99	+29:36:56.7	20.213	1.624	0.898	1.54
12:10:37.65	+31:57:04.9	17.053	-0.734	0.297	22.04
12:10:51.96	+30:31:25.7	20.734	0.071	...	1.66
12:11:08.91	+31:36:31.8	21.121	-0.942	...	2.99
12:11:34.78	+29:29:41.4	19.831	1.107	0.688	0.70
12:11:57.92	+32:10:41.6	20.466	0.99
12:11:58.14	+28:41:52.1	19.113	-0.055	-0.342	1.17
12:12:10.49	+29:33:01.6	20.653	-0.256	-0.339	1.30
12:12:14.41	+31:01:21.1	18.996	-0.702	0.280	9.20
12:12:31.36	+31:45:54.5	21.109	-0.775	...	11.80
12:13:52.09	+28:12:55.4	19.177	0.175	-0.069	275.78
12:13:59.06	+30:39:09.2	20.003	1.431	0.156	1.83
12:14:42.37	+28:03:28.5	17.374	-0.087	0.373	2.90
12:14:45.62	+31:31:03.4	19.748	1.294	0.362	3.43
12:15:03.34	+27:58:32.5	20.009	1.177	0.300	0.93

Low redshift quasar candidates (continued)

R.A. (J2000)	Dec. (J2000)	r	$g - r$	$r - i$	Int. Radio flux (mJy)
12:15:25.86	+28:25:22.0	18.340	1.589	0.390	0.96
12:16:04.87	+29:04:20.2	20.330	-0.114	...	4.36
12:16:34.37	+27:10:51.9	19.334	1.036	0.768	2.34
12:16:53.41	+31:22:59.5	20.855	1.030	...	2.61
12:17:21.47	+30:56:29.9	16.533	-0.532	0.219	8.67
12:17:48.51	+27:40:08.4	19.370	-0.404	-0.106	6.23
12:17:49.76	+31:34:10.5	19.346	-0.387	-0.475	13.79
12:18:10.66	+28:58:04.2	19.757	-0.690	-0.067	8.97
12:18:31.49	+31:43:40.8	21.173	-0.566	...	282.67
12:18:41.52	+30:15:18.2	21.425	3.89
12:18:41.66	+32:17:11.9	20.177	0.666	...	3.19
12:19:04.08	+29:03:10.6	21.303	0.819	1.052	0.84
12:19:17.40	+28:59:07.1	20.357	0.190	1.449	0.81
12:19:39.31	+27:51:51.8	19.556	-0.246	-1.084	15.23
12:20:03.88	+27:17:21.6	19.775	-0.685	0.113	1.73
12:20:04.42	+31:11:47.3	18.832	-0.270	-0.710	28.41
12:20:15.55	+27:10:53.4	18.524	-0.651	-0.296	20.48
12:20:18.82	+32:43:00.6	19.706	-0.711	0.128	52.82
12:20:40.07	+30:51:45.6	19.491	1.044	0.325	1.82
12:20:56.85	+27:49:20.0	20.266	0.757	-0.006	6.38
12:21:12.49	+28:44:38.1	20.593	0.776	-0.009	4.95
12:21:13.20	+30:35:02.6	21.193	121.38
12:21:25.24	+28:44:32.8	20.652	0.202	...	2.95
12:21:30.99	+27:35:25.5	20.912	-0.877	...	1.48
12:21:54.21	+30:51:45.7	19.303	0.034	0.568	295.37
12:22:38.02	+28:50:52.7	21.002	-0.688	...	23.71
12:22:43.25	+29:34:40.7	18.631	-0.353	0.262	100.19
12:23:10.96	+28:47:29.2	19.230	-0.130	-0.425	77.57
12:23:12.92	+29:04:58.5	18.504	-0.499	0.019	1.27
12:23:13.41	+29:08:23.6	17.985	-0.427	-0.024	0.82
12:23:23.11	+32:16:08.7	19.757	-0.803	-0.799	3.26
12:23:44.67	+31:56:36.1	20.067	-0.523	0.067	3.05
12:23:54.50	+31:12:05.9	21.664	6.52
12:24:52.62	+32:16:58.0	20.740	-0.781	...	15.71
12:25:16.98	+31:45:34.3	18.491	-0.546	0.476	7.59
12:25:20.56	+29:24:19.5	18.558	-0.042	0.088	1.93
12:26:02.03	+28:53:32.7	21.021	0.649	1.238	0.90
12:26:14.93	+29:33:49.9	20.369	1.744	0.933	2.18
12:26:37.19	+30:24:53.9	19.816	0.678	0.888	20.31
12:27:12.84	+30:19:45.5	20.906	2.19
12:27:17.49	+28:08:23.7	19.202	-0.699	-0.048	9.12
12:27:43.87	+27:41:26.4	19.018	0.060	-0.118	1.35
12:27:58.24	+30:31:00.8	18.871	-0.670	-0.088	2.19
12:28:14.00	+29:30:50.9	19.259	1.540	0.222	2.84
12:28:24.97	+31:28:36.5	15.860	-0.873	0.101	323.78
12:28:29.87	+29:43:11.6	19.658	0.705	0.604	4.47
12:29:12.50	+31:14:44.8	20.129	-0.943	0.780	2.52
12:29:53.11	+30:25:57.4	19.372	-0.852	0.532	31.48
12:29:53.27	+30:23:16.4	19.799	0.229	-0.927	23.93
12:29:53.20	+31:23:30.3	20.220	-1.232	0.047	1.29
12:30:01.03	+29:03:56.5	16.778	-0.426	-0.283	1.99
12:30:10.41	+28:30:40.4	18.689	-0.144	0.189	1.89
12:30:10.67	+28:28:53.4	21.259	2.34
12:30:47.33	+27:19:00.3	19.018	-0.624	-0.073	11.11
12:30:51.81	+32:13:47.7	19.951	-0.647	...	5.13
12:30:53.57	+30:23:27.0	21.065	0.262	...	1.46
12:31:27.28	+27:05:29.5	18.000	0.559	1.108	1.47
12:50:28.83	+32:37:07.2	19.592	1.366	0.667	1.57
12:51:07.79	+29:18:58.4	18.230	-0.156	-0.141	3.27
12:51:38.13	+28:35:48.9	21.717	0.431	0.958	11.95
12:52:19.48	+31:00:38.9	21.147	-0.558	0.561	1.63
12:52:25.01	+29:13:20.4	17.341	-0.619	-0.012	0.76
12:53:06.44	+29:05:13.1	17.830	-0.324	-0.088	61.78
12:53:07.73	+28:57:21.7	19.754	-0.004	-0.146	31.36
12:53:17.63	+31:05:50.3	16.810	-0.156	-0.114	1.60
12:53:25.78	+30:36:35.2	22.046	-1.239	...	453.52
12:54:41.58	+29:51:28.3	20.413	-0.879	0.947	39.30
12:54:49.81	+31:24:28.6	21.191	-0.049	...	1.75
12:54:51.18	+31:36:29.7	20.704	-0.069	...	2.46
12:55:42.62	+31:10:48.2	18.630	0.057	-0.321	6.90
12:55:43.29	+29:45:14.7	21.814	-0.985	1.604	19.74
12:55:52.27	+31:53:00.7	17.317	1.346	1.012	4.35
12:56:02.08	+27:55:02.2	22.132	-2.232	...	1.08
12:56:03.63	+29:50:08.6	19.512	-0.439	0.046	7.00
12:56:10.07	+29:31:52.7	19.857	0.651	0.343	1.22

Low redshift quasar candidates (continued)

R.A. (J2000)	Dec. (J2000)	r	$g - r$	$r - i$	Int. Radio flux (mJy)
12:56:16.78	+31:06:14.9	21.184	-0.824	...	0.86
12:56:31.11	+27:01:07.7	20.127	-0.200	0.437	128.47
12:56:39.90	+30:40:55.3	19.979	-0.466	0.642	17.84
12:56:59.51	+30:14:38.7	19.226	-0.022	0.405	1.50
12:57:46.40	+30:59:55.3	21.258	-0.326	...	38.04
12:57:57.29	+32:29:28.3	18.084	-0.933	-0.306	594.62
12:58:03.31	+31:21:07.6	20.020	0.168	0.544	1.68
12:58:32.17	+29:09:02.0	19.058	0.414	-0.065	24.73
12:58:40.86	+28:35:03.9	20.246	-0.054	...	1.74
13:00:21.98	+27:09:33.1	19.572	-0.346	0.292	1.01
13:00:23.46	+27:03:11.7	20.395	-0.156	0.088	16.33
13:00:40.26	+28:00:11.3	20.180	1.014	0.099	8.49
13:00:46.58	+30:29:10.1	21.325	-0.799	...	4.55
13:01:00.95	+32:07:27.0	20.753	-0.159	0.586	0.74
13:01:20.16	+28:21:35.9	18.648	-0.104	0.060	100.47
13:01:56.56	+29:04:54.5	20.363	-1.116	0.281	97.31
13:02:03.10	+26:58:07.5	17.644	-0.878	-0.076	7.31
13:02:20.77	+27:09:40.0	20.362	-0.099	0.175	76.67
13:02:35.19	+32:11:33.2	19.678	1.547	0.946	1.02
13:03:00.36	+30:46:43.6	19.803	-0.618	-0.491	0.94
13:04:09.60	+29:19:42.2	19.291	-0.084	0.046	72.18
13:04:16.86	+30:53:01.6	22.001	57.87
13:04:31.78	+30:51:54.9	19.882	0.570	0.942	1.00
13:04:33.49	+32:06:35.5	18.437	-0.168	-0.272	10.15
13:04:34.67	+28:04:50.8	20.305	-0.105	1.016	2.24
13:04:43.08	+27:54:30.0	20.449	0.797	1.304	3.08
13:04:44.59	+27:53:59.6	22.012	1.20
13:05:10.20	+26:56:47.7	21.454	-1.040	...	1.69
13:05:12.38	+29:27:56.6	20.901	...	0.357	1.82
13:05:16.80	+29:07:41.5	19.253	-0.931	-0.050	1.09
13:05:31.82	+29:16:20.5	20.822	-0.152	0.305	9.23
13:05:40.51	+29:49:59.9	19.739	-0.300	1.026	8.16
13:05:49.65	+29:43:45.3	20.680	0.028	0.344	1.13
13:05:57.53	+32:05:37.0	21.715	-0.871	0.377	12.29
13:06:00.53	+29:05:22.3	20.028	-0.094	-0.465	3.69
13:06:06.20	+30:26:39.8	20.096	1.541	0.602	4.16
13:07:29.29	+27:46:58.4	18.347	-0.412	-0.865	15.07
13:07:33.25	+32:33:07.6	19.875	0.407	-0.745	6.14
13:08:41.23	+30:57:27.2	20.305	0.302	0.181	18.07
13:08:48.60	+28:19:42.0	19.818	0.383	0.786	3.25
13:08:56.26	+30:05:10.4	22.375	0.74
13:08:56.83	+27:08:10.9	18.198	-0.454	-0.579	203.00
13:08:59.92	+30:45:17.9	19.691	-0.097	0.221	2.12
13:09:06.75	+31:57:59.2	19.942	0.675	-0.145	2.75
13:09:27.14	+31:22:26.1	20.731	0.592	0.227	0.84
13:09:33.34	+28:21:19.0	22.119	-0.422	1.656	0.95
13:09:52.42	+27:42:39.8	18.375	-0.353	0.038	2.13
13:10:05.80	+29:26:17.3	21.173	-1.090	...	76.31
13:10:28.70	+32:20:42.8	18.247	0.125	-0.377	1506.33
13:10:59.82	+31:13:19.5	21.169	0.611	0.383	44.57
13:11:04.31	+27:38:32.7	21.911	-1.674	1.069	9.18
13:11:30.19	+31:16:06.0	18.921	-0.577	-0.250	3.52
13:11:38.11	+32:01:46.1	19.342	-0.599	0.054	20.82
13:12:13.30	+28:48:00.2	19.424	-0.194	-0.192	9.02
13:12:41.78	+28:41:29.9	21.417	-1.240	0.460	23.53
13:12:48.79	+31:12:59.6	18.257	-0.593	-0.139	80.51
13:13:08.33	+31:47:18.1	19.777	-0.526	0.334	2.37
13:13:15.51	+31:18:23.2	21.927	1.38
13:13:44.20	+31:18:29.0	19.928	-1.252	0.085	1.82
13:13:58.97	+27:19:06.4	21.172	0.515	0.502	1.22
13:14:23.18	+29:10:00.8	18.467	-0.210	-0.040	7.22
13:14:35.19	+30:18:02.2	18.479	-0.293	0.256	7.30
13:15:13.49	+28:40:52.8	20.549	-1.188	0.102	70.89
13:15:29.60	+27:20:53.2	22.135	-0.689	...	55.91
13:15:48.51	+29:28:25.8	19.309	-0.230	-0.152	1.10
13:16:18.68	+27:13:38.5	19.534	-0.598	-0.195	2.04
13:16:37.47	+29:03:00.7	19.830	0.849	0.579	1.90
13:16:49.27	+30:24:10.7	19.765	0.141	0.116	4.24
13:16:54.63	+30:14:53.1	19.833	0.161	0.803	3.50
13:35:59.04	+31:19:17.8	18.668	1.079	...	2.32
13:36:15.15	+31:10:40.2	18.847	1.518	...	0.86
13:38:09.78	+28:44:34.9	19.986	0.264	...	17.50
13:38:58.21	+30:00:59.1	21.269	...	1.875	2.52
13:39:06.26	+30:58:53.6	19.618	-0.240	-0.959	9.30
13:40:35.51	+28:27:26.1	20.012	0.087	...	2.41

Low redshift quasar candidates (continued)

R.A. (J2000)	Dec. (J2000)	r	$g - r$	$r - i$	Int. Radio flux (mJy)
13:40:50.76	+30:42:07.9	19.920	...	-0.376	2.01
13:41:03.80	+32:14:28.2	19.590	0.434	-0.130	42.13
13:41:23.40	+27:49:55.1	19.004	-0.079	0.183	1.21
13:41:37.90	+27:01:54.7	-95.774	-4.530	...	3.34
13:42:08.46	+27:09:31.4	17.529	0.423	-0.758	245.89
13:42:54.45	+28:28:05.2	18.057	-0.221	-0.563	68.41
13:43:00.21	+28:44:06.6	17.225	-0.077	-0.069	246.65
13:43:29.96	+32:07:59.3	20.766	-0.096	...	23.33
13:43:58.32	+31:29:14.9	19.771	...	0.529	5.82
13:44:00.20	+31:28:07.0	20.825	...	0.979	3.06
13:44:12.08	+30:45:56.2	19.926	0.646	-1.246	1.51
13:44:14.56	+28:52:34.6	20.374	-0.972	...	193.48
13:45:04.03	+27:28:59.8	20.208	0.152	...	2.32
13:45:20.42	+32:41:11.6	18.772	-0.300	0.410	14.62
13:45:49.70	+26:43:17.2	20.339	2.17
13:46:43.06	+32:21:46.8	19.574	0.034	-1.006	3.58
13:46:47.96	+26:51:18.9	19.975	1.438	...	29.59
13:47:26.53	+32:34:14.8	19.810	1.550	0.630	4.07
13:48:04.37	+28:40:24.3	18.390	-0.832	-0.144	78.07
13:48:06.09	+30:09:59.9	18.680	-0.059	0.290	10.64
13:48:09.04	+28:02:12.6	18.135	-0.638	-0.026	2.02
13:48:17.01	+31:03:14.4	19.954	0.544	-0.706	6.56
13:48:20.92	+30:20:05.0	17.406	-0.224	0.131	23.53
13:48:32.31	+29:57:28.9	19.932	0.029	0.021	0.97
13:49:31.51	+30:08:02.3	20.582	2.52
13:49:44.91	+32:15:27.8	19.197	0.718	-0.823	1.60
13:49:47.00	+30:41:47.7	19.860	0.161	-0.642	5.38
13:50:52.80	+30:34:53.2	18.890	-0.358	-0.531	325.61
13:51:01.22	+30:42:26.4	18.890	-0.122	-1.194	3.54
13:51:31.27	+30:25:02.3	20.986	0.099	...	57.26
13:51:34.95	+32:39:03.9	20.462	1.235	...	2.10
13:52:05.83	+29:09:51.9	19.580	0.435	...	1.06
13:52:32.67	+32:39:12.8	20.181	0.163	0.392	2.92
13:52:39.39	+28:30:13.8	20.645	...	1.208	1.19
13:53:05.53	+29:37:08.1	20.171	-0.472	0.195	3.35
13:53:08.38	+28:09:08.2	19.396	-0.408	0.109	16.20
13:53:31.92	+28:53:12.1	20.271	-0.746	-0.115	3.83
13:53:59.56	+27:52:50.9	19.131	1.762	0.682	20.56
13:55:04.61	+31:32:13.2	19.436	0.350	-0.382	8.43
13:55:29.97	+29:30:58.6	18.004	-0.217	0.590	1.54
13:55:41.20	+30:24:11.7	18.532	0.257	-0.682	125.24
13:56:27.88	+28:01:58.4	17.438	0.541	0.137	0.94
13:57:02.89	+31:54:56.7	18.860	-0.348	0.282	18.38
13:57:13.99	+31:03:40.9	19.192	-0.117	-0.166	22.62
13:57:23.50	+29:32:04.6	20.154	0.954	-0.115	3.55
13:58:07.30	+31:50:35.8	19.521	0.328	-1.084	1.55
13:59:44.51	+28:14:11.4	19.939	-0.034	-0.392	1.81
13:59:47.89	+27:08:29.5	18.881	0.256	-0.612	134.24
14:00:30.52	+26:46:34.5	20.718	-0.899	...	60.02
14:01:01.10	+29:00:10.9	18.399	0.923	0.341	0.87
14:01:06.89	+31:10:15.3	21.116	-0.855	-0.192	3.45
14:01:22.02	+27:39:09.3	20.164	-0.767	0.057	18.12
14:01:27.22	+31:38:10.7	18.159	0.871	-0.263	2.20
14:02:59.10	+28:23:15.8	21.115	-0.894	...	3.94
14:03:07.55	+32:03:18.4	19.760	-0.817	-0.472	2.30
14:04:10.81	+29:30:37.0	19.154	-0.333	-0.560	6.21
14:04:14.63	+28:46:35.3	16.623	0.081	...	12.43
14:04:47.45	+32:06:17.3	20.029	8.47

6.4.3 High redshift quasar candidates

Quasars at $z > 4$ are valuable probes of the early universe, galaxy formation, and the physics and evolution of the intergalactic medium at large redshifts. A systematic statistical study of a large sample of these quasars would help constrain theoretical models. The continuum drop blueward of the Ly α emission line (see Figure 6.2) gives these objects a distinctive color signature: extremely *red* in $(g - r)$, yet *blue* in $(r - i)$, thus standing away from the stellar sequence on a color-color plot. Traditionally, the major contaminants in this type of work are red galaxies. However, accurate star-galaxy classification techniques used in the construction of the DPOSS catalog lead to a manageable number of color-selected candidates, and an efficient spectroscopic follow-up.

Table 6.4: High redshift quasar candidates. The identification criteria used are discussed in the text.

R.A. (J2000)	Dec. (J2000)	r	$g - r$	$r - i$	Int. Radio flux (mJy)
12:10:42.21	+29:51:36.4	20.088	2.212	-0.318	1.50
12:11:34.43	+32:26:14.1	19.244	0.995	-0.463	3.49
13:10:59.45	+32:33:33.3	18.737	0.888	-0.512	245.97
13:15:30.71	+28:11:19.1	19.372	0.803	-0.840	20.80
13:37:24.83	+31:52:53.2	18.570	0.801	-1.005	83.30
13:39:42.13	+29:41:26.8	19.722	1.917	0.203	4.51
13:40:15.03	+28:56:36.9	19.247	1.191	-0.805	1.84
13:40:48.79	+28:29:39.2	19.715	2.099	0.660	3.78
13:41:15.34	+28:16:04.5	18.700	2.599	0.194	88.36
13:42:47.65	+27:59:25.9	19.652	2.716	-0.921	2.15
13:45:01.00	+28:29:55.8	20.446	1.487	-0.265	1.71
13:46:43.78	+31:27:34.7	20.338	1.488	-0.324	1.31
13:49:35.79	+29:52:40.5	19.204	3.065	0.184	1.88
13:51:54.28	+29:53:24.8	18.040	1.192	-0.375	2.68
13:55:59.96	+29:07:35.1	20.713	2.281	0.218	1.69
14:03:49.92	+31:35:44.7	19.215	1.226	-1.510	0.72

We follow the color criteria derived by Stern et al. (2000, as communicated to us by A. Mahabal) to obtain the list of *high z* quasar candidates. They plotted calibrated $r - i$ magnitudes versus $g - r$ magnitudes, obtained the standard deviation σ from the locus of stellar color distribution, and chose objects with a deviation greater than 5σ . They found that at least one of the following color criteria needs to be satisfied for a “stellar” source to be considered as a high z quasar candidate.

- $(r - i) > 0.4$ and $(g - r) > 1.8$
- $(r - i) < -0.6$ and $(g - r) > 0.8$
- $-0.6 \leq (g - r) \leq 0.4$ and $(g - r) > (r - i) + 1.4$

We designate the 16 “stellar” sources with a FIRST identification and satisfying these color criteria as the high z quasar candidates in our sample. Table 6.4 lists coordinates, calibrated magnitudes and colors and integrated radio flux for these candidates.

In Figure 6.3 we plot $r - i$ versus $g - r$ colors for all the quasar candidates. The low z quasar candidates are shown as circles. The filled circles are for sources with a FIRST counterpart brighter than 10 mJy while the open circles are for sources fainter than this limit. The high z quasar candidates with a radio counterpart brighter than 10 mJy are shown as filled stars while unfilled stars show the high z candidates with a radio counterpart fainter than 10 mJy.

6.5 Future work - a proposed FIRST faint quasar survey

This work is intended to be a *pilot project* to test the techniques and computer codes for a correlation of the entire DPOSS source catalog with the entire FIRST source catalog. One of the major aims of this work is to generate large numbers of quasar candidates for spectroscopic follow-up. The quasar candidate sample that we have presented here will form a *complete* sample complementary to the FBQS, exploring a region of parameter space only sparsely sampled by that survey. In Figure 6.4, we show the distribution of the radio and optical fluxes of our quasar candidates as well as the FBQS quasars. It is apparent from the figure that our complete sample will nicely complement the FBQS, with very little overlap. Particularly, the high redshift quasar candidates (shown as stars), lie in a region of parameter space that has never previously been explored by any large quasar survey. Our work should discover quasars that have a radio flux that is on average 3 times lower than that of the FBQS quasars and an apparent magnitude that is on average about 3 magnitudes fainter. We will therefore detect quasars with a higher radio to optical flux ratio than those in the FBQS. In Figure 6.5 we compare the radio to optical flux ratio R^* (as defined by Stocke et al. 1992), for the FBQS quasars and our quasar candidates. Our proposed quasar survey will increase the number of known quasars in the interesting radio loud/radio quiet transition region ($\log R^* = 1-3$) by a significant factor.

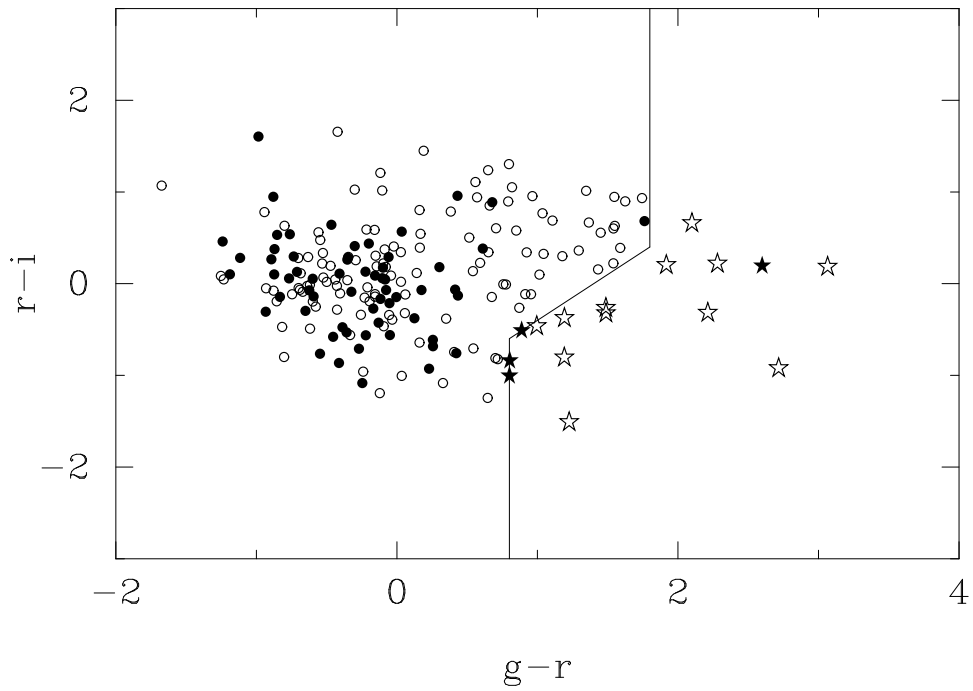


Figure 6.3: Color-color plot for the quasar candidates. The solid line divides the high z and low z quasar candidates. For an explanation of the various symbols used, see the text.

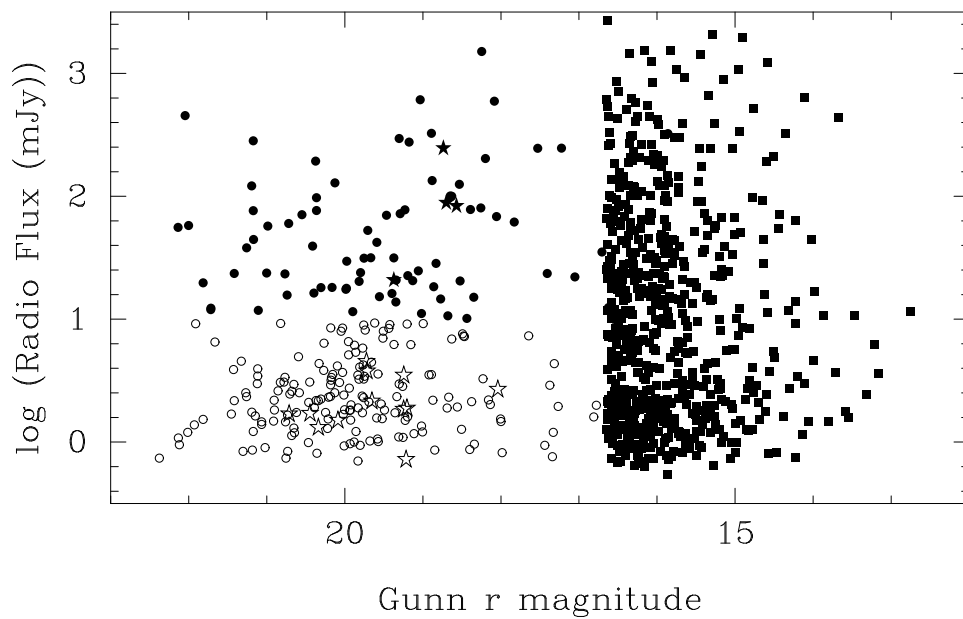


Figure 6.4: Integrated radio flux versus apparent magnitude. The filled squares indicate data points from the FBQS (White et al. 2000). The other symbols are as in Figure 6.3.

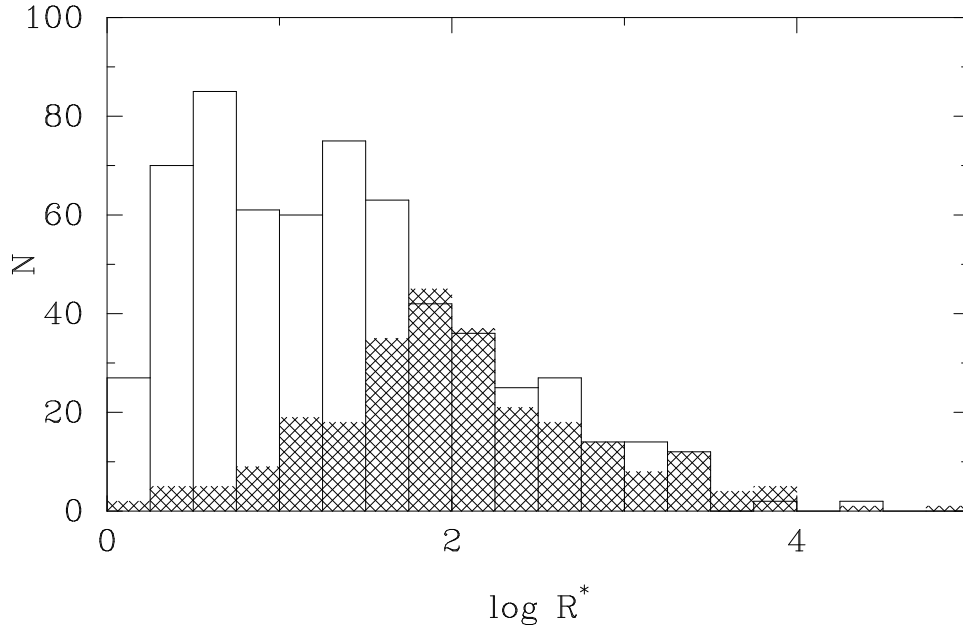


Figure 6.5: Histogram of the radio to optical flux ratio R^* for the FBQS quasars and our quasar candidates (cross hatched).

The results of our survey used in conjunction with the $z > 4$ survey of Stern et al. (2000) and the FBQS, will allow us to determine the luminosity function of quasars over very large ranges of redshift and radio and optical luminosity, aiding the study of the formation and evolution of quasars. Since many of these objects are very faint, such followup will require the use of large telescopes. A meaningful statistical analysis of the optical and radio properties of the sources identified in this work will only be possible after redshift information is available for these sources.

Although star galaxy classification in the DPOSS catalog is very accurate, distant galaxies with an angular extent comparable to the full width at half maximum (FWHM) of the point spread function (PSF) of the image will not be correctly identified. The effect will be particularly severe in cases where a strong optical nucleus is present. We examine the extent of this effect, as a function of the optical properties of the host galaxy in the next chapter.

Chapter 7

On the detectability of AGN at high redshifts

This chapter is largely based on Kembhavi, Wadadekar & Misra (2000) and Kembhavi, Misra & Wadadekar (2000).

Various classes of AGN have been identified as the optical counterparts of FIRST sources in the last few chapters. The next question is to determine to what redshift these optical counterparts can be identified and classified reliably. In this chapter, we consider the appearance of host galaxies of such AGN at optical wavelengths as a function of redshift, taking into account the effects of cosmological expansion and the presence of a luminous nucleus. We obtain the maximum redshift to which a host galaxy remains identifiable as an extended object above the sky background, as a function of galaxy type, other galaxy parameters, the active nucleus to host galaxy luminosity ratio, and observing conditions. We show that the most important parameters are the AGN and host galaxy luminosities, and the colors of the host galaxy. We compare our model predictions with some results from the imaging of high redshift radio-loud and radio-quiet quasars.

7.1 Introduction

In an Euclidean non-expanding Universe, the surface brightness of a galaxy, defined as the flux received from the galaxy per unit solid angle, is independent of the distance of the galaxy from the observer. However, the angular size of a given isophote is inversely proportional to the distance between the galaxy and the observer, and at some distance the galaxy of a given size and luminosity becomes indistinguishable from the point spread function (PSF). In contrast to this simple behavior, in an expanding Universe the surface brightness of a galaxy is a function of its redshift, because the expansion introduces an overall factor of $(1+z)^{-4}$ in the surface brightness, and the observed and emitted wavebands are different. A galaxy located at a large enough redshift can therefore be undetectable above the noise in the sky background. When an active galactic nucleus (AGN) is present, it can out shine the galaxy to some angular distance from the center, which depends on the luminosity ratio of the the AGN and the host galaxy. As a result, if the AGN is highly luminous and the object is at relatively large redshift, it is possible that the galaxy becomes non-detectable against the PSF of the AGN, even though it could have been observable as an extended object at its redshift if the AGN were absent.

The continuum and emission line properties of quasars are very similar to those of AGN, and it seems reasonable to expect that quasars too are nuclei of galaxies. But whereas the hosts of the other types of AGN are clearly visible even in short exposures, quasars show no evidence of extended optical structure in the discovery surveys. Since a majority of quasars are found at redshifts much higher than the active galaxies, their putative hosts are expected to be significantly dimmed because of the effects mentioned above. Moreover, the high luminosity of the quasar tends to swamp the host galaxy, which has a small angular size because of the high redshift. Nevertheless, if a host galaxy is present, it should be possible to detect it through deep exposures with large telescopes, particularly under excellent seeing conditions. Deep imaging at optical wavelengths of quasars at low redshift, $z \lesssim 0.6$, has indeed revealed the presence of host galaxies (see Kristian 1973, Wyckoff, Wehinger and Gehren 1981, Hutchings et al. 1982, Hutchings and Campbell 1983; see other references in Bahcall et al. 1997 to the early work). These pioneering photographic observations of low redshift quasars have by now been supplemented by CCD observations (e.g. Hutchings 1995, Hutchings & Neff 1987), in the near infra-red band (Dunlop et al. 1993) and with the Hubble Space Telescope (e.g. Hutchings & Morris 1995, Bahcall et al. 1997). These observations, especially images from

the HST, show that at low redshifts quasar hosts can be elliptical or spiral L^* galaxies, often found in interaction with other galaxies, or in environments of enhanced galaxy density.

Even when a fuzzy structure is found around a quasar, the morphology of the object remains unclear at high redshift. Though the estimated luminosity and size of the object are consistent with the fuzz being a bright galaxy (e.g. Lehnert et al. 1992, Aretxaga et al. 1995, Hutchings 1995, Lowenthal et al. 1995). From the available data it appears that the hosts of radio quiet quasars have a luminosity comparable to, or somewhat less than, local L^* galaxies (i.e. galaxies with $M_B \simeq -21$). The hosts of radio quasars are found to have much higher luminosities, being several magnitudes brighter than the most luminous galaxies in our neighborhood, but quite uncertain k-corrections are involved in these estimates. We argue that even in the cases of marginal detection of the host, it is possible to get clues about the underlying galaxy just by the virtue of it being detected.

The optical appearance of distant galaxies has been investigated in some detail by Pritchet and Kline (1981). However, they did not take into account the presence of an AGN, and exponential wings in the PSF. In this chapter, we will examine in detail the appearance of different galaxy-AGN combinations as a function of redshift. We will take into account the luminosity and morphological properties of the galaxy, the luminosity and continuum spectrum of the AGN, and the shape of the PSF. We will define criteria for the detection of an extended object over the sky background and the PSF, keeping in mind the practice followed by observers, so that our results can be used in the interpretation of actual observations.

In Section 7.2 we will discuss how the surface brightness of a galaxy depends upon the morphology, k-correction and the PSF. In Section 7.3 we will discuss how the limiting redshift for detecting a galaxy+AGN as an extended object can be computed. In Section 7.4 we will discuss the dependence of this limiting redshift on galaxy and quasar properties and in Section 7.5 we will discuss some implications of our findings.

7.2 Surface Brightness

7.2.1 The Host Galaxy

We will assume in our simple model that a host galaxy has bulge and disk components, with the radial intensity distribution of the bulge being given by de Vaucouleurs' $r^{1/4}$ law, and that of the disk by an exponential. Early type galaxies are dominated by the bulge component, while the disk becomes increasingly important towards the later types. The radial intensity distribution is completely specified by giving the central intensity of the bulge $I_b(0)$, the effective radius r_e within which half the total bulge luminosity is contained, the disk central intensity $I_d(0)$ and the disk scale length r_s . In general the three dimensional shape of the bulge is that of a triaxial ellipsoid, while the disk is taken to be thin and circular. In projection onto the sky each component produces elliptical isophotes, with the observed ellipticity of the disk depending only on the inclination of the normal to the disk with the line of sight. The radial intensity distribution is given by

$$I(r) = I_b(0)10^{-3.33(r/r_e)^{1/4}} + I_d(0)e^{-(r/r_s)}, \quad (7.2.1)$$

where the radial distance r is taken to be along the major axis of the image. In what follows, we shall consider only spherical bulges, which is a good approximation for our purposes, and disks which are viewed face-on. The isophotes of the image are therefore circularly symmetric, and convolution with a circularly symmetric Gaussian PSF reduces to an integration in one dimension, as described in subsection 7.2.4. This simplifying assumption does not qualitatively affect our results.

Integration of the bulge and disk intensity distributions separately over all values of r leads to the disk to bulge luminosity ratio

$$\frac{D}{B} = 5.93 \times 10^2 \left(\frac{I_d(0)}{I_b(0)} \right) \left(\frac{r_s}{r_e} \right)^2. \quad (7.2.2)$$

In terms of this ratio, the total absolute magnitude of the galaxy in some band is given by

$$M_G = \mu_b(0) - 5 \log r_e - 2.5 \log \left(1 + \frac{D}{B} \right) - 1.98, \quad (7.2.3)$$

where $\mu_b(0)$ is the bulge central surface brightness in magnitude, in the same wave length region as the luminosity, and r_e is in kiloparsec. When the redshift of the galaxy is so large that the observed and emitted wavelength regions are significantly different, a correction term has to be introduced, so that absolute magnitudes are obtained in a fixed waveband, regardless of the redshift; this will be done in subsection 7.2.3. Given the galaxy absolute magnitude M_G , the D/B ratio and the two scale lengths r_e and r_s , the intensity distribution is completely specified.

7.2.2 The Active Galactic Nucleus

Because of their very small angular size, AGN are not resolved in optical and near-IR observations, and can be considered to be point sources. However, the PSF spreads out the light, so that the AGN contributes to more than one pixel. We will assume for simplicity that in the wavelength region of interest to us, the continuum spectrum has a power-law form $L(\nu) \propto \nu^{-\alpha}$, where α is a constant. Emission lines which may contribute to the observed filter bandpass can be taken into account by applying a correction to the continuum magnitude (e.g. Kembhavi & Narlikar 1999). The apparent magnitude m of an AGN at redshift z is related to its absolute magnitude M through

$$m = M + 5 \log \left\{ \frac{1}{q_0^2} \left[q_0 z + (q_0 - 1)(\sqrt{1 + 2q_0 z} - 1) \right] \right\} - 2.5(1 - \alpha) \log(1 + z) + 42.39 - 5 \log h_{100}, \quad (7.2.4)$$

where q_0 is the cosmological deceleration parameter and Hubble's constant is $H_0 = 100h_{100} \text{ km sec}^{-1} \text{ Mpc}^{-1}$. In Equation 7.2.4, the apparent and absolute magnitude are both in the wavelength range corresponding to the filter bandpass in which the AGN is observed.

7.2.3 The k-Correction

When an object is at a redshift z , the flux from it observed in a wavelength range $(\lambda_{o1}, \lambda_{o2})$ is emitted in the rest frame of the object in the band $(\lambda_{o1}/(1+z), \lambda_{o2}/(1+z))$. Consequently, two identical objects located at different redshifts would have different regions of their spectrum probed by observation in the same band, leading to apparent differences in their spectral properties. To account for this discrepancy, it is necessary to introduce a *k-correction* term, which ensures that the observed and emitted spectral bands are the same regardless of the redshift. This k-correction term is defined as (Rocca-Volmerange & Guiderdoni 1988)

$$k(z) = -2.5 \log \left(\frac{\int_0^\infty L \left(\frac{\lambda_o}{(1+z)} \right) R(\lambda_o) d\lambda_o}{(1+z) \int_0^\infty L(\lambda_o) R(\lambda_o) d\lambda_o} \right), \quad (7.2.5)$$

where $L(\lambda_o)$ is the luminosity of the object as a function of its wavelength, and $R(\lambda_o)$ is the response function of the filter being used. The k-correction depends on the filter bandpass, the spectrum of the source and the redshift. For a quasar with a power-law spectrum $L(\nu) \propto \nu^{-\alpha}$, with $\alpha = \text{constant}$, the k-correction reduces to $k(z) = -2.5(1 - \alpha) \log(1 + z)$, and is already incorporated in Equation 7.2.4.

k-corrections have been computed by Rocca-Volmerange & Guiderdoni (1988), using synthetic spectra of galaxies over a wide spectral range. The corrections here are available in the standard U,B,V,R,I bandpasses, as function of the galaxy types E/SO, Sa, Sb, Sc, Sd and Im over the redshift range 0.0 to 2.0. We shall also use the k-corrections computed by Poggianti (1997), using synthetic spectra, in the U,B,V,R,I as well as in the near infra-red J,H,K filters, but only for galaxy types E, Sa and Sc. As an illustration, we have shown in Figure 7.1 the k-corrections in the Johnson B filter computed by Rocca-Volmerange & Guiderdoni (1988) and Poggianti (1997). The former data is extrapolated smoothly to $z = 3.0$ to enable us to make comparison with observations of host galaxies at high redshifts. Also shown in the figure are the cosmological $(1+z)^{-4}$ term which leads to dimming of the surface brightness with redshift, and the k-correction for a power-law spectrum $L(\nu) \propto \nu^{-0.5}$, which is the continuum spectrum often adopted for quasars. In the case of elliptical galaxies, the k-correction term dominates the dimming term, but is less important in the later types. We have shown in Figure 7.2 the corrections due to Poggianti in the K band. The

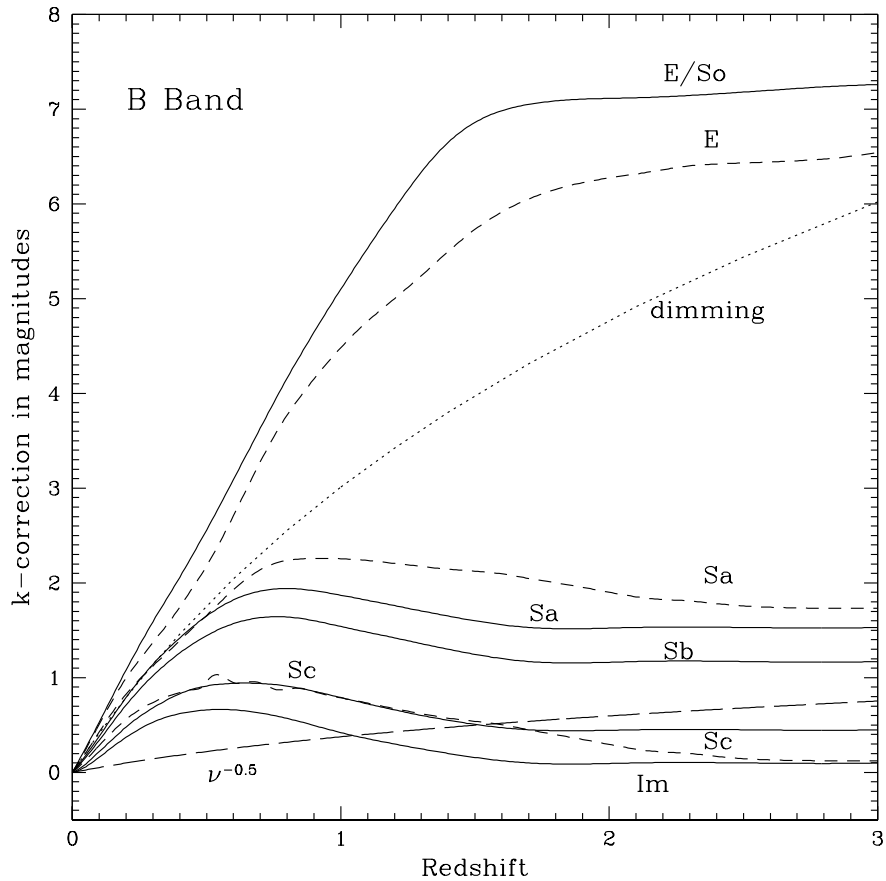


Figure 7.1: k-corrections obtained by Rocca-Volmerange & Guiderdoni (1989, continuous lines), and Poggianti (1997, dashed lines). The galaxy type is shown against each line. The dotted line is the dimming in magnitudes corresponding to the $(1+z)^{-4}$ term. The line with the long dashes indicates the k-correction for a power-law spectrum $L(\nu) \propto \nu^{-0.5}$.

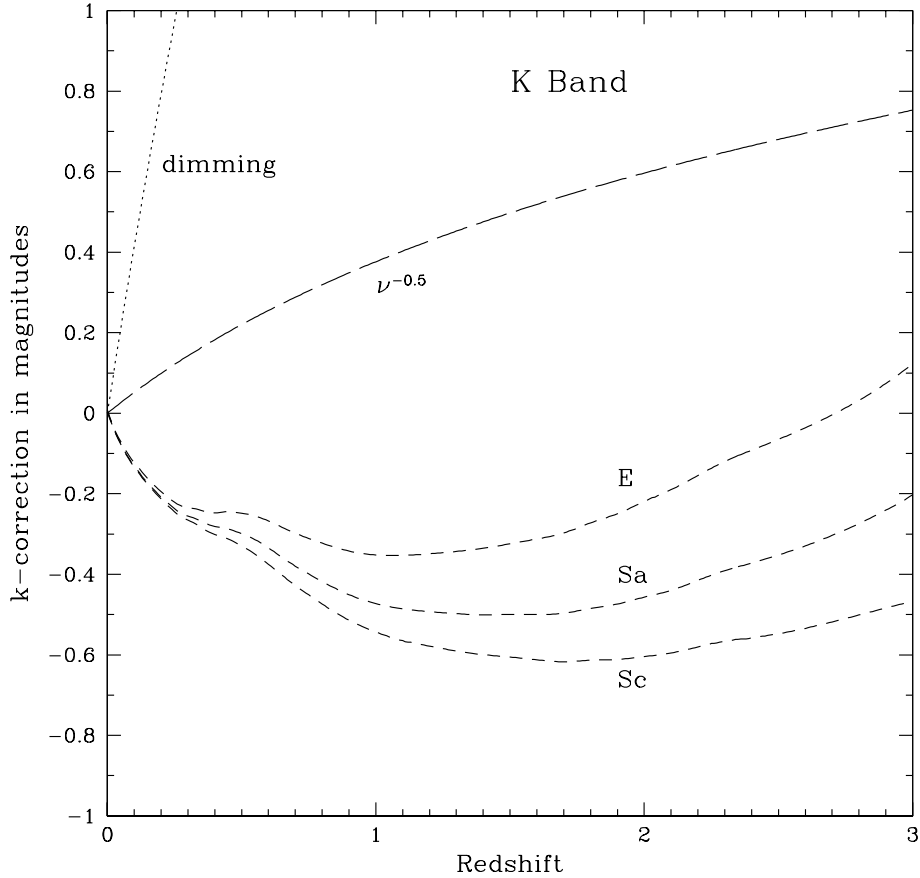


Figure 7.2: k-corrections obtained by Poggianti (1997, dashed lines) in the K-band. The galaxy type is shown against each line. The dotted line is the dimming in magnitudes corresponding to the $(1+z)^{-4}$ term. The line with the long dashes indicates the k-correction for a power-law spectrum $L(\nu) \propto \nu^{-0.5}$

corrections are small and *negative* through most of the redshift range. The surface brightness of a galaxy at redshift z , in magnitudes per square arcsecond $\mu(r)$, can now be written as

$$\mu(r) = M_G + 2.5 \log \left[\frac{r_e^2 (1+z)^4}{\left(1 + \frac{D}{B}\right) g(r)} \right] + k(z) + 31.63, \quad (7.2.6)$$

where the function $g(r)$ is given by

$$g(r) = 10^{-3.33(r/r_e)^{1/4}} + 1.69 \times 10^{-3} \left(\frac{D}{B}\right) \left(\frac{r_e}{r_s}\right)^2 e^{-(r/r_s)}, \quad (7.2.7)$$

and the parameters are as specified in subsection 7.2.1. In the above equations the scale lengths are in kpc and the surface brightness and absolute magnitude are taken to be in the same filter band.

7.2.4 The Point Spread Function

The point spread function (PSF) is often taken to be a circularly symmetric Gaussian function in two dimensions but, for more accurate work, departures from this simple form have to be taken into account. A real PSF can be elliptical in shape, and more importantly in the present context, can have non-Gaussian wings at some angular separation from the center. This region of the PSF carries only a small fraction of the total flux from a point source, but is important in determining to what redshift an extended object like a galaxy can be detected. When the PSF falls off very rapidly as in the case of a Gaussian, faint extensions of small angular size can be readily observed, while a flatter PSF can conceal such extended structure.

Following Schweizer (1979a, 1979b), we will consider a circularly symmetric PSF with a Gaussian core and exponential wings:

$$\begin{aligned} P(r) &= S_1 e^{-r^2/2\sigma^2}, & 0 \leq r \leq 2\sigma, \\ &= S_2 e^{-\beta r}, & 2\sigma \leq r \leq 12\sigma, \\ &= 0, & 12\sigma < r, \end{aligned} \quad (7.2.8)$$

where σ and β are constants. The full width at half maximum (FWHM) of the Gaussian core, or *seeing*, is 2.355σ . The constants S_1 and S_2 are determined by requiring continuity at $r = 2\sigma$ and normalizing the area under the PSF to unity:

$$S_1 = \frac{1}{2\pi} \left[0.865\sigma^2 + 0.135\beta^{-2}(1 + 2\beta\sigma) \right]^{-1}, \quad (7.2.9)$$

$$S_2 = S_1 \exp[2(\beta\sigma - 1)]. \quad (7.2.10)$$

When the intensity distribution of a galaxy as given by Equation 7.2.1 is convolved with a circularly symmetric PSF, the resulting surface brightness distribution is given by

$$I_c(r) = \int_0^\infty dr' r' I(r') \int_0^{2\pi} d\phi P\left(\sqrt{r^2 + r'^2 - 2rr' \cos \phi}\right). \quad (7.2.11)$$

For a PSF of the form above, the convolved intensity can be obtained by numerical integration. When the PSF has a pure Gaussian form, there is a further simplification possible, with the result

$$I_c(r) = \frac{e^{-r^2/2\sigma^2}}{\sigma^2} \int_0^\infty dr' r' e^{-r'^2/2\sigma^2} I(r') I_0\left(\frac{rr'}{\sigma^2}\right), \quad (7.2.12)$$

where I_0 is the modified Bessel function of order 0. In the case of a point source like an AGN, the intensity profile is simply given by the PSF times the total flux from the object, with the flux obtained from the apparent magnitude in Equation 7.2.4.

7.3 Limiting Redshift for Detection of Host Galaxy

7.3.1 Galaxy Without an AGN

We shall first consider the case of a galaxy which does not host an AGN. When a galaxy is at a redshift z , the angular size θ of some feature in the galaxy with linear size l is

$$\theta = \frac{6.87 \times 10^{-2} h_{100} (1+z)^2}{\left\{ \frac{1}{q_0^2} [q_0 z + (q_0 - 1)(\sqrt{1 + 2q_0 z} - 1)] \right\}} \left(\frac{l}{1 \text{ kpc}} \right) \text{ arcsec}. \quad (7.3.1)$$

For a galaxy to be detected, it should have flux sufficiently greater than the noise in the sky background, under given observing conditions. Further, to be recognized as an extended object, it should have an angular size sufficiently larger than the PSF. If the latter condition is not satisfied, the galaxy will appear to be an unresolved object.

The brightness of the sky background depends on the conditions at the observing site and the filter being used in the observations. Given a background level, the magnitude of the faintest feature which can be detected depends on the light collecting area of the mirror, the exposure time and the imaging detector being used. In deep observations, it is not unusual to detect features which are as faint as one percent of the sky background. Such detection does not require that each pixel of the image have a sufficient signal-to-noise to be observable to the limiting brightness. The counts from pixels are averaged over isophotes, which improves the signal-to-noise by a factor $\sim \sqrt{N}$, where N is the number of pixels in a given isophote. The radial distribution of the isophotal intensity is compared with a model functional form, like the one in Equation 7.2.1, to determine the parameters. For very faint objects, it may only be possible to say whether the object is extended by comparing the isophote averaged profile with the shape of the PSF. We shall use this technique in subsection 7.3.2.

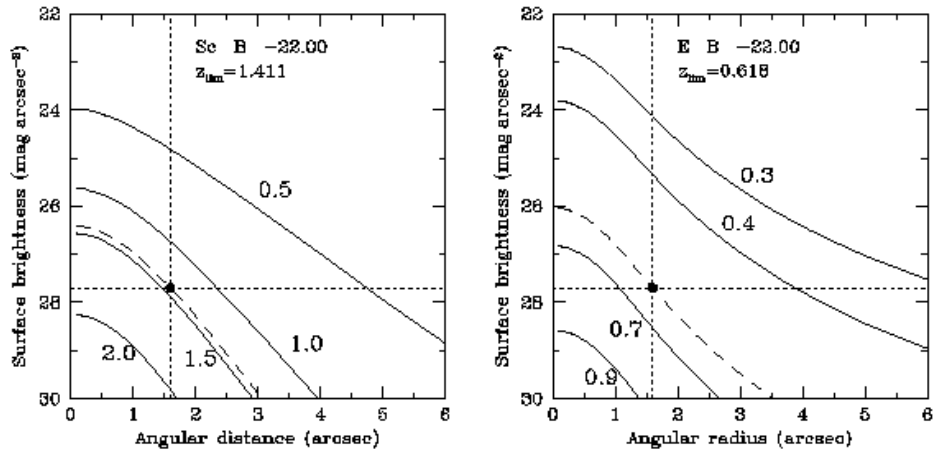


Figure 7.3: *Left panel:* The surface brightness in the B filter of an Sc galaxy, as a function of angular distance from the center. The brightness profiles for a range of redshifts are shown as solid lines. The number against each line indicates the redshift. The absolute magnitude of the galaxy is $M_B = -22$. The morphological parameters are $r_e = 3$ kpc, $r_s = 6$ kpc, and $D/B = 5$. The FWHM of the PSF and the limiting magnitude reached are shown as vertical and horizontal dotted lines. The dashed line indicates the surface brightness of the galaxy when it is at the limiting redshift for detection as an extended object; it passes through the intersection of the lines indicating the FWHM and the limiting magnitude. When the surface brightness lies below the dashed line, the galaxy appears to be a faint point source, or is lost in the background noise. *Right panel:* The limiting surface brightness of an elliptical galaxy with absolute magnitude $M_B = -22$, $r_e = 7$ kpc and $D/B = 0$.

Let μ_{lim} be the limiting brightness, in magnitudes per square arcsecond, which can be detected in some observation. A feature at angular distance θ in an object at a redshift z is then detectable if $\mu(\theta) < \mu_{\text{lim}}$. From the above discussion, given a galaxy at a redshift z , we shall adopt

$$\mu(\theta = \text{FWHM}, z) = \mu_{\text{lim}} \quad (7.3.2)$$

as the condition for a galaxy to be recognizable as extended. Since the surface brightness of a galaxy described by Equation 7.2.1 decreases outwards, if this condition is satisfied, then the surface brightness of the galaxy will be fainter than μ_{lim} for all $\theta > \text{FWHM}$. If the condition is satisfied for some z , then the galaxy will appear to be a point source for all redshifts $z' > z$ since, from Equation 7.2.6, the surface brightness decreases with increasing redshift for all reasonable galaxy spectral distributions. For a galaxy with given parameters, we define a *limiting redshift* z_{lim} at which the condition in Equation 7.3.2 is satisfied,

$$\mu(\theta = \text{FWHM}, z_{\text{lim}}) = \mu_{\text{lim}}. \quad (7.3.3)$$

For $z < z_{\text{lim}}$ the galaxy will be recognizable as being extended, while for $z > z_{\text{lim}}$, it will appear to be a point source. z_{lim} is a function of galaxy properties, μ_{lim} and the seeing conditions. Given the parameters of the galaxy, the FWHM and the limiting magnitude, it is possible to solve Equation 7.3.3 numerically to obtain z_{lim} . The limiting redshift will change somewhat if some multiple of the FWHM is used in Equation 7.3.3, but under the usual seeing conditions and CCD pixel scale, testing at FWHM provides just enough pixels to marginally detect extended structure.

We have shown in the two panels of Figure 7.3 the surface brightness distribution of a disk galaxy of type Sc and an elliptical galaxy respectively, observed in the B filter. The parameters for these galaxies are chosen from known ranges and the model intensity distribution is convolved with a PSF with a Gaussian core and exponential wings. The FWHM of the PSF is taken to be 1.6 arcsec, with the scale length of the exponential wings in Equation 7.2.9 being $\beta^{-1} = 2.5$ arcsec; these values have been chosen to match values which occur in actual observing situations (e.g. Lehnert et al. 1992) discussed below. We have taken the limiting surface brightness for detection to be 5 magnitudes fainter than the sky, which is again similar to the limit reached in practice.

The FWHM, and the limiting surface brightness for detection are indicated in Figure 7.3 by dotted lines. At low redshifts, each galaxy appears as an extended object well above the detection threshold. When the galaxy is at the limiting redshift for detection, which is obtained by solving Equation 7.3.3 numerically, the surface brightness reaches the detection limit exactly at the FWHM, and the galaxy cannot be distinguished from a point source. At the second highest redshift shown in each panel, the surface brightness of the disk galaxy is just above the threshold for detection close to the centre, but falls below the threshold even for some angular separations from the centre $\theta < \text{FWHM}$. The galaxy therefore appears to be a faint point source at that redshift. At the highest redshift in the two panels, the surface brightness of the galaxy is below the detection threshold for all values of θ , and it is simply lost in the background noise.

From Figure 7.3 it is seen that for the same absolute magnitude, the elliptical galaxy appears as an extended source only up to a limiting redshift of $z_{\text{lim}} = 0.75$, while the limiting redshift for a disk galaxy is $z_{\text{lim}} = 1.66$. The difference arises because of the higher k-correction which applies to the elliptical in the B band (see Figure 7.1), rapidly making it fainter with increasing redshift. Elliptical galaxies can be observed as extended sources to much higher redshift in the K band. Here the sky is much brighter, but the galaxy is more luminous as well. For typical colors, we can assume that the galaxies in Figure 7.3 are about 5 magnitudes brighter in the K band than in the B band. For illustrative purposes, we will assume that the sky background in K is 13 magnitudes per square arcsecond, and that the limiting magnitude that one reasonably reaches is 9 magnitudes fainter than the sky. In this case, the limiting redshift for the elliptical is $z_{\text{lim}} = 2.02$, while for the spiral it is 2.30. Going from the B to the K band affects the appearance of ellipticals much more than that of disk galaxies, because of the severe k-correction that the former suffer from at short wavelengths.

For a given type of galaxy and filter, the limiting redshift depends on the FWHM of the PSF, and the limiting magnitude, which in turn depends on the telescope aperture and the total exposure time. In the case of the disk galaxy in Figure 7.3, if the FWHM of the PSF is reduced from 1.6 arcsec to 0.6 arcsec, and all other parameters are left unchanged, the limiting redshift in the B filter increases from $z_{\text{lim}} = 2.31$ to 2.91. Here better seeing conditions allow the extended structure to be probed to smaller angular size, thus increasing the range of redshift over which the structure can be detected. If instead of reducing the FWHM, we make the limiting surface brightness which can be detected fainter by one magnitude, the limiting redshift increases from $z_{\text{lim}} = 2.31$ to 2.92. The limiting redshift also depends on the absolute magnitude of the galaxy, the scale lengths and the disk-to-bulge luminosity ratio. In subsection 7.4.2 we shall systematically examine the dependence of the limiting redshift on these parameters.

7.3.2 Galaxy With AGN

When an AGN is present, it has a surface brightness profile with the same shape as the PSF. When the AGN is bright, its surface brightness can significantly exceed the surface brightness of the host galaxy a few arcseconds from the centre. At low redshift, the galaxy can be detected at large angular separations where the surface brightness of the AGN has passed below the detection threshold. But at sufficiently high redshift, it is possible that the galaxy surface brightness passes below the threshold at small angular separations where it cannot be distinguished separately from the AGN. In such a case, the host will remain undetected and the object will appear to be unresolved.

The effect of an AGN is to add a point source at $r = 0$ to the profile in Equation 7.2.1. When the size of the image and the signal-to-noise ratio are sufficiently large, it is possible to determine the luminosity of such a source by including it as a parameter in a fitting procedure which simultaneously determines the parameters of the galaxy as well (Wadadekar, Robbason & Kembhavi 1999). But when the total angular extent of the image is small and it is faint, a fit is not possible. In such a circumstance, one can try to determine whether the total AGN+host galaxy profile is different from that of a point source with the same central surface brightness as the object under consideration. Such a criterion has been used by Lehnert et al. (1992) to detect host galaxies around high redshift radio-loud quasars.

In order to determine the limiting redshift to which a host galaxy can be detected in the presence of a bright AGN, we shall formalize the above criterion as follows. We consider the surface brightness of the total profile, and a point source profile with the same central surface

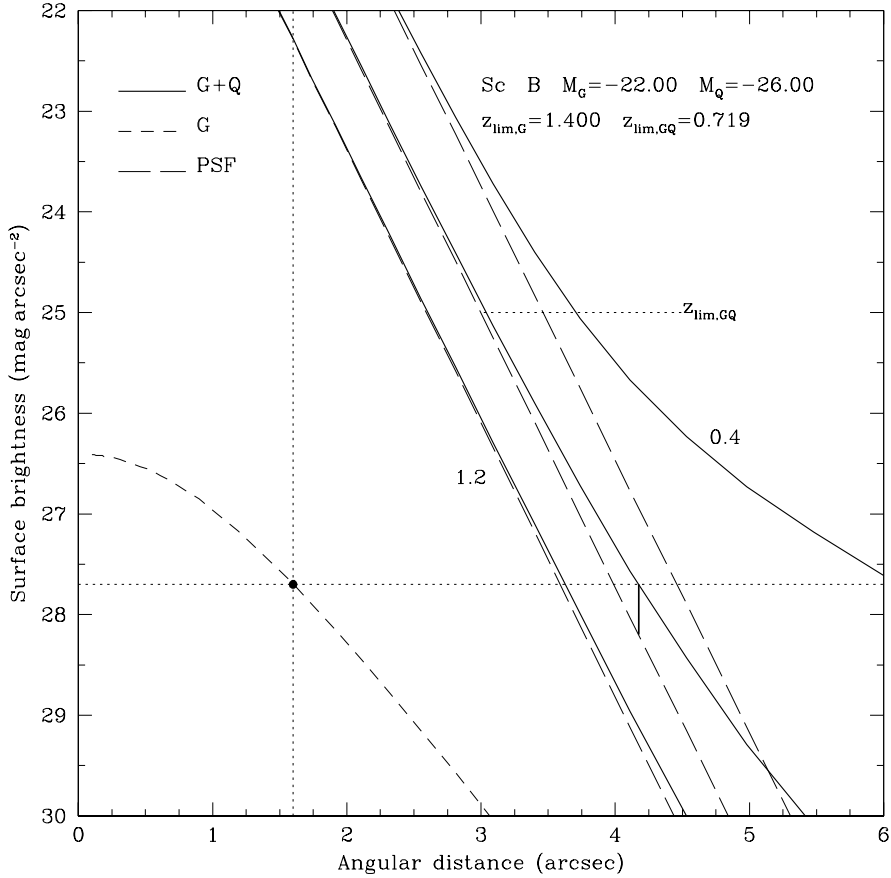


Figure 7.4: The total surface brightness profiles, at the redshifts indicated, of a Sc galaxy with parameters as in Figure 7.3 and an AGN with blue absolute magnitude $M_Q = -26$. At each redshift, the PSF with the same central surface brightness as the host galaxy+AGN combination is shown as a line with long dashes. The profiles for the limiting redshift $z_{\text{lim,GQ}} = 1.4$ are shown. The short dark vertical line connecting the profiles for the limiting redshift indicates $\Delta m = 0.5$. The other features in the figure are as in Figure 7.3.

brightness, at the angular separation at which the total profile crosses the detection threshold. If the excess brightness of the total profile at that separation, over the point source profile, exceeds some preselected value Δm , then we say that the object is extended; otherwise the object is taken to be indistinguishable from a point source. It should be noted here that the difference in brightness between the two profiles in general increases outwards from the centre. So if a profile is bright enough to be distinguished from a point source at some angular separation, it will appear extended at all larger angular separations, provided it remains above the detection threshold. Given an AGN and host galaxy combination which appears extended at low redshift, we can examine the profiles at increasing redshift to determine the limiting redshift $z_{\text{lim,GQ}}$ at which our criterion is fulfilled. At all higher redshifts, the galaxy will pass below the detection threshold before it can be separated from the AGN.

We have shown in Figure 7.4 the profile of the Sc galaxy in Figure 7.3, when it hosts an AGN with absolute blue magnitude $M_Q = -26$. To distinguish between an extended and starlike profile, we require $\Delta m = 0.5$ magnitude, which agrees with the difference found when an object is accepted to be extended in real observing situations, as in Lehnert et al. (1992). At the lowest redshift considered, 0.8, the total profile is clearly seen to be that of an extended object, when compared to the PSF. At the limiting redshift of $z_{\text{lim,GQ}} = 1.4$, the difference in brightness between the two profiles at the threshold for detection is exactly 0.5 magnitude, which is the adopted criterion for defining $z_{\text{lim,GQ}}$. At the higher redshift of 1.4, the total profile cannot be distinguished from the PSF, and the host galaxy is not detected. It should be noticed that the limiting redshift here is significantly smaller than the limiting redshift of $z_{\text{lim,G}} = 2.18$ which applies in the absence of the

AGN.

If we set a less stringent criterion of $\Delta m = 0.3$, the limiting redshift increases to $z_{\text{lim,GQ}} = 1.66$, while for the more stringent criterion of $\Delta m = 0.7$, the limiting redshift decreases to $z_{\text{lim,GQ}} = 1.25$. The redshift to which the host galaxy can be detected is very sensitive to the presence of the wings in the PSF. If instead of the Gaussian core and exponential wings combination that we have adopted, we use a PSF which has a pure Gaussian shape with the same FWHM, the limiting redshift increases to $z_{\text{lim,GQ}} = 2.08$ from 1.4. With a Gaussian PSF, the galaxy alone can be detected as an extended object to a redshift of $z_{\text{lim,G}} = 2.20$, so that the presence of the AGN does not make a significant difference. This is because with a purely Gaussian shape, the surface brightness profile of the AGN becomes rapidly faint at increasing angular separations from the centre.

7.4 Dependence of Limiting Redshift on Galaxy and Quasar Properties

7.4.1 Parameter Ranges and Correlations

We have seen above how the limiting redshift to which a galaxy can be seen can be obtained, given the galaxy type and luminosity, the parameters which determine its global morphology, and the luminosity of the AGN. Since a number of parameters go into building the model galaxy, we need to examine how sensitively the limiting redshift depends on the parameters, for the same observing conditions like sky brightness and seeing. Our aim in the present section will be to consider the observed distributions of the galaxy parameters, and to make random choices from these spreads, taking into account any known correlations between the parameters. For a number of model galaxies built up in this fashion, we will obtain the limiting redshift, and see how it depends on the choice of the parameters.

The structure of a de Vaucouleurs' elliptical is determined given its central surface brightness and effective radius r_e , or equivalently, its luminosity and r_e . The observed range of r_e , as obtained by Kormendy (1982) is $2h_{100}^{-1}$ kpc to $15h_{100}^{-1}$ kpc. Kormendy (1982, and references therein), found that for ellipticals there exists a linear correlation between the logarithm of the effective radius and the surface brightness at the effective radius. This can be expressed as a dependence of the effective radius in kiloparsec on the elliptical galaxy absolute magnitude M_G as

$$\log r_e = - (M_G + 19.52 - 3.28 \log h_{100} + C), \quad (7.4.1)$$

where M is the absolute magnitude in the band under consideration and $C = M_G(B) - M_G$ with $M_G(B)$ the galaxy absolute magnitude in the B band. For a given absolute magnitude, there is a spread of about 0.1 in $\log r_e$ about this line. To make an elliptical galaxy with some absolute magnitude, we can obtain its effective radius r_e , by making a random choice from the spread around the mean value obtained from Equation 7.4.1. The central surface brightness is then given by

$$\mu_G(0) = M_G + 5 \log r_e + 39.96. \quad (7.4.2)$$

In the case of disk galaxies, bulge as well as disk parameters have to be specified. The basic parameters are the bulge and disk central surface brightness $\mu_b(0)$ and $\mu_d(0)$ respectively, the effective radius r_e of the de Vaucouleurs' bulge and the scale length r_s of the exponential disk. These four parameters can be obtained given the total (bulge+disk) absolute magnitude M_G of the galaxy, the disk-to-bulge luminosity ratio D/B , $\mu_d(0)$ and rd . For different disk galaxy types we use the range of values given by Kent (1985), with his ratios in the r band converted to the B band using $B = r + 1.3$ for the bulge and $B = r + 0.9$ for the disk. For converting bulge and disk luminosities between the other bands, we use the average colors $B - V = 0.8$, $B - K = 3$ for a disk, and $B - V = 1.0$, $B - K = 4.4$ for a bulge. Within the the specified ranges for D/B , we assume that the distribution of D/B values is uniform. We will assume that the disk central surface brightness $\mu_d(0)$ is uniformly distributed in the range of 20.5 to 22.5 magnitudes per square arcsec in the blue band (Kent 1985).

From M_G and D/B the disk absolute magnitude M_d can be obtained. The disk scale length is then given by

$$\log r_s = 0.2 [\mu_d(0) - M_d - 38.57]. \quad (7.4.3)$$

The observed range of disk scale lengths is $1h_{100}^{-1}$ kpc to $7.5h_{100}^{-1}$ kpc. If r_s obtained from Equation 7.4.3 exceeds $7.5h_{100}^{-1}$ kpc, we replace it by a randomly chosen value within 10% of this maximum. Such a disk will have an anomalously bright central surface brightness for its r_s . We obtain the bulge effective radius r_e by using Figure 5 of Kent (1985). We first convert the $\mu_b(0)$ - $\log r_e$ line shown in that figure to the relation (in the B band)

$$\log r_e = -0.4(M_B + 18.16 - 2.5 \log h_{100}), \quad (7.4.4)$$

and assume that for a fixed bulge absolute magnitude, $\log r_e$ is uniformly distributed between -0.5 and a maximum given by this line. A model disk galaxy with a given total absolute magnitude can be constructed by choosing values of D/B and $\mu_d(0)$ at random from their ranges, and obtaining r_s from Equation 7.4.3 and r_e from Equation 7.4.4.

For our purposes, the AGN is completely described by its absolute magnitude and power-law spectral index, which we take to be uniformly distributed in the range 0.3 to 1.3. We have used information available in the literature to specify the ranges of various galaxy parameters and correlations between them where these are known. Choosing somewhat different ranges and correlations will not significantly affect our results.

7.4.2 Results

We have shown in Figure 7.5 the limiting redshifts obtained for Sa galaxies with a range of absolute magnitudes in the B filter. Also shown is the locus of limiting redshifts for the combination of Sa galaxies and an AGN with a B band absolute magnitude of -26. The various parameters used in the simulation are listed in the caption to the figure. For each galaxy luminosity, a hundred choices of D/B , $\mu_d(0)$ and r_e and the quasar spectral index were made at random, following the prescriptions given in subsection 7.4.1. For each choice the limiting redshift $z_{\text{lim,G}}$ for just the galaxy and $z_{\text{lim,GQ}}$ for the galaxy and quasar combination were obtained. The mean limiting redshifts obtained in the 100 trials for each galaxy luminosity, and the rms dispersion in the redshifts, are shown in Figure 7.5. The size of the error bars is rather small at faint galaxy luminosities, and grows to an rms value of ~ 0.1 at galaxy absolute magnitude of about -23, which corresponds to the brightest observed galaxies. We have continued the curves to even brighter magnitudes, extrapolating the observed parameter distributions and correlations to these values, since some of the host galaxies detected (e.g. Lehnert et al. 1992) appear to have extraordinarily high luminosities.

In optical surveys for quasars it is usual to select as candidates only those objects which do not show an observable extension; but it is of interest to attempt to detect the galaxy through observations which go deeper than the discovery survey. The question then is: to what limiting redshift one may expect to detect a host galaxy under given observing conditions, in the case of an object for which only the total absolute magnitude, made up of light from the quasar and the putative host galaxy, is known? We have shown in Figure 7.6 the limiting redshifts for the detection as a function of total absolute magnitude. We have considered Sa galaxies in the B band, with absolute magnitude $M_B = -22$ and -19 respectively, which host quasars with a range of luminosities. The limiting redshift for a range of galaxy absolute magnitudes, when no AGN is present, is also shown for comparison. The error bars again indicate the rms dispersion in redshift obtained in a hundred simulations with parameters chosen as in Figure 7.5. Even at its worst, the 1σ dispersion in redshift is only ~ 0.15 . The limiting redshift is determined mainly by galaxy type, absolute magnitude and the filter, and depends little on the other parameters.

In Figure 7.7 we have shown the limiting redshifts achieved for different combinations of quasar and galaxy luminosities, for Sa galaxies in the B (upper panel) and K (lower panel) bands. For each combination of galaxy and AGN luminosity, we have selected a hundred parameter sets in the manner described above. The limiting redshift shown is the mean of the hundred values obtained, as in Figure 7.6. We have omitted the error bars for clarity. The total absolute magnitude of the combination is shown on the abscissa. The abscissa in the lower panel is shifted relative to the upper panel to account for the average color of $\langle B - K \rangle = 3$ for Sa galaxies. With this arrangement, the B and K luminosities of an object with $B - K \simeq 3$ would lie on a vertical line running through the two panels. The dotted line shows the limiting redshift for galaxies with no AGN. The full lines are for galaxy+AGN combinations, with each line corresponding to a single galaxy luminosity combined with different quasar luminosities. Each such line ends in a point on the dotted galaxy line, with the

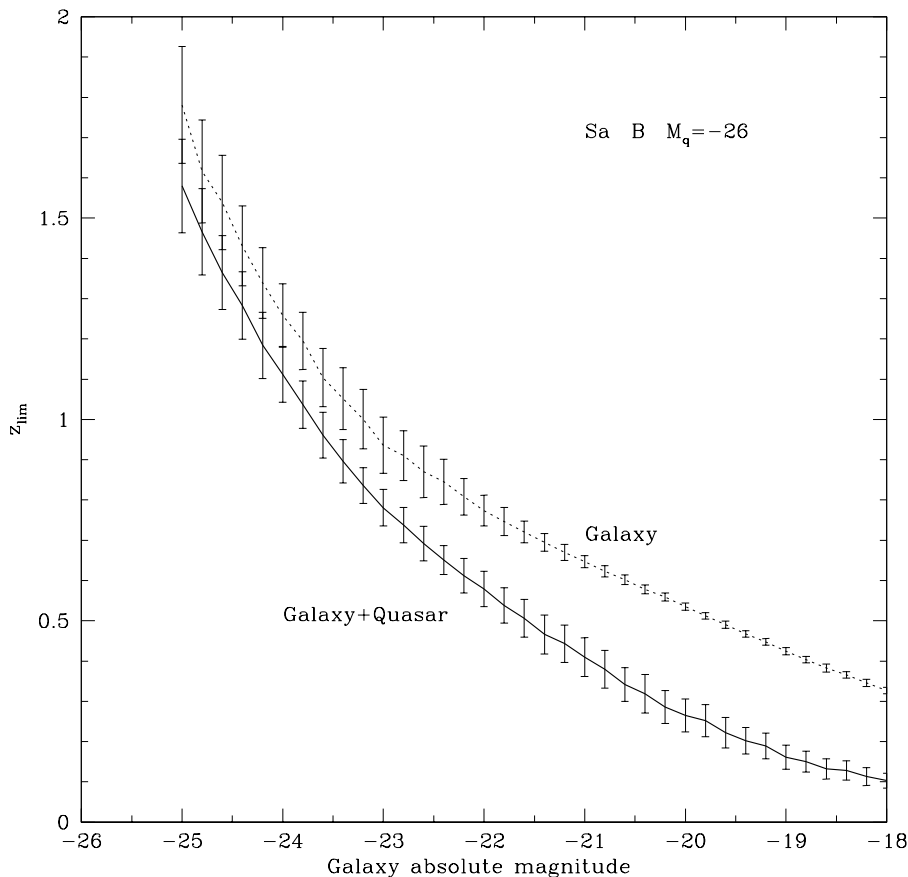


Figure 7.5: Limiting redshifts for an Sa galaxy for a range of absolute magnitudes (dotted line), and for an Sa with an AGN of absolute magnitude -26 in the B filter. The error bars at each absolute magnitude indicate the range of limiting redshifts obtained by varying morphological and other parameters as described in the text. We have used a sky brightness of $22.7 \text{ mag arcsec}^{-2}$ in the B band and assumed that the faintest feature observable has a surface brightness $5 \text{ mag arcsec}^{-2}$ fainter than the sky. The PSF is assumed to be circularly symmetric, with a Gaussian core and exponential wings. We assume that the FWHM of the PSF is 1.6 arcsec and that the scale length of the exponential part is 2.5 arcsec . When an AGN is present, we have adopted the criterion described in subsection 7.3.2 to distinguish between the profiles of extended and point-source like images.

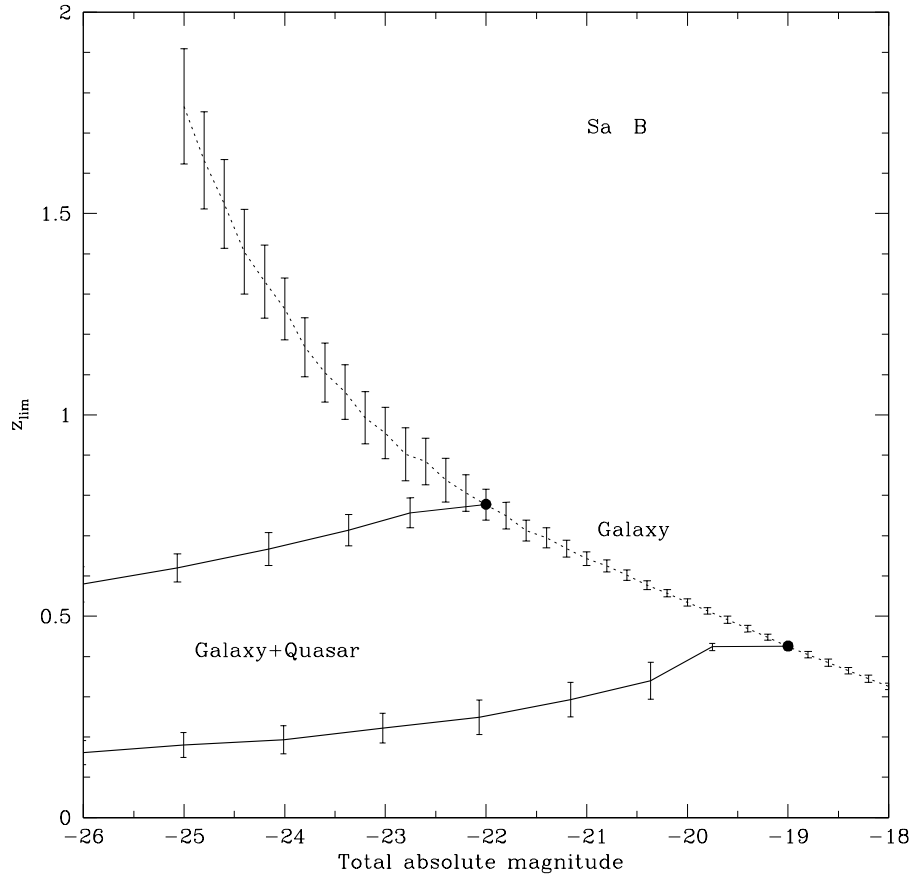


Figure 7.6: Limiting redshifts for Sa galaxies with B band absolute magnitudes -22 and -19 respectively, and containing AGN with different luminosities. The dotted line indicates limiting redshift for an Sa galaxy, not containing an AGN, for a range of galaxy absolute magnitudes. The range of parameters, observing conditions and error bars are as in Figure 7.5. The large dots indicate the points at which the luminosity of the galaxy-AGN combination becomes indistinguishable from the galaxy luminosity.

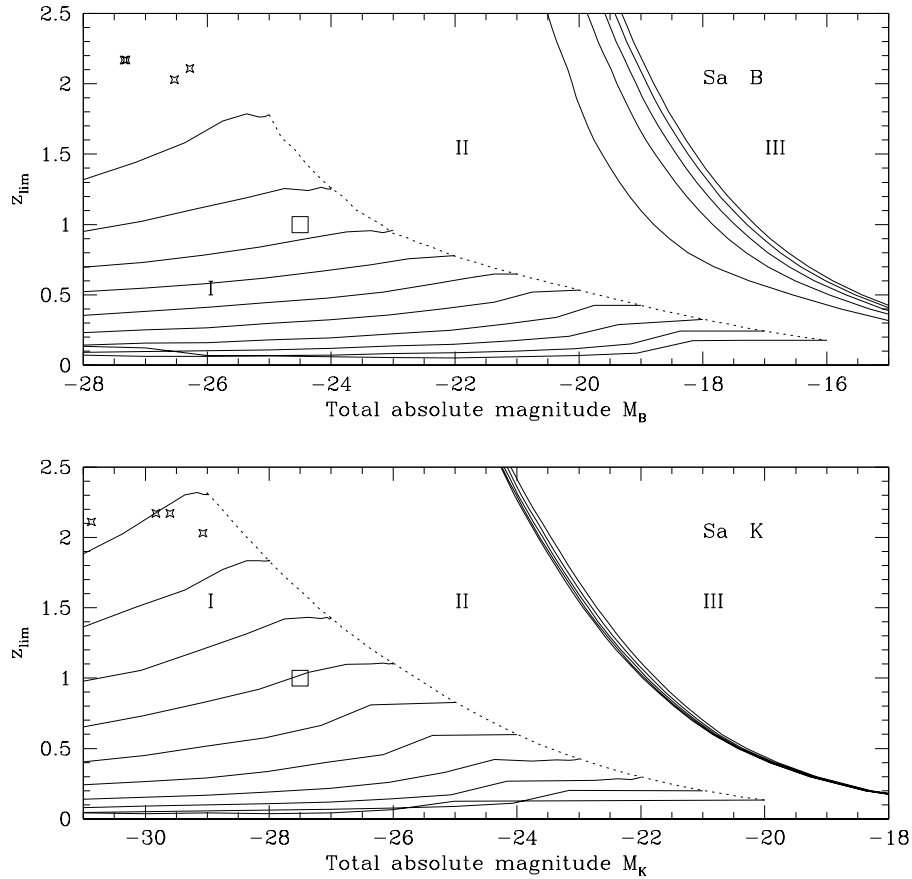


Figure 7.7: Limiting redshift for detection as an extended source against total absolute magnitude for different galaxy+AGN combinations. Results are shown for Sa galaxies in the B (upper panel) and K (lower panel) bands. In each panel the dotted line shows the limiting redshift for a galaxy without an AGN. Each full line ends on the dotted line, with the luminosity corresponding to this point being the galaxy luminosity in the combination. The curves in the upper right hand part of each panel indicate the redshift at which a galaxy+AGN combination with a given total absolute magnitude would become too faint to be detected above the sky background, even as a point source. The five curves are for the ratios 0.0, 0.25, 0.50, 0.75 and 1.0, with the outermost curve corresponding to the highest ratio. The significance of the three regions marked I, II and III is described in the text. The star like points indicate quasars from the sample of Lehnert et al. (1992), while the small square in each panel indicates the approximate position of radio-quiet quasars with $z \simeq 1$ from Lowenthal et al. 1995 (see subsection 7.4.3 for a discussion). The galaxy parameters and observing conditions are as in Figure 7.5.

position of the point indicating the absolute magnitude of the galaxy for that line. For the galaxy and AGN models adopted in this chapter, an object with a given total luminosity must lie below the appropriate full line for it to be recognized as an extended object. Above such a line, the object will appear to be unresolved, and will be classified as a quasar. For a given quasar luminosity, the limiting redshift is the least for the highest AGN to host galaxy luminosity ratio. As this ratio decreases, the limiting redshift increases, and reaches its maximum value when the AGN luminosity becomes small compared to the host galaxy luminosity. For a given total absolute magnitude, the limiting redshift runs over a substantial range. For example, at total absolute magnitude $M_B = -26$, the limiting redshift ranges from ~ 0.1 to ~ 1.1 for galaxy absolute magnitudes ranging from -19 to -24. The curves in the upper right hand part of each panel indicate the redshift at which a galaxy+AGN combination with a given total absolute magnitude would become too faint to be detected above the sky background even as a point source. Each curve corresponds to a specific value of the ratio of the AGN luminosity to the host galaxy luminosity. The curves are for values 0.0, 0.25, 0.50, 0.75 and 1.0 of this ratio. For a given total absolute magnitude, the maximum redshift for detection increases with the ratio.

Figure 7.7 is divided by the various curves into three broad regions I, II and III as indicated. An object with total luminosity and redshift which are such that it is placed in region III, would not be detected at all. A galaxy in region II always appears unresolved, and could be either a normal or an active galaxy. It is straightforward to distinguish between the two types of objects on the basis of their spectra, provided of course that the objects are bright enough for their spectra to be obtained. In region I, which is the region below the dotted line, whether an object appears to be extended or unresolved depends on the way its total luminosity is divided between the host galaxy and the AGN. A normal galaxy, i.e. one not containing an AGN, would always appear to be extended in this region. Any unresolved galaxy to be found here will therefore be an active galaxy, while an extended object may be a normal or an active galaxy. So a survey for active objects, with the criterion that they appear to be "starlike" (unresolved, but with emission lines or other features which distinguish them from stars), should be limited to region II. Region I can be extended into region II by considering even brighter galaxies than shown, but such objects may not exist.

When an object with known redshift appears to be unresolved in the discovery survey, Figure 7.7 makes it possible to estimate the range of host galaxy luminosity for which the object would appear to be extended in a deeper survey with given observing conditions. The figure also provides the conditions under which unresolved objects could be detected above the background noise. Consider a volume limited survey in the K band which extends to, say, $z = 1.0$. It is clear from Figure 7.7 that, for an Sa host galaxy, such a survey will be complete only for objects brighter than $M_K = -22$, as fainter objects would go undetected. The non-trivial fact here is that such a statement would not be possible for a survey in the B band, as here the detection lines depend on the AGN to host galaxy luminosity ratio, and the degree of completeness would not be uniform for all ratios. The level of completeness will also change further with galaxy type.

We have shown in Figure 7.8 the limiting redshifts for elliptical galaxies in the B and K bands. Here the abscissa in the lower panel is shifted through 4.5 magnitudes relative to the upper panel to allow for the average $B - K$ color of elliptical galaxies. For a given total luminosity in the B band, the limiting redshift in this case is much lower than for Sa galaxies. This is because of the substantially larger k-correction which has to be applied to elliptical galaxies. We see from Figure 7.2 that k-corrections for different types of galaxies are very similar in the K band. As a result the limiting redshift in this band depends very little on galaxy type. When a host galaxy is suspected to be an elliptical, there is substantial advantage in observing it in the K band.

We have shown in Figure 7.9 the limiting redshifts for spiral galaxies of type Sc in the B and K band. Because of the reduced k-correction for these objects relative to Sa galaxies, the limiting redshifts reached are higher. We shall see below that galaxies of type Sc or later are more likely to be the hosts of luminous quasars than galaxies of earlier types. To facilitate comparison between different galaxy types and bands, we have plotted in Figure 7.10 the limiting redshifts against total absolute magnitude for galaxies of different types. The upper panel shows limiting redshifts for E, Sa, Sc and Im host galaxies with absolute magnitude $M_B = -22$. The spread in redshift in going from one type of galaxy to another is maximum at total absolute magnitudes approaching the host galaxy magnitude. The dotted lines show the limiting redshifts in the K band. Here we have chosen

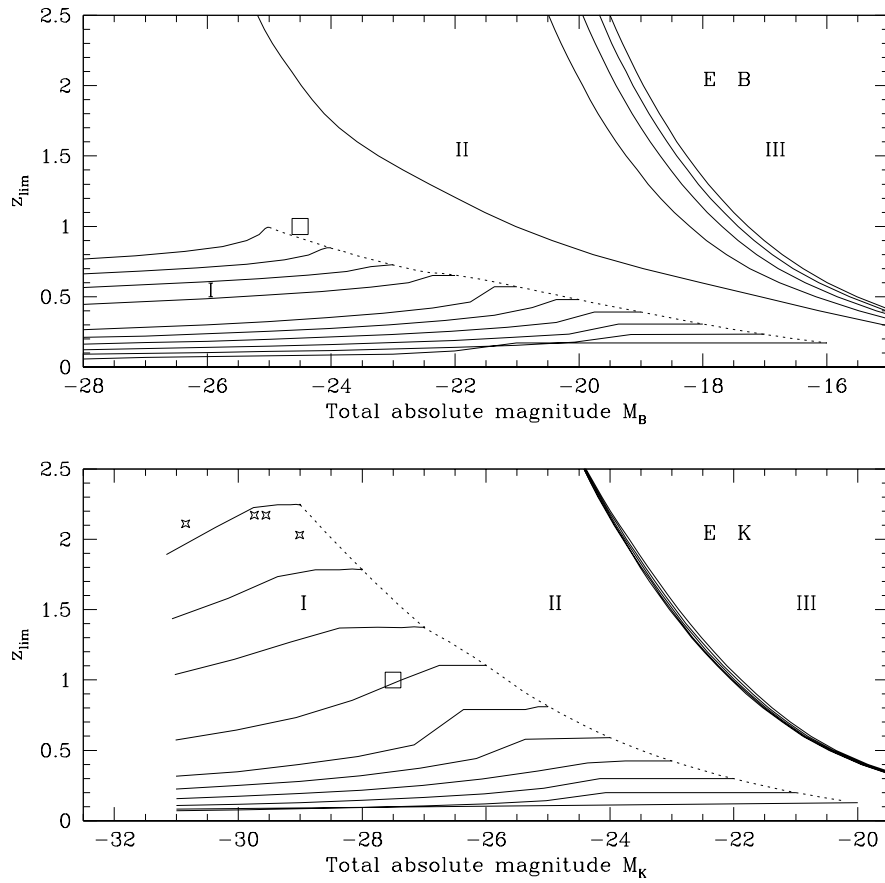


Figure 7.8: Limiting redshift for detection as an extended source against total absolute magnitude for different galaxy+AGN combinations. The hosts are assumed to be elliptical galaxies. Various features here are as in Figure 7.7.

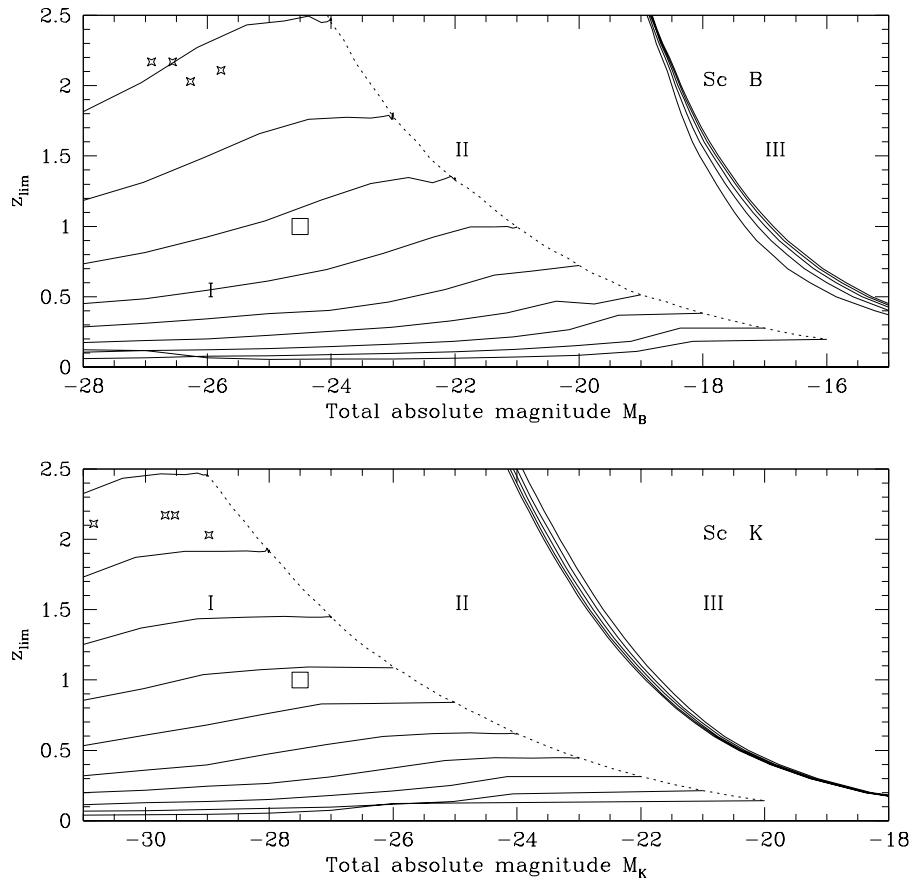


Figure 7.9: Limiting redshift for detection as an extended source against total absolute magnitude for different galaxy+AGN combinations. The hosts are assumed to be Sc galaxies. Various features here are as in Figure 7.7.

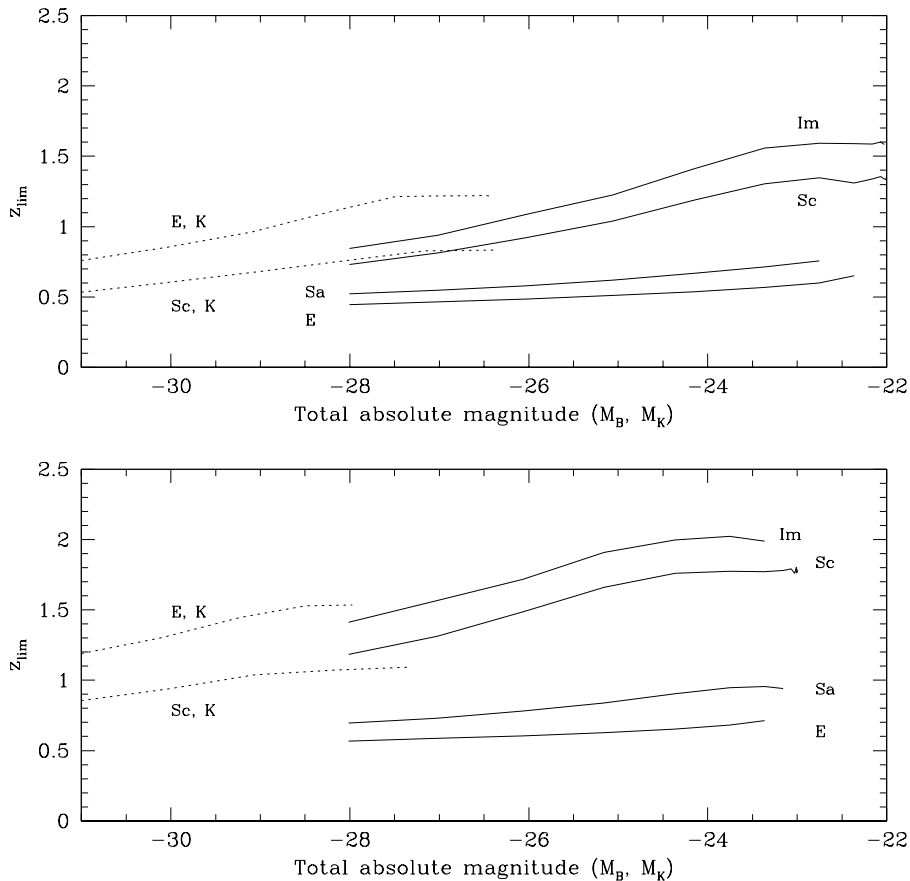


Figure 7.10: Limiting redshifts against total absolute magnitude for galaxies of different types. We have indicated absolute magnitudes in the B as well as the K band along a single axis in both panels of the figure. The full lines indicate limiting redshifts reached in the B band and the dotted lines the limiting redshifts in the K band. In the upper panel, the galaxies have $M_B = -22$, with $M_K = -25$ for the spiral galaxies and $M_K = -26.5$ for elliptical galaxies. In the lower panel, $M_B = -23$, with $M_K = -26$ for the spiral galaxies and $M_K = -27.5$ for elliptical galaxies.

a host galaxy magnitude of $M_K = -25$ for the spirals and $M_K = -26.5$ for the ellipticals, to agree with the the average $B - K$ colors of these galaxies. It should be noted that for Sc galaxies going from the B to the K band does not make a substantial difference to the limiting redshift reached, but in the case of E galaxies it is highly advantageous to observe in the K band. In the case of Sc and Im galaxies, the limiting redshift is spread over a significant range for the AGN to host galaxy luminosity ratios considered. The likelihood of detecting a host galaxy of these types, with a given luminosity ratio, is significantly improved for the lower luminosity AGN. The lower panel in the figure displays limiting redshifts for host galaxy absolute magnitude $M_B = -23$, to illustrate the change with increasing host galaxy luminosity.

In Figures 7.11 and 7.12 we have shown limiting redshifts as a function of host galaxy absolute magnitudes for Sa and E galaxies respectively. The conventions followed are as in Figure 7.7. A diagram in this form is useful to determine the redshift up to which a locally observed Seyfert or radio galaxy, say, would remain visible as an extended source.

7.4.3 Comparison With Observations

Lehnert et al. (1992) have obtained deep images of a set of six radio-loud quasars with redshift ranging from 2.032 to 2.877. They used a 4 m telescope to obtain images in the optical band, and a 3.5 m telescope for images in the K band. The sky brightness level and parameters defining the PSF were similar to the values adopted by us (we in fact chose our values to match approximately those of the Lehnert et al. observations for ease of comparison). The faintest features observable

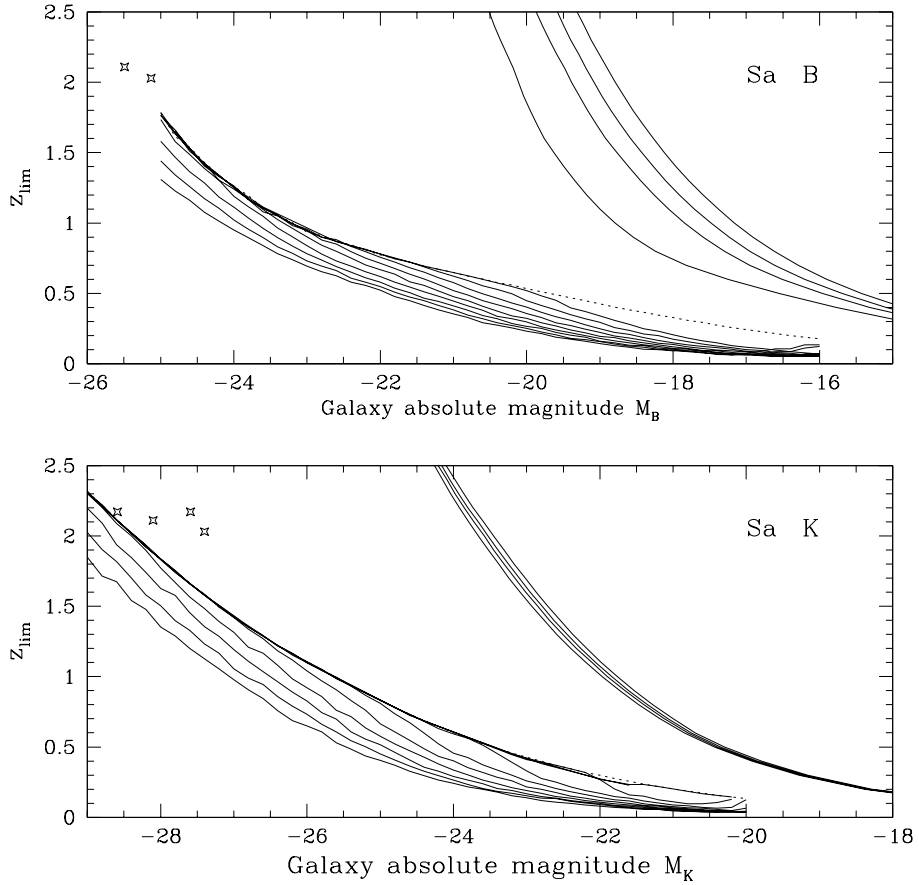


Figure 7.11: Limiting redshift for detection as an extended source as a function of host galaxy absolute magnitude for different AGN luminosities. The host galaxy is of type Sa. The full lines below the dotted line correspond to AGN absolute magnitudes in the B (upper panel) band of -28, -27, -26, -25, -24, -23, -22, -21 and -20. For a given galaxy absolute magnitude, the lowest limiting redshift corresponds to the brightest AGN. In the K band (lower panel), the absolute magnitudes range from -31 to -22, again with a difference of one magnitude between successive curves. Other features are as in Figure 7.7.

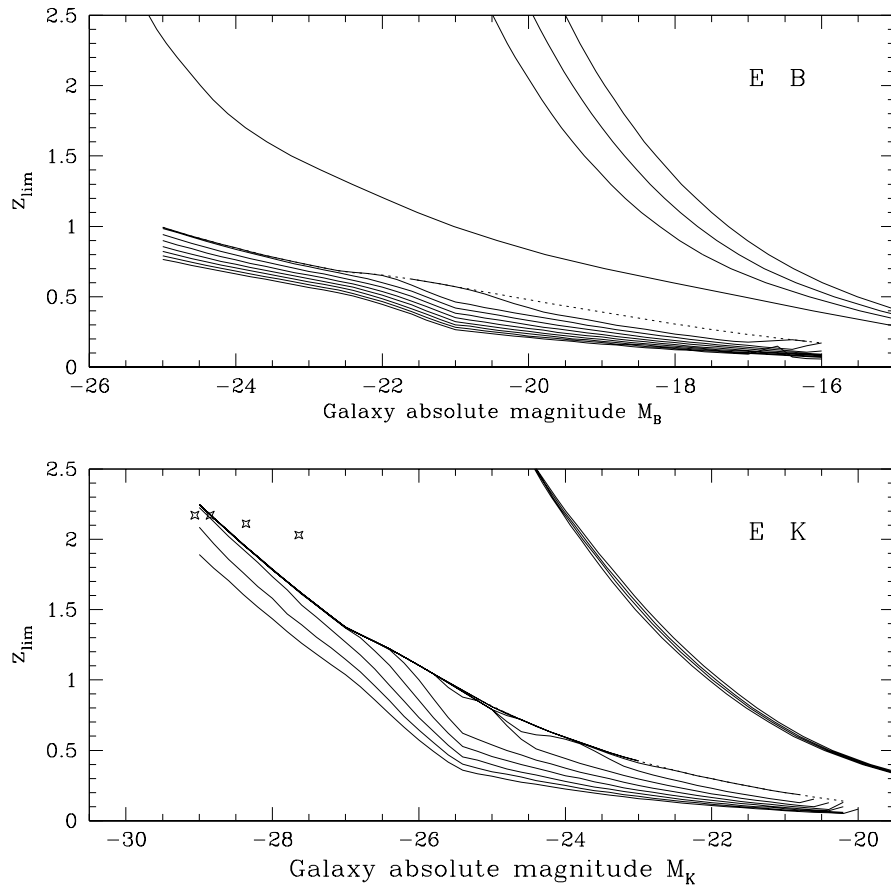


Figure 7.12: Limiting redshift for detection as an extended source as a function of host galaxy absolute magnitude for different AGN luminosities. The host galaxy is of type E and various features are as in Figure 7.11.

were $\sim 1\%$ of the sky background, which we have emulated by assuming that discernible features in our models are up to 5 magnitudes fainter than the background.

Lehnert et al. found that all six quasars were well resolved in the K band, while only four quasars were resolved in the B band. The extended structures had 4% to 40% of the total flux from the object, and angular sizes in the ~ 5 arcsec to ~ 10 arcsec range. The absolute magnitude in the V band was in the range $-26 < M_V < -24.2$, which makes them considerably brighter than first-ranked giant cluster ellipticals, which are the brightest galaxies in the local universe, as well as the most luminous galaxies in the Revised Shapley-Ames catalogue. The K band absolute magnitudes of these galaxies are estimated to be in the range $-28 \lesssim M_K < -30$

We have shown in Figure 7.7 four of the Lehnert et al. quasars, with the total absolute magnitude in the B and K bands obtained from their data. We find from the figure that *if the host galaxies of these quasars have the morphology and colors of Sa galaxies in our neighborhood*, they should appear to be point sources in the B band, but extended in the K band, providing the K band *host galaxy luminosities* are brighter than $M_K = -28$. Since in the observations the host galaxies were also detected in the B band, our results imply that either the host galaxy is not of the Sa type, or it is unusually bright ($M_B \lesssim -26$). Given the uncertainties in the estimated host galaxy luminosities in Lehnert et al. , the observed host galaxy luminosities could very well be as high as this. We have not shown the other two quasars from Lehnert et al. , since their redshifts are outside the range of the figure, and they would appear to be point sources. We see from Figure 7.8 that if the hosts of the four quasars were elliptical galaxies, they would appear extended in the K band, but not in the B band. As we pass along the sequence of spiral galaxies towards the later types, the colors become bluer, and the optical band k-corrections are less severe (see Figure 7.1). It therefore becomes easier to detect the host galaxies. From Figure 7.9 we find that Sc host galaxies would be resolved for galaxy absolute magnitudes $M_B \lesssim -24$ and $M_K \lesssim -28.5$. Detection of Im hosts is possible to fainter absolute magnitudes, and Lehnert et al. in fact find from their broad-band data that the host galaxies have colors which resemble those of Im galaxies.

Lowenthal et al. (1995) obtained deep optical and K band images of four radio-quiet quasars at $z \simeq 1$ and six radio-quiet quasars at $z \simeq 2.5$. The absolute magnitude of the high redshift sample is centered at $M_B \simeq -26$, and that of the low redshift sample around $M_B \simeq -24.5$. None of the high redshift objects showed any extension, while only two of the low redshift objects showed marginal extension in the K band. From Figure 7.7 it can be seen that the high redshift quasars from this sample would be unresolved in the B and K band if their hosts were Sa galaxies, as they would be at top of the redshift range covered. We have indicated the approximate position of the low redshift objects in the diagram by small squares. Because these objects are unresolved in the B band, we can say, from the position of the square in the upper panel, that the host galaxy must be fainter than $M_B \sim -23.5$. From the position of the two marginally resolved low redshift objects in the lower panel of Figure 7.7, it is possible to constrain the $B - K$ color of their host galaxy.

7.5 Discussion

Host galaxies of quasars at high redshift, $z \sim 2$, suffer from low surface brightness, small angular extent and from “noise” due to a highly luminous AGN. Such hosts are therefore much more difficult to detect than Seyfert or radio galaxies in our neighborhood. Even when a fuzzy structure is found in deep observations, the morphology of high redshift hosts remains unclear. From available data it appears that the hosts of radio quiet quasars have a luminosity comparable to, or somewhat less than, local L^* galaxies. The hosts of radio quasars are found to have much higher luminosities, being significantly brighter than the most luminous galaxies in our neighborhood, but rather uncertain k-corrections are involved in these estimates. The high luminosities and colors imply a star formation rate of several hundred Solar masses per year in the radio quasar hosts. In this chapter, we have shown that even with the meager knowledge that an extended image is just about detected in one band but not in another, it is possible to get clues about the nature of the host galaxy.

It is known that that radio galaxies at low redshift have rather smooth elliptical morphologies (e.g. Mahabal, Kembhavi and McCarthy, 1999). While at low redshift at least some radio-loud quasars are known to be associated with elliptical galaxies, our results show that hosts at high redshift simply cannot be normal elliptical galaxies. It can be seen from Figure 7.8 that even the

brightest ellipticals in our neighborhood would not be detectable as extended objects in the B band beyond a redshift of ~ 0.7 , and a galaxy even three magnitudes brighter would be unresolved beyond $z \simeq 1$. The limiting redshifts are higher in the K band, but even there the limit is at $z \simeq 2$. We have seen that an unresolved host cannot be made to appear extended by changing its morphological parameters in any reasonable way. But the situation is quite different if the galaxy colors are altered. If we take a host with an elliptical morphology, and superpose on this the colors of an Im galaxy, then the limiting redshift even in the B band can easily be increased to values beyond the redshifts in the Lehnert et al. (1992) sample. Radio galaxies at high redshift are known to have complex morphologies and blue colors (e.g. van Breugel et al. 1998), indicating massive star bursts, and these must later evolve to the giant elliptical galaxy hosts of relatively local radio sources. If the hosts of distant radio quasars have colors similar to those of high redshift radio galaxies, then it should be possible to detect them as well. It is interesting to note that if the hosts were luminous Sc or later type galaxies, they could be detected in the B and K bands to redshifts $z \gtrsim 2$.

In discovery surveys, an object is classified as a quasar or an AGN, depending on whether it appears to be unresolved, or a host galaxy can clearly be seen. In most surveys, all objects with total absolute magnitude fainter than some limit are put into the non-quasar class, to avoid contaminating the quasar sample with objects which are just resolved. We have seen that whether an object appears to be resolved or not depends on the AGN to host galaxy luminosity ratio, the properties of the host galaxy, the redshift and the observing conditions. The relative numbers of objects with unresolved and extended structures will therefore depend, most importantly, on the redshift and the colors of the host galaxy. This can introduce a seeming redshift dependence in the luminosity function, which can be confused with evolution. Moreover, because at higher redshifts it is difficult to detect a galaxy with normal colors, the hosts which are actually detected will be those with “abnormal” colors, even though normal hosts may very well be present. The extent of such a bias towards associating quasar activity with abnormal galaxy types can be examined by imaging a complete sample of quasars in more than one band, including K , and finding the proportion of unresolved and extended objects under the observing conditions.

Our considerations in this work have been entirely based on terrestrial observing conditions. Observations of host galaxies with the Hubble space telescope will increase the limiting redshift for detection of host galaxies greatly, because of the narrower PSF and the darker sky background. Space telescope observations at low redshift have revealed a wealth of detail about the morphology of quasar host galaxies (e.g. Bahcall et al. 1997). Deeper observations will be able to tell us about the proportion of such normal structures at high redshift.

Chapter 8

Optical morphology of low flux radio sources: astrometry and photometry

This chapter presents the data for a study of the optical counterparts of low radio flux VLA FIRST survey sources. We present optical identifications for ~ 60 FIRST radio sources from the equatorial strip of the survey, most of which have a radio flux < 10 mJy. We describe the observations and data reduction techniques and present calibrated photometry for a significant fraction of the sources identified as the optical counterparts of FIRST survey sources. This chapter is largely based on Wadadekar, Kembhavi & McCarthy (2000).

8.1 Introduction

Over the last two decades considerable progress has been made in optical identifications of radio sources. Optical work on bright source samples such as the 3CR and 4C surveys has been extensive and the optical counterparts of almost all the sources have been detected (e.g. Riley, Longair & Gunn 1980; Olsen 1970; more references are listed in Djorgovski et al. 1988). At these bright flux levels, elliptical galaxies dominate the optical identifications. For moderately bright source samples such as the Bologna survey, the identification percentage drops to 80% (Allington-Smith et al. 1982) even at an optical magnitude of 23, showing that the redshift and/or radio luminosity distribution differs already from that at the 3CR level.

At still lower flux densities (< 10 mJy) the identification fraction decreases quickly and the morphology and color of the identifications change as well. This occurs because a *new* population of radio galaxies makes its appearance at millijansky and submillijansky levels. This population, composed primarily of actively star forming galaxies out to $z \sim 1$, was first revealed by the changing slope of the 1.4 GHz radio source count distribution (Windhorst et al. 1985) and has been confirmed by subsequent spectroscopic and multicolor studies (Thuan & Condon 1987; Benn et al. 1993; Windhorst et al. 1993; Hammer et al. 1995; Hopkins et al. 1998; Richards et al. 1998). Their numbers increasingly dominate the classical radio sources (powered by active galactic nuclei) as the flux density limit falls below 1 mJy. The evolution of these galaxies, their morphological type composition and the role of interactions and mergers in the population, are only partially understood at the present time.

In this chapter and the next, we take the third approach, as described in Section 3.4, for obtaining optical counterparts of FIRST sources. We present deep optical data with a limiting magnitude $m_V \sim 24$ for about one square degree of sky. Most of the radio sources for which we have optical counterparts have flux < 10 mJy. Many of our identifications are thus expected to correspond to the star forming population of galaxies, although there will be some weak nuclear sources (AGN) too.

In this chapter we describe the observations, basic data reduction procedures, astrometry and photometry. The next chapter presents a description of the optical morphology of the identifications along with finding charts and the results of our attempts at bulge disk decomposition of the brighter identifications.

Night	Date	FWHM (arcsec)	Conditions
1	1997 Nov 1	1.5	photometric
2	1997 Nov 2	1.8	mixed
3	1997 Nov 3	1.8	most of the night clouded out
4	1997 Nov 4	1.8	mostly photometric

Table 8.1: Weather conditions

8.2 Observations and reductions

8.2.1 Sample definition

In 1995/6 the FIRST survey covered a strip of about 600 square degrees around the South Galactic Cap, which is accessible from the Southern hemisphere optical telescopes and that is the region we have used to obtain the observations reported here. Although the FIRST data were obtained with the VLA before 1996, the version of the catalog we used was constructed later by the FIRST team, using an improved pipeline script that substantially reduced the sidelobe levels in a small fraction of the fields.

We chose 9 fields for deep observations, covering a wide range in RA. This was done to allow us to observe each field at the lowest possible airmass. For each field, we took some short trial exposures. If there were extremely bright stars in the field, the pointing was changed slightly to exclude such stars. This was always possible as all our fields were located at moderate to high galactic latitudes. *No* other selection criterion (e.g. the clustering of FIRST sources) was applied in the selection of our data fields.

8.2.2 CCD Imaging Observations

The CCD imaging camera was located at the Cassegrain focus of the 2.5 m Du Pont Telescope at the Las Campanas Observatory (LCO), Chile. A 2048 × 2048, thinned and UV flooded Textronix CCD with 24 μm pixels was used in conjunction with a wide field reimaging camera which gives a large effective field of view of 24'×24' and a pixel scale of 0".776 pixel⁻¹. The pixel scale was determined from our astrometric measurements, based on available plate solutions for the digitized POSS survey. 5 × 5 inch *V* and *R* filters of the Johnson system were used. The detector was aligned in the north-south direction to within a degree. This was checked by making trailed exposures of bright stars.

The observations were made during an observing run in November 1997. The dates of the observing run and a short summary of the prevailing weather conditions on each night are listed in Table 8.1. A typical observation of one CCD field consisted of several exposures of 600 s duration, with the telescope offset by about 1 arcmin between two exposures. About 6000 seconds of total exposure was obtained in the *V* band and 3000 seconds of exposure was obtained in the *R* band for each field. This provided for a reasonably uniform signal to noise ratio in the ensemble data set. Nine fields were imaged in the *V* band; of these three fields were also imaged in the *R* band. The remaining fields could not be imaged in the *R* band because of poor weather conditions on the third night. Coordinates of the centers of the observed fields, the filter(s) used and the exposure time in each filter are listed in Table 8.2. A short 60 second exposure was obtained for each field for astrometry purposes.

For all nights we obtained photometric calibration data by observing *UBVRI* standards from Landolt (1992). Standard star fields SA-92, SA-98 and SA-113 were observed each night at a range of airmass.

The latitude of the observatory (-29.5 degrees) is such that the observed area never passed closer than about 30 degrees from the zenith. It was difficult to maintain an airmass of better than 1.3 during our observing, but we tried to do so, whenever possible.

Number	$\alpha_{2000.0}$ hh:mm:ss	$\delta_{2000.0}$ dd:mm:ss	Filter	Exp. time (sec)
1	21:20:00	-00:30:02	V	5400
2	23:30:02	-00:29:56	V,R	5400, 3300
3	01:59:20	-01:39:55	V	5400
4	03:03:05	-01:14:52	V,R	5400, 2700
5	22:01:12	-01:07:03	V	5400
6	00:00:49	-00:50:37	V	5400
7	01:51:04	-00:29:55	V	5400
8	02:59:45	-00:58:52	V,R	3000, 2700
9	01:02:42	-00:50:00	V	5400

Table 8.2: Observed fields

8.2.3 Basic reductions of the CCD images

We used tasks from the IRAF¹ image processing system for basic reductions of the CCD images. The read-out noise for the CCD was 6.6 electrons per pixel and the gain was 2.0 e⁻/ADU (ADU: Analog-to-digital-unit).

Each exposure was first bias subtracted using a 16 column wide overscan region using the *colbias* task in IRAF. A master sky flat for each filter was constructed from several sky flats using a mode weighted averaging process. High and low pixels beyond the 3σ level were rejected using an averaged sigma clipping algorithm to avoid the effect of bright stars that appeared in some twilight flats. Images flattened using this technique were carefully examined. They were found to be flat to 1% or better in both filters. Each object frame was divided by the normalized flat field. There is one bad column on the CCD and a few hot and cold pixels. We used an image constructed from two twilight flat field images of different exposure levels to construct a bad pixel mask image using the *ccdmask* task. Pixels in the bad pixel mask image were replaced with values of the nearest pixels not identified as bad, using linear interpolation. Interpolation was performed across the narrowest dimension spanning bad pixels, with interpolation along image lines if the two dimensions were equal. Multiple exposures of the same field were registered by a linear shift in each coordinate. The shift was computed from the centroids of one to three stars in each frame. The individual frames were then summed to produce the final image, which typically reached a depth of $V \sim 25$ mag (3σ) for detection of an optical counterpart. Each summed field was normalized to an exposure time of one second for convenience in subsequent computation of the photometric zero point transformations.

8.2.4 Astrometry

As a first step in the astrometry, we compiled a grid of astrometric stars for each CCD field. For every field we extracted a $24' \times 24'$ image from the digitized POSS. The pixel coordinates of the centroid of 5-8 stars were measured on the POSS images. The centroid of each star was determined by fitting a two dimensional gaussian to the profile using the *imexam* task; saturated stars were not used. The 1.7 arcsecond pixels of the digitized sky survey images result in a somewhat poor positional accuracy. Yet the uncertainty in the plate solution derived from 5 stars did not limit our ability to identify any of the sources. The POSS plate solutions were used to compute the RA-Dec of each astrometric star. Each of these stars was then identified on the CCD image and the RA-Dec determined from the POSS plate solutions were used to compute plate solutions for the CCD images using the *ccmap* task in the *immatch* package in IRAF. The World Coordinate System (WCS) information was added to the FITS header of the image. The median RMS error in the fit was 0.30 arcsec which is less than half a pixel on the CCD image. We tested the accuracy of the astrometry using stars which were not included in the original grid. The mean error in position was 0.45 arcsec. This means that the mean error in our astrometry is smaller than a pixel and

¹IRAF is distributed by the National Optical Astronomy Observatories, which are operated by the Association of Universities for Research in Astronomy, Inc., under cooperative agreement with the National Science Foundation.

will *not* contribute significantly towards incorrect optical counterpart identification. We tested the reliability of the astrometry by recomputing the plate solution after omitting a few astrometric stars. The plate solutions were not significantly affected by this procedure.

8.2.5 Source identification and photometry

The reimaging camera optics in our setup are such that vignetting effects are quite serious towards the edge of the CCD. About 45% percent of the total area on the chip is significantly affected by the vignetting. The vignetting effects are complete at the edges but there is a small zone on the CCD where partial vignetting occurs. In order to maintain a uniform completeness limit for our source identification and photometry, we excluded the vignetted regions from further analysis.

In order to ensure that criteria for identification were uniform and objective within each field and across different fields, we used version 2.0.21 of the SExtractor package (Bertin & Arnouts 1996) for automated source identification and photometry. As SExtractor is primarily intended to process large amounts of survey data, special attention has been paid to speed and robustness in the extraction of objects in the image, regardless of their shape and size. In SExtractor the complete analysis of the image is carried out in seven steps: estimation of the (local) sky background, thresholding, deblending, filtering of detections, photometry, classification and finally catalog output. We did not use the image filtering and object classification capabilities of SExtractor in this work. A useful feature of this software is the robust deblending of overlapping extended objects. This feature is particularly useful for our data because we have several identifications which are composed of overlapping (interacting? merging?) extended sources which are correctly deblended by SExtractor. We confirmed that the deblending done by SExtractor was correct by a detailed visual examination of three fields. An optical source was treated as an optical counterpart of a FIRST source if:

1. at least 10 connected pixels each had a count above the local background higher than 5σ of the background AND
2. the barycentre of the optical source was less than 6 arcsec away from the centre of the FIRST source.

These criteria were arrived at iteratively after several SExtractor runs on a representative field, by changing input parameters to SExtractor, until the optical counterparts detected by SExtractor substantially matched the identifications by visual inspection.

For about 10% of FIRST sources we found more than one (usually two) optical counterparts within 6 arcsec. In such situations, we chose the brighter optical source as the optical counterpart.

The operational procedure used for obtaining the optical counterpart was as follows. A subsection of each frame that contained only the unvignetted region was constructed. The radio position in J2000 coordinates was obtained from the most recent (July 29, 1999) version of the FIRST radio source catalog (available at <http://sundog.stsci.edu/>). Using the astrometric plate solution of the image subsection, each FIRST position in sky coordinates was converted to pixel coordinates using the *sky2xy* program from the *wcstools* package (Mink 1998). Off-image sources were discarded. The remaining pixel coordinates were written to the ASSOC_DATA file used by the SExtractor software. For each field, the sources in the optical image were then detected using SExtractor and matched with the ASSOC_DATA list of FIRST sources in the ASSOC_DATA file.

FK4 precession formulae have not yet been implemented in SExtractor and astrometry of optical identifications performed by it is therefore slightly inaccurate. To get accurate astrometric positions we recomputed the sky coordinates of the optical identification using pixel coordinates from SExtractor and the *xy2sky* program from the *wcstools* package. The coordinates of the optical identifications have been listed in Table 8.3.

Instrumental magnitudes were determined using the MAG_BEST algorithm in SExtractor. The following procedure is used by SExtractor to give the best estimate of the total magnitude of an object. An adaptive aperture method based on Kron's *first moment* algorithm (Kron 1980) is used unless a neighbor is suspected to bias the magnitude by more than 0.1 magnitude. In these cases (which are not uncommon in deep fields such as ours) the corrected isophotal magnitude based on formulae from Maddox, Efstathiou & Sutherland (1990) is used. Tests on simulated CCD images by Bertin & Arnouts (1996) have shown that the MAG_BEST algorithm leads to a mean zero-point

offset of 0.06 magnitude for galaxies and 0.03 magnitudes for stars with less than 2% rms variation. These zero-point offsets are considerably smaller than the error bars on the magnitudes of almost all of our identifications.

8.2.6 Photometric calibration with standard stars

The source photometry was tied to the *UBVRI* system defined by the stars in Landolt (1983) by observing standard area fields SA 92, SA 98 and SA113 from Landolt (1992).

The standard fields were observed 3-6 times each night over the same range of airmass corresponding to the fields covered during that night. Typically 10 standard stars in each special area field were used to derive an extinction coefficient for the night and a zero point transformation for each field. We have only applied a first order atmospheric extinction correction to the magnitude to get the values reported here. Galactic extinction corrections have not been applied. Calibrated photometry (along with errors) for our identifications is presented in Table 8.3.

Table 8.3 lists each FIRST source for which we found an optical counterpart. The contents of the table are:

Column 1: The IAU designation for the FIRST source in the form Jhhmmss.s+ddmms. The coordinates are equinox J2000.0 and are truncated (not rounded).

Columns 2, 3: Peak and integrated flux density in mJy as listed in the FIRST source catalog.

Columns 4, 5: Right Ascension and Declination of the optical identification for the equinox J2000.0

Columns 6, 7, 8: Filter, magnitude in that filter and error in magnitude measurement respectively.

Column 9: Separation between the centers of the optical and radio sources in arcsec.

Column 10: The object class of the optical identification estimated visually from V band CCD images. More morphological information is provided in the next chapter:

C: Galaxy in a rich environment.

G: Galaxy in a sparse environment.

F: Extended source but too faint and/or small for morphological classification.

S: Stellar source (very likely a quasar) in a sparse galactic environment.

SC: Stellar source (very likely a quasar) in a rich galactic environment, possibly in a cluster.

Table 8.3: Optical counterparts of FIRST survey sources. The parameters listed in the various columns are described in the text.

FIRST IAU Desn.	F_{peak} (mJy)	F_{int} (mJy)	$\alpha_{optical}(2000)$ (hh:mm:ss.ss)	$\delta_{optical}(2000)$ (dd:mm:ss.s)	F.	m	Δm	Sep (arcsec)	Morph. class
J000024.97-005050.6	13.40	13.55	00:00:24.978	-00:50:50.66	V	22.40	0.26	4.3	G
J000049.30-005042.9	14.28	16.25	00:00:49.309	-00:50:42.90	V	20.29	0.08	0.8	C
J000113.44-005935.2	3.58	3.76	00:01:13.448	-00:59:35.21	V	19.15	0.05	0.3	C
J000117.85-005611.6	2.63	3.33	00:01:17.852	-00:56:11.67	V	19.12	0.06	0.7	G
J000117.85-005611.6	2.63	3.33	00:01:17.852	-00:56:11.67	V	20.97	0.13	5.2	G
J010213.42-005153.3	1.07	2.75	01:02:13.424	-00:51:53.35	V	13.80	0.02	4.9	S
J010227.34-004836.6	1.04	2.28	01:02:27.341	-00:48:36.65	V	12.52	0.04	1.4	G
J010227.34-004836.6	1.04	2.28	01:02:27.341	-00:48:36.65	V	13.17	0.07	5.8	G
J010230.08-004343.6	2.32	4.11	01:02:30.081	-00:43:43.65	V	11.43	0.01	5.9	G
J010236.57-005007.6	2.56	6.10	01:02:36.579	-00:50:07.69	V	9.50	0.00	2.4	C
J010237.85-005012.6	5.47	17.41	01:02:37.856	-00:50:12.62	V	11.41	0.02	5.4	C
J010242.42-005032.9	7.19	11.82	01:02:42.429	-00:50:32.98	V	9.35	0.01	3.0	C
J010252.33-005359.0	2.09	1.27	01:02:52.335	-00:53:59.05	V	10.60	0.00	1.7	G
J010255.02-005202.1	4.04	4.02	01:02:55.027	-00:52:02.14	V	12.71	0.01	1.9	S
J015040.83-003802.5	4.18	4.00	01:50:40.832	-00:38:02.52	V	22.78	0.31	2.9	G
J015105.84-003426.0	1.76	4.15	01:51:05.846	-00:34:26.01	V	20.71	0.10	3.1	S
J015109.61-002119.2	1.91	3.53	01:51:09.613	-00:21:19.27	V	20.71	0.10	2.4	C
J015109.61-002119.2	1.91	3.53	01:51:09.613	-00:21:19.27	V	21.78	0.16	4.9	C
J015127.94-002217.3	1.23	0.65	01:51:27.940	-00:22:17.30	V	18.23	0.03	2.1	F
J015127.94-002217.3	1.23	0.65	01:51:27.940	-00:22:17.30	V	20.65	0.11	5.2	F
J015915.09-014553.2	1.31	1.56	01:59:15.096	-01:45:53.24	V	19.00	0.05	3.4	G
J015919.14-013311.9	1.42	1.82	01:59:19.147	-01:33:11.90	V	18.09	0.04	2.4	C
J015919.14-013311.9	1.42	1.82	01:59:19.147	-01:33:11.90	V	21.37	0.16	5.2	C
J015920.59-014625.7	11.37	11.41	01:59:20.594	-01:46:25.78	V	21.54	0.14	3.1	G
J015925.24-014553.7	1.10	1.58	01:59:25.241	-01:45:53.72	V	21.25	0.12	5.2	G
J015925.24-014553.7	1.10	1.58	01:59:25.241	-01:45:53.72	V	22.29	0.20	2.1	G
J015928.42-013914.2	1.43	0.99	01:59:28.426	-01:39:14.29	V	19.59	0.06	2.0	G
J015943.67-013321.2	2.61	3.57	01:59:43.671	-01:33:21.25	V	23.64	0.40	4.9	F
J025947.83-005041.0	1.46	1.21	02:59:47.834	-00:50:41.08	R	18.61	0.04	3.2	G
J025947.83-005041.0	1.46	1.21	02:59:47.834	-00:50:41.08	V	19.64	0.06	3.2	G

Optical counterparts of FIRST survey sources (continued)

FIRST IAU Desn.	F_{peak} (mJy)	F_{int} (mJy)	$\alpha_{optical}(2000)$ (hh:mm:ss.ss)	$\delta_{optical}(2000)$ (dd:mm:ss.s)	F.	m	Δm	Sep (arcsec)	Morph. class
J025954.83-005401.2	2.80	3.24	02:59:54.835	-00:54:01.22	R	22.71	0.24	3.9	S
J030007.47-005200.2	1.05	1.51	03:00:07.474	-00:52:00.27	R	20.71	0.11	2.5	S
J030007.47-005200.2	1.05	1.51	03:00:07.474	-00:52:00.27	V	22.39	0.25	2.5	S
J030238.04-012116.4	3.57	4.16	03:02:38.048	-01:21:16.45	R	20.26	0.10	4.0	SC
J030238.04-012116.4	3.57	4.16	03:02:38.048	-01:21:16.45	V	22.45	0.31	4.0	SC
J030240.47-012055.3	1.43	2.00	03:02:40.475	-01:20:55.36	R	21.79	0.20	2.1	C
J030240.47-012055.3	1.43	2.00	03:02:40.475	-01:20:55.36	V	22.23	0.27	2.1	C
J030251.21-011425.5	4.22	4.40	03:02:51.215	-01:14:25.57	R	20.41	0.09	2.2	G
J030251.21-011425.5	4.22	4.40	03:02:51.215	-01:14:25.57	V	22.55	0.25	2.2	G
J030255.03-011448.6	1.19	0.80	03:02:55.030	-01:14:48.64	R	22.00	0.19	2.5	S
J030255.03-011448.6	1.19	0.80	03:02:55.030	-01:14:48.64	V	24.00	0.45	2.5	S
J030256.83-011722.5	2.71	3.48	03:02:56.837	-01:17:22.58	R	23.23	0.35	1.8	S
J030300.46-012223.2	1.10	3.58	03:03:00.466	-01:22:23.29	R	16.54	0.02	3.1	G
J030300.46-012223.2	1.10	3.58	03:03:00.466	-01:22:23.29	V	16.36	0.01	3.1	G
J030334.49-011406.0	3.24	3.14	03:03:34.498	-01:14:06.00	R	14.14	0.00	3.1	S
J030334.49-011406.0	3.24	3.14	03:03:34.498	-01:14:06.00	V	14.88	0.01	3.5	S
J030338.68-011432.5	1.12	1.47	03:03:38.684	-01:14:32.50	R	21.32	0.15	2.9	S
J030338.68-011432.5	1.12	1.47	03:03:38.684	-01:14:32.50	V	22.52	0.28	2.9	S
J211931.08-003051.8	1.92	1.63	21:19:31.087	-00:30:51.81	V	19.83	0.11	1.3	G
J212030.12-002555.9	23.83	24.51	21:20:30.128	-00:25:55.90	V	19.35	0.06	5.9	F
J220111.74-011510.2	45.79	48.27	22:01:11.748	-01:15:10.24	V	20.87	0.10	4.8	SC
J220113.53-011051.3	2.85	3.45	22:01:13.531	-01:10:51.39	V	22.88	0.26	0.6	S
J232933.10-003020.3	36.75	37.76	23:29:33.105	-00:30:20.35	R	23.21	0.36	3.3	S
J232956.02-002740.2	1.69	2.85	23:29:56.025	-00:27:40.24	R	20.63	0.10	2.0	G
J232956.02-002740.2	1.69	2.85	23:29:56.025	-00:27:40.24	V	21.08	0.12	2.0	G
J232959.30-003242.1	1.41	2.80	23:29:59.307	-00:32:42.12	R	23.09	0.30	5.7	S
J232959.30-003242.1	1.41	2.80	23:29:59.307	-00:32:42.12	V	23.54	0.37	5.7	S
J233001.27-002617.5	2.02	1.95	23:30:01.277	-00:26:17.55	R	21.36	0.13	1.5	S
J233001.27-002617.5	2.02	1.95	23:30:01.277	-00:26:17.55	V	22.51	0.22	1.5	S
J233002.37-003617.0	1.72	2.42	23:30:02.378	-00:36:17.06	R	18.62	0.04	1.2	G
J233002.37-003617.0	1.72	2.42	23:30:02.378	-00:36:17.06	V	18.83	0.04	1.2	G
J233002.97-002247.1	7.93	27.81	23:30:02.978	-00:22:47.11	R	21.61	0.15	4.5	G
J233002.97-002247.1	7.93	27.81	23:30:02.978	-00:22:47.11	V	24.10	0.45	4.5	G
J233034.92-002503.9	1.58	1.65	23:30:34.921	-00:25:03.98	R	19.34	0.06	0.9	C
J233034.92-002503.9	1.58	1.65	23:30:34.921	-00:25:03.98	V	19.94	0.07	0.9	C

8.3 Finding charts for our optical identifications

Figure 8.1 presents finding charts for all sources identified as the optical counterparts of FIRST sources using the criteria listed in subsection 8.2.5. Each image here is a 128×128 pixel subsection of a larger CCD frame with north at the top and east to the left. Each image covers about 1.66 arcmin on a side. The radio source is placed at the central pixel in all cases. The centroid of the optical identification is marked by the two horizontal and vertical tick marks. These charts were constructed from images in the V band.

Notes about the morphology of each identification and attempts at bulge disk decomposition are described in the following chapter.

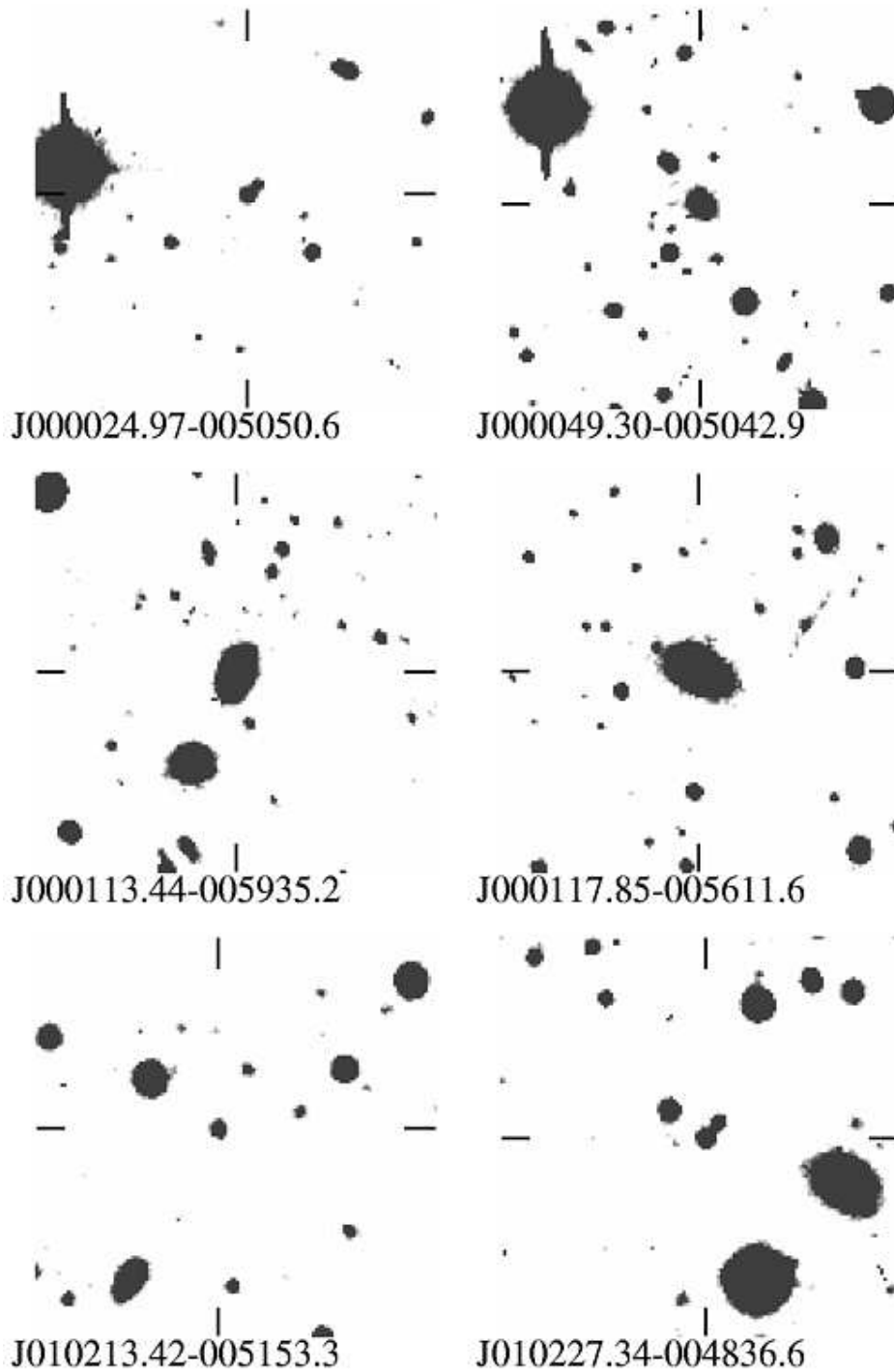


Figure 8.1: Finding charts for each FIRST survey source for which we have an optical identification. Each chart is a V band CCD image with north at the top and east to the left. The field of view is 128×128 pixels ($\sim 50 \times 50$ arcsec). The IAU name is marked at the bottom of each chart. The radio source is located at the center of the chart. The barycentre of the optical identification is marked by the intersection of the four tick marks at the edge of the field.

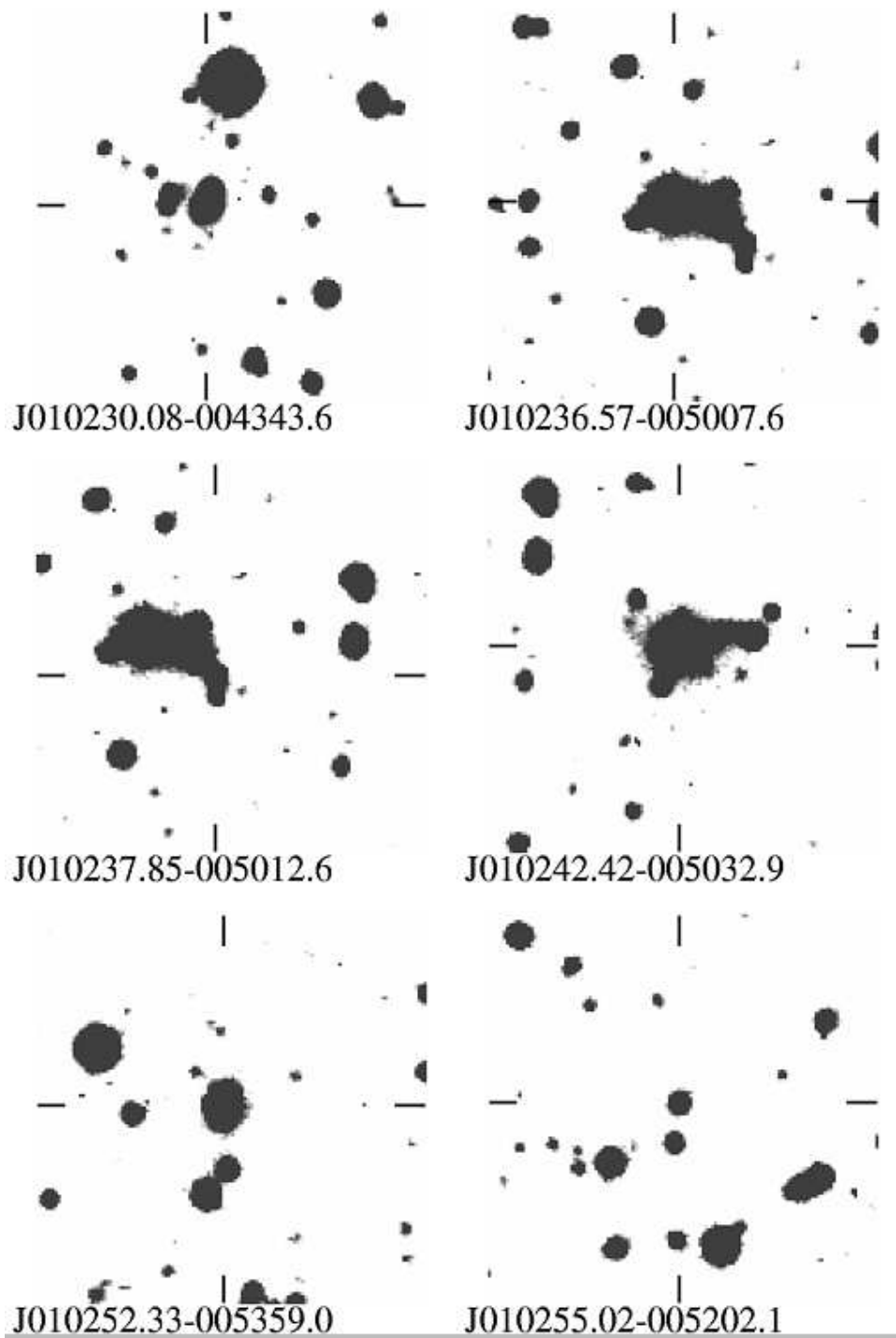


Figure 8.1: continued...

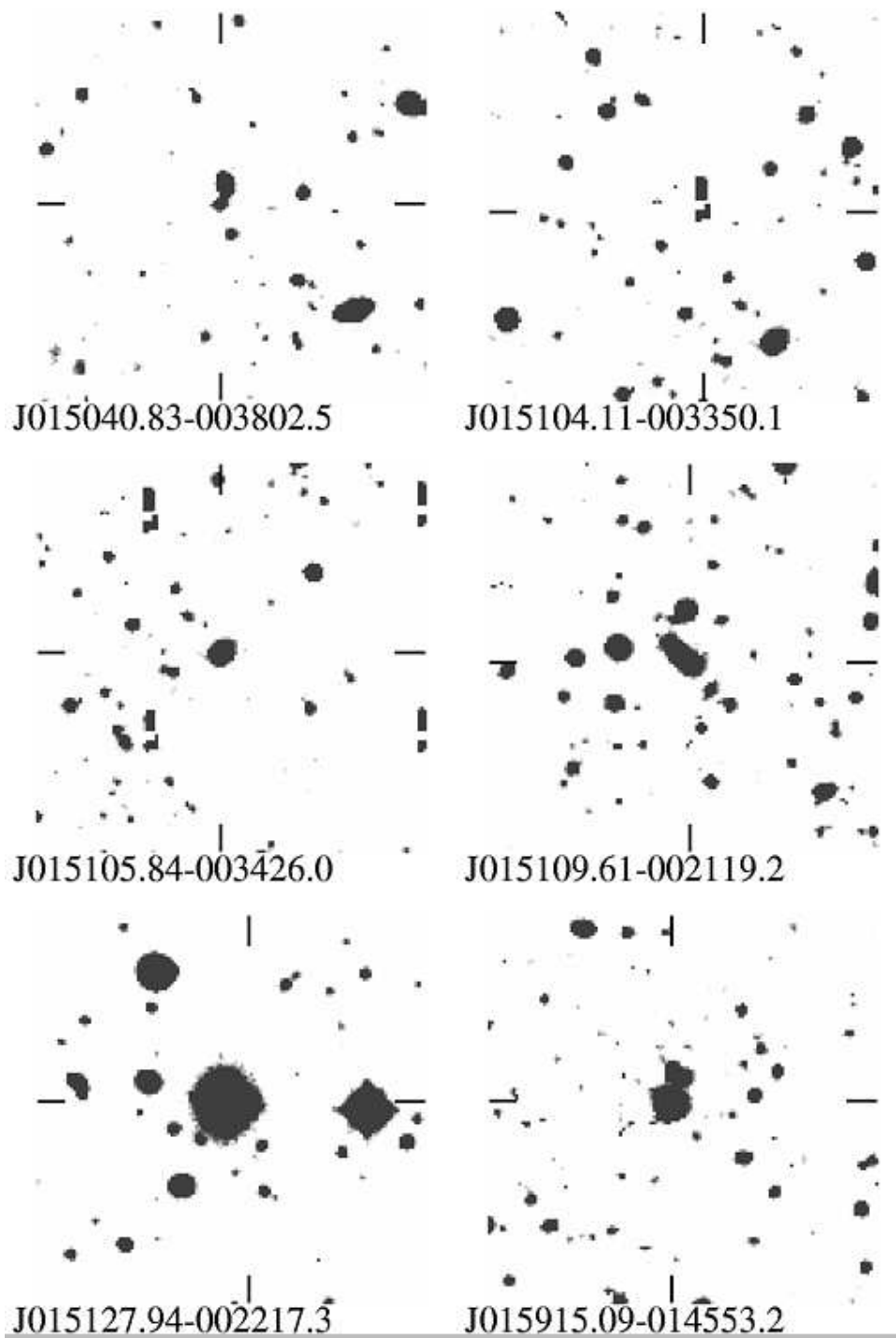


Figure 8.1: continued...

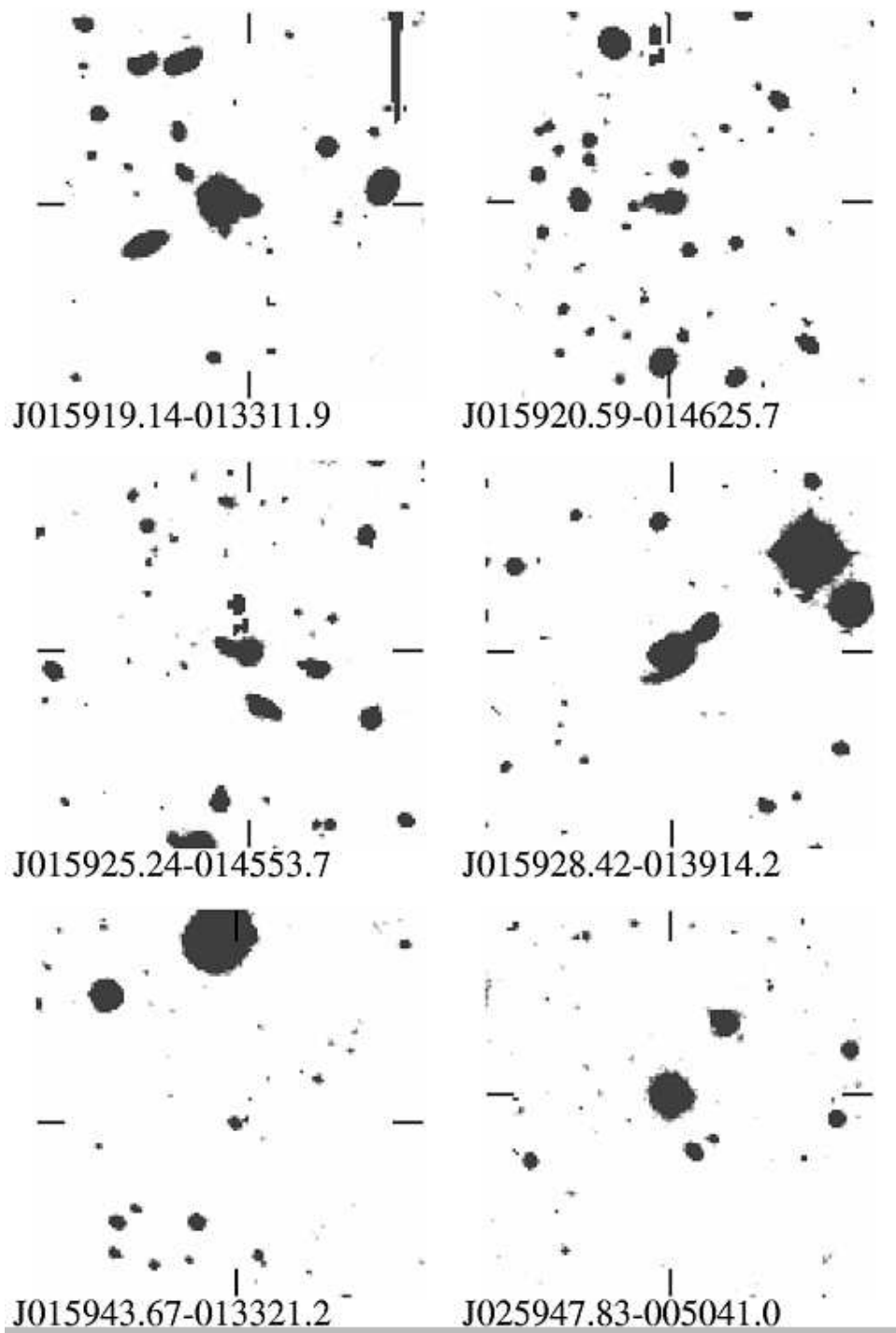


Figure 8.1: continued...

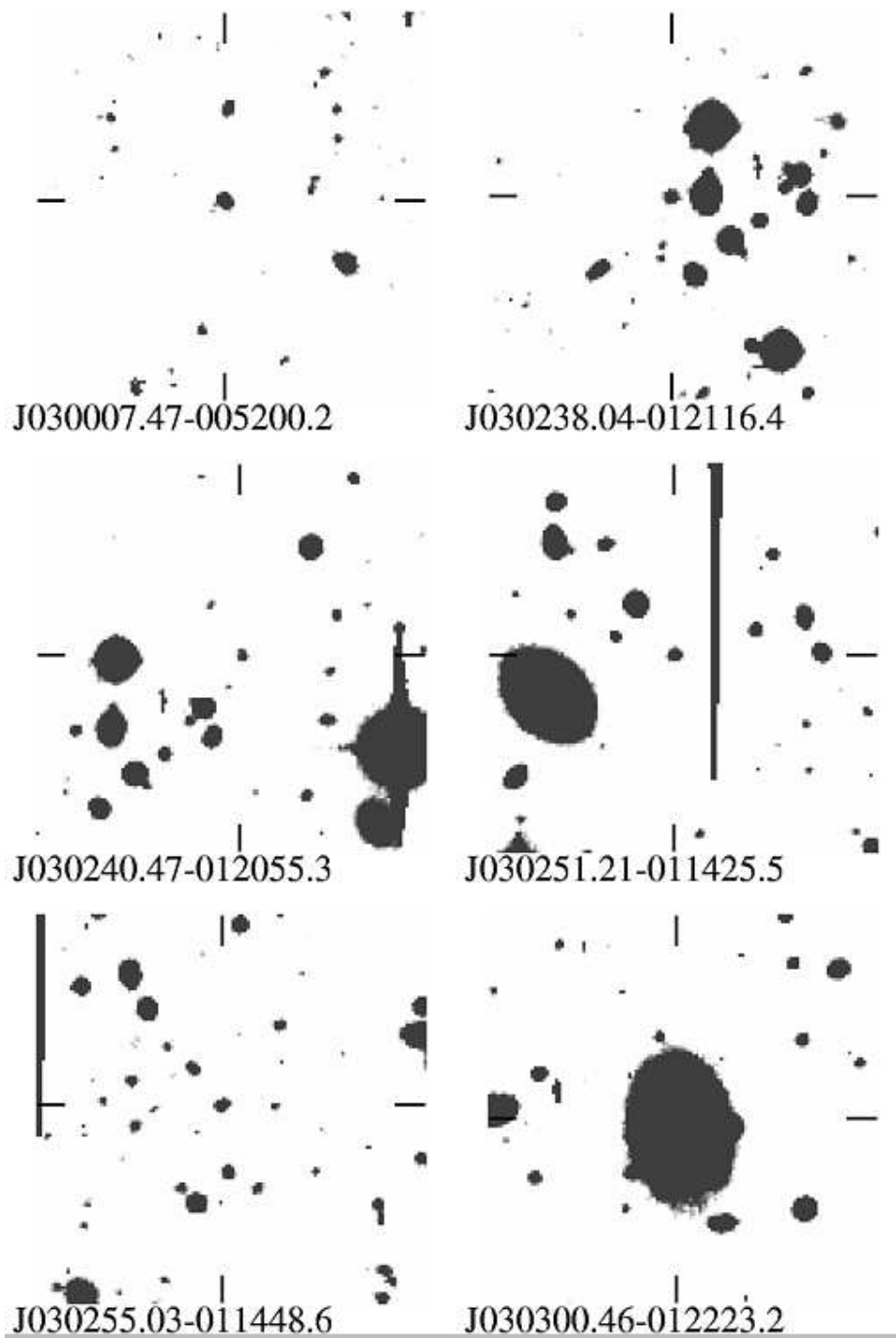


Figure 8.1: continued...

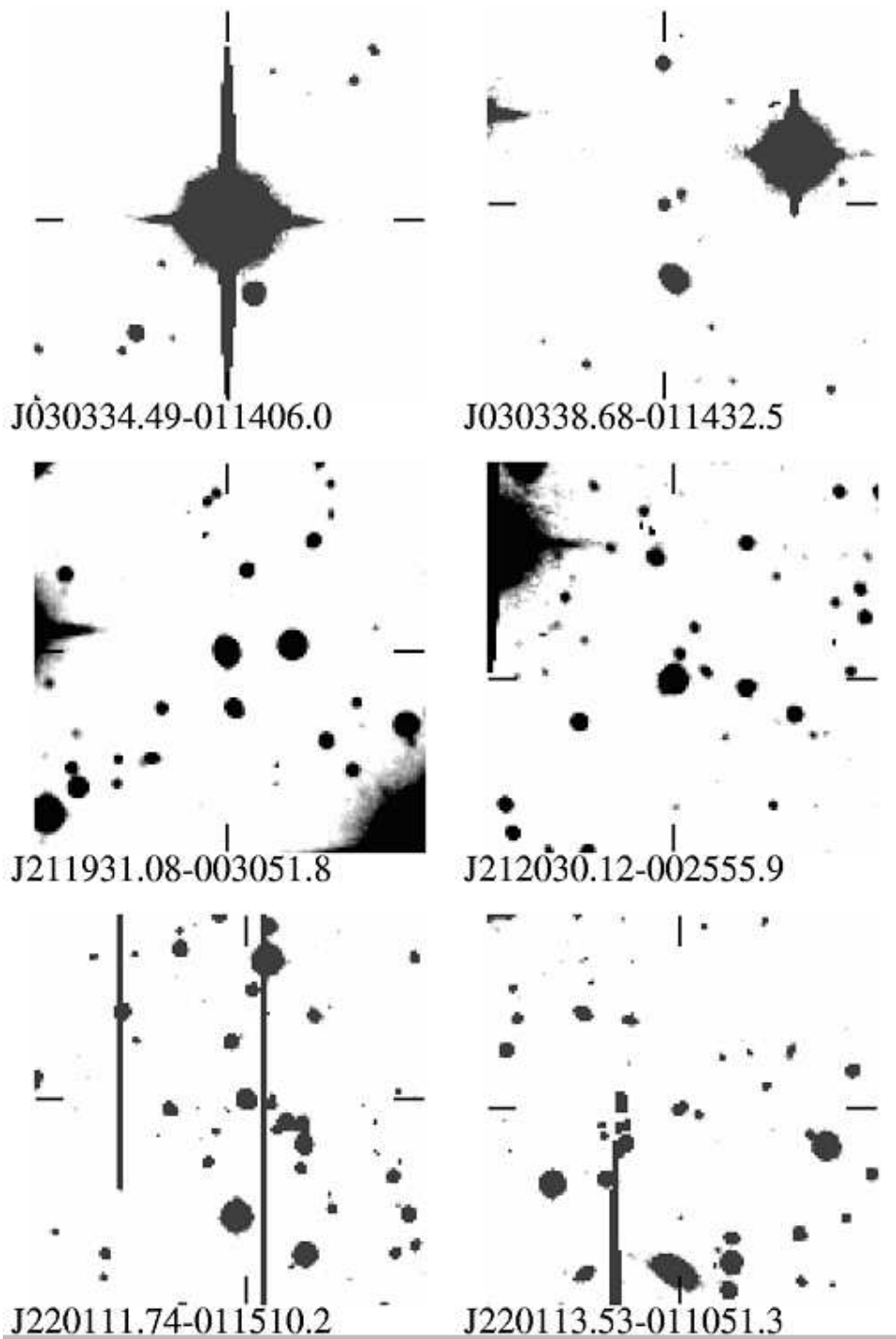


Figure 8.1: continued...

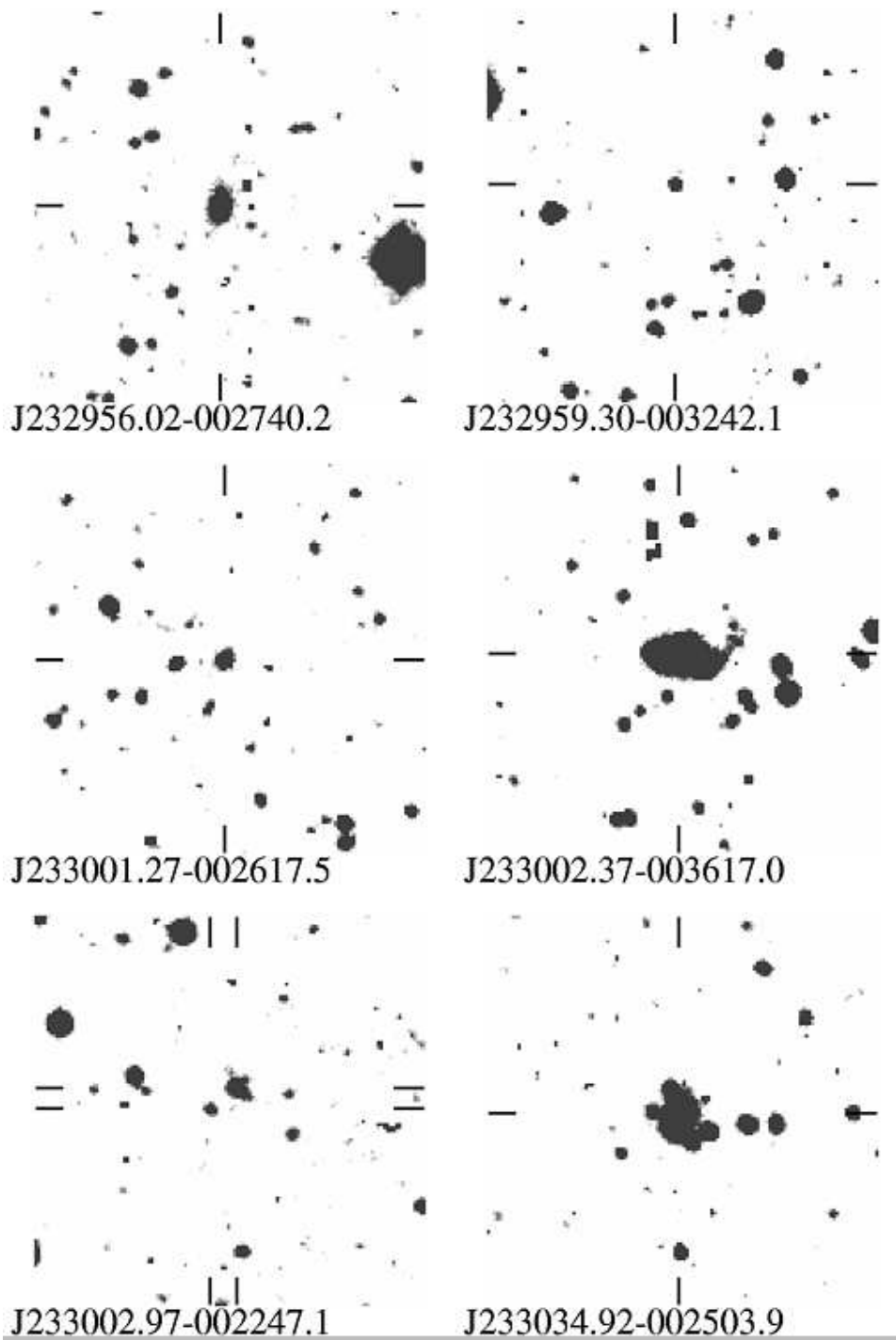


Figure 8.1: continued...

Chapter 9

Optical imaging of low flux radio sources: morphology and decomposition

This chapter presents morphological descriptions of the optical identifications of FIRST radio sources presented in Chapter 8. Some simple correlations and our attempts at two dimensional bulge disk decomposition of the extended sources in our identification set are also described.

9.1 Morphology of the identifications

Here we give brief notes about the morphologies of the optical identifications based on visual inspection of the images. Several sources were also detected on the vignetted regions of the CCD. Since their photometry is unreliable we have not listed them in Table 8.3. However, we present morphological information about such sources in this section. They may be identified by their FIRST designation which is printed in *italics*.

Sources listed in the NASA Extragalactic database (NED), (excepting NVSS sources, of which there are several) which are coincident with our optical identifications are noted:

J000024.97-005050.6: Small galaxy with a clear double nucleus. Radio emission does not coincide with either nucleus.

J000027.87-010235.2: Small galaxy with a fainter companion about 5 arcsec away.

J000049.30-005042.9: Elliptical galaxy with possibly non-nuclear radio emission. At least three other smaller galaxies within 10 arcsec.

J000113.44-005935.2: Disky galaxy with asymmetric isophotes (NED: Ultraluminous IR galaxy: IRAS 23586-0116). Nuclear radio emission. One faint galaxy within 10 arcsec, about half a dozen faint and one bright galaxy within 30 arcsec.

J000117.85-005611.6: Elliptical galaxy with nuclear emission.

J010213.42-005153.3: Stellar object. Extended radio emission to one side.

J010227.34-004836.6: Double nucleus galaxy with another galaxy about 10 arcsec away.

J010230.08-004343.6: Double nucleus galaxy with another galaxy about 5 arcsec away. Radio emission is non-nuclear.

J010236.57-005007.6: A quintet of merging galaxies? Radio emission from the brightest member.

J010237.85-005012.6: Radio emission associated with faintest member of the quintet in J010236.57-005007.6

J010242.42-005032.9: A four galaxy system with radio emission associated with the brightest galaxy.

J010252.33-005359.0: Bright galaxy with nuclear radio emission.

J010255.02-005202.1: Stellar source.

J010318.51-005350.4: Elliptical with two other galaxies about 10 arcsec away.

J015040.83-003802.5: Close pair of galaxies. Radio emission from the fainter southern member of the pair.

J015105.84-003426.0: Stellar source.

J015109.61-002119.2: Merging pair of faint galaxies. About ten faint galaxies within 30 arcsec.

J015127.94-002217.3: Radio emission from small (partially obscured?) galaxy very close to a large elliptical.

J015153.30-002850.2: Stellar source.

J015835.38-014516.6: Radio emission envelops a faint galaxy with irregular morphology.

J015915.09-014553.2: Elliptical galaxy with distorted isophotes.

J015919.14-013311.9: Two galaxies within 6 arcsec. Both galaxies are probably ellipticals. 5 galaxies within 30 arcsec.

J015920.59-014625.7: Small galaxy with distorted isophotes.

J015925.24-014553.7: Two galaxies merging. Radio emission in between the two galaxy centers.

J015928.42-013914.2: Galaxy with a asymmetric spiral arm like structure. Another galaxy about 7 arcsec away.

J015943.67-013321.2: Faint galaxy.

J015952.11-014931.5: Elliptical with a companion about 10 arcsec away.

J025947.83-005041.0: Elliptical galaxy with nuclear emission from core.

J025954.83-005401.2: Stellar source.

J030007.47-005200.2: Stellar source.

J030027.79-005608.8: Faint galaxy coincident with radio source, that just fails to meet our criteria for an optical detection. A stellar source 5 arcsec away.

J030028.88-010350.2: Small galaxy.

J030238.04-012116.4: Stellar source in a rich galaxy environment.

J030240.47-012055.3: Radio emission between two small circular galaxies. 5 galaxies within 30 arcsec.

J030251.21-011425.5: Small galaxy. Large bright elliptical 45 arcsec away.

J030255.03-011448.6: Stellar object.

J030256.83-011722.5: Stellar object nearly obscured by a brighter galaxy.

J030300.46-012223.2: Large galaxy with a double nucleus. (NED: MRK 1403 - UV Excess system)

J030334.49-011406.0: Bright saturated star. Only non extra-galactic source amongst all our identifications.

J030338.68-011432.5: Radio emission between two stellar sources.

J030349.15-010612.9: Galaxy with distorted isophotes, radio emission from non-nuclear regions. (NED: NGC 1194 a Seyfert 1 galaxy, also IR source IRAS 03012-0117)

J211931.08-003051.8: Elliptical galaxy.

J211942.91-002042.6: Small faint galaxy.

J212030.12-002555.9: Small faint galaxy. A brighter elliptical 5 arcsec away.

J220022.65-010856.8: Stellar source.

J220111.74-011510.2: Stellar source. About 10 faint galaxies within 30 arcsec.

J220113.53-011051.3: Stellar source.

J232921.39-003239.5: Stellar source.

J232933.10-003020.3: Faint stellar source.

J232956.02-002740.2: Galaxy with distorted isophotes.

J232959.30-003242.1: Faint stellar source.

J233001.27-002617.5: Stellar source.

J233002.37-003617.0: Disky galaxy with close (merged?) companion which seems highly distorted.

J233002.97-002247.1: Small galaxy with distorted isophotes. Radio emission does not coincide with the galaxy.

J233030.94-002354.0: Faint radio source. does not coincide with galaxy.

J233031.46-002354.0: Faint radio source. associated with J233030.94-002354.0

J233034.92-002503.9: Complicated (merging?) system of up to five galaxies. Difficult to determine with which one the radio source is associated.

Many of the identifications in rich environments (of which there are several) are likely to be close associations of galaxies in the cores of distant clusters.

9.2 Some statistical correlations

We now investigate three basic statistical indicators: the identification rate as a function of radio and of optical flux density, and the correlation between optical and radio fluxes of the detections.

9.2.1 Identification rate as a function of radio flux

In Figure 9.1 we plot the detection fraction as a function of integrated and peak flux densities at 1.4 GHz in the upper and lower panels respectively. In any flux bin the detection fraction is simply the ratio of FIRST sources with an optical identification, to the total number of FIRST sources in the field. Note that we only use the unvignetted regions of our CCD images to compute both these numbers. The error bar shown is the $\pm 1\sigma$ deviation about the detected fraction for a random binomial distribution in the detection fraction. The number of sources with integrated flux density $\log F_{int} > 1$ is small and consequently the errors are so large that the weak correlation between detection fraction and $\log F_{int}$ is not very reliable. However for $\log F_{int} < 1$ a clear trend is visible. For $0.3 < \log F_{int} < 1.0$, the detection fraction increases as flux decreases. For $\log F_{int} < 0.3$, there seems to be a decrease in detection fraction. A similar trend can be seen in the lower panel of Figure 9.1 where we plot the peak radio flux density F_{peak} of the FIRST source.

It is likely that the turnaround in radio detection fraction seen at $\log F_{int} = 0.3$, corresponding to $F_{int} \sim 2$ mJy occurs due to increasing dominance of the *blue* galaxy population below this flux. The blue galaxy population probably has a lower detection probability because its radio emission is very weak. Our hypothesis can be tested by studying the colors of galaxies as a function of radio flux. The limited color information available to us at the present time does not permit us to perform a statistically significant comparison.

9.2.2 Identification rate as a function of optical flux

In Figure 9.2 we plot the detection fraction as a function of apparent V band magnitude. The bin size used is one magnitude. For each bin, the detection fraction is the ratio of the number of FIRST sources with optical counterparts to the total number of optical sources in the field as extracted by SExtractor. The error bars shown are computed as in Figure 9.1. The selection criteria used to select the optical sources without the FIRST identifications are the same as in subsection 8.2.5. No systematic trends in the detection fraction are visible.

9.2.3 Radio and optical flux distributions

In Figure 9.3 we plot the integrated radio flux of the identifications as a function of their total V band magnitude. Note that both optical and radio fluxes have been plotted on a logarithmic scale. We have used different symbols to indicate the morphological class of the identification. Filled stars indicate starlike sources in a sparse field while open stars are stellar sources in a rich environment. Galaxies in sparse environments are denoted by triangles while galaxies in rich environments are represented by filled squares. Extended sources that are too small and/or too faint to be reliably classified as galaxies are indicated by diamonds. The vertical and horizontal lines divide the radio-optical flux space into 4 quadrants. Each quadrant spans an equal range (in logarithmic space) of radio and optical flux.

As would be expected, the highest density of sources is found in the bottom right quadrant of the diagram which corresponds to the lowest radio and optical fluxes. As discussed in subsection 6.3.2, the sources in the top right quadrant will mostly correspond to distant galaxies and quasars, while the sources in the bottom left quadrant will be dominated by nearby galaxies. The latter are dominated by sources in sparse environments, possibly an effect of the low redshift and consequent large angular size of these sources.

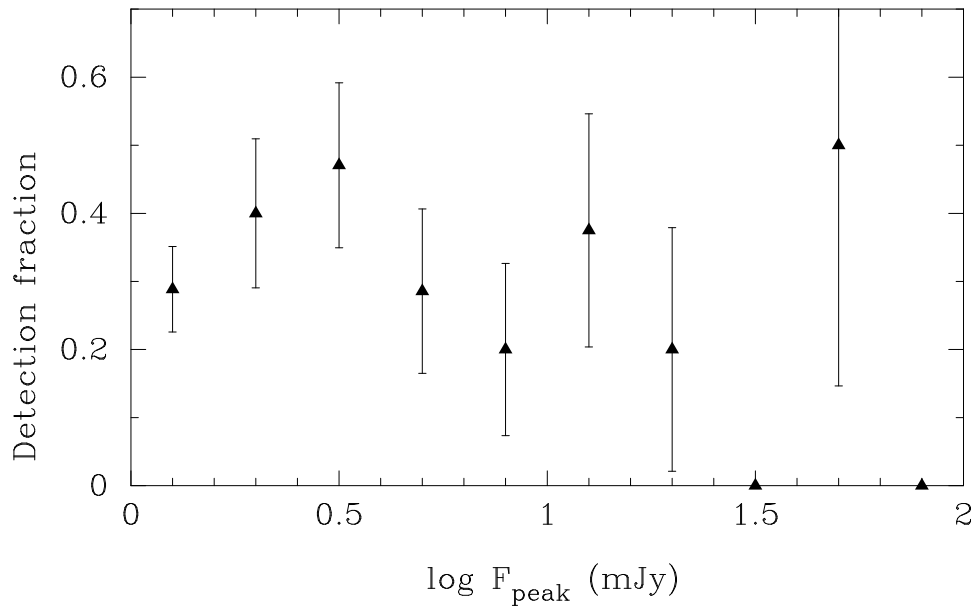
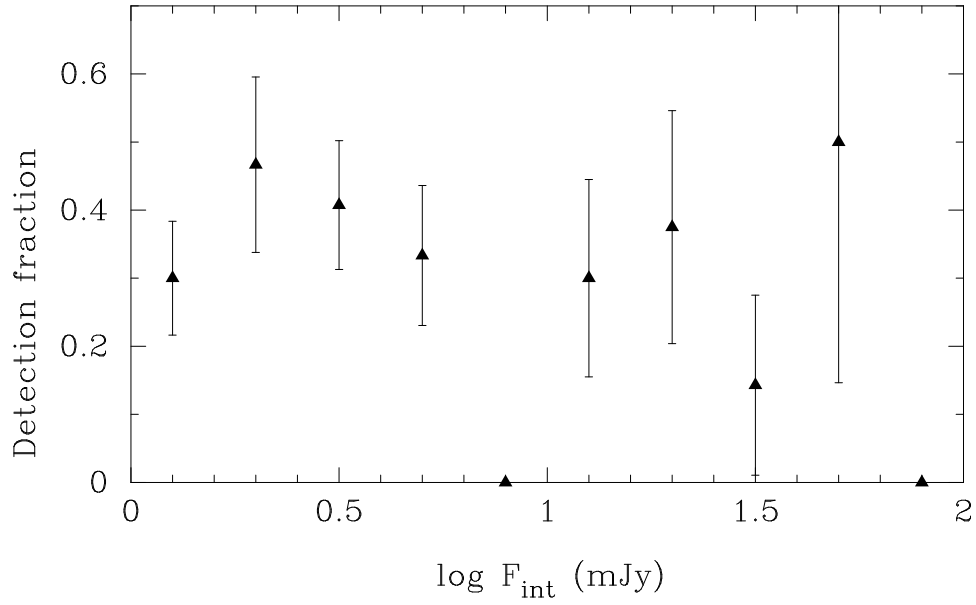


Figure 9.1: Detection fraction as a function of integrated and peak radio flux densities. The error bar shown is the standard deviation for a random binomial distribution in the detection fraction.

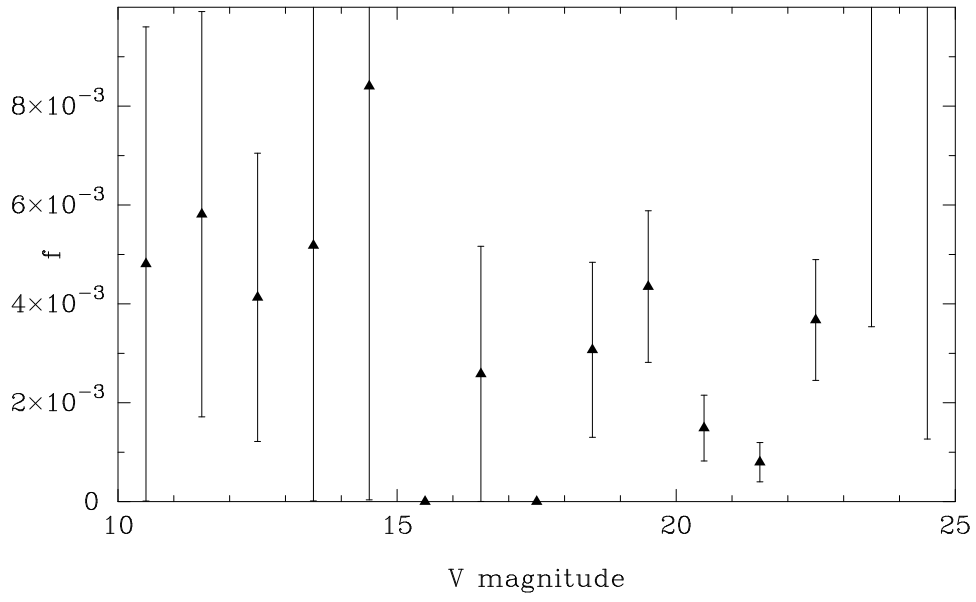


Figure 9.2: Detection fraction as a function of total V band magnitude. The errors were obtained as in Figure 9.1.

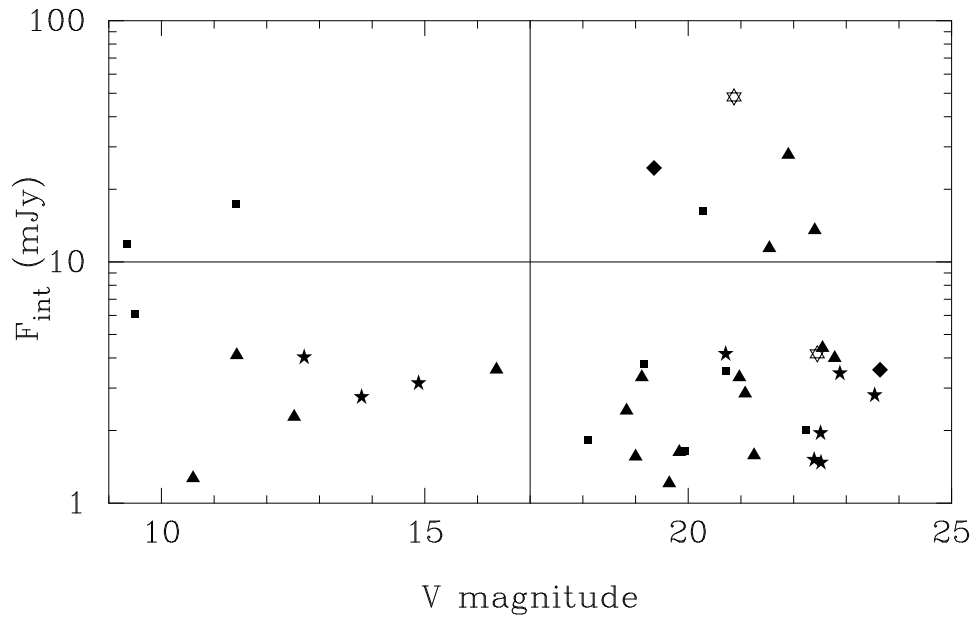


Figure 9.3: Integrated radio flux of the identifications as a function of V band total magnitude. The Y-axis has been plotted on a logarithmic scale. See the text for an explanation of the various symbols used.

9.3 Bulge disk decomposition of bright identifications

9.3.1 Modeling galaxy light distributions

As discussed in Chapter 7, the luminosity profile of a typical spiral or S0 galaxy most often contains two components, a spheroidal bulge and a circular disk. If the galaxy possesses an active nucleus, then a high central point intensity may also be present. The projected bulge intensity profile is usually represented by an $r^{1/4}$ law (de Vaucouleurs 1948), where r is the distance along the major axis. In recent times, a generalized $r^{1/n}$ law is increasingly being used. The intensity profile of the disk component is usually represented by an exponential (Freeman 1970). These profiles are entirely empirical, and have not been derived from a formal physical theory. However, numerical simulations in simplified situations such as those by van Albada (1982) have been able to recreate $r^{1/4}$ profiles for the bulge.

The photometric decomposition of galaxies into bulge and disk and the extraction of the parameters characterizing these components has been approached in a number of ways. Early attempts at such decomposition assumed that the disk would be the dominant component in the outer regions of galaxies and that the bulge would dominate the inner regions. Disk and bulge parameters were extracted by Kormendy (1977) and Burstein (1979) by fitting for each component separately in the region in which it was dominant. Kent (1985) first introduced simultaneous fitting of bulge and disk components to major and minor axis light profiles of galaxies obtained by fitting ellipses to the isophotes of CCD images. One major advantage of Kent's method is its ability to extract galaxy parameters in a model independent way provided that the disk and the bulge have very different ellipticities. His method works well for edge on galaxies where the ellipticity of the disk is generally much higher than the ellipticity of the bulge. Schombert and Bothun (1987) employed a similar technique for initial estimation of bulge and disk parameters of simulated galaxy profiles, with standard laws describing the bulge and the disk with simulated noise. These parameters were then used as initial input to a χ^2 fitting procedure. Tests on simulated profiles indicated good recovery of both bulge and disk parameters¹. These techniques of fitting standard laws to a 1-D intensity profiles extracted from galaxy images were critically examined by Knapen and van der Kruit (1991). They found that even for the same galaxy different authors derive disk scale length values with an average scatter as high as 23%. Such large uncertainty in the extracted structural parameters is a hindrance in the study of structure, formation and evolution of the bulge and disk of galaxies. Accurate, reliable determination of parameters is a prerequisite for differentiating between competing galaxy formation and evolution models. The conventional one dimensional technique is also limited because it assumes 1-D image profiles can be uniquely extracted from galaxy images. This is not possible if a strong but highly inclined disk is present.

Andredakis, Peletier and Balcells (1995, henceforth APB95) used a 2-D generalization of Kent's method to fit K-band luminosity profiles of bulges of a sample of disk galaxies with morphological types ranging from S0 to Sbc. They used azimuthally averaged profiles from various radial cuts of the image of the galaxy. An important innovation in this paper was the use of a $r^{1/n}$ law for the bulge. A full two dimensional technique which uses the entire galaxy image rather than one dimensional profiles was proposed by Byun and Freeman (1995, henceforth BF95). A similar approach was used by R. S. de Jong to extract parameters for a sample of 86 face on disc dominated galaxies (de Jong 1996, henceforth DJ96). We have independently developed a 2-D decomposition technique and code called *fitgal*, similar to the one employed in BF95. Extending that work, we fit for a central point source in addition to a bulge and disk. In addition, our method takes into account the effects of convolution with the PSF and photon shot noise from the sky background and the galaxy. We also use the $r^{1/n}$ law for the bulge as in APB95. Details of the decomposition technique, its implementation and testing are included in Appendix A.

9.3.2 Bulge disk decomposition for our identifications

One of the initial aims of our development of the bulge-disk decomposition code *fitgal* was to employ it to obtain galaxy parameters for galaxies identified as the optical counterparts of the FIRST survey. Our code works well for galaxies brighter than about magnitude 16 in the V band. Unfortunately,

¹For a review of various 1-D decomposition techniques see Simien (1989).

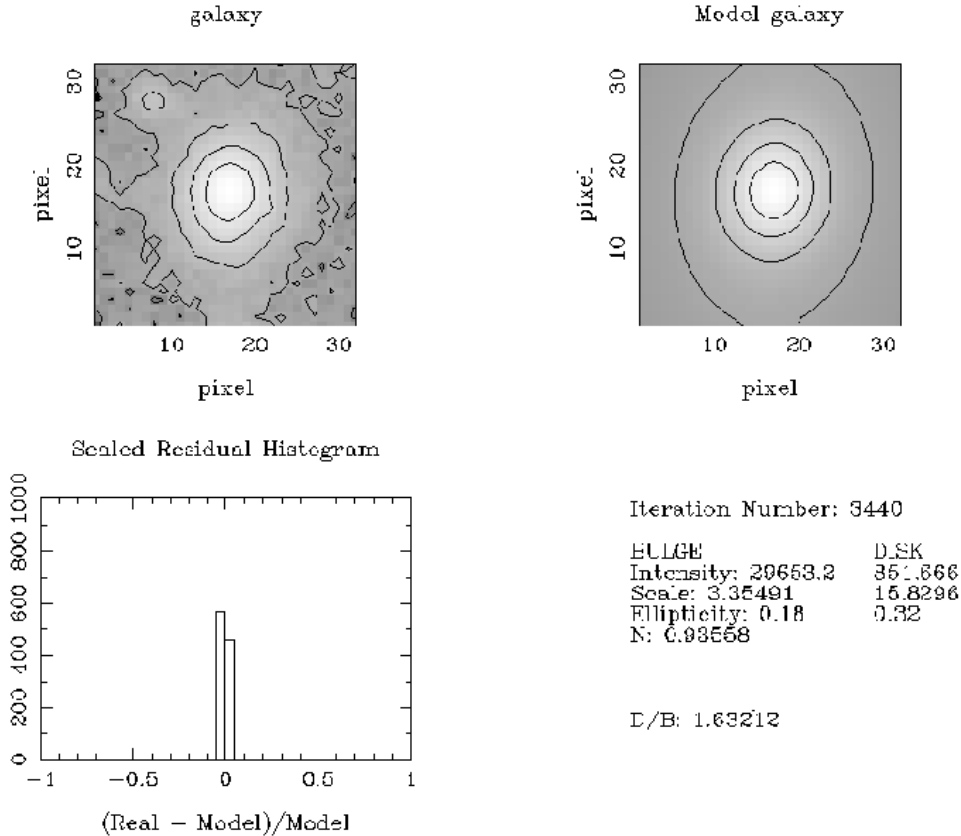


Figure 9.4: Results of a bulge disk decomposition of J010252.33-005359.0. For a description of the various panels in the figure see the caption to Figure A.1.

most of our FIRST identifications are fainter than this limit. Those that are brighter do not form a large enough set for a statistically significant study of their properties. We believe that reliable bulge disk decomposition for the faint identifications is not possible by any currently known technique, including our own.

We present in Figure 9.4 the results of a fit to one of our brighter optical identifications of the FIRST radio source J010252.33-005359.0. Similar decompositions have been successfully performed on 7 other optical counterparts. We present in Table 9.1, the results of the bulge disk decomposition of these 8 relatively bright identifications. These parameters were obtained by fitting the image with a two component model consisting of a bulge and a disk. We did not fit for a point source.

Strong radio sources have historically been identified with elliptical galaxies (Urry & Padovani, 1995). However weak radio sources, like the ones we are considering, may be associated with either elliptical or spiral galaxies. Such a trend is indeed visible in our data. Six of the eight galaxies listed in the table have a D/B ratio consistent with that of elliptical galaxies ($0 < D/B < 0.3$). However, two objects J010252.33-005359.0 and J030300.46-012223.2 have a large D/B ratio indicating that these radio sources are associated with a disk galaxy. However, other morphological indicators of disk nature, such as spiral arms, are not visible in either of the two galaxies. It should be noted that a large disk (indicated by a relatively high value of r_s), of the kind seen in these objects, is fundamentally different from the small disks ($r_s < r_e$) found in a small fraction of radio galaxies by Mahabal (1998).

The physical mechanism for the weak radio emission may also be very different. Starburst activity may play a more significant role here than in the brighter radio galaxies where accretion onto a super-massive black hole seems to be the favored mechanism for the origin of the radio emission.

Unfortunately the number of galaxies for which we have been able to perform a successful decomposition is not large enough to make possible a statistical analysis of correlations between extracted parameters, of the kind that we have carried out for a larger sample of elliptical and early type disk galaxies (Khosroshahi, Wadadekar & Kembhavi 2000, Khosroshahi et al. 2000).

FIRST desn.	n	D/B	r_e (pixels)	r_s (pixels)	e_b	e_d	F_{int} (mJy)
J000113.44-005935.2	0.94	0.00	5.04	...	0.58	...	3.76
J000117.85-005611.6	1.47	0.05	6.73	0.56	0.49	0.83	3.33
J010252.33-005359.0	0.94	1.63	3.35	15.83	0.18	0.32	1.27
J015105.84-003426.0	1.75	0.05	1.30	0.88	0.20	0.70	4.15
J015127.94-002217.3	2.68	0.17	12.68	1.22	0.00	0.26	0.65
J025947.83-005041.0	1.30	0.00	3.21	...	0.15	...	1.21
J030300.46-012223.2	2.21	8.86	14.96	8.41	0.33	0.66	3.58
J233002.37-003617.0	1.44	0.14	10.09	1.02	0.29	0.00	2.42

Table 9.1: Results of bulge disk decomposition for some of the brighter identifications. The table lists the bulge n parameter, the disk-to-bulge luminosity ratio D/B , the bulge effective radius r_e , the disk scale length r_s , the bulge and disk ellipticities e_b and e_d and the integrated radio flux F_{int} .

Chapter 10

Summary and future prospects

10.1 Summary

This thesis is about the properties of the optical counterparts of the sources detected by the ongoing, VLA Faint Images of the Radio Sky at Twenty centimeters (FIRST) survey. We provide below a brief “executive summary” of the original findings of this thesis.

1. We have reported radio detections of 69 previously undetected quasars. We have found additional evidence that the close pair of quasars 1343+266A and 1343+266B are *not* gravitationally lensed. We have found no correlation between radio luminosity and optical luminosity for the non-radio selected quasars. Our data is consistent with a bimodal distribution in radio luminosity. The distribution of the ratio of radio to optical luminosity is also bimodal, but this may have little relevance because of the lack of a clear correlation between radio and optical luminosities. The radio loud fraction does not seem to be strongly dependent on absolute magnitude, which is consistent with the lack of correlation between radio and optical luminosities. In contrast to some earlier findings, the radio loud fraction does not vary significantly with redshift.
2. We have reported detections of nuclear radio emissions from 206 AGN, previously undetected in the radio. We have detected nuclear emission from $\sim 32\%$ of the known AGN at a flux limit of 1 mJy. Our study nearly doubles the number of AGN with known radio emission over 6000 degrees of sky. We find no correlation between the nuclear radio luminosity and the optical luminosity of the galaxy that hosts the active nucleus. We find no significant statistical difference in either the radio luminosity or the radio source size between Seyfert 1 and Seyfert 2, contrary to some previous studies. The radio detection fraction too does not depend strongly on Seyfert type, which is consistent with the expectation from standard Seyfert unification models.
3. We have used data from the DPOSS survey to identify optical counterparts for over 2100 stars and galaxies and to generate a candidate list for 244 low redshift quasar candidates and 16 high redshift quasar candidates.
4. We have provided optical identifications from deep observations for ~ 40 faint FIRST sources, along with accurate photometry and astrometry. Many FIRST sources are found in interacting galaxies and/or galaxies in a rich galactic environment. These identifications represent some of the faintest (and possibly very distant) optical counterparts of radio sources ever recorded.
5. Taken together the various approaches and data sets in this thesis have provided optical identifications for over 2900 FIRST sources, spanning a wide variety of radio and optical properties.
6. We have developed a sophisticated two dimensional bulge disk decomposition software. This decomposition code, which we have made publicly available, can be used for analyzing the data from other optical surveys such as the Sloan survey.

7. We have determined to what redshift these optical counterparts can be identified and classified reliably by considering the appearance of host galaxies of AGN at optical wavelengths as a function of redshift. We have obtained the maximum redshift to which a host galaxy remains identifiable as an extended object above the sky background, as a function of galaxy type, other galaxy parameters, the active nucleus to host galaxy luminosity ratio, and observing conditions.

10.2 Where to go from here?

I outline below some ongoing and future projects that extend the work reported in this thesis.

1. **Correlations with other catalogs:** The ROSAT all sky survey bright source catalog has recently been released (Voges et al. 1999). Combining data from this X-ray survey with our earlier work on radio emission from quasars (Chapter 4), we can study correlations between radio, optical and X-ray luminosities and their implications to the physical mechanisms and unification schemes for quasars.
2. **Quasar candidate followup:** Two different datasets in this sample have together produced a sample of nearly 300 quasar candidates. We propose to carry out follow up spectroscopic observations using large telescopes to confirm their character. Additionally, using extremely deep ($K \sim 22$) near infrared images from the NTT (R. Srianand, private communication), we have obtained extremely faint near IR counterparts for FIRST sources. These objects are potentially high redshift galaxies or quasars. We propose to obtain spectra of these sources using the VLT.
3. **Quasar host galaxies:** Identification of quasar host galaxies at high redshift, and a systematic study of their radio and optical properties can provide valuable clues about the origin and evolution of the quasar phenomenon. Using the formulation developed in Chapter 7 as a guideline we have constructed a target sample of quasars for host galaxy identification. We have already initiated an observing program for optical and near infrared imaging of these moderate to high redshift quasars. The two dimensional bulge-disk decomposition algorithm described in Appendix A will prove useful in modeling the quasar light as a combination of bulge, disk and point source.
4. **Sloan survey:** Much of the work contained in this thesis can be carried over to the next level with SDSS data. The first release of calibrated photometric and spectroscopic data is scheduled for the summer of 2001. The computer programs and techniques of analysis developed in this thesis, particularly the two dimensional bulge disk decomposition technique, can be easily carried over to SDSS data. The results of this thesis can be reexamined with uniform optical data several times larger than the data available at the present time. The new data will decide how the results reported in this thesis survive in the glare of new observational evidence.
5. **Quasar radio morphology:** A high sensitivity, high resolution, large area sky survey such as FIRST can be a valuable tool for comparative statistical studies of the radio morphology of radio-quiet and radio-loud quasars. A study like this would need to be carried out keeping in mind the poor uv -plane coverage of the FIRST survey.

10.3 Surveys: the future of astronomy

We stand at the threshold of a new millennium of data-rich astronomy. Several ongoing sky surveys (including the few described in this thesis) spanning a wide range of wavelengths, from ground and space based instruments, will generate data sets measured in terabytes (1 terabyte = 2^{40} bytes, equivalent to textual information contained in about 2 million PhD theses the size of the present one). The surveys are creating catalogs of objects numbering in millions, with up to a hundred measured parameters for each object.

This vast amount of new information about the universe presents us with a great scientific opportunity as well as a great technological challenge (Djorgovski et al. 1998b). The opportunities are immense. In the new age, astronomers will be able to tackle some major outstanding problems with unprecedented accuracy, e.g., mapping of the large-scale structure of the universe, evolution of properties of different classes of objects with redshift, mapping the structure of our Galaxy, etc. which have proved intractable in past decades, because of insufficient data. The unprecedented size of the data sets will encourage searches for extremely rare types of astronomical objects, and may very well lead to the surprising new discoveries of previously unknown types of objects, possibly involving previously unknown astrophysical phenomena. Combining surveys done at different wavelengths, from radio to X-rays and γ -rays, would provide a new picture of our universe that can clarify (or confuse?) mankind's understanding of the cosmos. Multi-wavelength astronomy will become commonplace - the restricting divide between astronomers working at different wavelengths will disappear.

The full information content of the data will far exceed the capabilities of astronomers to exhaust it with a few studies. This will open up an entirely new field - that of *data-mining* of digital sky surveys, using the data for ever newly conceived projects and exploring the vast unknown regions of parameter space spanned by the data (Djorgovski et al. 1998b). This will fundamentally affect the methodology of observational astronomy: astronomers will work increasingly with a computer, rather than a telescope. Access to multi million dollar telescope facilities will not be paramount; anyone, anywhere, with a fast network connection, an affordable computer and a smart idea would be able to do high quality research. This new way of doing science will enable talented people anywhere to make their valuable contributions to astronomy, while simultaneously pursuing other careers. Such a scenario will be particularly advantageous to a developing country like India, which cannot afford to divert scarce resources toward professional astronomers and yet wants to get ahead in fundamental research.

This great new opportunity comes weighted with a commensurately large technological challenge: how to store, process and analyze these vast amounts of information, and to do it quickly and efficiently? The data volumes will be several orders of magnitude larger than what astronomers are used to dealing with today, and the old methods of storage and analysis will not be good enough. Other issues that will need to be tackled include how to optimally store and access such complex data, how to combine sky surveys done at different wavelengths, how to visualize them, to search through them, etc. These technical problems, which are common to all data-intensive fields, require a development of the next generation in computing software and hardware. If generalized software tools are developed they may well find applications in other fields beyond astronomy. The data mining tools that need to be developed will include applications of neural networks, and many other aspects of artificial intelligence. Global software and hardware *standards* to handle this mind-boggling torrent of data will need to be evolved through consensus. These developments will require a synergy of the talents of hundreds of astronomers and database professionals to keep the oldest science where it belongs - at the forefront of scientific research.

Appendix A

Two Dimensional Galaxy Image Decomposition Technique

This appendix is largely based on Wadadekar, Robbason & Kembhavi (1999). Here we describe our new two dimensional galaxy fitting algorithm and code to extract parameters of the bulge, disk, and a central point source from broad band images of galaxies, such as those which form the optical counterparts of FIRST survey sources. We discuss our technique and the extensive tests we have carried out using a large number of model galaxy images. We elucidate our procedures by extracting parameters for 3 disk galaxies - NGC 5326, NGC 5587 and NGC 7311.

A.1 Introduction

Fitgal is a new code that we have developed to extract global photometric parameters characterizing the bulge, disk, and central point source of galaxies. In this appendix, we describe the decomposition technique along with its implementation and testing with simulated and real data.

The information is organized as follows. In Section A.2, we describe our method of constructing artificial galaxy images as test cases for our bulge-disk decomposition procedure and in Section A.3 the decomposition procedure. Section A.4 is a detailed analysis of the testing we performed to test our decomposition algorithm, using simulated galaxy images. Section A.5 is a description of application of the technique to three galaxies and a comparison of the results with previously published values. Section A.6 contains a discussion about error bars on the parameters extracted and Section A.7 contains the conclusions.

A.2 Simulation of Galaxy Images

In order to test the decomposition procedure, we have developed a simulation code called *simu* to generate galaxy images closely resembling those obtained using CCD detectors on optical telescopes. Using the code it is possible to simulate a CCD image of a galaxy with desired bulge, disk and point components at any position and orientation on the CCD. The image can be convolved with a circular gaussian PSF and Poisson noise can be added if required. Stars can be introduced into the image at random positions and additional features such as absorbing dust lanes can be added. All parameters used by the program to generate these features can be easily modified by the user through a parameter file. The simulated images can be used to test the efficacy of our decomposition procedure to extract parameters from real galaxy images. Model galaxies generated by the code are also used in the fitting procedure.

The observed light distribution in galaxies is the projection of the three dimensional luminosity distribution onto the plane of the sky. If the disk is taken to be inherently circular, it projects as an ellipse. The inclination angle of the disk with respect to the plane of the sky completely determines its ellipticity in the image. Bulges, taken to be triaxial ellipsoids in the general case, also project as ellipses but the ellipticity of the bulge does not reach such high values as the disk. For a triaxial ellipsoid with major axis a , minor axis b , and an intermediate axis c , the highest possible ellipticity is $1 - b/c$. Therefore the projected galaxy shows elliptical bulge isophotes and, in many cases, more elliptical disk isophotes. At a given point on the image plane, contribution to the intensity from the bulge and the disk depends on their respective central intensities, ellipticities

and scale lengths. Near the galaxy center there is an additional contribution from the point source, if one is present.

In our galaxy simulation, the projected bulge component is represented by the $r^{1/n}$ law with effective (half light) radius r_e (which is the radius within which half the total light of the galaxy is contained), intensity at the center of the galaxy I_0 and a constant ellipticity $e_b = 1 -$ (minor axis length/major axis length):

$$\begin{aligned} I_{bulge}(x, y) &= I_0 e^{-2.303b(r_{bulge}/r_e)^{1/n}}, \\ r_{bulge} &= \sqrt{x^2 + y^2 / (1 - e_b)^2}, \end{aligned} \tag{A.2.1}$$

where x and y are the distances from the center along the major and minor axis respectively and b is the root of an equation involving the incomplete gamma function $P(a, x)$:

$$P(2n, 2.303b) = 0.5.$$

This equation can be solved numerically as we do in our code. However, a simplification can be introduced in the procedure because the b and n values satisfy the relation:

$$b = 0.8689n - 0.1447.$$

The projected disk is represented by an exponential distribution with central intensity I_s , scale length r_s and a constant ellipticity e_d ,

$$\begin{aligned} I_{disk}(x, y) &= I_s e^{-r_{disk}/r_s}, \\ r_{disk} &= \sqrt{x^2 + y^2 / (1 - e_d)^2}. \end{aligned} \tag{A.2.2}$$

The disk is inherently circular. The ellipticity of the disk in the image is due to projection effects alone and is given by:

$$e_d = 1 - \cos(i), \tag{A.2.3}$$

where i is the angle of inclination between the line of sight and the normal to the disk plane. Finally, the point source is represented by an intensity added to the central pixel of the galaxy prior to convolution with the PSF. Foreground stars are added at random positions as intensities at a single pixel prior to convolution with the PSF. The convolution with the PSF is performed in the Fourier domain. For adding photon shot noise, a constant sky background is added to every pixel. The resultant count (which includes intensity from the galaxy as well as the sky background) is multiplied by the gain (electrons/ADU). A random Poisson deviate about this value is obtained. The deviate is then divided by the gain and the background is subtracted out.

The program takes about one second to generate a 256×256 pixel galaxy image, when running on a SUN Ultra 10. A copy of the *simu* code (written entirely in ANSI C) is available upon request.

A.3 2-D Decomposition Technique

A.3.1 Building The Model

The 2-D decomposition technique involves building 2-D image models that best fit the observed galaxy images. The model to be fit is constructed using the same procedure as the simulated images described in the previous section, except that features of the image that are not contributed by the galaxy such as Poisson noise are not added. The galaxy position and position angle are *not* parameters that are fitted for in our decomposition. The position angles of the bulge and the disk are also assumed to be identical.

A.3.2 The Decomposition Procedure

To effect the decomposition, we attempt to iteratively minimize the difference between our model and the observed galaxy (or a simulated one), as measured by a reduced χ^2_ν value. For each pixel the observed galaxy counts are compared with those predicted by the test model. Each pixel is weighted

with the variance of its associated intensity as determined by photon shot noise of the combined sky and galaxy counts at that pixel. This weightage scheme has been used as it gives importance to pixels in proportion to their signal to noise ratio. Our scheme makes the fit less sensitive to the contribution of the bulge in the outer region of the galaxy where the disk dominates. Thus an effect similar to the earlier decompositions where the disk was fitted to the outer region and a bulge to the inner region of the galaxy is obtained automatically. Since photon shot noise obeys Poisson statistics the variance is equal to the intensity value. Hence

$$\chi_\nu^2 = \frac{1}{\nu} \sum_{i,j} \frac{[I_{model}(i,j) - I_{obs}(i,j)]^2}{I_{obs}(i,j)}, \quad (\text{A.3.1})$$

where i, j range over the whole image, $\nu = N -$ (number of fitted parameters) is the number of degrees of freedom with N being the number of pixels in the image involved in the fit, and I_{obs} is assumed to be greater than zero in all cases.

For real galaxies, our decomposition program assumes that pixel values I represent real photon counts. If the image has been renormalized in any way (divided by the exposure time for example), the extracted χ_ν^2 value should be multiplied by the appropriate factor to account for that normalization.

Eight fitting parameters are used in our scheme. These are $I_0, I_s, r_e, r_s, n, e_b, e_d$, and a central point source intensity I_p . The first 4 parameters were used by Schombert and Bothun (1987), and parameters 1 to 4 along with parameters 6 and 7 were used by the authors of BF95 and DJ96. We have added capability in our code to fit for position angle and a constant background, although the background is not fitted for in the simulations reported here. During our preprocessing we estimate the background carefully and subtract it out. CCD images of galaxies contain features such as foreground stars and bad pixels that may contaminate the decomposition procedure. In the case of real galaxies, we take care to mask out bad pixels and visible foreground stars before commencing decomposition.

The minimization uses MINUIT 94.1, a multidimensional minimization package from CERN, written in standard FORTRAN 77 (James 1994). MINUIT allows the user to set the initial value, the resolution, and the upper and lower limits of any parameter in the function to be minimized. Values of one or more parameters can be kept fixed during a run. MINUIT can use several strategies to perform the minimization. Our choice is MIGRAD, a stable variation of the Davidon-Fletcher-Powell variable metric algorithm. It calls the user function (in our case χ_ν^2) iteratively, adjusting the parameters until certain criteria for a minimum are met. Our code typically takes 0.01 seconds per iteration on a SUN Ultra 10 workstation, when working on a 64×64 pixel galaxy image. Since we are using fast Fourier transforms to convolve the model with a gaussian PSF, the execution time can be expected to scale as $N \log N$, with N the total number of pixels in the image. We do find that execution time scales almost linearly with the number of pixels in the image. About 2000 iterations are required for convergence criteria to be satisfied when all 8 parameters are kept free, so a typical run takes about one minute. Computation time is reduced as the number of free parameters are reduced.

A copy of this code, called *fitgal*, (written mostly in ANSI C with optional display routines using the PGPLOT library) is available upon request. In Figure A.1 we show a sample graphical output of *fitgal*.

A.4 Reliability of Galaxy Image Decomposition

We have conducted elaborate tests of the effectiveness of the program in extracting parameters under different input conditions.

A.4.1 Large-Scale Testing under Idealized Conditions

We expect that our method can be used for unsupervised, automatic parameter extraction for large sets of galaxies. To test the accuracy and reliability of our decomposition procedure, we constructed image sets of 500 model galaxies with an absolute magnitude of -21 with random uniform selection

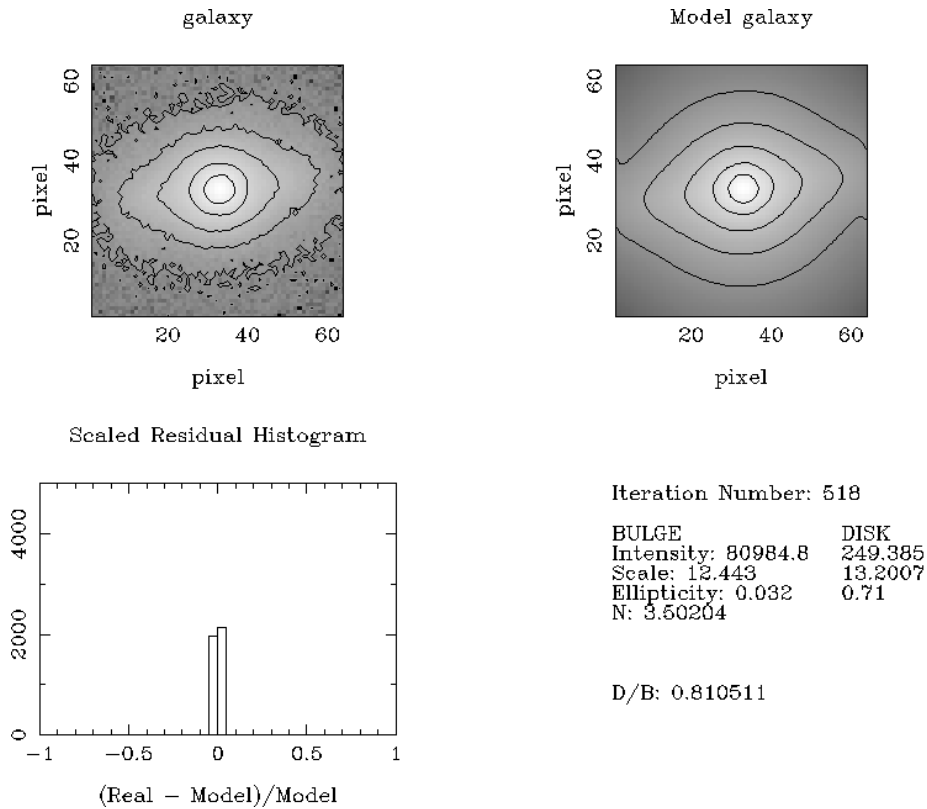


Figure A.1: Sample output from the graphical routines in fitgal. The data are a K-band image of the galaxy NGC 4971. The panels are Top left: a 64×64 pixel cutout of the disk galaxy NGC 4971. The contours of intensity shown have an interval of 1 magnitude. Top right: The best fit model galaxy. The intensity contours shown are identical to those in the previous panel. Bottom left: A scaled histogram of the residual of the fit. A sharply peaked histogram is indicative of a good fit. Bottom right: Fitted parameters for the bulge and the disk. The intensities are in counts, scale lengths are in pixels.

of disk to bulge ratio, scale lengths, bulge shape parameter n and ellipticities. The ranges we used for each parameter are,

$$\begin{aligned} 3 < r_e < 10 \text{ kpc}, \\ 0.0 < e_b < 0.4, \end{aligned}$$

for the bulge and

$$\begin{aligned} 0 < D/B < 3, \\ 3 < r_s < 15 \text{ kpc}, \\ 0 < e_d < 0.8 \end{aligned}$$

for the disk.

The ranges chosen for the parameters encompass most values encountered in real galaxies with Hubble types ranging from E to Sb. All simulated galaxies were assumed to be at a redshift of 0.15. The pixel scale used was 0.5 arcsecond/pixel, CCD gain was 1.0 ADU/electron, FWHM of the PSF was 1.0 arcseconds and the value of the Hubble constant used was $H_0 = 100 \text{ km sec}^{-1} \text{ Mpc}^{-1}$. We used a sky background value of 21.9 magnitudes/(arcsecond)². This corresponds to the value of the sky background measured in the V filter at KPNO (Massey, Gronwall & Pilachowski, 1990). The sky background was estimated in a trial run and then held fixed to that value thereafter. It was not a free parameter in these simulations. The scaling used to convert apparent magnitudes to CCD counts was estimated using photometric data on a 1m class telescope. On such a telescope, an exposure time of about 30 minutes would be required to get the S/N ratio used in these simulations. The galaxies generated by the galaxy simulation program were then used as input to the bulge disk decomposition program. We studied how accurate and reliable the decomposition program is in recovering the input parameters.

In the first set of trials, we generated 500 galaxies with $n = 4$. During the extraction, the parameter n was held fixed at a value of 4. We placed no additional relative constraints on permissible parameter values such as those used in BF95. We found that the χ_ν^2 for the fits is worse than 2 in 120 cases out of 500, giving a 24% failure rate. These failures are all caused by one or more parameters hitting their limits, causing the gradient-driven minimization routine to fail. It is possible for us to reduce the failure rate to about 10% by carefully changing starting values and parameter ranges by trial and error. In every case of failure due to parameters hitting limits, MINUIT generates appropriate warning messages, so there is no danger that such failures will contaminate the good results. The failure rate decreases as the number of free parameters decreases. It is possible to completely eliminate such failure by changing the initial value and constraining the range of parameters narrowly around the *expected* value which we have knowledge of, in the case of a simulation. While dealing with real galaxies, in case of a failure to obtain a satisfactory fit, the situation could be addressed by trying different initial values and ranges, with guesses based on inspection of the intensity profile. We find that a $\chi_\nu^2 < 2$ almost always corresponds to good recovery of input parameters, and a $\chi_\nu^2 > 2$ always corresponds to poor recovery of input parameters. Poor recovery of one parameter almost always implies poor recovery of all other parameters, a high value of χ_ν^2 and at least one parameter hitting limits. In such a case, one would need to use a new set of starting values and parameter ranges and try again. It should be noted that failure in recovering parameters is easy to detect as it is always flagged by a high χ^2 value.

The extracted versus input data have been plotted in Figure A.2, with points having $0 < \chi_\nu^2 < 2$ marked with a \circ , while the remaining points are marked with a dot. Note that the points with a bad fit (i.e. $\chi_\nu^2 > 2$) generally lie far away from the line on which the input value equals the extracted value. Almost all the remaining points (those with $0 < \chi_\nu^2 < 2$) plotted on these graphs are tightly grouped along this line. The authors of APB 95 report that the ellipticity of the bulge is not easy to determine by any method, and errors of the order of 30% are possible. Our method however, seems to recover bulge ellipticity to a high degree of accuracy. In a second set of 500 runs, we varied n in the range

$$1 < n < 6.$$

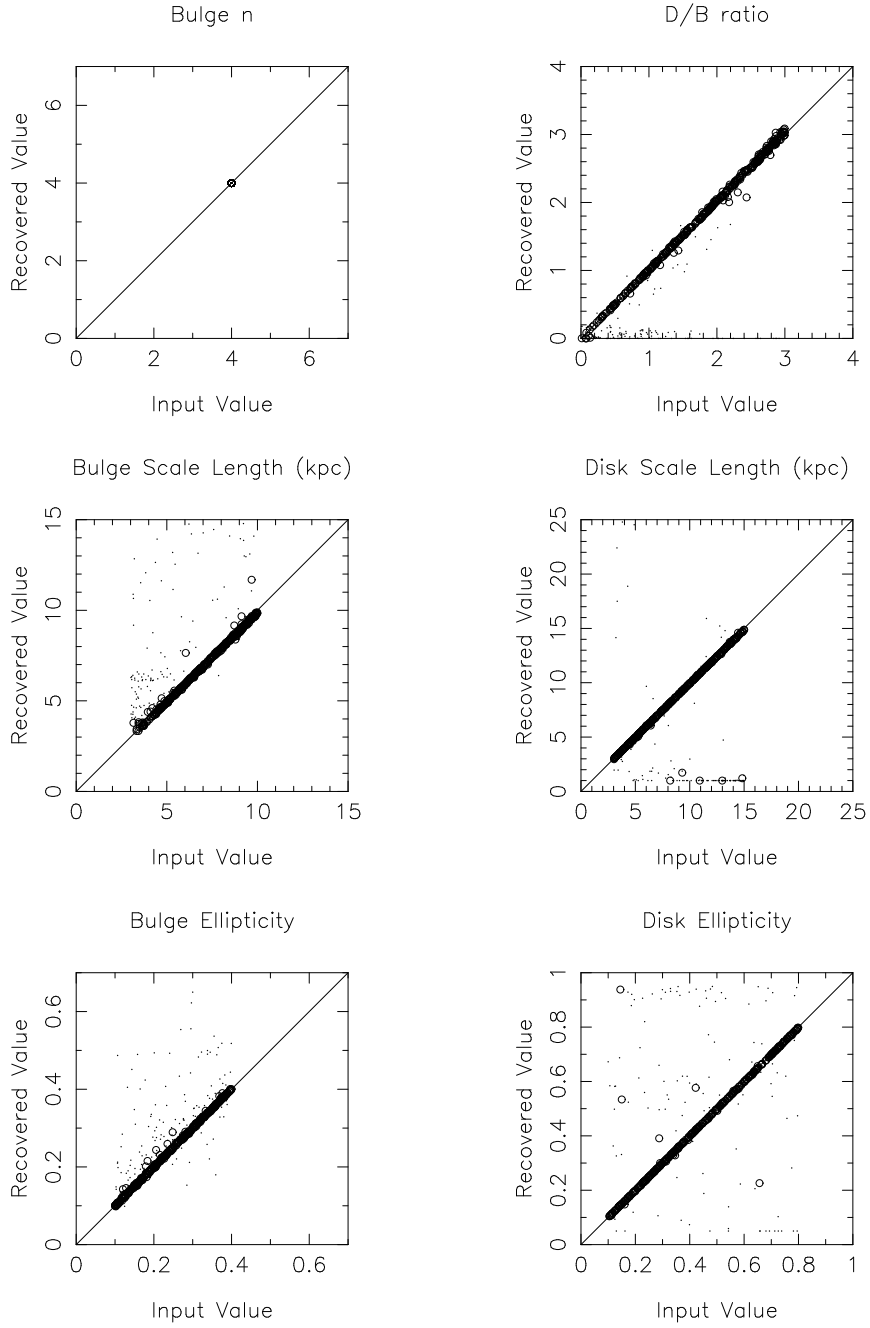


Figure A.2: Scatter plots of extracted versus input parameters for galaxies with $n = 4$. Points with $0 < \chi^2 < 2$ are indicated by a open circle while those with $\chi^2 > 2$ are indicated by a dot.

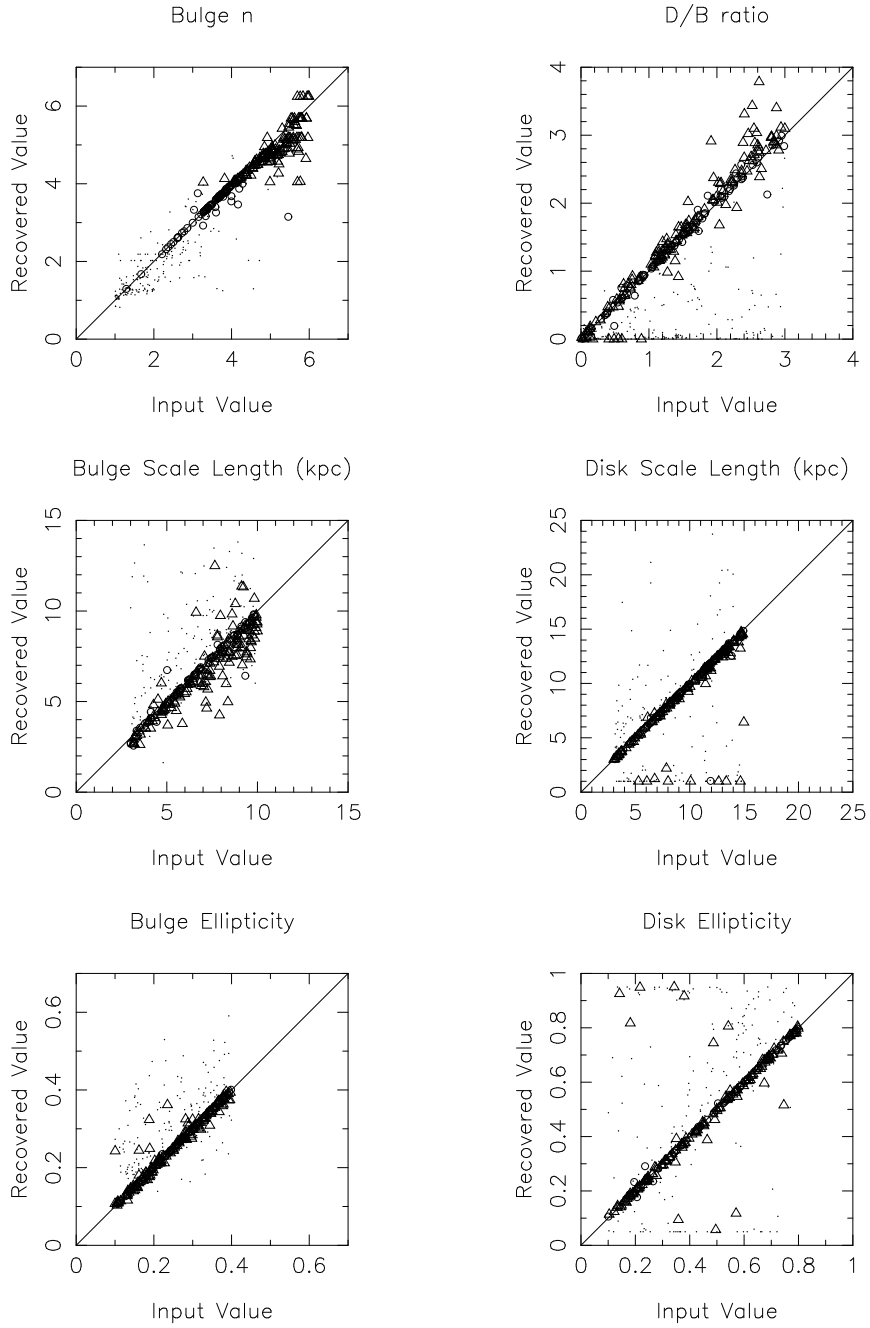


Figure A.3: Scatter plots of extracted versus input parameters with n in the range $1.0 < n < 6.0$. Points with $\chi^2_\nu > 2$ are indicated by a dot while those with $0 < \chi^2_\nu < 2$ are indicated by an open circle or a triangle. See the text for details.

Exp. time (sec)	χ_ν^2	Peak Counts	Input I_e	Extracted I_e	% Error in I_e
5	1.00	302	4.17	6.4	53.0
15	1.00	914	12.50	11.1	8.9
30	1.02	1923	25.00	24.2	3.2
60	1.04	3665	50.00	51.2	2.4
120	1.07	7623	100.00	101.0	1.0
240	1.11	14826	200.00	202.0	1.0
480	1.14	29740	400.00	415.0	3.8

Table A.1: Effect of changing exposure time.

All other parameters were varied within the same ranges as specified above. In this case, the “failure” rate was 25%. The extracted versus input data have been plotted in Figure A.3. As before, points with $\chi_\nu^2 > 2$ are marked with a dot. Points with $\chi_\nu^2 < 2$ and $n < 4$ are marked with a \circ while points with $\chi_\nu^2 < 2$ and $n > 4$ are marked with a Δ . There is a marked increase in scatter of all parameters as compared to the $n = 4$ case described above, even for points with $\chi_\nu^2 < 2$. Most significantly, the scatter in the extraction of n is rather large for $n > 4$. This occurs because the intensity profile of the bulge gets steeper as n increases. For large n the fall-off in intensity with distance from the center is so rapid that hardly any points with good S/N are available, for fitting the bulge of the galaxy. This leads to larger errors in estimation of n and other bulge parameters, contributing to the increased scatter seen in n , disk to bulge ratio and bulge scale length for $n > 4$. The only way to reliably extract the bulge profile for galaxies with a weak bulge resulting from an unfortunate combination of small bulge scale length, high D/B and large n is to use a higher exposure time to improve S/N . When we increased the exposure time by a factor of ten, there was a noticeable decrease in scatter for large n . In most real situations where it is not feasible to increase exposure time, it should be borne in mind that extracted values with large n and/or small bulge scale lengths are prone to error.

A.4.2 Tests of stability

We conducted a series of tests to determine how the program responds to deviations from the idealized conditions assumed in the previous section, to gain some insight into problems encountered when dealing with real galaxy images rather than simulated ones.

A.4.3 Effect of changing S/N ratio

The S/N ratio improves with increase in exposure time. We examined the image of the same simulated galaxy using pixel counts for a bright galaxy and sky background corresponding to exposure times ranging from about 5 seconds to 8 minutes on a 1 m class telescope. The exposure times (and hence the pixel counts) varied by a factor of 96 and S/N ratio by a factor of about 10 ($\simeq \sqrt{96}$). The background counts used were estimated from observations made on a 1m class telescope in the Cousins R filter. We expected that as S/N got better, the fit would improve and parameter recovery would get more accurate. We found that the accuracy of the extracted parameter values is strongly dependent on the exposure time only for short exposures of <30 seconds. The results for different exposure times are shown in Table A.1 which compares various input values of intensity at the effective radius I_e with the corresponding extracted value. Peak counts of less than one thousand for galaxies are not very useful for the purpose of bulge disk decomposition.

It is seen that χ_ν^2 increases slowly but monotonically with exposure time. This is an artifact of the way sky background is used in the program creating the input galaxies. When simulating galaxies, background is added, Poisson noise is calculated using the intensity of both background and galaxy, and the background is subtracted out. Then, when the fitting program runs, it estimates the noise at each pixel as the square root of the number of counts at that pixel, but the actual noise is the square root of the sum of the number of counts and the background. This causes the points with low counts to be weighted more than they should be (resulting in higher χ_ν^2), but the difference

is small.

A.4.3.1 Effect of erroneous measurement of PSF

With real data it is often impossible, even if a large number of stars are used, to measure the FWHM of the PSF to an accuracy of better than about 5%. One reason for this is the variation of the PSF over different regions of the CCD. Therefore, it is important to know how the fit will react to an over- or under-estimation of the FWHM of the PSF, and to an elliptical PSF. The value of the point source is expected to be affected the most because of errors in PSF estimation. If the bulge scale length r_e is very small, then bulge parameters will also be seriously affected by an incorrect estimation of the PSF. We ran two separate tests, one with a circular PSF, with the FWHM overestimated or underestimated by up to 20%, and another where the width along one axis of the PSF changed by 20% while the other remained constant, thereby generating elliptical PSFs. During the fitting we used a constant circular Gaussian PSF with FWHM $\Gamma_{fit} = 1$ pixel in all the test cases described below.

For these tests, our simulated images were generated using a PSF with varying FWHM, denoted by Γ_{image} . $\Gamma_{image}/\Gamma_{fit} \neq 1$ corresponds to the situation where an error is made in the estimation of the FWHM of the PSF used in modeling the intensity distribution of observed galaxies. In the first test we assumed that the PSF shape is circular and the only error is in estimating the value of the FWHM. When $\Gamma_{image}/\Gamma_{fit} < 1$ the spreading of the image due to seeing is overestimated by the decomposition program. The excess deconvolved intensity at the center causes it to report a fictitious point source. The minimum value for the ratio we have used in the test is 0.8. At this ratio, the fitted intensity of the fictitious point source is very high, as can be seen from Figure A.4. The bulge intensity is at its minimum value. The intensity of the fictitious point source decreases and that of the bulge increases continuously as $\Gamma_{image}/\Gamma_{fit} \rightarrow 1$. If the FWHM of the PSF is underestimated, i.e. $\Gamma_{image}/\Gamma_{fit} > 1$, the point intensity becomes negative.¹

The variation of $\Gamma_{image}/\Gamma_{fit}$ did not affect the extracted disk scale length, which only once deviated by more than 1 pixel. The disk intensity increased with increasing input PSF, analogous to the increase in bulge intensity discussed above. The extracted bulge and point source intensities, and bulge radius, all vary systematically and approximately linearly with the error in PSF estimation. χ^2_ν is very good in all cases, decreasing somewhat as the PSF gets to be closer to our estimate of 1. These results are plotted on the left panel of Figure A.4.

To see the effect of errors in determining the shape of the PSF, we generated galaxies with different elliptical PSFs. Such PSFs are observed, for example, if the plane of the CCD is inclined to the focal plane of the telescope. The decomposition program continued to use a fixed circular PSF. The sequence of image PSFs was generated by keeping one of the principal axes of the ellipses always equal to Γ_{fit} , and varying the other principal axis so that ratio of the two changed from 0.8 to 1.2. The results of parameter extraction are plotted on the right panel of Figure A.4, as a function of $\Gamma_{image}/\Gamma_{fit}$, where the ratio is now taken along the changing principal axis.

When the PSFs used in the simulation as well as fitting are both circular, but have different Γ_{image} , the fitting procedure leads to a positive or negative fictitious point source. A good overall fit is obtained with χ^2_ν close to unity in the latter case, i.e. when $\Gamma_{image}/\Gamma_{fit} > 1$, because here the overall intensity at the centre remains small and best fit bulge parameters which give a good fit, together with the negative point source can be found. In the case of a positive point source, changed bulge parameters cannot compensate for the error in the PSF and the quality of the fit is diminished. In the case of the elliptical PSFs, χ^2_ν is greater than unity on both sides of $\Gamma_{image}/\Gamma_{fit} = 1$.

Bulge ellipticity, which was set to 0.1 in all simulated images, was extracted very well in the case of the circular PSF as it varied over its range of FWHM. When the PSF becomes elliptical, we expect the extracted ellipticity to increase as well, and it does, but only to 0.12 for the most elliptical PSF, which had ellipticity 0.2. The ellipticity close to the centre of the galaxy is of course wholly determined by the shape of the PSF, while further away, the effects on the extracted ellipticity are much smaller.

¹A negative point is non physical, of course, but in general we will allow for it because the law describing the bulge does not hold near the center of most galaxies. In our simulation however we have assumed that the law holds right to the center.

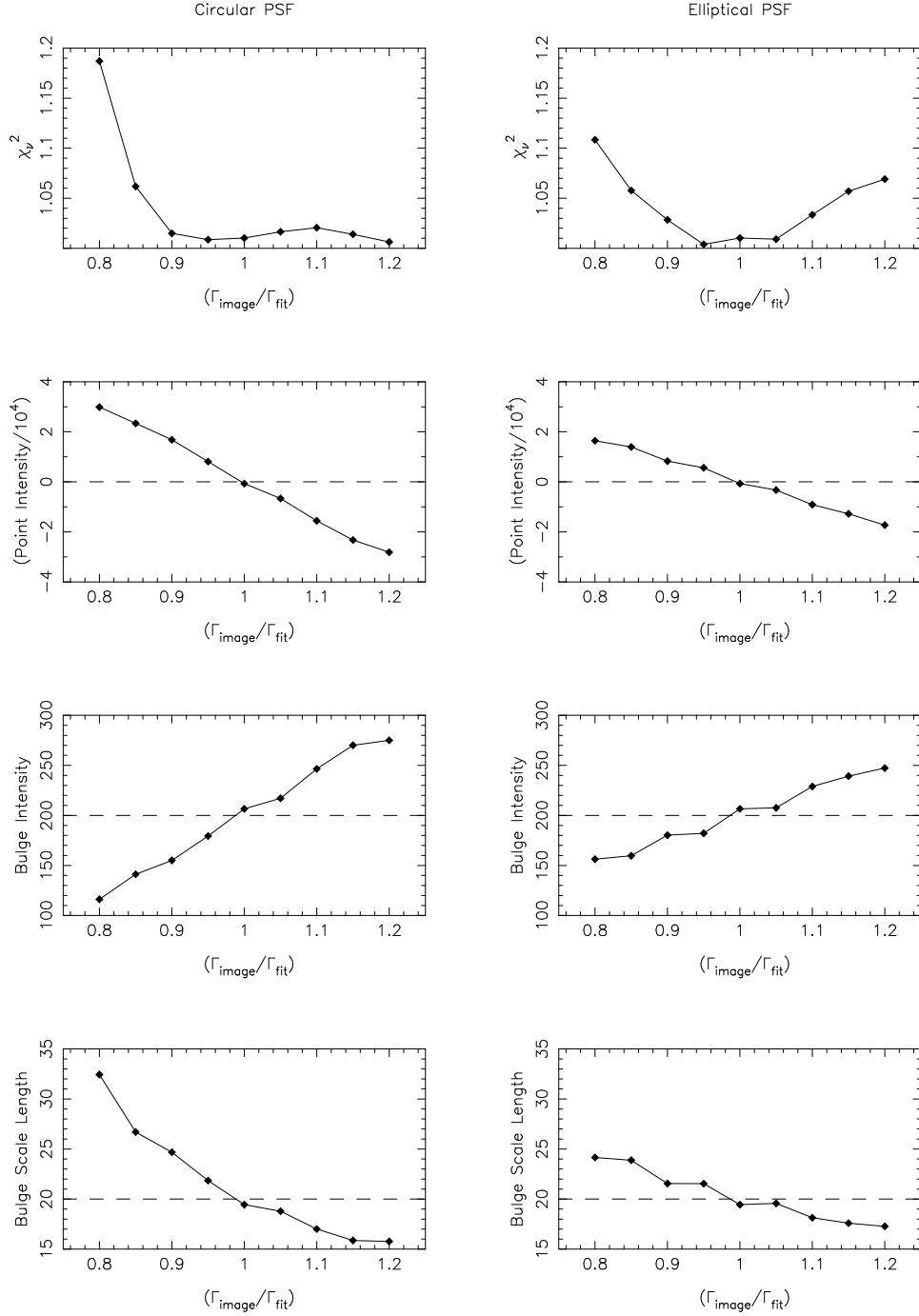


Figure A.4: Effects of incorrect estimation of PSF on extracted parameters. The panels show changes in point intensity, bulge intensity and bulge scale length under a changing circular PSF (left panels) and changing ellipticity of the PSF (right panel). In each panel, the dashed line indicates the fixed value of the input parameters, while the Y-axis shows the corresponding fitted value. The negative point intensity obtained for some values of $(\Gamma_{image}/\Gamma_{fit})$ is explained in the text.

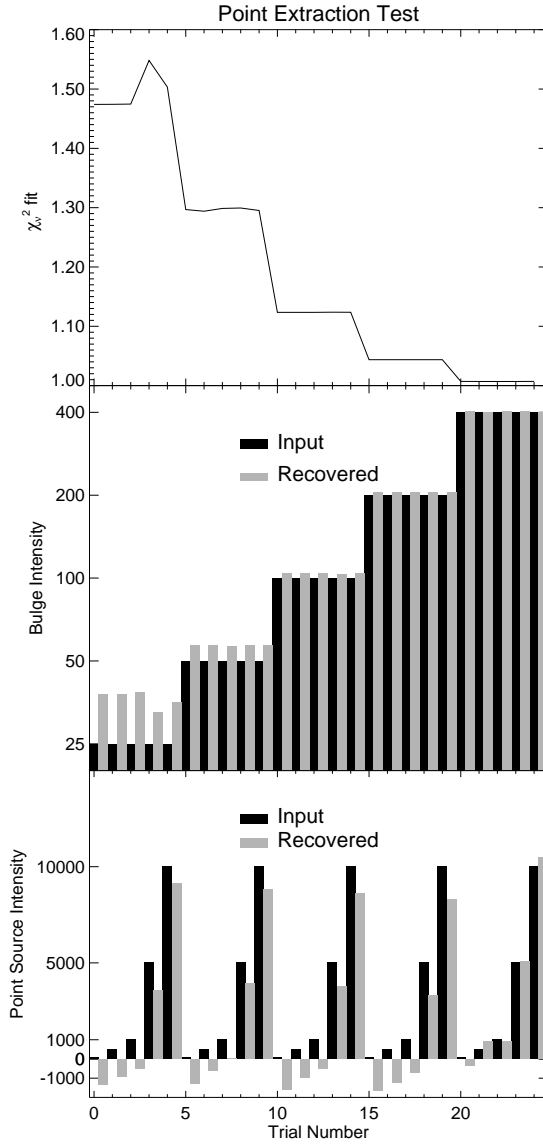


Figure A.5: Results of point source extraction in 25 runs. The top panel shows the χ^2_{ν} value obtained in 25 runs. The bulge intensity increases after every 5 runs, resulting in a steep drop in χ^2_{ν} , due to improved S/N ratio. The middle panel shows 25 input values for bulge intensity and the corresponding recovered value adjacent to each other. The lowest panel shows input point source intensities for each run and the corresponding recovered value. Note that the middle panel has the Y axis plotted on a logarithmic scale. See the text for further explanation.

A.4.3.2 Fitting in the presence of stars

Our aim here was to check if the presence of bright foreground stars on the galaxy could cause a systematic deviation in extracted parameters. To test this, we added upto 20 randomly positioned stars to a 128×128 pixel image, and ran the decomposition program without blocking out the stars. The presence of the stars worsened the χ^2_{ν} considerably but the extracted parameters were not affected in any significant or systematic way. Masking out the stars improved the χ^2_{ν} to normal values (≈ 1), and the parameters were also accurately extracted as before.

A.4.4 Detecting a point source

We have examined the extraction of a point source at the centre of the galaxy. Since the bulge intensity has a very sharp peak near the center, a point source can be easily swamped by the bulge unless it is very bright. The objective here is to find powerful sources, and not very weak ones where the point intensity is less than the bulge intensity at the central pixel. We looked at various strengths of the point relative to the bulge, by examining a uniform grid of 5×5 values of point and

bulge central intensities, over which the bulge and point each varied by a factor of thirty. There was no detection of a fictitious point. Weak points were absorbed into the bulge, while strong points were extracted well, as shown in Figure A.5. For higher bulge intensities, the point intensity was extracted better, because higher S/N far from the center served to constrain the bulge intensity more precisely.

A.5 Fitting real galaxy images

The immediate goal of this program is to extract parameters from a large sample of galaxies of different morphological types of the kind reported in APB95, and RF96. To elucidate what our program can do, and to compare results with those obtained by other workers, we have used our program to extract parameters for three disk galaxies chosen from the data in APB95. Our program does not model bars, spiral arms and such other features, so we chose galaxies where these features did not dominate when the images were visually inspected. We used the online data available at <http://www.elsevier.nl/locate/newast> and described in Peletier and Balcells (1997). More extensive work on a larger sample of ellipticals and early type disk galaxies has been reported by us separately (Khosroshahi, Wadadekar & Kembhavi 2000, Khosroshahi et al. 2000). Here we wish to merely compare the results of our approach with that reported in APB95.

A.5.1 Possible pitfalls

Going from fitting simulated models to fitting real galaxies has several attendant dangers. Significant errors in the PSF can cause the detection of a fictitious point source (Section 4.2.2). Since the PSF is never known exactly, any extraction of a point must be examined very carefully. HST data shows that a single power law describing the bulge is a poor approximation to the intensity profile near the center of the galaxy (Byun et al. 1996). Without very precise knowledge of the PSF, measuring systematic deviations from the law is not reasonable. Images are often normalized, averaged, or background subtracted during processing. Knowledge of the normalization used is required before we get an accurate estimate of the S/N ratio which is a prerequisite for determining the weighting function for our χ^2 minimization.

In extreme cases, the luminosity distribution of two physically different components are very similar and they can give very similar values of reduced χ^2 . Our method can give incorrect results under such circumstances. For example, a bulge with a very small scale length can be easily confused with a point source. Similarly an extremely large but weak circular disk can appear like background sky. High redshift galaxies with small scale length in angular terms do not have sufficient number of high S/N pixels for a reliable fit.

A.5.2 Comparison of extracted parameters

Table A.2 shows extracted values from our program, as compared with values published in APB95 for three disk galaxies NGC 5326, NGC 5587 and NGC 7311. Both the bulge and disk ellipticities match very well. Correct extraction of ellipticities is a prerequisite for the APB95 method of decomposition to work but is not required in our method. In two out of three cases, the discrepancy in n is larger than the error bar reported in APB95 but the deviation is not large. There is little discrepancy in the value of bulge scale length too. We have also reported the disk scale length for these galaxies, which is held fixed at 25 arcsecond for all galaxies in APB95. In Table A.2 we have converted the angular scale length reported in APB95 to a linear scale. Our extracted values for disk scale length match those in APB95 to within a factor of two.

It should be noted that our technique is fundamentally different from that used in APB95. We use the 2-D images directly, not azimuthally averaged luminosity profiles. Our method extracts all galaxy parameters at one go, with no prior knowledge of ellipticities. We expect our method to work well for disk galaxies at any orientation.

Parameter	Source	NGC 5326	NGC 5587	NGC 7311
Bulge ellipticity	APB95	0.20	0.20	0.00
	This work	0.31	0.22	0.07
Disk ellipticity	APB95	0.55	0.70	0.53
	This work	0.55	0.78	0.56
D/B	APB95	4.00	20.00	5.26
	This work	3.04	26.48	4.38
n	APB95	2.19	1.53	1.32
	This work	1.78	2.10	1.90
Bulge Scale length (kpc)	APB95	0.54	0.48	0.87
	This work	0.44	0.40	0.70
Disk Scale Length (kpc)	APB95	1.69	1.93	3.60
	This work	0.74	1.64	1.62

Table A.2: Comparison of extracted parameters.

A.6 Error estimation

In minimization problems, two methods are commonly employed for parameter error estimation. The first is to estimate the error from the second derivative of the function being minimized with respect to the parameter under consideration. The second is to gradually move away from the minimum until a predetermined χ^2 is exceeded. The second method will work for a single parameter fit irrespective of whether the χ^2 function near the minimum is parabolic in shape, or of a more complicated nature. MINUIT can perform error estimations using both methods.

In any multi-parameter minimization process, formal errors on the parameters can be generated from the the covariance matrix of the fit only if: (i) the measurement errors are normally distributed and either, (ii-a) the model is linear in its parameters or (ii-b) the sample size is large enough that the uncertainties in the fitted parameters do not extend outside a region where the model could be replaced by a suitable linearized model. It should be noted that this criterion does not preclude the use of a non-linear fitting technique to find the fitted parameters (Press et al. 1992).

Amongst the bulge and disk parameters that we use in the fit, two are linear (I_0 and I_s) and the rest are non-linear. Non-linearity is highest for e_b and e_d . Leaving all parameters free, results in rather large formal error bars on extracted parameters ($\sim 20\text{-}30\%$). The χ^2 function is not parabolic near the minimum, which causes incorrect error estimation by MINUIT when the derivative method is used. Even moving away from the minimum until some χ^2 is exceeded does not work here as there are multiple free parameters that are correlated. MINUIT is therefore unable to compute errors using this technique when all parameters are free. Fixing the most non-linear parameters i.e. the ellipticities to their extracted value enables MINUIT to compute formal errors using this technique as the function can be approximated by a linearized model. The errors are however still large. If more parameters are fixed, the error bars are further reduced. Formal errors match those obtained from parameter recovery in the 500 model test if only *one* parameter is left free. Given the strong inherent non-linearity of our model, the problem of obtaining formal error bars on extracted parameters, when more than one parameter is left free simultaneously, will be mathematically difficult.

A.7 Conclusions

Unprecedented amounts of CCD imaging data on galaxies will be generated by the new optical surveys such as the Sloan Digital Sky Survey. Cross-correlations with other catalogs such as FIRST will provide samples of thousands of interesting galaxies for further study. Analysis of these tera byte size datasets will require completely automated, fast and reliable algorithms for tasks such as morphological classification (eg. Abraham et al. 1994) followed by bulge-disk decomposition for an appropriate subset of galaxies. Our extensive tests on simulated galaxy images show that the two

dimensional fitting procedure described here is very successful at accurately extracting a wide range of input parameters, and that the cases where it fails can be easily detected from the χ^2 value since failure is always accompanied by a high χ^2 value.

One major limitation of our method is that it assumes that the observed luminosity profile of the galaxy under consideration actually follows the empirical laws we have chosen irrespective of the great variation seen in galaxy morphologies. Studies of the effects of morphological features (such as dust absorption in disks modeled by Evans 1994) on scale parameters are required if we are to develop a reliable methodology to extract parameters for galaxies with strong features such as bars, spiral arms etc.

For galaxies with very steep luminosity profiles (i.e. small bulge scale length or large n), conventional 1-D fitting may provide a better solution than 2-D methods because in such galaxies, a very large fraction of pixels have poor signal to noise. This works against a good determination by the 2-D method, which uses individual pixels over the whole image in the fit. When there is large isophotal twist in the galaxy, a 1-D method may work better than the 2-D one, because most 1-D methods follow the twisting of the ellipses by changing the position angle with radius. All 2-D methods proposed to date hold the position angle constant. When effects of shape parameters are significant, a 2-D technique is better. For example when a highly inclined disk is present, 1-D fits might miss it altogether, or provide a very poor fit. 2-D methods are also better in extraction of ellipticities of the bulge and the disk, and for extraction of the point source, as the larger number of data points available help constrain the extracted value better.

Our extracted galaxy parameters are consistent with those reported in APB95. Our method does not require galaxies to have significantly different bulge and disk ellipticities as required in the method described in APB95. Thus it is well suited for decomposition of face-on as well as edge-on disk galaxies. We wish to sound a note of caution about the lack of reliability of bulge disk decomposition for galaxies with strong features such as a bar or spiral arms, those with $n > 4$ and those with a poorly estimated PSF. Although a good fit can be probably be obtained even for such galaxies using our method, our χ^2 value would no longer be a powerful tool to distinguish between good and bad fits.

Recently, we have incorporated into the *fitgal* code the ability to use model Hubble Space Telescope PSFs constructed using the *tinytim* package. This important enhancement will allow *fitgal* to be used with WFPC/2 and NICMOS data from the HST.

Appendix B

Angular cross-correlation Code

B.1 Description

This short Perl program computes the angular separation between two sources - one source from each of the two catalogs chosen for comparison - having equatorial coordinates (α_1, δ_1) and (α_2, δ_2) respectively. The angular separation θ between these two sources is given by:

$$\theta = \arccos(\sin \delta_1 \sin \delta_2 + \cos \delta_1 \cos \delta_2 \cos(\alpha_1 - \alpha_2))$$

where $\theta, \alpha_1, \delta_1, \alpha_2, \delta_2$ are all expressed in radians. The above formula can be readily derived by expressing the two positions as unit vectors- in spherical polar coordinates- and then using the scalar product between those two vectors, to compute the angle between them. The angular separation in arcsecond θ_{arcsec} is given by

$$\theta_{arcsec} = (180\theta/\pi) \times 3600$$

If this angular separation is less than the search radius θ_c set by the user, the pair of sources is counted as a match and the output parameters selected by the user are written to the *match* file. This code takes about 3 hours of CPU time on an Ultra 10 machine for correlation of 5,000 source catalog with the 500,000 source FIRST catalog (2.5 billion angular separation computations).

No attempt has been made to optimize the comparisons in this catalog. All sources in catalog 1 are compared with all sources in catalog 2. For significantly larger catalogs, optimizing the comparisons by breaking up the catalogs into smaller units for the comparison will be worthwhile.

B.2 The code

The code for the matching the FIRST source catalog with other catalogs was implemented in Perl, the programming language best suited for working with ASCII tables. The code has been extensively commented for the benefit of the user. In order to use the code with some other tables, only the input and output statements should need modification.

```
# This program performs angular cross correlation between the VERON AGN catalog and the
# VLA FIRST survey catalog. The input and output statements will need to modified
# for other catalogs.
# Author: Yogesh Wadadekar, yogesh@iucaa.ernet.in
# This Perl program may be freely modified and used under the terms of the GNU
# Public license

# open output files of makeradec.perl
open(FIRSTCATALOG,"</adata1/yogesh/programs/crosscorr/firstout") || die "Cant open catalog" ;
open(VERONCATALOG,"<seyferts.veron") || die "Cant open VERON catalog" ;

$error = 300; # Set the radius of the error circle in arc sec here..

open(MATCHES,">matches.$error") || die "Cant open MATCH file" ;

# defining useful constants and subroutines
sub acos { atan2(sqrt(1 - $_[0] * $_[0]), $_[0]) }
$i=0;
$j=0;

$pi = atan2(1,1) * 4 ;
$radperdegree = $pi / 180.0 ;

#defining the file template for each catalogs
$firsttemplate= "a21 a21 a2 x1 a2 x1 a6 x1 a3 x1 a2 x1 a5 x1 a10
```


Bibliography

- [1] Abraham, R. G., Valdes, F., Yee, H. K. C., & van den Bergh, S. 1994, *ApJ* **432** 75
- [2] Allington-Smith, J. R., Perryman, M. A. C., Longair, M. S., Gunn, J. E., & Westphal, J. A. 1982, *MNRAS* **201** 331
- [3] Andredakis, Y. C., Peletier, R. F., & Balcells, M. 1995, *MNRAS* **275** 874 (APB95)
- [4] Antonucci, R. 1993, *ARA&A* **31** 473
- [5] Aretxaga, I., Boyle, B. J., & Terlevich, R. J. 1995, *MNRAS* **275** L27
- [6] Bahcall, J. N., Kirhakos, S., Saxe, D., & Schneider, D. P. 1997, *ApJ* **479** 642
- [7] Barthel, P. D. 1989, *ApJ* **336** 606
- [8] Becker, R. H., Gregg, M. D., Hook, I. M., McMahon, R. G., White, R. L., & Helfand, D. J. 1997, *ApJ* **479** L93
- [9] Becker, R. H., White, R. L., & Helfand, D. J. 1995, *ApJ* **450** 559
- [10] Benn, C. R., Rowan-Robinson, M., McMahon, R. G., Broadhurst, T. J., & Lawrence, A. 1993, *MNRAS* **263** 98
- [11] Bertin, E. & Arnouts, S. 1996, *A&AS* **117** 393
- [12] Bischof, O.B., & Becker, R. H. 1997, *AJ* **113** 6 (BB97)
- [13] Blandford, R. D., Netzer, H., & Woltjer, L. 1990, *Active Galactic Nuclei* (Berlin: Springer-Verlag)
- [14] Bock, D. C.-J., Large, M. I., & Sadler, E. M. 1999, *AJ* **117** 1578
- [15] Burstein, D. 1979, *ApJ* **234** 435
- [16] Byun, Y. I., & Freeman, K. C. 1995, *ApJ* **448** 563 (BF95)
- [17] Byun, Y. I., et al. . 1996, *AJ* **111** 1889
- [18] Condon, J. J. 1984, *ApJ* **284** 44
- [19] Condon, J. J. 1989, *ApJ* **338** 13
- [20] Condon, J. J., Anderson, M. L. & Helou, G. 1991, *ApJ* **376** 95
- [21] Condon, J. J., Cotton, W. D., Greisen, E. W., Yin, Q. F. Perley, R. A., Taylor, G. B., Broderick, J. J. 1998, *AJ* **115** 1693
- [22] Condon, J. J., Odell, S. L., Puschell, J. J., & Stein, W. A. 1981, *ApJ* **246** 624
- [23] Crampton, D. et al. 1988, *ApJ* **330** 184
- [24] Cress, C. M., Helfand, D. J., Becker, R. H., Gregg, M. D., & White, R. L. 1996, *ApJ* **473** 7
- [25] Crotts, A. P. S., Bechtold, J, Fang, Y., & Duncan, R. C. 1994, *ApJ* **437** L79
- [26] de Bruyn, A. G., & Wilson, A. S. 1976, *A&A* **53** 93
- [27] de Bruyn, A. G., & Wilson, A. S. 1978, *A&A* **64** 433
- [28] de Jong, R. S. 1996, *A&AS* **118** 557 (DJ96)
- [29] de Vaucouleurs, G. 1948, *Ann. d'Astrophys.* **11** 247
- [30] Djorgovski, S. G. et al. 2000, (under preparation)
- [31] Djorgovski, S. G., Carvalho, R. R., Gal, R. R., Pahre M. A., Scaramella R. & Longo, G. 1998a, IAU Symp. 179, eds. B. McLean et al.
- [32] Djorgovski, S. G., Odewahn S. R., Gal, R. R., Carvalho, R. R., Longo, G. & Scaramella R. 1998b, Wide Field Surveys in Cosmology, 14th IAP meeting
- [33] Djorgovski, S., Spinrad, H., McCarthy, P., Dickinson, M., van Breugel, W., & Strom, R. G. 1988, *AJ* **96** 836
- [34] Djorgovski, S.G., Carvalho, R. R., Gal, R. R., Pahre M. A., Scaramella R. & Longo, G. 1997, IAU Symp. 179, eds. B. McLean et al.
- [35] Dunlop, J. S., Taylor, G. L., Hughes, D. H., & Robson, E. I. 1993, *MNRAS* **264** 455
- [36] Edelson, R. A. 1987, *ApJ* **313** 651
- [37] Evans, I. N., Ford, H. C., Kinney, A. L., Antonucci, R. R. J., Armus, L., & Caganoff, S. 1991, *ApJ* **369** L67
- [38] Evans, R. 1994, *MNRAS* **266** 511
- [39] Feigelson, E. D., & Nelson, P. I. 1985, *ApJ* **293** 192

- [40] Fomalont, E. B., Windhorst, R. A., Kristian, J. A., & Kellerman, K. I. 1991, *AJ* **102** 1258
- [41] Freeman, K. C. 1970, *ApJ* **160** 811
- [42] Gehren, T., Fried, J., Wehinger, P. A., & Wyckoff, S. 1984, *ApJ* **278** 11
- [43] Gregg, M. D. Becker, R. H., White, R. L., Helfand, D. J., McMahon, R. G., & Hook, I. M. 1996, *AJ* **112** 407
- [44] Hammer, F., Crampton, D., Lilly, S. J., Le Fevre, O., & Kenet, T. 1995, *MNRAS* **276** 1085
- [45] Havilcek, L. L. & Crain, R. D. 1988, *Practical statistics for the physical sciences* (Washington DC: American Chemical Society)
- [46] Helfand, D. J., Becker, R. H., White, R. L., & McMahon, R. G. 1998a, *BAAS* **189** 1404
- [47] Helfand, D. J., Schnee, S., Becker, R. H., White, R. L., & McMahon, R. G. 1999, *AJ* **117** 1568
- [48] Helfand, D. J., Yadigaroglu, I. A., Berger, R., Postman, M., White, R. L., Lauer, T. R., Oegerle, W. R. & Becker, R. H. 1998b, *BAAS* **193** 4002
- [49] Hewitt, A., & Burbidge, G. 1993, *ApJS* **87** 451 (HB93)
- [50] Hooper, E. J., Impey, C. D., Foltz, C. B., & Hewett, P. C. 1995, *ApJ* **445** 62
- [51] Hooper, E. J., Impey, C. D., Foltz, C. B., & Hewett, P. C. 1996, *ApJ* **473** 746
- [52] Hopkins, A. M., Mobasher, B., Cram, L., & Rowan-Robinson, M. 1998, *MNRAS* **296** 839
- [53] Hutchings, J. B. 1995, *AJ* **110** 994
- [54] Hutchings, J. B., Holtzman, J., Sparks, W. B., Morris, S. C., Hanisch, R. J., & Mo, J. 1982, *ApJ* **429** L1
- [55] Hutchings, J. B., & Campbell, B. 1983, *Nature* **303** 16
- [56] Hutchings, J. B., & Morris, S. C. 1995, *AJ* **109** 1541
- [57] Hutchings, J. B., & Neff, S. G. 1987, *AJ* **104** 1
- [58] James F. 1994, *MINUIT: Function Minimization and Error Analysis* (CERN Program Libr. Long Writeup D506 version 94.1 Geneva: CERN)
- [59] Kellermann, K. I., Sramek, R. A., Schmidt, M., Green, R. F., & Shaffer, D. B. 1994, *AJ* **108** 1163
- [60] Kellermann, K. I., Sramek, R., Schmidt, M., Shaffer, D. B., & Green, R. 1989, *AJ* **98** 1195
- [61] Kembhavi, A., Misra, R., & Wadadekar, Y. 2000, *ApJ* (submitted)
- [62] Kembhavi, A., Wadadekar, Y., & Misra, R. 2000, *Proceedings X Recontres de Blois "The Birth of Galaxies"* eds. B. Guiderdoni et al. Editions Frontiere (in press)
- [63] Kembhavi, A., & Narlikar, J. 1999, *Quasars and Active Galactic Nuclei: an Introduction* (Cambridge: Cambridge Univ. Press)
- [64] Kent, S. M. 1985, *ApJS* **59** 115
- [65] Khosroshahi, H. G., Wadadekar, Y., Kembhavi, A., & Mobasher, B. 2000, *ApJ* **531** L103
- [66] Khosroshahi, H. G., Wadadekar, Y., & Kembhavi, A. 2000, *ApJ* **533** 162
- [67] Knapen, J. H., & van der Kruit, P. C. 1991, *A&A* **248** 57
- [68] Koo, D. C., & Szalay, A. S. 1984, *ApJ* **282** 390
- [69] Kormendy, J. 1977, *ApJ* **217** 406
- [70] Kormendy, J. 1982, in *Morphology and dynamics of galaxies* Eds. Martinet, L., & Meyer, M., (Geneva: Geneva Observatory)
- [71] Kristian, J. 1973, *ApJ* **179** L61
- [72] Kron, R. G. 1980, *ApJS* **43** 305
- [73] Kukula, M. J., Dunlop, J. S., Hughes, D. H., & Rawlings, S. 1998, *MNRAS* **297** 366
- [74] LaValley, M., Isobe, T., & Feigelson, E. 1992, *A.S.P. Conference Series* **Vol. 25** 245
- [75] Landolt, A. U. 1992, *AJ* **104** 340
- [76] Landolt, A. U. 1983, *AJ* **88** 439
- [77] Lehnert, M. D., Heckman, T. M., Chambers, K. C., & Miley, G. K. 1992, *ApJ* **393** 68
- [78] Lowenthal, J. D., Heckman, T. M., Lehnert, M. D., & Elias, J. H. 1995, *ApJ* **439** 588
- [79] Maddox, S.J., Efstathiou, G. & Sutherland, W.J. 1990, *MNRAS* **246** 433
- [80] Mahabal, A. 1998, Phd thesis, University of Pune
- [81] Mahabal, A., Kembhavi, A. K., & McCarthy, P. 1999, *ApJ* **516** L61
- [82] Marshall, H. L. 1987, *ApJ* **316** 84
- [83] Massey, P., Gronwall, C., & Pilachowski, C. A. 1990, *PASP* **102** 1046
- [84] Miller, L., Peacock, J. A., & Mead, A. R. G. 1990, *MNRAS* **244** 207 (MPM 90)
- [85] Mink, D. J. 1998, *Astronomical Data Analysis Software and Systems VIII, A.S.P. Conference Series* **Vol. 172** 498

- [86] Nonino, M. et al. 1999, *A&AS* **137** 51
- [87] Olsen, E. T. 1970, *AJ* **75** 764
- [88] Osterbrock, D. E. 1981, *ApJ* **249** 462
- [89] Peacock, J. A., Miller, L. & Longair, M. S. 1986, *MNRAS* **218** 265
- [90] Peletier, R.F., & Balcells, M. 1997, *New Astronomy* **1** 349
- [91] Poggianti, B. M. 1997, *A&AS* **122** 399
- [92] Press, W. H., Teukolsky, S. A., Vetterling, W. T., & Flannery, B. P. 1992, *Numerical Recipes in C* (2d ed. Cambridge: Cambridge Univ. Press)
- [93] Pritchett, C., & Kline, M. I. 1981, *AJ* **86** 1859
- [94] Rengelink, R. B. et al. 1997, *A&AS* **124** 259
- [95] Richards, E. A., Kellermann, K. I., Fomalont, E. B., Windhorst, R. A., & Partridge, R. B. 1998, *AJ* **116** 1039
- [96] Riley, J. M., Longair, M. S., & Gunn, J. E. 1980, *MNRAS* **192** 233
- [97] Rocca-Volmerange, B., & Guiderdoni, B. 1988, *A&AS* **75** 93
- [98] Roy, A. L., Norris, R. P., Kesteven, M. J., Troup, E. R., & Reynolds, J. E. 1998, *MNRAS* **301** 1019
- [99] Sandage, A. 1965, *ApJ* **141** 1560
- [100] Schmidt, M. 1970, *ApJ* **162** 371
- [101] Schmidt, M., & Green, R. F. 1983, *ApJ* **269** 352
- [102] Schombert, J. M., & Bothun, G. D. 1987, *AJ* **93** 60
- [103] Schweizer, F. 1979b, *AJ* **86** 662
- [104] Schweizer, F. 1979a, *ApJ* **233** 23
- [105] Simien, F. 1989, in *The World of Galaxies* ed. H. G. Corwin, Jr., & L. Bottinelli (New York: Springer) 293
- [106] Sopp, H. M., & Alexander, P. 1991, *MNRAS* **251** 14
- [107] Sramek, R.A., & Weedman, D.W. 1980, *ApJ* **238** 435
- [108] Stern, D. et al. 2000, *ApJ* (under preparation)
- [109] Stocke, J. T., Morris, S. L., Weymann, R. J., & Foltz, C. B. 1992, *ApJ* **396** 487
- [110] Terlevich, R., Tenorio-Tagle, G., Franco, J., & Melnick, J. 1992, *MNRAS* **255** 713
- [111] Thuan, T. X., & Condon, J. J. 1987, *ApJ* **322** L9
- [112] Ulvestad, J. S., & Wilson, A. S. 1984, *ApJ* **285** 439
- [113] Ulvestad, J. S., & Wilson, A. S. 1989, *ApJ* **343** 659
- [114] Urry, C. M. & Padovani, P. 1995, *PASP* **107** 803
- [115] van Albada, T. S. 1982, *MNRAS* **201** 939
- [116] van Breugel, W. J. M., Stanford, S. A., Spinrad, H., Stern, D., & Graham, J. R. 1998, *ApJ* **502** 614
- [117] Veron-Cetty, M. P. & Veron, P. 2000, *ESO Scientific Report No. 19* (Garching: ESO) (VV00)
- [118] Veron-Cetty, M.P., & Veron, P. 1991, *ESO Scientific Report No. 10* (Garching: ESO)
- [119] Visnovsky, K. L. et al. 1992, *ApJ* **391** 560
- [120] Voges, W. et al. 1999, *A&A* **349** 389
- [121] Wadadekar, Y. & Kembhavi, A. 2000, *AJ* (submitted)
- [122] Wadadekar, Y., Kembhavi, A., & McCarthy, P. 2000, *AJ* (submitted)
- [123] Wadadekar, Y., Robbason, R., & Kembhavi, A. 1999, *AJ* **119** 1219
- [124] Wadadekar, Y., & Kembhavi, A. 1999, *AJ* **118** 1435
- [125] Wall, J.V., & Peacock, J. A. 1985, *MNRAS* **216** 173
- [126] Weedman, D. W. 1980, *Quasar Astronomy* (Cambridge: Cambridge Univ. Press)
- [127] Weir, N., Fayyad, U. M., Djorgovski, S. G. & Roden, J. 1995, *PASP* **107** 1243
- [128] White, R. L. et al. 2000, *ApJS* **133** 207
- [129] White, R. L., Becker, R. H., Helfand, D. J., & Gregg, M. D. 1997, *ApJ* **475** 479
- [130] Windhorst, R. A., Fomalont, E. B., Partridge, R. B., & Lowenthal, J. D. 1993, *ApJ* **405** 498
- [131] Windhorst, R. A., Miley, G. K., Owen, F. N., Kron R. G. & Koo, D. C. 1985, *ApJ* **289** 494
- [132] Wunderlich, E.; Wielebinski, R., & Klein, U. 1987, *A&AS* **69** 487
- [133] Wyckoff, S., Wehinger, P. A., & Gehren, T. 1981, *ApJ* **247** 750
- [134] Yadigaroglu, I. A., Buchalter, A., Helfand, D. J, Becker, R. H. & White, R. L. 1998, *BAAS* **193** 401